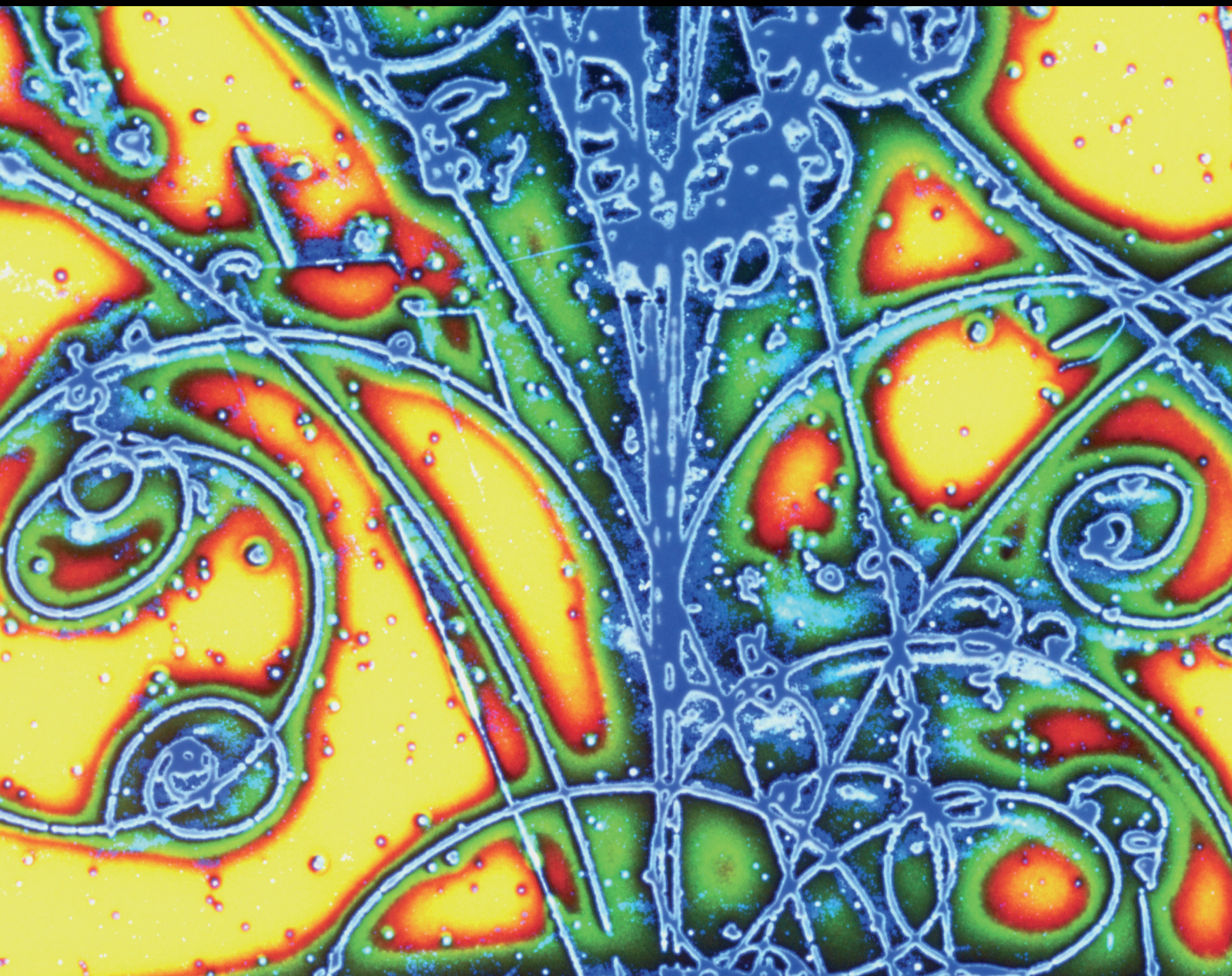


Advances in High Energy Physics

Neutrino Physics in the Frontiers of Intensities and Very High Sensitivities 2018

Special Issue Editor in Chief: Theocharis Kosmas

Guest Editors: Hiroyasu Ejiri and Athanasios Hatzikoutelis





**Neutrino Physics in the Frontiers of Intensities
and Very High Sensitivities 2018**

Advances in High Energy Physics

**Neutrino Physics in the Frontiers of Intensities
and Very High Sensitivities 2018**

Special Issue Editor in Chief: Theodoros Kosmas

Guest Editors: Hiroyasu Ejiri and Athanasios Hatzikoutelis



Copyright © 2019 Hindawi. All rights reserved.

This is a special issue published in “Advances in High Energy Physics.” All articles are open access articles distributed under the Creative Commons Attribution License, which permits unrestricted use, distribution, and reproduction in any medium, provided the original work is properly cited.

Editorial Board

Antonio J. Accioly, Brazil
Giovanni Amelino-Camelia, Italy
Luis A. Anchordoqui, USA
Michele Arzano, Italy
T. Asselmeyer-Maluga, Germany
Alessandro Baldini, Italy
Marco Battaglia, Switzerland
Lorenzo Bianchini, Switzerland
Roelof Bijker, Mexico
Burak Bilki, USA
Rong-Gen Cai, China
Anna Cimmino, France
Osvaldo Civitarese, Argentina
Andrea Coccaro, Italy
Shi-Hai Dong, Mexico
Lorenzo Fortunato, Italy
Mariana Frank, Canada
Ricardo G. Felipe, Portugal

Chao-Qiang Geng, Taiwan
Philippe Gras, France
Xiaochun He, USA
Luis Herrera, Spain
Filipe R. Joaquim, Portugal
Aurelio Juste, Spain
Theocharis Kosmas, Greece
Ming Liu, USA
Enrico Lunghi, USA
Salvatore Mignemi, Italy
Omar G. Miranda, Mexico
Grégory Moreau, France
Piero Nicolini, Germany
Carlos Pajares, Spain
Sergio Palomares-Ruiz, Spain
Giovanni Pauletta, Italy
Yvonne Peters, UK
Anastasios Petkou, Greece

Alexey A. Petrov, USA
Thomas Rössler, Sweden
Diego Saez-Chillon Gomez, Spain
Takao Sakaguchi, USA
Juan José Sanz-Cillero, Spain
Edward Sarkisyan-Grinbaum, USA
Sally Seidel, USA
George Siopsis, USA
Luca Stanco, Italy
Jouni Suhonen, Finland
Mariam Tórtola, Spain
Smarajit Triambak, South Africa
Jose M. Udías, Spain
Elias C. Vagenas, Kuwait
Sunny Vagnozzi, Sweden
Yau W. Wah, USA

Contents

Neutrino Physics in the Frontiers of Intensities and Very High Sensitivities 2018

Theocharis Kosmas , Hiroyasu Ejiri , and Athanasios Hatzikoutelis 
Editorial (3 pages), Article ID 4123108, Volume 2019 (2019)

High Scale Type-II Seesaw, Dominant Double Beta Decay within Cosmological Bound and LFV Decays in SU(5)

M. K. Parida  and Rajesh Satpathy
Research Article (19 pages), Article ID 3572862, Volume 2019 (2019)

Simulations of Gamma-Ray Emission from Magnetized Microquasar Jets

Odysseas Kosmas  and Theodoros Smponias 
Research Article (11 pages), Article ID 9602960, Volume 2018 (2019)

Neutral-Current Neutrino-Nucleus Scattering off Xe Isotopes

P. Pirinen , J. Suhonen , and E. Ydrefors
Research Article (11 pages), Article ID 9163586, Volume 2018 (2019)

Degeneracy Resolution Capabilities of NO ν A and DUNE in the Presence of Light Sterile Neutrino

Akshay Chatla , Sahithi Rudrabhatla , and Bindu A. Bambah
Research Article (11 pages), Article ID 2547358, Volume 2018 (2019)

Novel Neutrino-Floor and Dark Matter Searches with Deformed Shell Model Calculations

D. K. Papoulias , R. Sahu, T. S. Kosmas , V. K. B. Kota, and B. Nayak
Research Article (17 pages), Article ID 6031362, Volume 2018 (2019)

Deep Learning the Effects of Photon Sensors on the Event Reconstruction Performance in an Antineutrino Detector

Chang-Wei Loh, Zhi-Qiang Qian, Rui Zhang, You-Hang Liu, De-Wen Cao, Wei Wang, Hai-Bo Yang, and Ming Qi 
Research Article (7 pages), Article ID 7024309, Volume 2018 (2019)

Effects of Leptonic Nonunitarity on Lepton Flavor Violation, Neutrino Oscillation, Leptogenesis, and Lightest Neutrino Mass

Gayatri Ghosh  and Kalpana Bora 
Research Article (10 pages), Article ID 5093251, Volume 2018 (2019)

Neutrino Emission from Cooper Pairs at Finite Temperatures

Lev B. Leinson 
Review Article (11 pages), Article ID 8963453, Volume 2018 (2019)

Light WIMP Searches Involving Electron Scattering

J. D. Vergados , Ch. C. Moustakidis , Yeuk-Kwan E. Cheung, H. Ejiri , Yeongduk Kim, and Jeong-Yeon Lee
Research Article (14 pages), Article ID 6257198, Volume 2018 (2019)

Heavy Sterile Neutrino in Dark Matter Searches

Paraskevi C. Divari  and John D. Vergados 
Research Article (14 pages), Article ID 1479313, Volume 2018 (2019)

Editorial

Neutrino Physics in the Frontiers of Intensities and Very High Sensitivities 2018

Theocharis Kosmas ¹, Hiroyasu Ejiri ², and Athanasios Hatzikoutelis ³

¹Division of Theoretical Physics, University of Ioannina, GR-45110 Ioannina, Greece

²Research Center for Nuclear Physics, Osaka University, Ibaraki Osaka 567-0047, Japan

³Physics Department, University of Tennessee, Knoxville, TN, USA

Correspondence should be addressed to Theocharis Kosmas; hkosmas@uoi.gr and Hiroyasu Ejiri; ejiri@rcnp.osaka-u.ac.jp

Received 27 January 2019; Accepted 27 January 2019; Published 17 February 2019

Copyright © 2019 Theocharis Kosmas et al. This is an open access article distributed under the Creative Commons Attribution License, which permits unrestricted use, distribution, and reproduction in any medium, provided the original work is properly cited.

Neutrinos continue being widely studied, just as many decades ago, and have generated an intense scientific interest due to the wide variety of potential applications in particle physics, astro-nuclear physics, and cosmology based on the amassing properties they exhibit like their extremely small mass, their extremely small weak interaction with matter, the neutrino oscillations, and many others. Also, the neutrino production sources at the Earth and in other structures of the Universe are an essential cornerstone for the description of the structure and evolution of the stars.

After the very recent measurement, for the first time, coherent elastic neutrino-nucleus scattering (CE ν NS) events COHERENT experiment at Oak Ridge laboratory, neutrinos are understood to be involved in many aspects of the physics processes that are in the forefront of modern theoretical and experimental research. In particular, they play key role in probing physics beyond the Standard Model, explaining the matter-antimatter imbalance in the observable universe, and in operating as messengers from far objects like supernova, quasars, and many others. Furthermore, they have a place in national security applications and provide the research subject of a large number of new physicists around the world.

In the present special issue, we have once again collected, a list of articles showcasing the various themes of neutrino frontier research, from theoretical calculations on precision estimation of their interaction cross-section to ideas for mechanisms of pinpointing the neutrino mass in accelerators. We followed again the worldwide hunt for the neutrino parameters. The parameter space has been reduced to even narrower ranges of values at regularly increasing

confidence levels. The values of the mixing angles are now a common-place product of the neutrino sector research industry. Improved detailed simulations and ever increasing data samples, from the running experiments, exclude now the maximal mixing of theta-13 and the lower octant of the theta-23. Therefore, they are favoring the normal neutrino mass hierarchy for the moment, but if this is not the case, then this will cause the serious exclusion of CP violation in the neutrino sector. These ideas affect, critically, the grand-unified theories and the interpretation of the numerous neutrinoless double beta decay experiments.

This special issue consists 10 original research articles. Various open problems are investigated, like coherent elastic neutrino-nucleus scattering, conventional and exotic neutrino phenomena, neutrino properties including neutrino oscillations, nontrivial neutrino electromagnetic properties, neutrino-floor in dark matter detection experiments, and more. The last type is also employed to probe potential applications for unraveling a large variety of theories, within and beyond the standard model, that have appeared during the last decades, in an effort to answer the open questions through current neutrino searches.

In modeling neutrino properties and specifically neutrino mass and neutrino mass hierarchy, *M. K. Parida and R. Satpathy*, inspired by the new implementation of type-II seesaw mechanism in SU(5) grand unified theory, examine a possible application of the type-I seesaw cancellation mechanism in this SU(5) framework. The authors show that, in this context, they may predict, among other things, verifiable lepton flavor violation decays and phenomena predicted

by theories beyond the standard model (assuming normal or inverted hierarchy with/without heavy or light neutrino mass) as for example dominant double beta decay within the Cosmological Bound.

The emission of high energy neutrinos from astrophysical sources like Active Galactic Nuclei, binary stars, core collapse supernova, and others may be studied by 3D relativistic magneto-hydro-dynamical simulations. Using as a main computational tool the PLUTO hydrocode, *O. Kosmas and T. Smpontias* studied the high energy γ -ray and high energy neutrino emission from hadronic jets of binary stellar systems. They focus on black hole microquasar jets like those of the SS433 microquasar which consists of a compact object (BH) and a companion (donor) star. The authors primarily explore through simulations the dependence of the neutrino and γ -ray emissivity on the dynamical and radiative properties of the jet (the mass-flow density, gas-pressure, temperature of the ejected matter, high energy proton population inside the jet plasma, etc.).

In order to investigate the neutrino-floor in dark matter detection experiments, *D. K. Papoulias et al.* studied the potential efficiency of various promising nuclear isotopes (like ^{71}Ga , ^{73}Ge , ^{75}As etc.) as direct dark matter detectors in WIMP-nucleus interaction experiments. They carried out extensive calculations for the event detection rates of WIMP-nucleus reactions on the basis of the deformed shell model. One of the main aims of this investigation is to explore how important is the neutrino-floor as a source of background to dark matter searches within coherent elastic neutrino-nucleus scattering (CE ν NS). As it is known, events of this process have only recently been measured at Oak Ridge laboratory. The method employed for the required nuclear structure calculation was the deformed nuclear shell model based on the self-consistent solutions of the Hatree-Fock single particle equations in order to obtain the nuclear states.

The investigation of the various effects of nuclear structure impacting the neutrino-nucleus scattering processes is an interesting open issue. Towards this aim, *P. Pirinen et al.* made an attempt to contribute to the importance of distinguishing the neutrino backgrounds in various dark matter (DM) detection experiments focusing on the large liquid xenon detectors used in DM direct detection. The nuclear structure calculations are performed in the nuclear shell model (for elastic scattering) and also in the quasi-particle random-phase approximation (QRPA) and microscopic quasi-particle phonon model (MQPM) for both elastic and inelastic scattering of Xe isotopes. For neutrino sources, these authors consider the ^8B solar neutrinos and supernova neutrinos.

A. Chatla et al. investigate the degeneracy resolution capabilities of the NO ν A and DUNE neutrino experiments in the presence of light sterile neutrino. They investigate implications of a sterile neutrino on the physics potential of the proposed experiment DUNE and the future runs of NO ν A using the latest results. This work is of interest to the experimental study of the possible sterile neutrino.

G. Ghosh and K. Bora study the possibility of existence of (small) effects on lepton flavor violation, neutrino oscillation,

leptogenesis, and lightest neutrino mass, due to the fact that up to now the unitarity in the leptonic sector (leptonic mixing matrix) has not yet been established, despite the precise measurements of the neutrino oscillations and neutrino mixing parameters (mass squared differences, mixing angles, etc.) existing from many experiments. The authors extract the bounds on the nonunitarity parameters from the existing experimental data (e.g., on the cLFV processes like the $\mu \rightarrow e\gamma$, $\mu \rightarrow e$ conversion).

C.-W. Loh et al. describe how deep learning improves the event reconstruction performance of photon sensors in an antineutrino detector. The Daya Bay detector's vertex position resolution follows a multiexponential relationship with respect to the number of PMTs. This work shows the power of deep learning in helping in the detector design, which is crucial for high-sensitivity neutrino experiments.

In the various neutrino-sources, neutrinos are produced through several emission mechanisms. *L. B. Leinson* investigate the case of neutrino emission from breaking and formation of Cooper-pairs at finite temperatures through a neutral currents weak process. This reaction may take place in superfluid baryon matter at thermal equilibrium in neutron stars and collapsing stellar interior that considerably slows down the cooling rate of neutron stars with superfluid cores. The relevant phenomena play an important role for the correct description of the anomalous weak interactions in both the vector and axial channels.

The possibilities of detecting a heavy sterile neutrino (with mass about 50 keV) in dark matter experiments through several detection mechanisms and experimental techniques are examined in the contribution of *P. C. Divari and J. D. Vergados*. Some examples are the measuring of electron recoils in materials with low electron binding, the low-temperature crystal bolometers, the spin induced atomic excitations at low temperatures, observation of resonances in antineutrino absorption resonances in electron capture on nuclei, and β^- decay induced by neutrinos (e.g., KATRIN experiment).

Among the most attractive cold dark matter candidates, the weakly interacting massive particles (WIMPs) have attracted the investigation of many authors the last decades. In their contribution, *J. D. Vergados et al.* focus on light WIMP searches involving electron scattering. They examined the possibility for detecting electrons in light dark matter searches. These detectors are appropriate for light dark matter particles with a mass of the MeV region. The authors analyze theoretically key issues of such a detector for a specific particle model involving scalar particles as WIMPs communicating with both electrons and quarks with Higgs exchange. They also examine experimental aspects of detecting low energy electrons in these dark matter searches. This work presents interesting theoretical and experimental views on possible studies of light dark matter particles.

In summary, this special issue provides a detailed account of the present status of neutrino physics. It highlights recent developments on the novel and important aspects of these particles and their studies with the ongoing and the planned, remarkably sensitive, experiments. The race for the determination of the mass hierarchy at an observation level is

expected to conclude in next few years, while the effort for coverage of the CP violation range will last a decade more as it is understood now. Regardless, each step of understanding that comes from the work of groups (large and small) published in articles, like the ones we include in this special issue, brings us one step closer towards unraveling the last of the mysteries of the Standard Model and open the chapter to the New Physics beyond.

Disclosure

Theocharis Kosmas and Hiroyasu Ejiri are co-first authors.

Conflicts of Interest

The authors declare that they have no conflicts of interest.

Acknowledgments

The editors would like to thank all authors who submitted their research to this special issue, as well as all reviewers for their valuable contribution.

Theocharis Kosmas
Hiroyasu Ejiri
Athanasios Hatzikoutelis

Research Article

High Scale Type-II Seesaw, Dominant Double Beta Decay within Cosmological Bound and LFV Decays in SU(5)

M. K. Parida  and Rajesh Satpathy

Centre for Excellence in Theoretical and Mathematical Sciences, Siksha 'O' Anusandhan (SOA) Deemed to be University, Khandagiri Square, Bhubaneswar 751030, India

Correspondence should be addressed to M. K. Parida; minaparida@soa.ac.in

Received 2 September 2018; Accepted 17 December 2018; Published 3 February 2019

Guest Editor: Hiroyasu Ejiri

Copyright © 2019 M. K. Parida and Rajesh Satpathy. This is an open access article distributed under the Creative Commons Attribution License, which permits unrestricted use, distribution, and reproduction in any medium, provided the original work is properly cited. The publication of this article was funded by SCOAP³.

Very recently novel implementation of type-II seesaw mechanism for neutrino mass has been proposed in SU(5) grand unified theory with a number of desirable new physical phenomena beyond the standard model. Introducing heavy right-handed neutrinos and extra fermion singlets, in this work we show how the type-I seesaw cancellation mechanism works in this SU(5) framework. Besides predicting verifiable LFV decays, we further show that the model predicts dominant double beta decay with normal hierarchy or inverted hierarchy of active light neutrino masses in concordance with cosmological bound. In addition a novel right-handed neutrino mass generation mechanism, independent of type-II seesaw predicted mass hierarchy, is suggested in this work.

1. Introduction

Renormalizable standard model (SM) predicts neutrinos to be massless whereas oscillation experiments prove them to be massive [1–5]. All the generational mixings have been found to be much larger than the corresponding quark mixings. Theoretically [6–13] neutrino masses are predicted through various seesaw mechanisms [14–43]. In a minimal left-right symmetric [44–47] grand unified theory (GUT) like SO(10) [48, 49] where parity (P) violation in weak interaction is explained along with fermion masses [50–55], a number of these seesaw mechanisms can be naturally embedded while unifying the three forces of the SM [56–72]. More recently precision gauge coupling unification has been successfully implemented in direct symmetry breaking of SO(18) \rightarrow SM which may have high potential for new physics [73].

The SO(10) model that predicts the most popular canonical seesaw as well as the type-II seesaw has also the ability to explain baryon asymmetry of the universe via leptogenesis through heavy RH neutrino [74] or Higgs triplet decays [75–77]. But because of underlying quark lepton symmetry [44], the type-I seesaw scale as well as RH ν masses are so large that the model predicts negligible lepton flavor violating

(LFV) decays like $\mu \rightarrow e\gamma$, $\tau \rightarrow \mu\gamma$, $\tau \rightarrow e\gamma$, and $\mu \rightarrow e\bar{e}e$. Similarly direct mediation of large mass of scalar triplet required for type-II seesaw gives negligible contribution to lepton number violating (LNV) and lepton flavor violating (LFV) decays. Ever since the proposal of left-right symmetry, extensive investigations continue in search of experimentally observable double beta decay [78–82] in the $W_R - W_R$ channel [83, 84]. Adding new dimension to such lepton number violating (LNV) process, the like-sign dilepton production has been suggested as a possible means of detection of W_R -boson at accelerator energies [85], particularly the LHC [43]. However, no such signals of TeV scale W_R - have been detected so far. Even if W_R mass and seesaw scales are large and inaccessible for direct verification, neutrinoless double beta decay ($0\nu 2\beta$) in the $W_L - W_L$ channel [20, 86–91] is predicted close to observable limit with $\tau_{\beta\beta} \geq 10^{25}$ yrs provided light neutrino masses predicted by such high scale seesaw mechanisms are quasidegenerate (QD) with each mass $m_i \geq \mathcal{O}(0.2)$ eV [78] and their sum > 0.6 eV. But as noted by the recent Planck data such QD type masses violate the cosmological bound [92].

$$\Sigma_\nu \equiv \Sigma_i \hat{m}_i \leq 0.23 \text{ (eV)}. \quad (1)$$

The fact that such QD type ν masses violate the cosmological bound may be unravelling another basic fundamental reason why detection of double beta decay continues to elude experimental observation for several decades. On the other hand, if neutrinos have smaller NH or IH type masses, there is no hope for detection of these LNV events in near future with RH ν extended SM. In other words, predicting observable double beta decay in the $W_L - W_L$ channel with left-handed helicities of both the beta particles has been a formidable problem confronting theoretical and experimental physicists. However, it has been shown that in case of dynamical seesaw mechanism generating Dirac neutrinos the seesaw scale is accessible for direct experimental verification [93].

The path breaking discovery of inverse seesaw [25–31] with one extra singlet fermion per generation not only opened up the neutrino mass generation mechanism for direct experimental tests, but also lifted up lepton flavor violating (LFV) decays [94] from the abysmal depth of experimental inaccessibility of negligible branching ratios ($Br.(l_\alpha \rightarrow l_\beta \gamma) \sim 10^{-50}$) to the illuminating salvation of profound observability ($Br. \approx 10^{-8} - 10^{-16}$) [95–100] which has been discussed extensively [99, 101–118]. Despite inverse seesaw, observable double beta decay in the $W_L - W_L$ channel and the non-QD type neutrino masses remained mutually exclusive until both the RH neutrinos and singlet fermions (S_i) were brought into the arena of LFV and LNV conundrum through the much needed extension of the Higgs sector. The King-Kang [119] mechanism cancelled out the ruling supremacy of canonical seesaw which was profoundly exploited in SO(10) models with the introduction of both the SO(10) Higgs representations 16_H and 126_H^\dagger [13, 84, 120–125] with successful prediction of observable double beta decay in the $W_L - W_L$ channel [20, 86]. Very interestingly, even though high scale type-II seesaw can govern light neutrino masses of any hierarchy, possibility of observable LFV and double beta decay prediction in the $W_L - W_L$ channel irrespective of light neutrino mass hierarchies has been realized at least theoretically [13, 125].

The purpose of this work is to point out that there are new interesting physics realizations with suitable extension of a non-SUSY SU(5) GUT model proposed recently [126] where type-II seesaw, precision coupling unification, verifiable proton decay, scalar dark matter, and vacuum stability have been already predicted. However with naturally large type-II seesaw scale $> 10^{9.2}$ GeV, observable double beta decay accessible to ongoing experiments [78–82] is possible in this model too with QD type neutrinos only of common mass with $|m_0| \geq 0.2$ eV like many other high scale seesaw models as noted above. In this work we make additional prediction that dominant double beta decay in the $W_L - W_L$ channel can be realized with NH or IH type hierarchy consistent with much lighter neutrino masses $|m_i| \ll 0.2$ eV. Thus, this realization is consistent with cosmological bound of (1). Although such possibilities were realized earlier in SO(10) with TeV scale W_R or Z' bosons as noted above, in SU(5) without the presence of left-right symmetry and associated gauge bosons, we have shown here for the first time that the dominant double beta decay is mediated by a sterile

neutrino (Majorana fermion singlet) of $\mathcal{O}(1)$ GeV mass of first generation. The model further predicts LFV decay branching ratios only 4–5 orders smaller than the current experimental limits. An additional interesting part of the present work is the first suggestion of a new mechanism for heavy RH ν mass generation that permits these masses to have hierarchies independent of conventional type-II seesaw prediction. Thus highlights of the present model are as follows:

- (i) first implementation of type-I seesaw cancellation mechanism leading to the dominance of type-II seesaw in SU(5);
- (ii) prediction of verifiable LFV decays only 4 – 5 orders smaller than the current experimental limits;
- (iii) prediction of dominant double beta decay in the $W_L - W_L$ channel close to the current experimental limits for light neutrino masses of NH or IH type in concordance with cosmological bound;
- (iv) suggestion of a new right-handed neutrino mass generation mechanism independent of type-II predicted mass hierarchy;
- (v) precision gauge coupling unification with verifiable proton decay which is the same as discussed in [126].

This paper is organised in the following manner. In Section 2 we briefly review the SU(5) model along with gauge coupling unification and predictions of the intermediate scales. In Section 3 we discuss how type-I seesaw formula for active neutrino masses cancels out giving rise to dominance of type-II seesaw and prediction of another type-I seesaw formula for sterile neutrino masses. Fit to neutrino oscillation data is discussed in Section 4. In Section 5 we suggest a new mechanism of RH ν mass generation. Prediction on LFV decay branching ratios is discussed in Section 6. Lifetime prediction for double beta decay is presented in Section 7. In Section 8 we discuss the results of this work and state our conclusion. Block diagonalization procedure is explained in more detail in Appendix A.

2. A Non-Supersymmetric SU(5) Model

2.1. Extension of SU(5). As noted in [127], inclusion of the scalar $\kappa(3, 0, 8) \subset 75_H$ with mass $M_\kappa = 10^{9.23}$ GeV in the extended non-SUSY SU(5) achieves precision gauge coupling unification. Then it has been shown in [126] that type-II seesaw ansatz for neutrino mass is realized by inserting the entire Higgs multiplet $15_H \subset SU(5)$ containing the LH Higgs triplet $\Delta_L(3, -1, 1)$ at the same mass scale $M_{15_H} = 10^{12}$ GeV.

$$\begin{aligned} \kappa(3, 0, 8) \subset 75_H, \quad M_\kappa &= 10^{9.23} \text{ GeV}, \\ \Delta_L(3, -1, 1) \subset 15_H, \quad M_{15_H} &= 10^{12} \text{ GeV}, \quad (2) \\ \xi(1, 0, 1), \quad M_\xi &\sim \mathcal{O}(1) \text{ TeV}. \end{aligned}$$

The scalar singlet $\xi(1, 0, 1)$ has played two crucial interesting roles of stabilising the SM scalar potential as well as serving as WIMP DM candidate. The introduction of 15_H at any scale

$> 10^{9.23}$ GeV in this model maintains precision coupling unification. In the present model we extend the model further by the inclusion of the following fermions and an additional scalar $\chi_S(1, 0, 1)$:

- (i) three right-handed neutrino singlets N_i ($i = 1, 2, 3$), one for each generation, with masses to be fixed by this model phenomenology;
- (ii) three left-handed Majorana fermion singlets S_i ($i = 1, 2, 3$), one for each generation, similar to those introduced in case of inverse seesaw mechanism [25–31];
- (iii) a Higgs scalar singlet $\chi_S(1, 0, 1)$ to generate $S - N$ mixings through its VEV.

Being singlets under the SM gauge group, they do not affect precision gauge coupling unification of [126].

2.2. Coupling Unification, GUT Scale, and Proton Lifetime. As already discussed [126, 127] using renormalization group equations for gauge couplings and the set of Higgs scalars of (2), precision unification has been achieved with the PDG values of input parameters [128–130] on $\sin^2 \theta_W(M_Z)$, $\alpha_S(M_Z)$ resulting in the following mass scales and the GUT fine-structure constant α_G :

$$\begin{aligned} M_U &= 10^{15.23} \text{ GeV}, \\ M_\kappa &= 10^{9.23} \text{ GeV}, \\ M_{\Delta_L} &= M_{15_H} = 10^{12} \text{ GeV}, \\ \frac{1}{\alpha_G} &= 37.765. \end{aligned} \quad (3)$$

Using threshold effects due to superheavy Higgs scalars [131–138], proton lifetime prediction for $p \rightarrow e^+ \pi^0$ turns out to be in the experimentally accessible range [139]:

$$\begin{aligned} \tau_p(p \rightarrow e^+ \pi^0) &= (1.01 \times 10^{34 \pm 0.44}) \\ &- (5.5 \times 10^{35 \pm 0.44}) \text{ yrs.} \end{aligned} \quad (4)$$

Extensive investigations with number of SU(5) GUT extensions have been carried out with proton lifetime predictions consistent with experimental limits [140–149]. But implementation of type-II seesaw dominance due to type-I seesaw cancellation resulting in dominant LFV and LNV decays as discussed below is new especially in the context of non-SUSY SU(5).

3. Cancellation of Type-I and Dominance of Type-II Seesaw

Due to introduction of heavy RH ν s in the present model which were absent in [126], it may be natural to presume a priori that besides type-II seesaw, type-I seesaw may also contribute substantially to light neutrino masses and mixings. But it has been noted that there is a natural mechanism

to cancel out type-I seesaw contribution while maintaining dominance of inverse seesaw [84, 119, 120, 122–124] or type-II seesaw or even linear seesaw [13, 125] as the case may be. Briefly we discuss below how this cancellation mechanism operates in the present extended model resulting in type-II seesaw dominance even in the presence of heavy RH ν s.

The SM invariant Yukawa Lagrangian of the model is

$$\begin{aligned} \mathcal{L}_{\text{Yuk}} &= Y^\ell \bar{\psi}_L \psi_R \phi + f \psi_L^c \psi_L \Delta_L + y_\chi \bar{N}^C S \chi_S \\ &+ \left(\frac{1}{2}\right) M_N \bar{N}^C N + h.c. \end{aligned} \quad (5)$$

Using the VEVs of the Higgs fields and denoting $M = y_\chi \langle \chi_S \rangle = y_\chi V_\chi$, $M_D = Y \langle \phi \rangle$, a 9×9 neutral fermion mass matrix has been obtained which, upon block diagonalization, yields 3×3 mass matrices for each of the light neutrino (ν_α), the right-handed neutrino (N_α), and the sterile neutrino (S_α) [120, 124, 125]. The block diagonalization of 9×9 neutral fermion mass matrix was presented in useful format in [32] but without cancellation of type-I seesaw. Later on, this diagonalization procedure has been effectively utilized to study the type-I seesaw cancellation mechanism in SO(10) models [13, 120, 124, 125].

In this model the left-handed triplet Δ_L and RH neutrinos M_N being much heavier than the other mass scales with $M_{\Delta_L} \gg M_N \gg M \gg M_D$ are at first integrated out from the Lagrangian leading to

$$\begin{aligned} -\mathcal{L}_{\text{eff}} &= \left(m_\nu^H + M_D \frac{1}{M_N} M_D^T\right)_{\alpha\beta} \nu_\alpha^T \nu_\beta \\ &+ \left(M_D \frac{1}{M_N} M^T\right)_{\alpha m} (\bar{\nu}_\alpha S_m + \bar{S}_m \nu_\alpha) \\ &+ \left(M \frac{1}{M_N} M^T\right)_{mn} S_m^T S_n, \end{aligned} \quad (6)$$

which, in the (ν, S) basis, gives the 6×6 mass matrix

$$\mathcal{M}_{\text{eff}} = \begin{pmatrix} M_D M_N^{-1} M_D^T + m_\nu^H & M_D M_N^{-1} M^T \\ M M_N^{-1} M_D^T & M M_N^{-1} M^T \end{pmatrix}, \quad (7)$$

while the 3×3 heavy RH neutrino mass matrix M_N is the other part of the full 9×9 neutrino mass matrix. This 9×9 mass matrix $\widetilde{\mathcal{M}}_{BD}$ which results from the first step of block diagonalization procedure as discussed above and in the Appendix is

$$\mathcal{W}_1^\dagger \mathcal{M}_\nu \mathcal{W}_1^* = \widetilde{\mathcal{M}}_{BD} = \begin{pmatrix} \mathcal{M}_{\text{eff}} & 0 \\ 0 & M_N \end{pmatrix}. \quad (8)$$

Defining

$$\begin{aligned} X &= M_D M^{-1}, \\ Y &= M M_N^{-1}, \\ Z &= M_D M_N^{-1}, \end{aligned} \quad (9)$$

the transformation matrix \mathcal{W}_1 has been derived as shown in (10) [120, 125]

$$\mathcal{W}_1 = \begin{pmatrix} 1 - \frac{1}{2}ZZ^\dagger & -\frac{1}{2}ZY^\dagger & Z \\ -\frac{1}{2}YZ^\dagger & 1 - \frac{1}{2}YY^\dagger & Y \\ -Z^\dagger & -Y^\dagger & 1 - \frac{1}{2}(Z^\dagger Z + Y^\dagger Y) \end{pmatrix}. \quad (10)$$

After the second step of block diagonalization, the type-I seesaw contribution cancels out and gives in the (ν, S, N) basis

$$\mathcal{W}_2^\dagger \widetilde{\mathcal{M}}_{\text{BD}} \mathcal{W}_2 = \mathcal{M}_{\text{BD}} = \begin{pmatrix} m_\nu & 0 & 0 \\ 0 & m_S & 0 \\ 0 & 0 & m_{\mathcal{N}} \end{pmatrix}, \quad (11)$$

where \mathcal{W}_2 has been derived in (12) [120, 125]. We have used the bare mass of S_i and VEV of $\chi_L(2, -1/2, 1)$ to be vanishing, i.e., $\mu_S = 0, \langle \chi_L \rangle = 0$, to get the form suitable for this model building.

$$\mathcal{W}_2 = \begin{pmatrix} 1 - \frac{1}{2}XX^\dagger & X & 0 \\ -X^\dagger & 1 - \frac{1}{2}X^\dagger X & 0 \\ 0 & 0 & 1 \end{pmatrix} \quad (12)$$

$$\mathcal{V} \equiv \begin{pmatrix} \mathcal{V}_{\alpha i}^{\nu\bar{\nu}} & \mathcal{V}_{\alpha j}^{\nu\bar{S}} & \mathcal{V}_{\alpha k}^{\nu\bar{N}} \\ \mathcal{V}_{\beta i}^{S\bar{\nu}} & \mathcal{V}_{\beta j}^{S\bar{S}} & \mathcal{V}_{\beta k}^{S\bar{N}} \\ \mathcal{V}_{\gamma i}^{N\bar{\nu}} & \mathcal{V}_{\gamma j}^{N\bar{S}} & \mathcal{V}_{\gamma k}^{N\bar{N}} \end{pmatrix} \quad (17)$$

$$= \begin{pmatrix} \left(1 - \frac{1}{2}XX^\dagger\right)U_\nu & \left(X - \frac{1}{2}ZY^\dagger\right)U_S & ZU_N \\ -X^\dagger U_\nu & \left(1 - \frac{1}{2}\{X^\dagger X + YY^\dagger\}\right)U_S & \left(Y - \frac{1}{2}X^\dagger Z\right)U_N \\ 0 & -Y^\dagger U_S & \left(1 - \frac{1}{2}Y^\dagger Y\right)U_N \end{pmatrix}, \quad (18)$$

as shown in the Appendix. In (18), $X = M_D M^{-1}$, $Y = M M_N^{-1}$, and $Z = M_D M_N^{-1}$.

The mass of the singlet fermion is acquired through a type-I seesaw mechanism:

$$m_S = -M \frac{1}{M_N} M^T \quad (19)$$

where M is the $N - S$ mixing mass term in the Yukawa Lagrangian (6).

4. Type-II Seesaw Fit to Oscillation Data

4.1. Neutrino Mass Matrix from Oscillation Data. Using diagonalization of neutrino mass matrix (m_ν) by the PMNS matrix U_{PMNS}

$$m_\nu = U_{\text{PMNS}} \text{diag}(m_1, m_2, m_3) U_{\text{PMNS}}^T, \quad (20)$$

In (11) the three 3×3 matrices are

$$m_\nu = m_\nu^{\text{II}} = f \nu_L \quad (13)$$

$$m_S = -M M_N^{-1} M^T \quad (14)$$

$$m_{\mathcal{N}} = M_N, \quad (15)$$

the first of which is the well-known type-II seesaw formula and the second is the emergence of the corresponding type-I seesaw formula for the singlet fermion mass. The third of the above equations represents the heavy RH ν mass matrix.

In the third step, m_ν, m_S , and $m_{\mathcal{N}}$ are further diagonalized by the respective unitary matrices to give their corresponding eigenvalues:

$$U_\nu^\dagger m_\nu U_\nu^* = \widehat{m}_\nu = \text{diag}(m_1, m_2, m_3),$$

$$U_S^\dagger m_S U_S^* = \widehat{m}_S = \text{diag}(m_{S_1}, m_{S_2}, m_{S_3}), \quad (16)$$

$$U_N^\dagger m_{\mathcal{N}} U_N^* = \widehat{m}_N = \text{diag}(M_{N_1}, M_{N_2}, M_{N_3}).$$

The complete mixing matrix [32, 120] diagonalizing the above 9×9 neutrino mass matrix occurring in (8) and in (A.1) of the Appendix turns out to be

where m_i ($i = 1, 2, 3$) denote the mass eigen values. For neutrino mixings we use the abbreviated cyclic notations $t_i = \sin \theta_{jk}$, $c_i = \cos \theta_{jk}$, where i, j, k are cyclic permutations of generational numbers 1, 2, 3. Following the standard parametrisation we denote the PMNS matrix [128–130]

$$U_{\text{PMNS}} = \begin{pmatrix} c_3 c_2 & t_3 c_2 & t_2 e^{-i\delta_D} \\ -t_3 c_1 - c_3 t_1 t_2 e^{i\delta_D} & c_3 c_1 - t_3 t_1 t_2 e^{i\delta_D} & t_1 c_2 \\ t_3 t_1 - c_3 c_1 s_2 e^{i\delta_D} & -c_3 t_1 - t_3 c_1 t_2 e^{i\delta_D} & c_1 c_2 \end{pmatrix} \cdot \text{diag}(e^{i\alpha_M/2}, e^{i\beta_M/2}, 1), \quad (21)$$

where δ_D is the Dirac CP phase and (α_M, β_M) are Majorana phases.

Here we present numerical analyses within 3σ limit of the neutrino oscillation data in the type-II seesaw framework [126]. As we do not have any experimental information about Majorana phases, they are determined by means of random sampling; i.e., from the set of randomly generated values, each confined within the maximum allowed limit of 2π , only one set of values for (α_M, β_M) is chosen. Very recent analysis of the oscillation data has determined the 3σ and 1σ limits of Dirac CP phase δ_D [1]. The best fit values of δ_D in the normally ordered (NO) and inverted ordered (IO) cases are near 1.2π and 1.5π , respectively, which we utilize for the sake of simplicity. A phenomenological model analysis has yielded $\delta_D = \pm 1.32\pi$ [150].

Global fit to the oscillation data [1] is summarized below including respective parameter uncertainties at 3σ level:

$$\begin{aligned}
\theta_{12}^\circ &= 34.5 \pm 3.25, \\
\theta_{23}^\circ \text{ (NO)} &= 41.0 \pm 7.25, \\
\theta_{23}^\circ \text{ (IO)} &= 50.5 \pm 7.25, \\
\theta_{13}^\circ \text{ (NO)} &= 8.44 \pm 0.5, \\
\theta_{13}^\circ \text{ (IO)} &= 8.44 \pm 0.5, \\
\frac{\delta_D}{\pi \text{ (NO)}} &= 1.40 \pm 1.0, \\
\frac{\delta_D}{\pi \text{ (IO)}} &= 1.44 \pm 1.0, \\
\Delta m_{21}^2 &= (7.56 \pm 0.545) \times 10^{-5} \text{ eV}^2, \\
|\Delta m_{31}|^2 \text{ (NO)} &= (2.55 \pm 0.12) \times 10^{-3} \text{ eV}^2, \\
|\Delta m_{31}|^2 \text{ (IO)} &= (2.49 \pm 0.12) \times 10^{-3} \text{ eV}^2.
\end{aligned} \tag{22}$$

We denote the cosmologically constrained parameter, the sum of the three active neutrino masses, as

$$\Sigma_\nu = \Sigma_i \widehat{m}_i. \tag{23}$$

For normally hierarchical (NH), inverted hierarchical (IH), and quasidegenerate (QD) patterns, the experimental values of mass squared differences have been fitted by the following values of light neutrino masses and the respective values of the cosmological parameter Σ_ν ,

$$\begin{aligned}
\widehat{m}_\nu &= (0.00127, 0.008838, 0.04978) \text{ eV} \quad \text{(NH)} \\
\Sigma_\nu &= 0.059888 \text{ eV}, \\
\widehat{m}_\nu &= (0.04901, 0.04978, 0.00127) \text{ eV} \quad \text{(IH)} \\
\Sigma_\nu &= 0.059888 \text{ eV}, \\
\widehat{m}_\nu &= (0.2056, 0.2058, 0.2) \text{ eV} \quad \text{(QD)}, \\
\Sigma_\nu &= 0.6114 \text{ eV}.
\end{aligned} \tag{24}$$

Using oscillation data and best fit values of the mixings, we have also determined the PMNS mixing matrix numerically:

$$\begin{aligned}
U_{\text{PMNS}} &= \begin{pmatrix} 0.816 & 0.56 & -0.0199 - 0.0142i \\ -0.354 - 0.0495i & 0.675 - 0.0346i & 0.650 \\ 0.450 - 0.0568i & -0.485 - 0.0395i & 0.75 \end{pmatrix}. \tag{25}
\end{aligned}$$

4.2. Determination of Majorana Yukawa Coupling Matrix.

Now inverting the relation $\widehat{m}_\nu = U_{\text{PMNS}}^\dagger \mathcal{M}_\nu U_{\text{PMNS}}^*$ where \widehat{m}_ν is the diagonalized neutrino mass matrix, we determine \mathcal{M}_ν for three different cases and further determine the corresponding values of the f matrix using $f = \mathcal{M}_\nu / \nu_L$ where we use the predicted value of $\nu_L = 0.1 \text{ eV}$.

NH

$$\begin{aligned}
f &= \begin{pmatrix} 0.117 + 0.022i & -0.124 - 0.003i & 0.144 + 0.025i \\ -0.124 - 0.003i & 0.158 - 0.014i & -0.141 + 0.017i \\ 0.144 + 0.025i & -0.141 + 0.017i & 0.313 - 0.00029i \end{pmatrix} \tag{26}
\end{aligned}$$

IH

$$\begin{aligned}
f &= \begin{pmatrix} 0.390 - 0.017i & 0.099 + 0.01i & -0.16 + 0.05i \\ 0.099 + 0.01i & 0.379 + 0.02i & 0.176 + 0.036i \\ -0.16 + 0.05i & 0.176 + 0.036i & 0.21 - 0.011i \end{pmatrix} \tag{27}
\end{aligned}$$

QD

$$\begin{aligned}
f &= \begin{pmatrix} 2.02 + 0.02i & 0.0011 + 0.02i & -0.019 + 0.3i \\ 0.0011 + 0.02i & 2.034 + 0.017i & 0.021 + 0.21i \\ -0.019 + 0.3i & 0.021 + 0.21i & 1.99 - 0.04i \end{pmatrix} \tag{28}
\end{aligned}$$

Randomly chosen Majorana phases [126] $\alpha_M = 74.84^\circ$, $\beta_M = 112.85^\circ$, and the central value of the Dirac phase $\delta_D = 218^\circ$ have been used in this analysis. Using the well-known definition of the Jarlskog-Greenberg [151, 152] invariant,

$$J_{\text{CP}} = -t_3 c_3 t_2 c_2^2 t_1 c_1 \sin \delta_D, \tag{29}$$

and keeping δ_D at its best fit values, we have estimated the predicted allowed ranges of the CP-violating parameter in both cases:

$$\begin{aligned}
J_{\text{CP}} &= 0.0175 - 0.0212 \quad \text{(NH)} \\
J_{\text{CP}} &= 0.0302 - 0.0365 \quad \text{(IH)}
\end{aligned} \tag{30}$$

where the variables have been permitted to acquire values within their respective 3σ ranges of the oscillation data. Besides these there are nonunitarity contributions which have been discussed extensively in the literature.

4.3. *Scaling Transformation of Solutions.* In general there could be type-II seesaw models characterizing different seesaw scales and induced VEVs matching the given set of neutrino oscillation data represented by the same neutrino mass matrix. For two such models,

$$\begin{aligned} m_\nu &= f^{(1)} v_L^{(1)} \\ &= f^{(2)} v_L^{(2)}, \end{aligned} \quad (31)$$

Then the f -matrix in one case is determined up to good approximation in terms of the other from the knowledge of the two seesaw scales.

$$f^{(1)} \simeq f^{(2)} \frac{M_{\Delta^{(1)}}}{M_{\Delta^{(2)}}} \quad (32)$$

At $M_{\Delta^{(1)}} = 10^{12}$ GeV our solutions are the same as in [126]. In view of this scaling relation, we can determine the values of the Majorana Yukawa matrix in the present case from the estimations of [126]. For example, if we choose $M_{\Delta^{(1)}} = 10^{10}$ GeV in the present case compared to $M_{\Delta^{(2)}} = 10^{12}$ GeV in [126], we rescale the solutions of [126] by a factor 10^{-2} to derive solutions in the present case. Thus graphical representations of solutions are similar to those of [126] for $M_{\Delta^{(2)}} = 10^{12}$ GeV which we do not repeat here. The values of magnitudes of f_{ij} at any new scale are obtained by rescaling them by the appropriate scaling factor while the phase angles remain the same as in [126].

4.4. *Dirac Neutrino Mass Matrix.* The Dirac neutrino mass matrix M_D plays crucial role in predicting LFV and LNV decays. In certain SO(10) models [50, 51, 125] this is usually determined by fitting the charged fermion masses at the GUT scale and equating it with the up-quark mass matrix. The fact that $M_D^0 \simeq M_u^0$ at the GUT scale follows from the underlying quark lepton symmetry [44] of SO(10). In SU(5) itself, however, there is no such symmetry to predict the structure of M_D in terms of quark matrices. Also in this SU(5) model we do not attempt any charged fermion mass fit at the GUT scale or above it. Since the Dirac neutrino mass matrix is not predicted by the SU(5) symmetry itself, for the sake of simplicity and to derive maximal effects on LFV and LNV decays, we assume M_D^0 to be equal to the up-quark mass matrix M_u^0 at the GUT scale. Noting that N is SU(5) singlet fermion, in the context of relevant Yukawa interaction Lagrangian

$$\begin{aligned} -\mathcal{L}_{\text{Yuk}} &= [Y_N \bar{5}_F \cdot \mathbf{1}_F \cdot 5_H + Y_u 10_F \cdot 10_F \cdot 5_H + \dots] \\ &+ h.c., \end{aligned} \quad (33)$$

this assumption is equivalent to alignment of the two Yukawa couplings:

$$Y_N \simeq Y_u. \quad (34)$$

This alignment is naturally predicted in SO(10) or SO(18) [73], but in the present SU(5) case it is assumed.

We realize this matrix M_D using renormalization group equations for fermion masses and gauge couplings and their

numerical solutions [153–155] starting from the PDG values [128–130] of fermion masses at the electroweak scale. Following the bottom-up approach and using the down-quark diagonal basis, the quark masses and the CKM mixings are extrapolated from low energies using renormalization group (RG) equations [153–157]. After assuming the approximate equality $M_D^0 \simeq M_u^0$ at the GUT scale where M_u^0 is the up-quark mass matrix, the top-down approach is exploited to run down this mass matrix M_D^0 using RG equations [153]. Then the value of M_D near 1–10 TeV scale turns out to be

$$\begin{aligned} M_D &= \\ &\simeq \begin{pmatrix} 0.014 & 0.04 - 0.01i & 0.109 - 0.3i \\ 0.04 + 0.01i & 0.35 & 2.6 + 0.0007i \\ 0.1 + 0.3i & 2.6 - 0.0007i & 79.20 \end{pmatrix} \text{ GeV}. \end{aligned} \quad (35)$$

As already noted above, although on the basis of SU(5) symmetry alone there may not be any reason for the rigorous validity of (35), in what follows we study the implications of this assumed value of M_D to examine maximum possible impact on LFV and LNV decays discussed in Sections 6 and 7. Another reason is that the present assumption on M_D may be justified in direct SO(10) breaking to the SM which we plan to pursue in a future work.

5. Right-Handed Neutrino Mass in SU(5) vs SO(10)

5.1. *RH ν Mass in SO(10).* The fermions responsible for type-I and type-II seesaw are the LH leptonic doublets and the RH fermionic singlets of three generations. In SO(10) the left-handed lepton doublet $(\nu, l)^T$ and the right-handed neutrino N are in the same spinorial representation 16_F .

$$\begin{aligned} (\nu, l)^T &\subset 16_F, \\ N &\subset 16_F. \end{aligned} \quad (36)$$

The Higgs representation $126_H^\dagger \subset \text{SO}(10)$ contains both the left-handed and the right-handed triplets carrying $B-L = -2$,

$$126_H^\dagger = \Delta_L(3, 1, -2, 1) + \Delta_R(1, 3, -2, 1) + \dots \quad (37)$$

where the quantum numbers are under the left-right symmetry group $SU(2)_L \times SU(2)_R \times U(1)_{B-L} \times SU(3)_C$. The common Yukawa coupling f_{10} in the Yukawa term

$$-\mathcal{L}_{\text{Yuk}10} = f_{10} 16_F 16_F 126_H^\dagger \quad (38)$$

generates the dilepton-Higgs triplet interactions both in the left-handed and right-handed sectors giving rise to type-I and type-II seesaw mechanisms. The RH neutrino mass is generated through the VEV of the neutral component of the Δ_R

$$\mathcal{M}_N = f_{10} \langle \Delta_R^0 \rangle. \quad (39)$$

The type-II seesaw contribution to light neutrino mass is

$$\mathcal{M}_\nu = f_{10} v_L \quad (40)$$

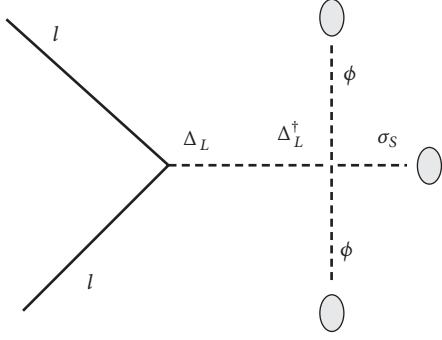


FIGURE 1: Feynman diagram representing type-II seesaw mechanism for neutrino mass generation in SU(5). Scalar fields ϕ , σ_S , and Δ_L represent SM Higgs doublet, singlet, and LH triplet as defined in the text. This diagram defines the trilinear coupling mass $\mu_\Delta = \lambda\langle\sigma_S\rangle$.

where v_L is the corresponding induced VEV of Δ_L

$$v_L = \lambda_{10} \frac{\langle\Delta_R^0\rangle v_{ew}^2}{M_{\Delta_L}^2}. \quad (41)$$

Here λ_{10} is the quartic coupling in the part of the scalar potential

$$V_{10} = \lambda_{10} \Delta_L^\dagger \Delta_R \phi^\dagger \phi \subset \lambda_{10} 126_H^\dagger 126_H 10_H 10_H. \quad (42)$$

Thus with type-II seesaw dominance, the predicted heavy RH neutrino masses in SO(10) follow the same hierarchical pattern as the active light neutrino masses

$$M_{N_1} : M_{N_2} : M_{N_3} :: m_1 : m_2 : m_3. \quad (43)$$

5.2. *RH ν Mass in SU(5)*. Feynman diagram for type-II seesaw mechanism in the present SU(5) model is shown in Figure 1.

In contrast to SO(10) where the LH leptonic doublet and the RH ν are in one and the same representation 16_F , in SU(5) they are in different representations

$$\begin{aligned} (\nu, l)^T &\subset \bar{5}_F, \\ N &\subset \mathbf{1}_F. \end{aligned} \quad (44)$$

In SU(5), while the dilepton-Higgs interaction is given by

$$-\mathcal{L}_{Yukll} = f \bar{5}_F \bar{5}_F 15_H, \quad (45)$$

the RH neutrino mass is generated through

$$-\mathcal{L}_{YukNN} = \left(\frac{1}{2}\right) f_N N N \sigma_S + h.c. \quad (46)$$

The fact that N is a singlet under SU(5) forces σ_S to be a singlet too. Further this singlet σ_S must carry $B - L = -2$ as its VEV generates the heavy Majorana mass

$$M_N = f_N \langle\sigma_S\rangle. \quad (47)$$

In sharp contrast to SO(10) where the LH triplet Δ_L and the RH triplet Δ_R scalars contained in the same representation

126_H^\dagger generate the type-II seesaw and M_N , the situation in SU(5) is different. Since LH triplet $\Delta_L(3, -1, 1)$ mediating type-II seesaw belongs to Higgs representation $15_H \subset SU(5)$ and σ_S belongs to a completely different representation (which is a singlet $\subset SU(5)$), the two relevant Majorana type couplings in general may not be equal

$$f_N \neq f. \quad (48)$$

Also this assertion is further strengthened if we do not assume SU(5) to be a remnant of SO(10). Then the RH neutrino mass hierarchy can be decoupled from the type-II seesaw prediction. It is interesting to note that in SU(5)

$$v_L = \frac{\mu_\Delta v_{ew}^2}{M_\Delta^2} \quad (49)$$

where μ_Δ is the trilinear coupling in the potential term

$$V_{tri} = \mu_\Delta \Delta_L \phi \phi + h.c. \quad (50)$$

The VEV of this singlet σ_S can explain the dynamical origin of such trilinear coupling through its VEV $v_\sigma = \langle\sigma_S\rangle$

$$\mu_\Delta = \lambda v_\sigma, \quad (51)$$

where λ is the quartic coupling in the potential term

$$V_{ql} = \lambda \sigma_S \Delta_L \phi \phi + h.c. \quad (52)$$

$$\subset \lambda \sigma_S 15_H 5_H 5_H + h.c. \quad (53)$$

where the second line represents the SU(5) origin. For GUT scale $U(1)_{B-L}$ symmetry breaking driving VEV $v_\sigma \simeq M_{GUT}$ in the natural absence of any intermediate symmetry, it is possible to ensure $\mu_\Delta \simeq M_{\Delta_L}$ for

$$\lambda \simeq \frac{M_{\Delta_L}}{M_{GUT}}. \quad (54)$$

Thus the SU(5) model gives similar explanation for quartic coupling as in direct breaking case of SO(10). But the predicted hierarchy of RH ν masses in SU(5) may not, in general, follow the same hierarchical pattern as given by SO(10) shown in (43). This is precisely so because (43) follows from the fact that the same matrix U_{PMNS} diagonalizes both the LH and the RH neutrino mass matrices which is further rooted in the fact that the same Majorana coupling f_{10} that generates the type-II seesaw mass term also generates M_N . But because of the general possibility in SU(5) that $f_N \neq f$, the RH ν s may acquire a completely different pattern depending upon the value of f_N . Unlike SO(10), these masses emerging from SU(5) are also allowed to be quite different from the type-II seesaw scale.

Even if the value of v_σ may be needed to be near M_{Δ_L} , the value of M_N is allowed to be considerably lower by fine-tuning the value of f_N . Our LFV and LNV decay phenomenology as discussed below may need $M_N = 1 - 10$ TeV which is realizable using this new technique in SU(5). In contrast SO(10) needs $U(1)_R \times U(1)_{B-L}$ [84, 125, 157] or

$SU(2)_R \times U(1)_{B-L}$ gauge symmetry and hence new gauge bosons near the TeV scale to generate such $RH\nu$ masses which should be detected at LHC [84, 125]. Thus a new mechanism for $RH\nu$ mass emerges here by noting the coupling $f_N \neq f$ which has the potential to generate $RH\nu$ masses over a wide range of values $M_N \sim 100 - 10^{15}$ GeV. Then the $RH\nu$ mass predictions in the two GUTs in the presence of type-II seesaw dominance are as follows:

Type-II Seesaw Dominated $SO(10)$

$$M_{N_i} \simeq \frac{m_i M_{\Delta_L}^2}{v_{ew}^2}. \quad (55)$$

Type-II Seesaw Dominated $SU(5)$

$$M_{N_i} = [\mathcal{O}(10) \text{ GeV} - \mathcal{O}(M_{\Delta_L})]. \quad (56)$$

Here $m_i, i = 1, 2, 3$, are the three mass eigen values of light neutrinos. It is to be noted that m_i is absent in the RHS of (56) in the $SU(5)$ case.

5.3. Realization of Mass Hierarchies. Here we discuss how the stated hierarchy in Section 3

$$M_{\Delta_L} \gg M_N \gg M \gg M_D, \quad (57)$$

for type-II seesaw dominance, is realized through fine tuning. At first noting that the mass squared term for $15_H \subset SU(5)$ in the scalar potential, $M_{15}^2 15_H^\dagger 15_H$, is $SU(5)$ invariant, M_{15} can have any mass below the GUT scale subject to proton stability and gauge coupling unification. Since 15_H , unlike 5_H , does not have Yukawa interactions with SM fermions, the Higgs mediated proton decay is suppressed. We now explain why we have used $M_{15} = M_{\Delta_L} = 10^{12}$ GeV. In our model it is possible to assign any mass $M_{15} = M_{\Delta_L} > M_\eta$ where the mass of $\eta(3, 0, 8) \subset 75_H$ is $M_\eta = 10^{9.23}$ GeV. Because of the presence of $\eta(3, 0, 8)$ at such intermediate mass value, precision gauge coupling unification is achieved which has been discussed separately [126, 127]. Following the standard symmetry breaking $SU(5) \rightarrow SM$ through the GUT scale VEV of the SM singlet scalar in the adjoint representation 24_H , $V_{GUT} = \langle 24_H^0 \rangle$, a $SU(5)$ invariant scalar potential V_η gives the mass of $\eta(3, 0, 8)$

$$V_\eta = M_{75}^2 75_H^2 + m_{(24,75)} 24_H 75_H^2 + \lambda_{(24,75)} 24_H^2 75_H^2 \\ \supset [M_{75}^2 + m_{(24,75)} V_{GUT} + \lambda_{(24,75)} V_{GUT}^2] \eta^2. \quad (58)$$

This leads to $M_\eta^2 = M_{75}^2 + m_{(24,75)} V_{GUT} + \lambda_{(24,75)} V_{GUT}^2$. Here $M_{75} \sim m_{(24,75)} \sim V_{GUT} \sim M_{GUT}$. Thus fine-tuning any one of these four parameters can give $M_\eta = 10^{9.23}$ GeV. The presence of 15_H below M_η destabilizes unification but protects it for $M_{15} > M_\eta$. This has led to the chosen value of $M_{\Delta_L} = M_{15} = 10^{12}$ GeV. We have noted in the following section that the value of $M_3 < 1$ TeV violates the observed

bound on the nonunitarity parameter $\eta_{\tau\tau} < 2.7 \times 10^{-3}$ leading to the lower bound on M in the degenerate case

$$M_1 = M_2 = M_3 \geq 1250 \text{ GeV}. \quad (59)$$

Here $M = \text{diag}(M_1, M_2, M_3)$. Noting the definition

$$M = y_\chi \langle \chi_S(1, 0, 1) \rangle = y_\chi V_\chi, \quad (60)$$

we now argue that even for GUT scale mass of χ_S and its VEV $V_\chi = V_{GUT}$, it is possible to satisfy (59). For $V_\chi \sim V_{GUT} \sim 10^{15}$ GeV we need a small fine-tuned value of Yukawa coupling

$$y_\chi > 10^{-12}, \quad (61)$$

which satisfies $M \geq 1$ TeV but does not affect any known fermion mass. This shows the interesting possibility that even without having a low mass nonstandard Higgs χ_S , it is possible to realize the extended seesaw with type-II seesaw dominance. However, if we insist on $y_\chi \leq 1$, we need $V_\chi \geq 1$ TeV and $M_{\chi_S} \geq 1$ TeV which is realizable as χ_S is a $SU(5)$ scalar singlet. As we have assumed $M_D = M_u$, this gives at GUT scale on extrapolation [153]

$$M_{D_{33}} \sim m_{\text{top}} \approx 85 \text{ GeV}. \quad (62)$$

Here m_{top} is the top-quark mass. Thus achieving precision unification and type-II seesaw dominance has already given us $M_{\text{Delta}} > M_\eta$ whereas fine-tuning the Majorana coupling, $f_N > 10^{-11}$, has yielded $M_N > 10^4$ GeV. Combining these with (59) and (62) gives the hierarchical relation of (57).

6. Lepton Flavor Violations

Using SM extensions there has been extensive investigation of lepton flavor violating phenomena $l_\alpha \rightarrow l_\beta + \gamma$, ($\alpha \neq \beta$) and other processes like $\mu \rightarrow e\bar{e}e$ including unitarity violations [101–108, 110–116]. In the flavor basis we use the standard charged current Lagrangian

$$\mathcal{L}_{CC} = -\frac{1}{\sqrt{2}} \sum_{\alpha=e,\mu,\tau} [g_{2L} \bar{l}_\alpha \gamma_\mu \nu_{\alpha L} W_L^\mu] + \text{h.c.} \quad (63)$$

In predicting the LFV branching ratios we have used the relevant formulas of [101] and assumed a simplifying diagonal structure for M ,

$$M = \text{diag.}(M_1, M_2, M_3). \quad (64)$$

Then (64), in combination with (35), gives the elements of the $\nu - S$ mixing matrix

$$\mathcal{V}^{(IS)} = \begin{pmatrix} \frac{M_{De1}}{M_1} & \frac{M_{De2}}{M_2} & \frac{M_{De3}}{M_3} \\ \frac{M_{D\mu1}}{M_1} & \frac{M_{D\mu2}}{M_2} & \frac{M_{D\mu3}}{M_3} \\ \frac{M_{D\tau1}}{M_1} & \frac{M_{D\tau2}}{M_2} & \frac{M_{D\tau3}}{M_3} \end{pmatrix}. \quad (65)$$

The $S - N$ mixing matrix,

$$V^{(SN)} = \frac{M}{M_N}, \quad (66)$$

is relatively damped out since $M_N \gg M$. In fact the type-I cancellation condition $M_N \gg M \gg M_D$ ensures this damping. Noting that the physical neutrino flavor state ν_α is a mixture of $\widehat{\nu}$, \widehat{S} , and \widehat{N} ,

$$\nu_\alpha = U_{\alpha i} \widehat{\nu}_i + V_{\alpha i}^{IS} \widehat{S} + V_{\alpha i}^{(SN)} \widehat{N}_i. \quad (67)$$

Here $U \sim U_{PMNS}$ and the other two mixings violate unitarity. For large $M_N \gg M$ the third term in the RHS of (67) can be dropped leading to the unitarity violation parameter η

$$U' \simeq (1 - \eta) U_{PMNS}. \quad (68)$$

Here

$$\eta_{\alpha\beta} = \left(\frac{1}{2} \right) (X \cdot X^\dagger)_{\alpha\beta}, \quad (69)$$

$$X = \frac{M_D}{M}.$$

There has been extensive discussion on the constraint imposed on this parameter [108, 111]. The largest out of these is $\eta_{\tau\tau} \leq 0.0027$. Theoretically

$$\frac{1}{2} \left[\sum_i \frac{M_{D_{ei}} \cdot M_{D_{ei}^*}}{M_i^2} \right] \leq 0.0027. \quad (70)$$

In the completely degenerate case of $S - N$ mixing, $M_1 = M_2 = M_3 = M$, we get the following.

$$M \geq 1250 \text{ GeV} \quad (71)$$

The RH neutrinos in the present model being degenerate with masses $M_{N_i} \gg m_S$, have much less significant contributions than the singlet fermions. The predicted branching ratios being only few to four orders less than the current experimental limits [95] are verifiable by ongoing searches,

$$\begin{aligned} BR(\mu \rightarrow e\gamma) &= 1.19 \times 10^{-16}, \\ BR(\tau \rightarrow e\gamma) &= 1.69 \times 10^{-14}, \\ BR(\tau \rightarrow \mu\gamma) &= 1.8 \times 10^{-12}. \end{aligned} \quad (72)$$

For the sake of completeness we present the variation of LFV decay branching ratios as a function of the lightest neutrino mass in Figure 2.

In this approach the LFV decay rate mediated by the W_L boson in the loop depends predominantly upon $N - S$ mixing matrix M and the Dirac neutrino mass matrix M_D , although subdominantly upon the RH ν mass matrix M_N . However in the high scale type-II seesaw ansatz followed here LFV decay rate is independent of light neutrino masses. This behavior of LFV decay rates is clearly exhibited in Figure 2 where the three branching ratios have maintained constancy with the variation of m_ν .

7. Dominant $W_L - W_L$ Channel Double Beta Decay within Cosmological Bound

7.1. Double Beta Decay Mediation by Sterile Neutrinos. In the absence of W_R bosons and right-handed $\Delta_R^{\pm\pm}$ in SU(5), there is

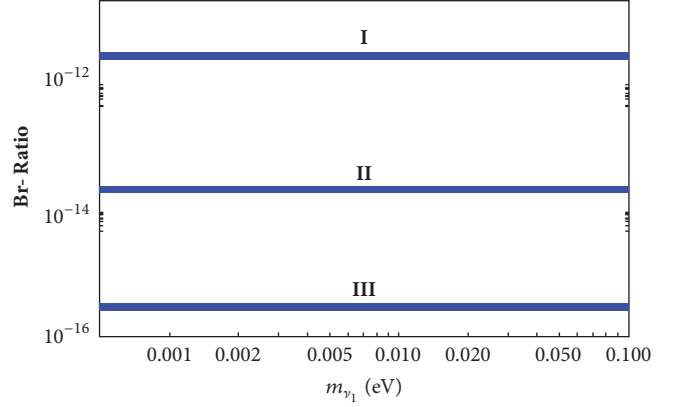


FIGURE 2: Variation of LFV decay branching ratios as a function of the lightest neutrino mass. Colored horizontal lines represent I : $BR(\tau \rightarrow \mu\gamma)$, II : $BR(\tau \rightarrow e\gamma)$, and III : $BR(\mu \rightarrow e\gamma)$.

no contribution to right-handed double beta production. The gauge coupling unification constraint sets the lower bound on the masses of left-handed doubly charged Higgs bosons $\Delta_L^{\pm\pm}$ to be $M_{\Delta_L} \simeq M_{15_H} > 10^{9.23}$ GeV. As such they have negligible contributions for direct mediations of $0\nu\beta\beta$ process with left-handed electrons. Thus the only significant contributions in the $W_L - W_L$ channel could be through the mediation of ν , S , and N . Feynman diagrams for $0\nu\beta\beta$ decay amplitude in the $W_L - W_L$ channel due to the exchanges of Majorana fermions ν , S , and N are shown in Figure 3. In Figure 4 we also present Feynman diagram for $0\nu\beta\beta$ decay amplitude due to the sterile neutrino exchange where its mass insertion has been explicitly indicated. Mass eigen values of different sterile neutrinos for different sets of (M_1, M_2, M_3) consistent with constraints on unitarity violating parameters $\eta_{\alpha\beta}$ are presented in Table 1. We have used the singlet fermion mass seesaw formula of (15) and $M_{N_1} = M_{N_2} = M_{N_3} = 4000$ GeV. These solutions are displayed in Figure 5.

We use normalizations necessary for different contributions [158–164] due to exchanges of light neutrinos, sterile neutrinos, and the heavy RH neutrinos in the $W_L - W_L$ channel. They lead to the inverse half-life [120, 124, 125],

$$\begin{aligned} [T_{1/2}^{0\nu}]^{-1} &\simeq G_{01} \left| \frac{\mathcal{M}_\nu^{0\nu}}{m_e} \right|^2 |\mathbf{M}_\nu^{ee} + \mathbf{M}_S^{ee} + \mathbf{M}_N^{ee}|^2, \\ &= K_{0\nu} |\mathbf{M}_\nu^{ee} + \mathbf{M}_S^{ee} + \mathbf{M}_N^{ee}|^2, \\ &= K_{0\nu} |\mathbf{M}_{\text{eff}}|^2. \end{aligned} \quad (73)$$

Here $G_{01} = 0.686 \times 10^{-14} \text{ yrs}^{-1}$, $\mathcal{M}_\nu^{0\nu} = 2.58 - 6.64$, and $K_{0\nu} = 1.57 \times 10^{-25} \text{ yrs}^{-1} \text{ eV}^{-2}$. In (73) the three effective mass parameters have been defined as

$$\mathbf{M}_\nu^{ee} = \sum_i (\mathcal{V}_{ei}^{\nu\nu})^2 m_{\nu_i} \quad (74)$$

$$\mathbf{M}_S^{ee} = \sum_i (\mathcal{V}_{ei}^{\nu S})^2 \frac{|p|^2}{\widehat{m}_S} \quad (75)$$

$$\mathbf{M}_N^{ee} = \sum_i (\mathcal{V}_{ei}^{\nu N})^2 \frac{|p|^2}{M_{N_i}}, \quad (76)$$

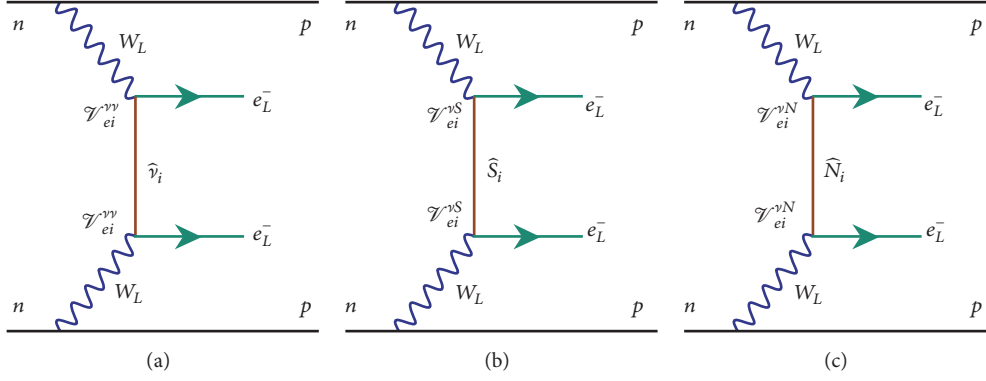


FIGURE 3: Feynman diagrams representing neutrinoless double beta decay due to exchanges of all three types of Majorana fermions ν , S , and N .

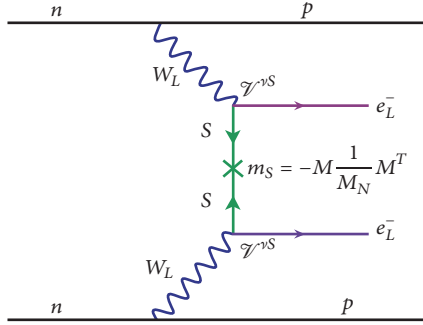


FIGURE 4: Feynman diagram representing neutrinoless double beta decay amplitude due to exchanges of singlet fermions S_i ($i = 1 - 3$) with explicit mass insertion $m_s = -M(1/M_N)M^T$.

TABLE 1: Prediction of singlet fermion masses for different values of (M_1, M_2, M_3) where we have used $M_{N_1} = M_{N_2} = M_{N_3} = 4000$ GeV.

M (GeV)	\widehat{m}_s (GeV)
(60, 1200, 1200)	(0.9, 360, 360)
(70, 1200, 1200)	(1.22, 360, 360)
(80, 1200, 1200)	(1.60, 360, 360)
(90, 1200, 1200)	(2.00, 360, 360)
(100, 1200, 1200)	(2.50, 360, 360)
(110, 1200, 1200)	(3.00, 360, 360)
(120, 1200, 1200)	(3.60, 360, 360)
(130, 1200, 1200)	(4.22, 360, 360)
(140, 1200, 1200)	(4.90, 360, 360)
(150, 1200, 1200)	(5.62, 360, 360)

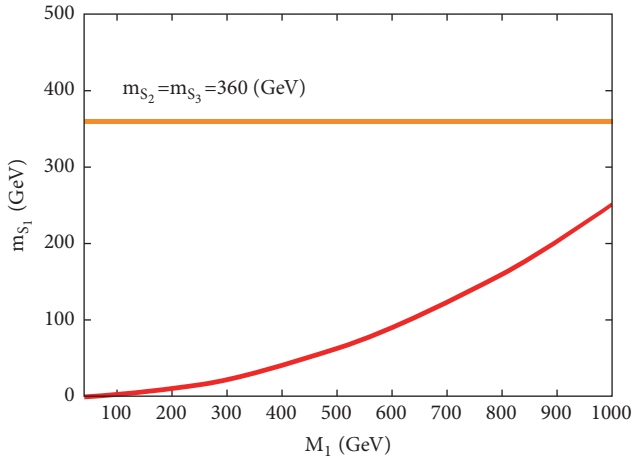


FIGURE 5: Prediction of singlet fermion mass eigen values as a function of $N - S$ mixing mass parameters M_i ($i = 1, 2, 3$) for $M_{N_i} = 4$ TeV ($i = 1, 2, 3$). The horizontal red colored line represents solutions for two other eigen values for $M_2 = M_3 = 1200$ GeV.

with

$$\mathbf{M}_{\text{eff}} = \mathbf{M}_\nu^{ee} + \mathbf{M}_S^{ee} + \mathbf{M}_N^{ee}. \quad (77)$$

The quantity \widehat{m}_{S_i} is the i -th eigen value of the S - fermion mass matrix m_S . The magnitude of neutrino virtuality momentum $|p|$ has been estimated to be in the allowed range $|p| = 120$ MeV–200 MeV [158–164]. The contributions of the $\text{RH}\nu$ s, being much heavier than the singlet fermions, have been neglected.

7.2. Singlet Fermion Assisted Enhanced Double Beta Decay Rate. We use neutrino oscillation data to estimate M_ν^{ee} for NH and IH cases with the values of Dirac phase and Majorana phases as discussed above. We further use the values of M_i from Table 1 and Figure 5 and the Dirac neutrino mass matrix from (35) to estimate M_S^{ee} while treating the $\text{RH}\nu$ mass at its assumed degenerate value of $M_{N_i} = 4\text{TeV}$ ($i = 1, 2, 3$). The variation of effective parameter m_{ee} as a function of lightest neutrino mass is shown in Figure 6 when $m_{s_1} = 2$ GeV.

As noted from the analytic formulas, the effective mass parameter in the singlet fermion dominated case, being inversely proportional to m_{s_1} , will proportionately decrease with increasing value of the mediating particle mass. This feature has been shown in Figure 7. We present predictions of double beta decay half-life as a function of the singlet fermion mass in Figure 8. It is clear that while for $m_{s_1} = 2$ GeV the half-life saturates the current experimental limit, for larger values of m_{s_1} the half-life is found to increase.

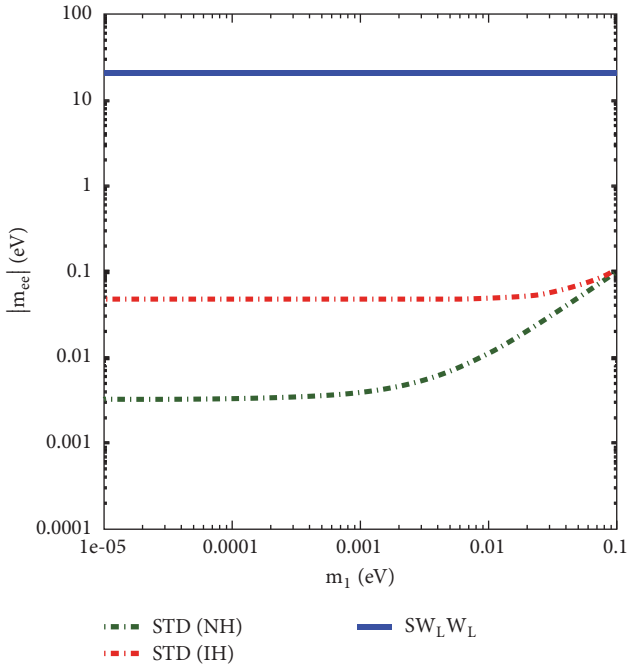


FIGURE 6: Variation of effective mass parameter as a function of lightest active neutrino mass m_1 for $m_{s_1} = 2$ GeV. For comparison, predictions in the standard model supplemented by light neutrino masses of NH type are shown by green dot-dashed curve. For IH pattern of mass hierarchy the standard prediction is shown by red dot-dashed curve.

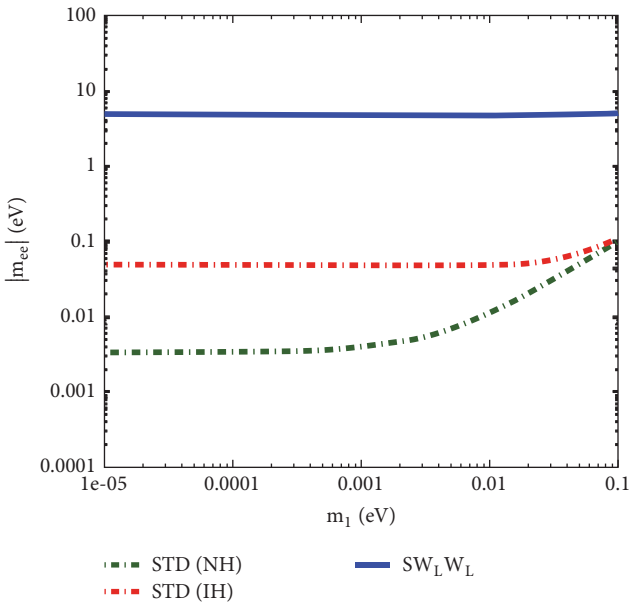


FIGURE 7: Same as Figure 6 but for $m_{s_1} = 4.0$ GeV.

Neglecting heavy $RH\nu$ contributions but including those due to the lightest sterile neutrino and the IH type light neutrinos, our predictions of half-life as a function of the lightest sterile neutrino mass are shown in Figure 9.

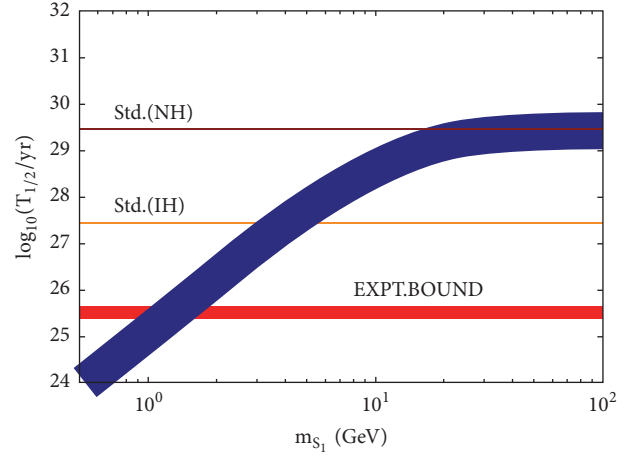


FIGURE 8: Prediction of double beta decay half-life as a function of sterile neutrino mass m_{s_1} GeV (blue shaded curve) where the NH type light neutrino and the sterile neutrino exchange contributions have been included. Effects of much larger masses (m_{s_2}, m_{s_3}) $\gg m_{s_1}$ have been neglected. The spread in the curve reflects uncertainty in the virtuality momentum $p = 120 - 190$ MeV. For comparison, the standard prediction with NH and IH pattern of light neutrino mass hierarchies is shown by the two respective horizontal lines. The bottom most thick red horizontal line closest to the X-axis represents overlapping experimental bounds from different groups [78–82].

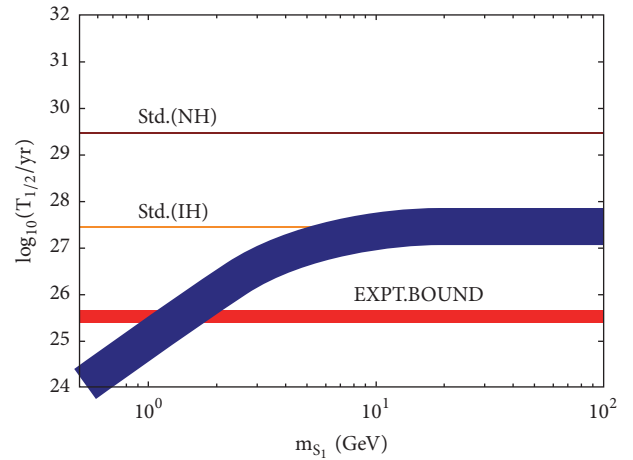


FIGURE 9: Same as Figure 8 but with contributions of IH type light neutrinos combined with lightest sterile neutrinos.

Predicted lifetimes are seen to decrease with increasing sterile neutrino mass. The sterile neutrino exchange contribution completely dominates over light neutrino exchange contributions for $m_{s_1} = 1.3 - 7$ GeV in case of IH but for $m_{s_1} = 1.5 - 20$ GeV in case of NH. At $m_{s_1} \approx 1.5$ GeV both types of solutions saturate the current laboratory limits reached by different experimental groups.

8. Summary, Discussion, and Conclusion

A recently proposed scalar extension of minimal non-SUSY SU(5) GUT has been found to realize precision gauge

coupling unification, high scale type-II seesaw ansatz for neutrino masses, and prediction of a WIMP scalar DM candidate that also completes vacuum stability of the scalar potential. But the LFV decays are predicted to have negligible rates inaccessible to ongoing searches in foreseeable future. Likewise experimentally verifiable double beta decay rates measurable by different search experiments are possible only for quasidegenerate neutrino mass spectrum with large common mass scale $|m_0| > 0.2$ eV or $\sum_i m_i > 0.6$ eV. This violates the recently measured cosmological bound $\sum_i m_i \leq 0.23$ eV. In order to remove these theoretical shortcomings in the context of SU(5), we have extended this model by the addition of three RH ν s, three extra Majorana fermion singlets S_i ($i = 1, 2, 3$), and a scalar singlet $\chi_S(1, 0, 1)$ that generates $N - S$ mixing mass term through its vacuum expectation value. In the original theory of type-I seesaw cancellation mechanism, although the choice of particles is the same as N_i , S_i , and $\chi_S(1, 0, 1)$, the neutrino mass is given by double seesaw [119]. Further, there is no grand unification of gauge couplings or prediction of proton decay in this model [119], and the scalar potential of the model has vacuum instability. In addition the N_i are not gauged. The model does not predict dominant contributions to double beta decay for NH or IH type neutrino masses. In non-SUSY SO(10) models of unification of three forces implementing the cancellation of type-I seesaw [84, 120, 124], the TeV scale RH neutrinos are gauged but the neutrino masses are controlled by inverse seesaw. But in [13, 125] the RH ν s are gauged and the neutrino mass formula is linear seesaw or type-II seesaw [13]. In all type-II seesaw dominated SO(10) models, the RH ν masses have the same hierarchy as the left-handed neutrino masses: $M_{N_1} : M_{N_2} : M_{N_3} :: m_1 : m_2 : m_3$. This happens precisely because the left-handed and the right-handed dilepton Yukawa interactions originate from the same SO(10) invariant term: $f 16_F 16_F 126^\dagger$. In SU(5), however, as the LH triplet $\Delta_L(3, -1, 1)$ generating type-II seesaw and the singlet $\sigma_S(1, 0, 1)$ generating RH ν s belong to different scalar representations, $15_H \subset SU(5)$ and $1_H \subset SU(5)$, respectively, they can possess different Majorana couplings in their respective Yukawa interactions: $f_H \Delta_L^C$ and $f_N \sigma_S N N$. Because of this reason the generated RH ν masses through $M_N = f_N \langle \sigma_S \rangle$ no longer follows the predicted type-II seesaw predicted hierarchical pattern. Then the allowed fine-tuning $|f_N| \ll |f|$ permits RH neutrino mass scale $M_N \sim \mathcal{O}(1 - 10)$ TeV even though, unlike SO(10) models, there are no possibilities of low mass W_R or Z' bosons at this scale. The apprehension of unacceptably large active neutrino mass generation through type-I seesaw mechanism is rendered inoperative through the well-established procedure of cancellation mechanism that is also shown to operate profoundly in this SU(5) model. Such RH ν s generating $N - S$ mixing mass $M \simeq \mathcal{O}(100 - 1000)$ GeV now reproduce the well-known results on LFV decay branching ratios only 4 - 5 orders lower than the current experimental limit as well as the extensively investigated nonunitarity effects. Through the sterile neutrino canonical seesaw formula emerging from this cancellation mechanism (in the presence of N_i), $m_S = -M(1/M_N)M^T$, this mechanism predicts their masses over a

wide range of values, $m_{S_1} = \mathcal{O}(1 - 100)$ GeV and $m_{S_2}, m_{S_3} \sim \mathcal{O}(10 - 1000)$ GeV. The lightest sterile neutrino mass m_{S_1} now predicts dominant double beta decay in the $W_L - W_L$ channel through the $\nu - S$ mixing close to the current experimental limits even though the light neutrino masses are of NH or IH type ($m_i \ll |0.2|$ eV) which satisfy the cosmological bound. For larger values of m_{S_1} the predicted decay rate decreases and the sterile neutrino contribution becomes negligible for $m_{S_1} \gg 50$ GeV. In the limiting case when all the singlet fermion masses have such large values, the double beta decay rates asymptotically approach the respective standard NH or IH type contributions. The new mechanism of RH ν mass generation also allows the second and the third generation sterile neutrino masses to be quasidegenerate (QD) near 1-10 TeV scale while keeping $m_{S_1} \sim 1 - 10$ GeV suitable for dominant double beta decay mediation. There is a possibility that such TeV scale QD masses while maintaining observable predictions on LFV decays can effectively generate baryon asymmetry of the universe via resonant leptogenesis [125]. A scalar singlet DM can be easily accommodated as discussed in [126, 165, 166] while resolving the issue of vacuum stability. Irrespective of scalar DM, the model can also accommodate a Majorana fermion singlet dark matter [167] which can emerge from the additional fermionic representation $24_F \subset SU(5)$.

The prediction of new fermions has an additional advantage over scalars as these masses are protected by leptonic global symmetries [168]. Also the prediction of such Majorana type sterile neutrinos can be tested by high energy and high luminosity accelerators through their like-sign dilepton production processes [169]. For example, at LHC they can mediate the process $pp \rightarrow W_L X \rightarrow l^+ l^- jj X$ where the jets could be manifested as mesons. It would be quite interesting to examine emergence of such SU(5) theory as a remnant of SO(10) or E_6 GUTs.

We conclude that even in the presence of SM as effective gauge theory descending from a suitable SU(5) extension, it is possible to predict experimentally accessible double beta decay rates in the $W_L - W_L$ channel satisfying the cosmological bound on active neutrino masses as well as verifiable LFV decays. The RH ν masses can be considerably different from those constrained by conventional type-I or type-II seesaw frameworks which are instrumental in predicting interesting physical phenomena even if there are no nonstandard heavy gauge bosons anywhere below the GUT scale.

Appendix

A. Diagonalization, Masses, and Mixings

The purpose of this Appendix is to provide certain details of mixings among the fermions ν , S , and N and also derive their masses by block diagonalization of the resulting 9×9 neutral fermion mass matrix discussed in Section 3. We write the complete 9×9 mass matrix in the flavor basis $\{\nu_L, S_L, N_R^C\}$ after the effect of Δ_L is integrated out

$$\mathcal{M}_\nu = \begin{pmatrix} m^{(II)} & 0 & M_D \\ 0 & 0 & M^T \\ M_D^T & M & M_N \end{pmatrix} \quad (\text{A.1})$$

where the type-II seesaw contribution has been noted as $m^{(II)} = f\nu_L$. The flavor basis to mass basis transformation and diagonalization of \mathcal{M}_ν is achieved by a unitary transformation matrix \mathcal{V} defined below

$$|\psi\rangle_f = \mathcal{V} |\psi\rangle_m \quad (\text{A.2})$$

$$\text{or, } \begin{pmatrix} \nu_\alpha \\ S_\beta \\ N_\gamma^C \end{pmatrix} = \begin{pmatrix} \mathcal{V}^{\nu\nu} & \mathcal{V}^{\nu S} & \mathcal{V}^{\nu N} \\ \mathcal{V}^{S\nu} & \mathcal{V}^{SS} & \mathcal{V}^{SN} \\ \mathcal{V}^{N\nu} & \mathcal{V}^{NS} & \mathcal{V}^{NN} \end{pmatrix} \begin{pmatrix} \hat{\nu}_i \\ \hat{S}_j \\ \hat{N}_k \end{pmatrix} \quad (\text{A.3})$$

$$\text{and } \mathcal{V}^\dagger \mathcal{M}_\nu \mathcal{V}^* = \widehat{\mathcal{M}}_\nu = \text{diag}(\widehat{m}_{\nu_i}; \widehat{m}_{S_j}; \widehat{m}_{N_k}) \quad (\text{A.4})$$

where subscripts f, m denote the flavor and mass basis, respectively. Also \mathcal{M}_ν is the mass matrix in flavor basis with α, β, γ running over three generations of light neutrinos, sterile neutrinos, and right-handed heavy-neutrinos. Here $\widehat{\mathcal{M}}_\nu$ is the diagonal mass matrix with $(i, j, k = 1, 2, 3)$ running over corresponding mass states at the sub-eV, GeV, and TeV scales, respectively.

The method of complete diagonalization will be carried out in two steps: (1) the full neutrino mass matrix \mathcal{M}_ν has to be reduced to a block diagonalized form as \mathcal{M}_{BD} ; (2) this block diagonal form is further diagonalized to give physical masses of the neutral leptons $\widehat{\mathcal{M}}_\nu$.

(1) *Determination of \mathcal{M}_{BD} .* We shall follow the parametrisation of the type given in [32] to determine the form of the diagonalizing matrices \mathcal{W}_1 and \mathcal{W}_2 . We define their product as

$$\mathcal{W} = \mathcal{W}_1 \mathcal{W}_2 \quad (\text{A.5})$$

where \mathcal{W}_1 and \mathcal{W}_2 satisfy

$$\mathcal{W}_1^\dagger \mathcal{M}_\nu \mathcal{W}_1^* = \widehat{\mathcal{M}}_{\text{BD}}, \quad (\text{A.6})$$

$$\text{and } \mathcal{W}_2^\dagger \widehat{\mathcal{M}}_{\text{BD}} \mathcal{W}_2^* = \mathcal{M}_{\text{BD}}$$

where $\widehat{\mathcal{M}}_{\text{BD}}$ and \mathcal{M}_{BD} are the intermediate block diagonal and full block diagonal mass matrices, respectively.

$$\widehat{\mathcal{M}}_{\text{BD}} = \begin{pmatrix} \mathcal{M}_{\text{eff}} & 0 \\ 0 & m_{\mathcal{N}} \end{pmatrix} \quad (\text{A.7})$$

$$\text{and } \mathcal{M}_{\text{BD}} = \begin{pmatrix} m_\nu & 0 & 0 \\ 0 & m_S & 0 \\ 0 & 0 & m_{\mathcal{N}} \end{pmatrix} \quad (\text{A.8})$$

(2) *Determination of \mathcal{W}_1 .* We need to first integrate out the heavy state (N_R), being heavier than other mass scales in our theory, such that up to the leading order approximation the analytic expression for \mathcal{W}_1 is

$$\mathcal{W}_1 = \begin{pmatrix} 1 - \frac{1}{2} B^* B^T & B^* \\ -B^T & 1 - \frac{1}{2} B^T B^* \end{pmatrix}, \quad (\text{A.9})$$

where the matrix B is 6×3 dimensional and is described as

$$B^\dagger = M_N^{-1} (M_D^T, M^T) = (Z^T, Y^T) \quad (\text{A.10})$$

where $X = M_D M^{-1}$, $Y = M M_N^{-1}$, and $Z = M_D M_N^{-1}$ so that $Z = X \cdot Y \neq Y \cdot X$.

Therefore, the transformation matrix \mathcal{W}_1 can be written purely in terms of dimensionless parameters Y and Z

$$\mathcal{W}_1 = \begin{pmatrix} 1 - \frac{1}{2} Z Z^\dagger & -\frac{1}{2} Z Y^\dagger & Z \\ -\frac{1}{2} Y Z^\dagger & 1 - \frac{1}{2} Y Y^\dagger & Y \\ -Z^\dagger & -Y^\dagger & 1 - \frac{1}{2} (Z^\dagger Z + Y^\dagger Y) \end{pmatrix} \quad (\text{A.11})$$

while the light and heavy states can be now written as follows.

$$\mathcal{M}_{\text{eff}} = - \begin{pmatrix} M_D M_N^{-1} M_D^T & M_D M_N^{-1} M^T \\ M M_N^{-1} M_D^T & M M_N^{-1} M^T \end{pmatrix} \quad (\text{A.12})$$

$$m_{\mathcal{N}} = M_N + \dots \quad (\text{A.13})$$

Determination of \mathcal{W}_2 . From the above discussion, it is quite clear now that the eigenstates \mathcal{N}_i are eventually decoupled from others and the remaining mass matrix \mathcal{M}_{eff} can be block diagonalized using another transformation matrix

$$\mathcal{S}^\dagger \mathcal{M}_{\text{eff}} \mathcal{S}^* = \begin{pmatrix} m_\nu & 0 \\ 0 & m_S \end{pmatrix} \quad (\text{A.14})$$

such that

$$\mathcal{W}_2 = \begin{pmatrix} \mathcal{S} & 0 \\ 0 & 1 \end{pmatrix}. \quad (\text{A.15})$$

In a simplified structure,

$$\mathcal{M}_{\text{eff}} = \begin{pmatrix} m_\nu^{II} + M_D Z^T & M_D Y^T \\ Y M_D^T & M Y^T \end{pmatrix}. \quad (\text{A.16})$$

Under the assumption at the beginning $Z \ll Y$ and of course $M_D \ll M$, this structure is similar to type-(I+II) seesaw. Therefore we immediately get the light neutrino masses as follows.

$$\begin{aligned} m_\nu &= -M_D Z^T + m_\nu^{II} + M_D Y^T (M Y^T)^{-1} Y M^T \\ &= -M_D Z^T + M_D Z^T + m_\nu^{II} = m_\nu^{II} \end{aligned} \quad (\text{A.17})$$

$$m_S = -M M_N^{-1} M^T \quad (\text{A.18})$$

We see that in addition to $m_{\mathcal{N}}$, the m_S is also almost diagonal if M and M_N are assumed to be diagonal. The transformation matrix \mathcal{S} is

$$\mathcal{S} = \begin{pmatrix} 1 - \frac{1}{2} A^* A^T & A^* \\ -A^T & 1 - \frac{1}{2} A^T A^* \end{pmatrix} \quad (\text{A.19})$$

such that

$$A^\dagger = (MY^T)^{-1} Y M_D^T \approx (MY^T)^{-1} Y M_D^T = X^T. \quad (\text{A.20})$$

The 3×3 block diagonal mixing matrix \mathcal{W}_2 has the following form.

$$\mathcal{W}_2 = \begin{pmatrix} S & \mathbf{0} \\ \mathbf{0} & \mathbf{1} \end{pmatrix} = \begin{pmatrix} 1 - \frac{1}{2} X X^\dagger & X & 0 \\ -X^\dagger & 1 - \frac{1}{2} X^\dagger X & 0 \\ 0 & 0 & 1 \end{pmatrix} \quad (\text{A.21})$$

A.1. Physical Neutrino Masses from Complete Diagonalization.

The block diagonal matrices m_ν , m_S , and $m_{\mathcal{N}}$ can further be diagonalized to give physical masses for all neutral leptons by a unitary matrix \mathcal{U} as

$$\mathcal{V} = \mathcal{W} \cdot \mathcal{U} = \mathcal{W}_1 \cdot \mathcal{W}_2 \cdot \mathcal{U}$$

$$= \begin{pmatrix} 1 - \frac{1}{2} Z Z^\dagger & -\frac{1}{2} Z Y^\dagger & Z \\ -\frac{1}{2} Y Z^\dagger & 1 - \frac{1}{2} Y Y^\dagger & Y \\ -Z^\dagger & -Y^\dagger & 1 - \frac{1}{2} (Z^\dagger Z + Y^\dagger Y) \end{pmatrix} \begin{pmatrix} 1 - \frac{1}{2} X X^\dagger & X & 0 \\ -X^\dagger & 1 - \frac{1}{2} X^\dagger X & 0 \\ 0 & 0 & 1 \end{pmatrix} \begin{pmatrix} U_\nu & 0 & 0 \\ 0 & U_S & 0 \\ 0 & 0 & U_N \end{pmatrix} \quad (\text{A.24})$$

$$= \begin{pmatrix} 1 - \frac{1}{2} X X^\dagger & X - \frac{1}{2} Z Y^\dagger & Z \\ -X^\dagger & 1 - \frac{1}{2} (X^\dagger X + Y Y^\dagger) & Y - \frac{1}{2} X^\dagger Z \\ 0 & -Y^\dagger & 1 - \frac{1}{2} Y^\dagger Y \end{pmatrix} \cdot \begin{pmatrix} U_\nu & 0 & 0 \\ 0 & U_S & 0 \\ 0 & 0 & U_N \end{pmatrix}$$

It is straightforward to verify that the matrix product of the right-hand side of (A.24) agrees with (18) of Section 3.

Data Availability

The data used to support the findings of this study are included within the article.

Conflicts of Interest

The authors declare that there are no conflicts of interest regarding the publication of this manuscript.

Acknowledgments

M. K. Parida thanks the Science and Engineering Research Board, Department of Science and Technology, Government of India, for grant of research project SB/S2/HEP-011/2013. Rajesh Satpathy thanks Siksha 'O' Anusandhan University for research fellowship.

References

[1] P. F. de Salas, D. V. Forero, C. A. Ternes, M. Tortola, and J. W. F. Valle, "Status of neutrino oscillations 2018: first hint for normal mass ordering and improved CP sensitivity," *Physics Letters B*, vol. 782, pp. 633–640, 2018.

$$\mathcal{U} = \begin{pmatrix} U_\nu & 0 & 0 \\ 0 & U_S & 0 \\ 0 & 0 & U_N \end{pmatrix}. \quad (\text{A.22})$$

Here the unitary matrices U_ν , U_S , and U_N satisfy the following.

$$U_\nu^\dagger m_\nu U_\nu^* = \widehat{m}_\nu = \text{diag}(m_{\nu_1}, m_{\nu_2}, m_{\nu_3}),$$

$$U_S^\dagger m_S U_S^* = \widehat{m}_S = \text{diag}(m_{S_1}, m_{S_2}, m_{S_3}), \quad (\text{A.23})$$

$$U_N^\dagger m_{\mathcal{N}} U_N^* = \widehat{m}_N = \text{diag}(m_{N_1}, m_{N_2}, m_{N_3})$$

With this discussion, the complete mixing matrix is as follows.

- [2] T. Schwetz, M. Tórtola, and J. W. Valle, "Global neutrino data and recent reactor fluxes: the status of three-flavour oscillation parameters," *New Journal of Physics*, vol. 13, no. 6, Article ID 063004, 2011.
- [3] D. Forero, M. Tortola, and J. Valle, "Neutrino oscillations refitted," *Physical Review D: Particles, Fields, Gravitation and Cosmology*, vol. 90, no. 9, Article ID 093006, 10 pages, 2014.
- [4] G. L. Fogli, E. Lisi, A. Marrone, D. Montanino, A. Palazzo, and A. M. Rotunno, "Global analysis of neutrino masses, mixings and phases: entering the era of leptonic CP violation searches," *Physical Review D: Particles, Fields, Gravitation and Cosmology*, vol. 86, Article ID 013012, 2012.
- [5] M. C. Gonzalez-Garcia, M. Maltoni, and T. Schwetz, "Global analyses of neutrino oscillation experiments," *Nuclear Physics B*, vol. 908, pp. 199–217, 2016.
- [6] G. Altarelli, "Neutrinos Today: An Introduction," in *Proceedings of the 49th Recontres de Moriond on Electroweak Interactions and Unified Theories*, pp. 15–22, La Thuile, Italy, 2014.
- [7] A. Y. Smirnov, "Theories of Neutrino Masses and Mixings," *Il Nuovo Cimento C*, vol. 37, no. 3, p. 29, 2014.
- [8] R. N. Mohapatra, "From old symmetries to new symmetries: Quarks, leptons and B - L," in *50 Years of Quarks*, pp. 245–263, World Scientific, 2015.
- [9] R. N. Mohapatra, "Neutrino mass as a signal of TeV scale physics," *Nuclear Physics B*, vol. 908, pp. 423–435, 2016.
- [10] O. G. Miranda and J. W. Valle, "Neutrino oscillations and the seesaw origin of neutrino mass," *Nuclear Physics B*, vol. 908, pp. 436–455, 2016.

- [11] J. W. Valle, “Neutrino physics from A to Z : Two lectures at Corfu,” in *Proceedings of the Corfu Summer Institute 2016 “School and Workshops on Elementary Particle Physics and Gravity”*, p. 7, Corfu, Greece, August 2016.
- [12] G. Senjanovic, “Neutrino mass: From LHC to grand unification,” *La Rivista del Nuovo Cimento*, vol. 34, pp. 1–68, 2011.
- [13] M. K. Parida and B. P. Nayak, “Singlet fermion assisted dominant seesaw with lepton flavor and number violations and leptogenesis,” *Advances in High Energy Physics*, vol. 2017, Article ID 4023493, 24 pages, 2017.
- [14] P. Minkowski, “ $\mu \rightarrow e\gamma$ at a rate of one out of 10^9 muon decays?” *Physics Letters B*, vol. 67, pp. 421–428, 1977.
- [15] T. Yanagida, “Horizontal Gauge Symmetry and Masses of Neutrinos,” in *Proceedings of the Workshop on the Unified Theories and Baryon Number in the Universe*, O. Sawada and E. Sugamoto, Eds., Tsukuba, Japan, 1979, KEK Report:KEK-79-18-95.
- [16] M. Gell-Mann, P. Ramond, and R. Slansky, “Complex Spinors and Unified Theories,” in *Proceedings of the Conference: C79-09-27 (Stony Brook Supergravity Workshop 1979:0315)*, p. 315, Supergravity, Amsterdam, North Holland, 1979.
- [17] S. L. Glashow, *1979 Cargese Summer Institute on Quarks and Leptons*, Plenum, New York, NY, USA, 1979.
- [18] R. N. Mohapatra and G. Senjanovic, “Neutrino mass and spontaneous parity nonconservation,” *Physical Review Letters*, vol. 44, p. 912, 1980.
- [19] J. Schechter and J. W. F. Valle, “Neutrino masses in $SU(2) \otimes U(1)$ theories,” *Physical Review D: Particles, Fields, Gravitation and Cosmology*, vol. 22, article 2227, 1980.
- [20] J. Schechter and J. W. F. Valle, “Neutrinoless double- β decay in $su(2) \times u(1)$ theories,” *Physical Review D: Particles, Fields, Gravitation and Cosmology*, vol. 25, no. 11, article 2951, 1982.
- [21] M. Magg and C. Wetterich, “Neutrino mass problem and gauge hierarchy,” *Physics Letters B*, vol. 94, pp. 61–64, 1980.
- [22] G. Lazarides, Q. Shafi, and C. Wetterich, “Proton lifetime and fermion masses in an $SO(10)$ model,” *Nuclear Physics Section B*, vol. 181, no. 2, pp. 287–300, 1981.
- [23] R. N. Mohapatra and G. Senjanović, “Neutrino masses and mixings in gauge models with spontaneous parity violation,” *Physical Review D: Particles, Fields, Gravitation and Cosmology*, vol. 23, article 165, 1981.
- [24] R. N. Mohapatra and M. K. Parida, “Type-II seesaw dominance in nonsupersymmetric and split-supersymmetry $SO(10)$ models and proton lifetime,” *Physical Review D: Particles, Fields, Gravitation and Cosmology*, vol. 84, no. 9, Article ID 095021, 2011.
- [25] R. N. Mohapatra, “Mechanism for understanding small neutrino mass in superstring theories,” *Physical Review Letters*, vol. 56, no. 6, pp. 561–563, 1986.
- [26] R. N. Mohapatra and J. W. F. Valle, “Neutrino mass and baryon-number nonconservation in superstring models,” *Physical Review D: Particles, Fields, Gravitation and Cosmology*, vol. 34, no. 5, pp. 1642–1645, 1986.
- [27] D. Wyler and L. Wolfenstein, “Massless neutrinos in left-hand symmetric models,” *Nuclear Physics B*, vol. 218, no. 1, pp. 205–214, 1983.
- [28] C. H. Albright, “Search for a solution of the superstring neutrino mass problem without a high intermediate energy scale,” *Physics Letters B*, vol. 178, no. 2-3, pp. 219–225, 1986.
- [29] S. Nandi and U. Sarkar, “Solution to the neutrino-mass problem in superstring E6 theory,” *Physical Review Letters*, vol. 56, no. 6, pp. 564–567, 1986.
- [30] E. Witten, “New issues in manifolds of $SU(3)$ holonomy,” *Nuclear Physics B*, vol. 268, no. 1, pp. 79–112, 1986.
- [31] E. Ma, “Lepton-number nonconservation in E6 superstring models,” *Physics Letters B*, vol. 191, no. 3, pp. 287–289, 1987.
- [32] W. Grimus and L. Lavoura, “The seesaw mechanism at arbitrary order: disentangling the small scale from the large scale,” *Journal of High Energy Physics*, vol. 2000, no. 11, article no. 42, 2000.
- [33] E. K. Akhmedov and M. Frigerio, “Duality in Left-Right Symmetric Seesaw Mechanism,” *Physical Review Letters*, vol. 96, no. 6, Article ID 061802, 2006.
- [34] E. K. Akhmedov and M. Frigerio, “Interplay of type I and type II seesaw contributions to neutrino mass,” *Journal of High Energy Physics*, vol. 2007, no. 1, article no. 04, 2007.
- [35] M. K. Parida, B. P. Nayak, R. Satpathy, and R. L. Awasthi, “Standard Coupling Unification in $SO(10)$, Hybrid Seesaw Neutrino Mass and Leptogenesis, Dark Matter, and Proton Lifetime Predictions,” *Journal of High Energy Physics*, vol. 2017, no. 4, article no. 75, 2017.
- [36] E. Akhmedova, M. Lindner, E. Schnapka, and J. Valle, “Left-right symmetry breaking in NJL approach,” *Physics Letters B*, vol. 368, no. 4, pp. 270–280, 1996.
- [37] M. Malinsky, J. Romao, and J. Valle, “Novel supersymmetric $SO(10)$ seesaw mechanism,” *Physical Review Letters*, vol. 95, Article ID 161801, 2005.
- [38] S. M. Barr, “New Type of Seesaw Mechanism for Neutrino Masses,” *Physical Review Letters*, vol. 92, no. 10, Article ID 101601, 2004.
- [39] E. Ma, “Verifiable radiative seesaw mechanism of neutrino mass and dark matter,” *Physical Review D: Particles, Fields, Gravitation and Cosmology*, vol. 73, Article ID 077301, 2006.
- [40] M. K. Parida, “Radiative Seesaw in $SO(10)$ with Dark Matter,” *Physics Letters B*, vol. 704, p. 206, 2011.
- [41] M. K. Parida, “Radiative see-saw formula in nonsupersymmetric $SO(10)$ with dark matter,” *Pramana—Journal of Physics*, vol. 79, no. 5, pp. 1271–1274, 2012.
- [42] R. Foot, H. Lew, X. G. He, and G. C. Joshi, “See-saw neutrino masses induced by a triplet of leptons,” *Zeitschrift für Physik C: Particles and Fields*, vol. 44, no. 3, pp. 441–444, 1989.
- [43] B. Bajc and G. Senjanovic, “Seesaw at LHC,” *Journal of High Energy Physics. A SISSA Journal*, vol. 2007, no. 08, article no. 014, 2007.
- [44] J. C. Pati and A. Salam, “Lepton number as the fourth ‘color,’” *Physical Review D: Particles, Fields, Gravitation and Cosmology*, vol. 10, pp. 275–289, 1975, Erratum: *Physical Review D*, vol. 11, p. 703, 1975.
- [45] R. N. Mohapatra and J. C. Pati, “Left-right gauge symmetry and an ‘isoconjugate’ model of CP violation,” *Physical Review D: Particles, Fields, Gravitation and Cosmology*, vol. 11, pp. 566–571, 1975.
- [46] G. Senjanović and R. N. Mohapatra, “Spontaneous breakdown of parity in a class of gauge theories,” *Physical Review D*, vol. 12, p. 1502, 1975.
- [47] G. Senjanović, “Spontaneous breakdown of parity in a class of gauge theories,” *Nuclear Physics B*, vol. 153, no. 3-4, pp. 334–364, 1979.
- [48] H. Georgi, “Particles and Fields,” in *Proceedings of APS Division Particles and Fields*, C. Carlson, Ed., p. 575, American Institute of Physics, New York, NY, USA, 1975.
- [49] H. Fritzsch and P. Minkowski, “Unified interactions of leptons and hadrons,” *Annals of Physics*, vol. 93, no. 1-2, pp. 193–266, 1975.

- [50] K. S. Babu and R. N. Mohapatra, "Predictive neutrino spectrum in minimal SO(10) grand unification," *Physical Review Letters*, vol. 70, no. 19, pp. 2845–2848, 1993.
- [51] A. S. Joshipura and K. M. Patel, "Fermion masses in SO(10) model," *Physical Review D: Particles, Fields, Gravitation and Cosmology*, vol. 83, no. 9, Article ID 095002, 17 pages, 2011.
- [52] G. Altarelli and G. Blankenburg, "Different SO(10) paths to fermion masses and mixings," *Journal of High Energy Physics*, vol. 2011, no. 3, article no. 133, 2011.
- [53] S. Bertolini, T. Schwetz, and M. Malinský, "Fermion masses and mixings in SO(10) models and the neutrino challenge to supersymmetric grand unified theories," *Physical Review D: Particles, Fields, Gravitation and Cosmology*, vol. 73, no. 11, Article ID 115012, 2006.
- [54] M. K. Parida, "Intermediate left-right gauge symmetry, unification of couplings and fermion masses in SUSY SO(10)XS(4)," *Physical Review D: Particles, Fields, Gravitation and Cosmology*, vol. 78, no. 5, Article ID 053004, 2008.
- [55] H. S. Goh, R. N. Mohapatra, and S. Nasri, "SO(10) symmetry breaking and type II seesaw formula," *Physical Review D: Particles, Fields, Gravitation and Cosmology*, vol. 70, no. 7, Article ID 075022, 2004.
- [56] D. Chang, R. N. Mohapatra, and M. K. Parida, "Decoupling of parity- and SU(2)_R-breaking scales: a new approach to left-right symmetric models," *Physical Review Letters*, vol. 52, no. 13, pp. 1072–1075, 1984.
- [57] D. Chang, R. N. Mohapatra, and M. K. Parida, "New approach to left-right-symmetry breaking in unified gauge theories," *Physical Review D: Particles, Fields, Gravitation and Cosmology*, vol. 30, no. 5, article 1052, 1984.
- [58] D. Chang, R. N. Mohapatra, J. M. Gipsom, R. E. Marshak, and M. K. Parida, "Experimental tests of new SO(10) grand unification," *Physical Review D: Particles, Fields, Gravitation and Cosmology*, vol. 31, no. 7, pp. 1718–1732, 1985.
- [59] D. Chang, R. N. Mohapatra, and M. K. Parida, "New mechanism for baryon generation in SO(10) models with low mass WR-boson," *Physics Letters B*, vol. 142, no. 1-2, pp. 55–58, 1984.
- [60] M. K. Parida, "Natural mass scales for observable matter-antimatter oscillations in SO(10)," *Physics Letters B*, vol. 126, no. 3-4, pp. 220–224, 1983.
- [61] M. K. Parida, "Matter-antimatter oscillations in grand unified theories with high unification masses," *Physical Review D: Particles, Fields, Gravitation and Cosmology*, vol. 27, no. 11, pp. 2783–2786, 1983.
- [62] M. K. Parida and P. K. Patra, "Useful theorem on vanishing threshold contribution to $\sin^2\theta_W$ in a class of grand unified theories," *Physical Review Letters*, vol. 66, no. 7, pp. 858–861, 1991.
- [63] M. K. Parida and P. K. Patra, "Theorem on vanishing multiloop radiative corrections to $\sin^2\theta_W$ in grand unified theories at high mass scales," *Physical Review Letters*, vol. 68, no. 6, pp. 754–756, 1992.
- [64] M. K. Parida, "Vanishing corrections on an intermediate scale and implications for unification of forces," *Physical Review D: Particles, Fields, Gravitation and Cosmology*, vol. 57, no. 5, p. 2762, 1998.
- [65] R. N. Mohapatra, "A theorem on the threshold corrections in grand unified theories," *Physics Letters B*, vol. 285, no. 3, pp. 235–237, 1992.
- [66] N. G. Deshpande, E. Keith, and P. B. Pal, "Implications of the CERN LEP results for SO(10) grand unification," *Physical Review D: Particles, Fields, Gravitation and Cosmology*, vol. 47, no. 5, pp. 2261–2264, 1992.
- [67] T. W. B. Kibble, G. Lazarides, and Q. Shafi, "Walls bounded by strings," *Physical Review D: Particles, Fields, Gravitation and Cosmology*, vol. 26, no. 2, pp. 435–439, 1982.
- [68] Q. Shafi and C. Wetterich, "Modification of Predictions of Grand Unified Theories in the Presence of Spontaneous Compactification," *Physical Review Letters*, vol. 52, no. 11, pp. 875–878, 1984.
- [69] S. Bertolini, L. Di Luzio, and M. Malinský, "Intermediate mass scales in the nonsupersymmetric SO(10) grand unification: A reappraisal," *Physical Review D: Particles, Fields, Gravitation and Cosmology*, vol. 80, no. 1, Article ID 015013, 2009.
- [70] S. K. Majee, M. K. Parida, A. Raychaudhuri, and U. Sarkar, "Low intermediate scales for leptogenesis in supersymmetric SO(10) grand unified theories," *Physical Review D: Particles, Fields, Gravitation and Cosmology*, vol. 75, no. 7, Article ID 075003, 2007.
- [71] J. Chakraborty, S. K. Patra, and S. Mohanty, "Roadmap of left-right models based on GUTs," *Physics Review D*, vol. 97, no. 9, Article ID 095010, 2018.
- [72] M. K. Parida and A. Raychaudhuri, "Low-mass parity restoration, weak-interaction phenomenology, and grand unification," *Physical Review D: Particles, Fields, Gravitation and Cosmology*, vol. 26, no. 9, pp. 2364–2377, 1982.
- [73] M. Reig, J. W. Valle, C. Vaquera-Araujo, and F. Wilczek, "A model of comprehensive unification," *Physics Letters B*, vol. 774, pp. 667–670, 2017.
- [74] S. Fukuyama and T. Yanagida, "Baryogenesis without grand unification," *Physics Letters B*, vol. 174, no. 1, pp. 45–47, 1986.
- [75] T. Hambye, E. Ma, and U. Sarkar, "Supersymmetric triplet Higgs model of neutrino masses and leptogenesis," *Nuclear Physics B*, vol. 602, no. 1-2, pp. 23–38, 2001.
- [76] T. Hambye and G. Senjanović, "Consequences of triplet seesaw for leptogenesis," *Physics Letters B*, vol. 582, pp. 73–81, 2004.
- [77] G. D'Ambrosio, T. Hambye, A. Hektor, M. Raidal, and A. Rossi, "Leptogenesis in the minimal supersymmetric triplet seesaw model," *Physics Letters B*, vol. 604, no. 3-4, pp. 199–206, 2004.
- [78] H. V. Klapdor-Kleingrothaus, A. Dietz, L. Baudis et al., "Latest results from the Heidelberg-Moscow double beta decay experiment," *The European Physical Journal A*, vol. 12, no. 2, pp. 147–154, 2001.
- [79] C. Arnaboldi, D. R. Artusa, F. T. Avignone et al., "Results from a search for the 0 neutrino beta beta-decay of Te-130," *Physics Review C*, vol. 78, Article ID 035502, 27 pages, 2008.
- [80] C. E. Aalseth et al., "The IGEX Ge-76 neutrinoless double beta decay experiment: Prospects for next generation experiments," *Physical Review D*, vol. 65, Article ID 092007, 2002.
- [81] J. Argyriades, R. Arnold, C. Augier et al., "Measurement of the double beta decay half-life of Nd-150 and search for neutrinoless decay modes with NEMO-3 detector," *Physics Review C*, vol. 80, Article ID 032501, 2009.
- [82] I. Abt, M. F. Altmann, A. Bakalyarov et al., "A New Ge76 Double Beta Decay Experiment at LNGS: Letter of Intent," <https://arxiv.org/abs/hep-ex/0404039>.
- [83] M. Nemeššek, G. Senjanović, and V. Tello, "Connecting Dirac and Majorana Neutrino Mass Matrices in the Minimal Left-Right Symmetric Model," *Physical Review Letters*, vol. 110, no. 15, 2013.
- [84] M. K. Parida and B. Sahoo, "Planck-scale induced left-right gauge theory at LHC and experimental tests," *Nuclear Physics B*, vol. 906, pp. 77–104, 2016.
- [85] W.-Y. Keung and G. Senjanović, "Majorana neutrinos and the production of the right-handed charged gauge boson," *Physical Review Letters*, vol. 50, no. 19, pp. 1427–1430, 1983.

- [86] J. W. F. Valle, “Neutrinoless double- β decay with quasi-Dirac neutrinos,” *Physical Review D: Particles, Fields, Gravitation and Cosmology*, vol. 27, no. 7, pp. 1672–1674, 1983.
- [87] J. Schechter and J. W. F. Valle, “Neutrino decay and spontaneous violation of lepton number,” *Physical Review D: Particles, Fields, Gravitation and Cosmology*, vol. 25, p. 774, 1982.
- [88] G. Gelmini, D. N. Schramm, and J. W. F. Valle, “Majorons: A simultaneous solution to the large and small scale dark matter problems,” *Physics Letters B*, vol. 146, no. 5, pp. 311–317, 1984.
- [89] G. B. Gelmini and J. W. F. Valle, “Fast invisible neutrino decays,” *Physics Letters B*, vol. 142, no. 3, pp. 181–187, 1984.
- [90] J. W. F. Valle, “Leptonic CP violation and left-right symmetry,” *Physics Letters B*, vol. 138, no. 1-3, pp. 155–158, 1984.
- [91] V. Berezhinsky and J. W. F. Valle, “The keV majoron as a dark matter particle,” *Physics Letters B*, vol. 318, no. 2, pp. 360–366, 1993.
- [92] P. A. Ade, N. Aghanim, M. Arnaud et al., “Planck 2015 results. XIII. Cosmological parameter,” *Astronomy & Astrophysics*, vol. 594, no. article A13, 63 pages, 2016.
- [93] J. W. Valle and C. Vaquera-Araujo, “Dynamical seesaw mechanism for Dirac neutrinos,” *Physics Letters B*, vol. 755, pp. 363–366, 2016.
- [94] J. Bernabeu, A. Santamaria, J. Vidal, A. Mendez, and J. W. F. Valle, “Lepton flavour non-conservation at high energies in a superstring inspired standard model,” *Physics Letters B*, vol. 187, pp. 303–308, 1987.
- [95] J. Adam, X. Bai, A. M. Baldini et al., “New limit on the lepton-flavour violating decay $\mu^+ \rightarrow e^+ \gamma$,” *Physical Review Letters*, vol. 107, Article ID 171801, 2011.
- [96] K. Hayasaka, K. Abe, and I. Adachi, “New Search for tau \rightarrow mu gamma and tau \rightarrow e gamma Decays at Belle,” *Physics Letters B*, vol. 666, no. 1, pp. 16–22, 2008.
- [97] M. L. Brooks, Y. K. Chen, M. D. Cooper et al., “New Limit for the Lepton-Family-Number Nonconserving Decay $\mu^+ \rightarrow e^+ \gamma$,” *Physical Review Letters*, vol. 83, p. 1521, 1999.
- [98] B. Aubert, Y. Karyotakis, J. P. Lees et al., “Searches for Lepton Flavor Violation in the Decays tau \rightarrow e gamma and tau \rightarrow mu gamma,” *Physical Review Letters*, vol. 104, Article ID 021802, 2010.
- [99] Y. Kuno, “Prism/prime,” *Nuclear Physics B—Proceedings Supplements*, vol. 149, pp. 376–378, 2005.
- [100] F. R. Joaquim and A. Rossi, “Phenomenology of the triplet seesaw mechanism with Gauge and Yukawa mediation of SUSY breaking,” *Nuclear Physics B*, vol. 765, no. 1-2, pp. 71–117, 2007.
- [101] A. Ilakovac and A. Pilaftsis, “Flavour-violating charged lepton decays in seesaw-type models,” *Nuclear Physics B*, vol. 437, no. 3, pp. 491–519, 1995.
- [102] F. Deppisch and J. W. F. Valle, “Enhanced lepton flavour violation in the supersymmetric inverse seesaw model,” *Physical Review D: Particles, Fields, Gravitation and Cosmology*, vol. 72, Article ID 036001, 2005.
- [103] C. Arina, F. Bazzocchi, N. Fornengo, J. C. Romao, and J. W. Valle, “Minimal supergravity scalar neutrino dark matter and inverse seesaw neutrino masses,” *Physical Review Letters*, vol. 101, no. 16, Article ID 161802, 2008.
- [104] M. Malinský, T. Ohlsson, Z.-Z. Xing, and H. Zhang, “Non-unitary neutrino mixing and CP violation in the minimal inverse seesaw model,” *Physics Letters B*, vol. 679, no. 3, pp. 242–248, 2009.
- [105] M. Hirsch, T. Kernreiter, J. Romao, and A. Villanova del Moral, “Minimal supersymmetric inverse seesaw: neutrino masses, lepton flavour violation and LHC phenomenology,” *Journal of High Energy Physics*, vol. 2010, no. 10, article 103, 2010.
- [106] F. Deppisch, T. S. Kosmas, and J. W. F. Valle, “Enhanced $\mu^- - e^-$ conversion in nuclei in the inverse seesaw model,” *Nuclear Physics B*, vol. 752, pp. 80–92, 2006.
- [107] S. Das, F. Deppisch, O. Kittel, and J. Valle, “Heavy neutrinos and lepton flavor violation in left-right symmetric models at the LHC,” *Physical Review D: Particles, Fields, Gravitation and Cosmology*, vol. 86, Article ID 055006, 2012.
- [108] S. Antusch, J. Baumann, and E. Fernández-Martínez, “Non-standard neutrino interactions with matter from physics beyond the Standard Model,” *Nuclear Physics B*, vol. 810, no. 1-2, pp. 369–388, 2009.
- [109] S. Antusch, C. Biggio, E. Fernández-Martínez, M. Belen Gavela, and J. Lopez-Pavon, “Unitarity of the leptonic mixing matrix,” *Journal of High Energy Physics*, vol. 2006, no. 10, p. 84, 2006.
- [110] D. Forero, S. Morisi, M. Tortola, and J. W. F. Valle, “Lepton flavor violation and non-unitary lepton mixing in low-scale type-I seesaw,” *Journal of High Energy Physics*, vol. 2011, no. 9, article 142, 2011.
- [111] E. Fernández-Martínez, M. Gavela, J. López-Pavón, and O. Yasuda, “CP-violation from non-unitary leptonic mixing,” *Physics Letters B*, vol. 649, no. 5-6, pp. 427–435, 2007.
- [112] K. Kanaya, “Neutrino mixing in the minimal SO(10) model,” *Progress of Theoretical and Experimental Physics*, vol. 64, no. 6, pp. 2278–2281, 1980.
- [113] J. Kersten and A. Y. Smirnov, “Right-Handed Neutrinos at CERN LHC and the Mechanism of Neutrino Mass Generation,” *Physical Review D*, vol. 76, Article ID 073005, 2007.
- [114] M. Malinsky, T. Ohlsson, and H. Zhang, “Nonunitarity effects in a realistic low-scale seesaw model,” *Physical Review D: Particles, Fields, Gravitation and Cosmology*, vol. 79, no. 7, Article ID 073009, 2009.
- [115] G. Altarelli and D. Meloni, “CP violation in neutrino oscillations and new physics,” *Nuclear Physics B*, vol. 809, no. 1-2, pp. 158–182, 2009.
- [116] F. del Aguila and J. A. Aguilar-Saavedra, “Electroweak scale seesaw and heavy Dirac neutrino signals at LHC,” *Physics Letters B*, vol. 672, no. 2, pp. 158–165, 2009.
- [117] F. del Aguila, J. A. Aguilar-Saavedra, and J. de Blas, “Trilepton signals: the golden channel for seesaw searches at LHC,” *Acta Physica Polonica B*, vol. 40, pp. 2901–2911, 2009.
- [118] A. Van Der Schaaf, “Muon physics at a neutrino factory,” *Journal of Physics G: Nuclear and Particle Physics*, vol. 29, no. 12, pp. 2755–2762, 2003.
- [119] S. K. Kang and C. S. Kim, “Extended double seesaw model for neutrino mass spectrum and low scale leptogenesis,” *Physics Letters B*, vol. 646, no. 5-6, pp. 248–252, 2007.
- [120] R. L. Awasthi, M. K. Parida, and S. Patra, “Neutrino masses, dominant neutrinoless double beta decay, and observable lepton flavor violation in left-right models and SO(10) grand unification with low mass W_R, Z_R bosons,” *Journal of High Energy Physics*, vol. 2013, no. 8, article 122, 2013.
- [121] M. K. Parida and S. Patra, “Left-right models with light neutrino mass prediction and dominant neutrinoless double beta decay rate,” *Physics Letters B*, vol. 718, no. 4-5, pp. 1407–1412, 2013.
- [122] S. K. Majee, M. K. Parida, and A. Raychaudhuri, “Neutrino mass and low-scale leptogenesis in a testable SUSY SO(10) model,” *Physics Letters B*, vol. 668, no. 4, pp. 299–302, 2008.
- [123] M. K. Parida and A. Raychaudhuri, “Inverse see-saw, leptogenesis, observable proton decay and $\Delta_R^{\pm\pm}$ in SUSY SO(10) with heavy W_R ,” *Physical Review D: Particles, Fields, Gravitation and Cosmology*, vol. 82, no. 9, Article ID 093017, 2010.
- [124] M. K. Parida, R. L. Awasthi, and P. K. Sahu, “Proton decay and new contribution to $0\nu 2\beta$ decay in SO(10) with low-mass Z'

- boson, observable $n - \bar{n}$ oscillation, lepton flavor violation, and rare kaon decay,” *Journal of High Energy Physics*, vol. 2015, no. 01, article 45, 2015.
- [125] B. P. Nayak and M. K. Parida, “New mechanism for Type-II seesaw dominance in SO(10) with low-mass Z' , RH neutrinos, and verifiable LFV, LNV and proton decay,” *The European Physical Journal C*, vol. 75, article no. 183, 2015.
- [126] B. Sahoo, M. Chakraborty, and M. K. Parida, “Neutrino mass, coupling unification, verifiable proton decay, vacuum stability, and wimp dark matter in SU(5),” *Advances in High Energy Physics*, vol. 2018, 21 pages, 2018.
- [127] M. L. Kynshi and M. K. Parida, “Higgs scalar in the grand desert with observable proton lifetime in SU(5) and small neutrino masses in SO(10),” *Physical Review D: Particles, Fields, Gravitation and Cosmology*, vol. 47, no. 11, pp. R4830–R4834, 1993.
- [128] J. Beringer, R. M. Barnett, K. Copic et al., “Review of Particle Physics (RPP),” *Physics Review D*, vol. 86, Article ID 010001, 2012.
- [129] K. Olive, K. Agashe, and C. Amsler, “Review of Particle Physics (RPP),” *Chinese Physics C*, vol. 38, no. 9, Article ID 090001, 2014.
- [130] C. Patrignani, K. Agashe, G. Aielli et al., “Review of Particle Physics (RPP),” *Chinese Physics C*, vol. 40, no. 10, Article ID 100001, 2016.
- [131] S. Weinberg, “Effective gauge theories,” *Physics Letters B*, vol. 91, no. 1, pp. 51–55, 1980.
- [132] L. J. Hall, “Grand unification of effective gauge theories,” *Nuclear Physics B*, vol. 178, no. 1, pp. 75–124, 1981.
- [133] B. A. Ovrut and H. J. Schnitzer, “Effective field theory in background field gauge,” *Physics Letters B*, vol. 110, no. 2, pp. 139–142, 1982.
- [134] M. K. Parida, “Heavy particle effects in grand unified theories with fine-structure constant matching,” *Physics Letters B*, vol. 196, no. 2, pp. 163–169, 1987.
- [135] M. K. Parida and C. C. Hazra, “Superheavy-Higgs-scalar effects in effective gauge theories from SO(10) grand unification with low-mass right-handed gauge bosons,” *Physical Review D: Particles, Fields, Gravitation and Cosmology*, vol. 40, no. 9, pp. 3074–3085, 1989.
- [136] R. N. Mohapatra and M. K. Parida, “Threshold effects on the mass-scale predictions in SO(10) models and solar-neutrino puzzle,” *Physical Review D: Particles, Fields, Gravitation and Cosmology*, vol. 47, no. 1, pp. 264–272, 1993.
- [137] P. Langacker and N. Polonsky, “Uncertainties in coupling constant unification,” *Physical Review D: Particles, Fields, Gravitation and Cosmology*, vol. 47, no. 9, pp. 4028–4045, 1993.
- [138] D.-G. Lee, R. N. Mohapatra, M. K. Parida, and M. Rani, “Predictions for the proton lifetime in minimal nonsupersymmetric SO(10) models: an update,” *Physical Review D: Particles, Fields, Gravitation and Cosmology*, vol. 51, no. 1, pp. 229–235, 1995.
- [139] Y. Abe, Y. Haga, M. Hayato et al., “Search for Proton Decay via $p \rightarrow e^+ \pi^0$ and $p \rightarrow \mu^+ \pi^0$ in 0.31 megaton-years exposure of the Super-Kamiokande Water Cherenkov Detector,” *Physics Review D*, vol. 95, no. 1, Article ID 012004, 2017.
- [140] I. Doršner, S. Fajfer, A. Greljo, J. Kamenik, and N. Košnik, “Physics of leptiquarks in precision experiments and at particle colliders,” *Physics Reports*, vol. 641, pp. 1–68, 2016.
- [141] I. Doršner, “A scalar leptiquark in SU(5),” *Physical Review D: Particles, Fields, Gravitation and Cosmology*, vol. 86, no. 5, Article ID 055009, 2012.
- [142] I. Doršner, S. Fajfer, and I. Mustać, “Light vector-like fermions in a minimal SU(5) setup,” *Physical Review D: Particles, Fields, Gravitation and Cosmology*, vol. 89, no. 11, Article ID 115004, 2014.
- [143] M. K. Parida, P. K. Patra, and A. K. Mohanty, “Gravity-induced large grand-unification mass in SU(5) with higher-dimensional operators,” *Physical Review D: Particles, Fields, Gravitation and Cosmology*, vol. 39, no. 1, pp. 316–322, 1989.
- [144] I. Doršner, S. Fajfer, and N. Košnik, “Leptoquark mechanism of neutrino masses within the grand unification framework,” *The European Physical Journal C*, vol. 77, no. 6, p. 417, 2017.
- [145] I. Doršner, S. Fajfer, and N. Košnik, “Heavy and light scalar leptiquarks in proton decay,” *Physics Review D*, vol. 86, Article ID 015013, 2012.
- [146] I. Doršner and P. F. Pérez, “Upper bound on the mass of the type III seesaw triplet in an SU(5) model,” *Journal of High Energy Physics*, vol. 2007, no. 06, article no. 029, 2007.
- [147] P. F. Pérez, “Supersymmetric adjoint SU(5),” *Physical Review D: Particles, Fields, Gravitation and Cosmology*, vol. 76, no. 7, Article ID 071701, 2007.
- [148] P. Nath and P. Fileviez Perez, “Proton stability in grand unified theories, in strings and in branes,” *Physics Reports*, vol. 441, no. 5–6, pp. 191–317, 2007.
- [149] P. Langacker, “Grand unified theories and proton decay,” *Physics Reports*, vol. 72, no. 4, pp. 185–385, 1981.
- [150] M. H. Rahat, P. Ramond, and B. Xu, “An Asymmetric TBM Texture,” *Physics Review D*, vol. 98, Article ID 055030, 2018.
- [151] C. Jarlskog, “Commutator of the quark mass matrices in the standard electroweak model and a measure of maximal CP nonconservation,” *Physical Review Letters*, vol. 55, p. 1039, 1985.
- [152] O. W. Greenberg, “Rephasing invariant formulation of CP violation in the Kobayashi-Maskawa framework,” *Physical Review D: Particles, Fields, Gravitation and Cosmology*, vol. 32, no. 7, pp. 1841–1843, 1985.
- [153] C. Das and M. Parida, “New formulas and predictions for running fermion masses at higher scales in SM, 2HDM, and MSSM,” *The European Physical Journal C*, vol. 20, no. 1, pp. 121–137, 2001.
- [154] M. Parida and B. Purkayastha, “New formulas and predictions for running masses at higher scales in MSSM,” *The European Physical Journal C*, vol. 14, no. 1, pp. 159–164, 2000.
- [155] M. K. Parida and N. N. Singh, “Low-energy formulas for neutrino masses with a $\tan \beta$ -dependent hierarchy,” *Physical Review D: Particles, Fields, Gravitation and Cosmology*, vol. 59, Article ID 032002, 1998.
- [156] D. Meloni, T. Ohlsson, and S. Riad, “Renormalization group running of fermion observables in an extended non-supersymmetric SO(10) model,” *Journal of High Energy Physics*, vol. 2017, no. 3, article no. 45, 2017.
- [157] R. L. Awasthi and M. K. Parida, “Inverse Seesaw Mechanism in Nonsupersymmetric SO(10), Proton Lifetime, Nonunitarity Effects, and a Low-mass Z' Boson,” *Physical Review D: Particles, Fields, Gravitation and Cosmology*, vol. 86, no. 9, Article ID 093004, 2012.
- [158] G. Pantis, F. Šimkovic, J. D. Vergados, and A. Faessler, “Neutrinoless double beta decay within the quasiparticle random-phase approximation with proton-neutron pairing,” *Physical Review C: Nuclear Physics*, vol. 53, no. 2, pp. 695–707, 1996.
- [159] J. Suhonen and O. Civitarese, “Weak-interaction and nuclear-structure aspects of nuclear double beta decay,” *Physics Reports*, vol. 300, no. 3–4, p. 123, 1998.
- [160] J. Kotila and F. Iachello, “Phase-space factors for double- β decay,” *Physical Review C: Nuclear Physics*, vol. 85, no. 3, Article ID 034316, 2012.
- [161] R. N. Mohapatra, “New contributions to neutrinoless double-beta decay in supersymmetric theories,” *Physical Review D: Particles, Fields, Gravitation and Cosmology*, vol. 34, no. 11, pp. 3457–3461, 1986.

- [162] M. Doi, T. Kotani, and E. Takasugi, "The Systematic Structure-Change into the Molecule-like Structures in the Self-Conjugate $4n$ Nuclei," *Progress of Theoretical Physics Supplement*, vol. 83, p. 1, 1985.
- [163] F. Šimkovic, G. Pantis, J. D. Vergados, and A. Faessler, "Additional nucleon current contributions to neutrinoless double β decay," *Physical Review C: Nuclear Physics*, vol. 60, Article ID 055502, 1999.
- [164] A. Pilaftsis and T. E. J. Underwood, "Resonant leptogenesis," *Nuclear Physics B*, vol. 692, no. 3, pp. 303–345, 2004.
- [165] A. Falkowski, C. Gross, and O. Lebedev, "A second Higgs from the Higgs portal," *Journal of High Energy Physics*, vol. 2015, no. 5, article no. 057, 2015.
- [166] B. Sahoo, M. Parida, and M. Chakraborty, "Matter parity violating dark matter decay in minimal SO(10), unification, vacuum stability and verifiable proton decay," *Nuclear Physics B*, vol. 938, pp. 56–113, 2019.
- [167] M. Cirelli, A. Strumia, and M. Tamburini, "Cosmology and astrophysics of minimal dark matter," *Nuclear Physics B*, vol. 787, no. 1-2, pp. 152–175, 2007.
- [168] G. Hooft, "Recent Developments in Gauge Theories," in *Proceedings of the 1979 Cargese Summer Institute on Recent Developments in Gauge Theories*, G. Hooft et al., Ed., Plenum Press, New York, NY, USA, 1980.
- [169] B. P. Nayak and M. K. Parida, "Dilepton events with displaced vertices, double beta decay, and resonant leptogenesis with Type-II seesaw dominance, TeV scale Z' and heavy neutrinos," <https://arxiv.org/abs/1509.06192>.

Research Article

Simulations of Gamma-Ray Emission from Magnetized Microquasar Jets

Odysseas Kosmas ¹ and Theodoros Smpoulias ²

¹Modelling and Simulation Centre, MACE, University of Manchester, Sackville Street, Manchester, UK

²Division of Theoretical Physics, University of Ioannina, 45110 Ioannina, Greece

Correspondence should be addressed to Odysseas Kosmas; odysseas.kosmas@manchester.ac.uk

Received 26 June 2018; Accepted 19 August 2018; Published 31 October 2018

Academic Editor: Athanasios Hatzikoutelis

Copyright © 2018 Odysseas Kosmas and Theodoros Smpoulias. This is an open access article distributed under the Creative Commons Attribution License, which permits unrestricted use, distribution, and reproduction in any medium, provided the original work is properly cited. The publication of this article was funded by SCOAP³.

In this work, we simulate γ -rays created in the hadronic jets of the compact object in binary stellar systems known as microquasars. We utilize as the main computational tool the 3D relativistic magnetohydrodynamical code PLUTO combined with in-house derived codes. Our simulated experiments refer to the SS433 X-ray binary, a stellar system in which hadronic jets have been observed. We examine two new model configurations that employ hadron-based emission mechanisms. The simulations aim to explore the dependence of the γ -ray emissions on the dynamical as well as the radiative properties of the jet (hydrodynamic parameters of the mass-flow density, gas-pressure, temperature of the ejected matter, high energy proton population inside the jet plasma, etc.). The results of the two new scenarios of initial conditions for the microquasar stellar system studied are compared to those of previously considered scenarios.

1. Introduction

The emissions of γ -rays, neutrinos, etc. within the jets of microquasars (MQs) have recently gained great interest among researchers seeking to understand the structure properties and evolution of X-ray binary systems [1–3].

Special interests appeared on the γ -ray emission mechanisms inside the hadronic jets, as the photon-hadron interactions [4, 5] and the hadron-hadron interactions [6, 7] as well as the γ -ray absorption that help to deepen our knowledge on microquasars evolution [8].

On the other hand, the strong magnetic field in the jets may significantly affect the total internal γ -ray and neutrino emissions by tuning several processes determining the high energy proton population (synchrotron radio emission, etc.). Therefore, magnetic field effects should be appropriately incorporated and treated in jet models [9, 10].

Recently, neutrinos from galactic microquasars, even though not being detected so far, have been modelled and several simulations have been performed towards this aim. Such modelling may support future attempts to detect them (see, e.g., [7, 11]).

Invariably, the jets of microquasars as well as in general the astrophysical jets may be described as fluid flow emanating from the vicinity of the compact object. Such a microquasar system is the SS433 X-ray binary consisted of a donor (companion) star and a compact stellar object which emits relativistic jets in various wavelength bands. Currently it is the only microquasar observed with a definite hadronic content in its jets, as verified from observations of spectral lines [1, 2, 9].

Radiative transfer calculations may be performed at every point in the jet (for a range of frequencies/energies, at every location) [12], providing the relevant emission and absorption coefficients. In such cases, finally a line of sight integration may derive synthetic images of jet γ -ray emission, at the energy-window of interest [12, 13].

The relativistic treatment of jets takes into account various energy loss mechanisms that occur through several hadronic processes [4–7]. In the known fluid approximation, macroscopically the jet matter behaves as a fluid collimated by the magnetic field. At a smaller scale, consideration of the kinematics of the jet plasma becomes necessary for treating shock acceleration effects.

Many authors consider that the proton-proton (p-p) collisions between fast high energy protons (nonthermal protons) and bulk-flow slow (thermal) protons constitute the dominant cooling process of the high energy proton population of the jet. This mechanism explains the main part of the γ -rays and neutrinos produced in the binary SS433 system. The acceleration of thermal protons (diffusive first-order shock acceleration) occurs above a minimum threshold proton energy [7].

Assuming a Maxwellian energy distribution for the “slow” protons, only a tiny portion of the total bulk proton jet flow, i.e., the fastest of them, may undergo diffusive shock acceleration and may jump to the fast proton population. Hence, the fast protons constitute a small fraction of the total jet proton density which subsequently produce γ -rays, neutrinos, etc. In this work, we assume that this is the dominant mechanism generating high energy γ -rays in the SS433 microquasar jets.

For the sake of completeness, we mention that another rather important mechanism has been suggested based on the hadronic interactions occurring within the jet-wind interaction zone [7]. In this scenario, the γ -rays are generated from the decay of neutral pions, as $\pi^0 \rightarrow \gamma + \gamma$. Pions are created via inelastic collisions of jet protons, ejected from the compact object, and ions of the stellar wind (such a process may also occur in the vicinity of the extended disk of the binary system) [6]. The latter emission mechanism is rather weak in SS433 [7].

So far microquasar γ -ray emissions have been observed through Cherenkov telescopes (HESS, MAGIC, and CTA) and orbital telescopes (INTEGRAL, Fermi) [15–20]. We also mention that, for low energy γ -rays, ongoing and future or next generation measurements with INTEGRAL (ESA satellite) and Fermi (NASA orbital telescope) may provide new data. Furthermore, very high energy γ -rays, in general above about 30 GeV, can be studied with ground-based Cherenkov telescopes [21].

Phenomenologically, estimations of high energy γ -ray emission from MQs have extensively been carried out [9, 12]. In this work, using the 3D relativistic hydrocode PLUTO [22] and some in-house (mainly radiative transfer) code (now written both in Mathematica and in C) [23–25], we model γ -ray emissions from hadronic microquasar jets in the E_γ -energy range $1.2 \text{ GeV} \leq E_\gamma \leq 10^2 - 10^3 \text{ TeV}$.

The emission/absorption coefficients are computed on the basis of Monte Carlo simulations of terrestrial particle-particle collision experimental data [12, 26, 27] that describe γ -ray emission in MQs. Such simulations provide analytical parametrization for emission and absorption coefficients in a wide range of γ -ray energies (frequencies) produced in microquasar jets [12, 28].

Furthermore, by exploiting the hydrodynamic variable values supplied by PLUTO, our line of sight code may provide emission/absorption coefficients for every location in the jet. The results produced this way depend on the initial high energy proton distribution inserted in the hydrodynamical model jet [12, 29].

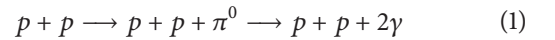
In the rest of the paper, at first (Section 2) the main MQs emissions mechanisms are briefly summarized. Then (Section 2.4), the radiative transfer method and the calculational procedure for obtaining gamma-ray emission are briefly described. The results of the 3D relativistic hydrocode PLUTO for the emission/absorption coefficients are presented in Section 4. Finally (Section 5), the main conclusions extracted in this work are summarized.

2. Outline of MQ Jet Emission Mechanisms

The SS433 microquasar, an eclipsing X-ray binary system with a compact object most likely a black hole, comprises two oppositely directed precessing hadronic jets. The spectrum of the companion (donor) star suggests that it is rather a late A-type MQ. In modelling γ -ray emission from SS433 in our present work, we assume that they are created mainly through p-p interactions between fast (relativistic) and slow (cold) protons within its hadronic jets.

Other production mechanisms, though not excluded, are considered less important. For example, some authors considered that the high energy γ -rays in hadronic MQ jets, are produced from p-p collisions taking place in the jets due to the interaction of relativistic protons with target protons of the rather weak stellar wind created in the companion star [6].

The main reaction chain that produces γ -rays starting from p-p interaction through the pion decay channel is written as



($m_p = 1.67 \times 10^{-24} \text{ g}$ and $m_\pi = 2.38 \times 10^{-25} \text{ g}$). References [6, 7, 26] present an analytical description of the evolution of reaction chain within the jet. Here we assume that a very energetic but small proton population, N_{fp} (formed due to shock fronts in the jet), interacts with the bulk-flow jet protons.

From the latter protons, high energy protons are produced through first-order Fermi acceleration that occurs at shocks within the jet [7]. Such shocks are considered rather homogeneously distributed throughout the jet. The jet matter density is closely related to the density of the aforementioned shocks; thus, the internal shocks convert a portion of the bulk kinetic energy of cold protons, K , to the fast protons energy E_p of the multidirectional motion. The rate, t_{acc}^{-1} , at which some slow protons are transferred to the high energy distribution is described in [1] by

$$r = t_{acc}^{-1} = E^{-1} \frac{dE}{dt} \simeq \beta^2 \frac{ceB}{E_p}, \quad (2)$$

where e denotes the proton charge, $\beta = u_{jet}/c$ with u_{jet} being the jet matter’s local velocity, and B denotes the magnetic field.

Concerning the magnetic field B , we assume that this is either constant or it decreases with the distance from the jet base as $B \sim z^{-1}$ [30, 31]. We stress that such a variation leads to a decrease of proton acceleration not more than two orders

TABLE 1: Scenario C (run 3) has artificially accelerated precession, while scenario D (run 4) has all the densities of the system increased by a few orders of magnitude, in order to account for a higher jet-mass flow-rate (jet’s kinetic luminosity). The parameter n refers to a “normalization” process that equates the results of two different methods of γ -ray emission calculations, one applied for energies above $E_\gamma=100$ GeV and the other below this limit.

Parameter/Scenario	C (run3)	D (run4)	Comments
cell size ($\times 10^{10}$ cm)	0.40	0.40	PLUTO’s computational cell
ρ_{jet} (cm^{-3})	1.0×10^{11}	1.0×10^{14}	jet’s matter density
ρ_{sw} (cm^{-3})	1.0×10^{11}	1.0×10^{12}	stellar wind density
ρ_{adw} (cm^{-3})	1.0×10^{11}	1.0×10^{13}	accretion disk wind density
t_{run}^{max} (s)	1.5×10^3	1.5×10^3	model execution time
Method	P. L.	P. L.	Piecewise Linear
Integrator	Ch. Tr.	Ch. Tr.	Characteristic Tracing
EOS	Ideal	Ideal	Equation of state
n	0.1005	0.1005	$E_\gamma = 100$ GeV normalisation
BinSep (cm)	4.0×10^{12}	4.0×10^{12}	Binary star separation
M_{BH}/M_\odot	3-10	3-10	Mass range of collapsed star
M_*/M_\odot	10-30	10-30	Mass range of Main Seq. star
$\beta = v_0/c$	0.26	0.26	Initial jet speed
L_k^p	10^{36}	10^{39}	Jet kinetic luminosity
grid resolution	300 * 500 * 300	300 * 500 * 300	PLUTO grid resolution (xyz)

of magnitude compared to its value around the jet’s base $z = z_0$. We further stress that the acceleration rate of fast protons, $r = t_{acc}^{-1}$, depends on the magnetic field B as indicated in (2).

Alternatively, (2) gives the production rate of fast protons at every “location” in the jet, though the production of γ -rays from these fast protons occurs at a next stage (by “location” we mean a hydrodynamical grid-cell which, microscopically, is very large); of the order of 10^{10} cm [7]. We note that the presence of β^2 in (2) cuts off γ -ray emission from slow-moving matter into the jet (acceleration sites are much less in slow matter).

Moreover, in jet emission calculations the β^2 is incorporated into the jet density. Also, the proton acceleration rate cannot affect the γ -ray emission rate, unless β drops below some value. As we will see below, in this work, instead of the proton density ρ , we also use the product of jet matter density times the velocity squared ρu^2 [7, 13].

Regarding the particles ejected from a hadronic jet, we consider that they are mostly slow (thermal) protons of density n_{sp} and a small portion of fast (nonthermal) protons of density n_{fp} . The energy distribution of the fast protons in the jet’s frame (see below) is described by [7, 13]

$$n_{fp}(E') = K_0 (E')^{-\alpha} \quad (3)$$

($E' \equiv E'_{fp}$) which is a power law type distribution. The parameter α takes the value $\alpha = 2$ and K_0 denotes a normalization constant [13].

In Table 1, we tabulate the values of some model jet parameters (together with explanation of their symbols) relevant to γ -ray emissions from the SS433 binary system (The scenarios C and D are described below).

2.1. Flux in Observation and Jet’s Frame. In our γ -ray flux calculations, we denote the flux density of the fast (slow)

proton populations as $J_{fp}(J_{sp})$, in the observation frame, and as $J'_{fp}(J'_{sp})$, in the jet’s frame. Moreover, at a given jet point, in the jet (moving) frame, the fast protons energy-spectrum is described by (3). For the corresponding fast protons spatial density we adopt the relation

$$n_{fp}(E') \propto w \frac{dN'_{fp}}{dE'} = w K_0 (E')^{-\alpha} \quad (4)$$

where

$$w = n_{sp} \beta^2 \quad (5)$$

($\beta \equiv u/c$, with $u = |\mathbf{u}|$ being the magnitude of the total velocity vector) where n_{sp} is in protons/cm³ [29]. From (5) one can conclude that the emission from the fast-moving matter of the jet is larger compared to the emission from slow-moving matter which is because in (2), t_{acc} is proportional to β^2 and creates fast proton jet density which subsequently allows for p-p collisions to occur and for γ -rays to be produced. [6].

2.2. The Model of Jet’s Dynamics. The jet is assumed to travel along the y axis (we consider particles of mass m_p). Then, for the flux densities, we can write (steady state)

$$J_{sp} = m_p w = m_p n_{sp} \beta^2 \quad (6)$$

In general, u is not necessarily parallel to the y -axis, but it may point almost anywhere which in turn means that emission may occur from jet matter moving in any direction. Furthermore, the emission mechanism is based on “randomly oriented turbulent shocks”, so the emission is considered multidirectional (no secondary emissions from scattering are assumed, since more shocks exist wherever the jet matter moves faster).

In our simulations, large turbulences of the jet flow may appear which favor shocks existence. This is due to the assumed strong dependence on the local velocity of the jet or ambient matter (acceleration rate is proportional to u^2 and further $J = \rho u^2$). Here, instead of the simple ρ dependence, we adopt, in addition, the ρu^2 dependence to distinguish the moving matter of the jet from that of the surrounding medium. This way, the calculation of γ -rays and neutrino emissions from the jet are decoupled from the influence of the surrounding matter. Then, the jet's contribution to high energy γ -ray emission is mostly dependent on its internal turbulence (turbulence here means spatial number density of proton accelerating shocks randomly oriented) [7].

From the above discussion, we note in short that the proton acceleration efficiency of the model jet is proportional to the square of the local velocity of the flow (the fast proton density is considered proportional to the square of the local velocity). Thus, the fast protons spatial density, n_{fp} , is also taken as proportional to the slow protons spatial density, n_{sp} as well as to the square of the local velocity.

Furthermore, for hydrodynamical jets [12, 13] the fast proton current density, $J'_{fp}(E')$, as a function of their energy, is given by

$$J'_{fp}(E') = \frac{c}{4\pi} K_1 n_j \beta_j^2 (E')^{-\alpha} \quad (7)$$

In the latter expression, n_j denotes the slow bulk jet protons local density hydrodynamical model (PLUTO code) [12].

2.3. The Current Density in the Observer's Frame. Regarding the transformation, to the observer frame, we write [32]

$$J_{fp}(E_p, t) = \frac{c}{4\pi} K_1 n_{sp} \beta^2 F. \quad (8)$$

F represents a function of stationary frame energy E_p written as

$$F = \frac{\gamma^{-\alpha+1} (E_p - \beta_b \sqrt{E_p^2 - m_p^2 c^4} \cos i_j)^{-\alpha}}{\left[\sin^2 i_j + \gamma^2 \left(\cos i_j - (\beta_b E_p) / \sqrt{E_p^2 - m_p^2 c^4} \right)^2 \right]^{1/2}} \quad (9)$$

In the latter equation, $i_j(t)$ denotes the angle between the jet axis and the line of sight (for SS433 microquasar $\beta_b = v_b/c = 0.26$), and

$$\gamma = [1 - \beta_b^2]^{-1/2} \quad (10)$$

is the jet Lorentz factor.

Thus, F provides the relation of J_{fp} (for laboratory frame) that depends on the γ -ray energy E_γ as measured in laboratory frame (see (7)). In conclusion, one can work with laboratory frame quantities only, which are also the jet model quantities (for other symbols the reader is referred to [12, 13, 28, 29])

2.4. The 3D Radiative Transfer in Time-Dependent Jet. The propagation of γ -rays along a one-dimensional line of sight (without scattering) we address here is based on the relation

$$\frac{dI_\gamma}{dl} = -I_\gamma \kappa_\gamma + \epsilon_\gamma \quad (11)$$

where κ_γ is the absorption coefficient at a given frequency (energy) ν and ϵ_γ is the relevant emission coefficient. I denotes the intensity and l is the length along the line of sight.

By considering the model jet artificially imaged in γ -rays, we calculate the emission from a small jet element corresponding to a computational cell (for simulated emissions). To this aim, we first define the quantity

$$dI_\gamma = J_\gamma dV = \rho dV \frac{dN_\gamma}{dE_\gamma} = dm_{cell} \frac{dN_\gamma}{dE_\gamma} \quad (12)$$

to represent the intensity created from a cell of volume dV , at a given frequency, or γ -ray energy E_γ , while ρ is the hydrodensity of the cell ($\rho = m_p n_{sp}$) and dN_γ stands for the emission coefficient of the cell at the same frequency. An alternative version of the above quantity is

$$dI_\gamma = \rho dV \frac{dN_\gamma}{dE_\gamma} u^2, \quad (13)$$

where u is the local jet matter velocity.

3. Use of PLUTO Code for Gamma-Ray Emission Calculations

Our calculation of the emission coefficient dN_γ proceeds directly starting from the hydrodynamical properties of the model jet (supplied by a check point of the PLUTO code). These quantities enter the calculation of the emission coefficients, ϵ_γ , at every computational cell of the 3D hydrodynamical model grid.

We mention that the production of synthetic images from the data is carried out by using the line of sight code constructed in [12] (here, instead of the radio emission and absorption coefficients we require their γ -ray equivalents, ϵ_γ and κ_γ ; in the case of neutrino production we need only emission coefficients).

In using the hydrodynamical code, PLUTO, the energy E_γ (in GeV) refers to the observed γ -ray energy. The quantity n_{sp} , i.e., the bulk-flow slow jet proton number density of ejected particles, is the dynamically important. This number density is taken to represent the hydrodynamic number density of the PLUTO code, namely,

$$n_{sp} = n_{j(PLUTO)} \quad (14)$$

The fast proton density, n_{fp} , though not-important dynamically, is radiatively important. For SS433, in the fast proton power law energy distribution, the index α takes the value $\alpha = 2$, and the ratio of the initial jet beam speed u_b divided by the speed of light is $u_b/c = \beta_b = 0.26$ [13].

In the hydrodynamic (HD) simulations with PLUTO code, as we have done previously [12, 13], the magnetic field lines are assumed to follow the matter flow. Their tangling with the jet material makes applicable the fluid approximation within the jet [33]. In this case, the magnetic field could not affect the flow dynamics which is however possible in the magnetohydrodynamic (MHD) treatment of PLUTO. In the relativistic hydrodynamical version of PLUTO, the magnetic

field within the jet's medium is assumed rather strong so as the coupling effects permit the fluid approximation to be applicable. At the same time, the dynamical effects of the magnetic field on the relativistic flow are not permitted [33].

We mention that, in modelling the microquasar SS433 system with PLUTO, only one of the twin jets is considered. The counterjet is presumed to exist outside the model space (at the bottom of $x - z$ plane), but its interference with our model system is considered very small [34]. The computational grid is 3D Cartesian (x, y, z) , homogeneous and the boundary conditions are adopted to be reflective at the jet's base ($x - z$ plane) and outflow at all other planes of the computational domain (box).

The grid spans $120 \times 200 \times 120$ (for x, y, z , respectively), in model length units (equal to 10^{10} cm) and the resolution used is $300 \times 500 \times 300$ (for x, y, z , respectively). The jet emanates from the middle of the $x - z$ plane, at the point $(60, 0, 60) \times 10^{10}$ cm and then advances while precessing around the $(60, y, 60)$ line (parallel to the y -axis). The precession angle for the SS433 jet used ($\delta = 0.2$ radians), is slightly smaller than the value of 21 degrees of [34], in order to allow the use of finer resolution.

The centre of the companion star is supposed to be outside of the box, at the point $(400, 0, 400)$ while compact object is situated at the point $(60, 0, 60)$, i.e., at the jet's base. We remind that, because the exact orbital separation in SS433 is not well known, this estimation is within an order of magnitude (the objects are orbiting around their centre-of-mass). We also mention that we assume that the companion star is not included in the model [12]. However, its wind is included through its density which is taken as decreasing with distance r (as $1/r^2$), away from its centre.

Furthermore, we also include a simplified accretion disk wind through the jet's dynamic interaction with both winds. This means that our model is less realistic as we approach the companion star and accretion disk locations but the results are reliable in the vicinity of the jet. For a detailed discussion related to important phenomena of the jet's interaction zone with nearby winds, the reader is referred to the Refs. [12, 13, 28, 29] and references therein.

4. Results of Simulations for the New Jet Model Scenarios

In this section, we present the results for two new scenarios of initial conditions (referred to the microquasar stellar system SS433) obtained as follows: (i) Hydrodynamical simulation carried out by utilizing as main computational tool the 3D relativistic hydrocode PLUTO and (ii) Gamma-ray emission synthetic images obtained with the line of sight integration.

In scenario C, the jet precesses faster than reality, therefore precession effects are enhanced. In this case, the jet involves artificially accelerated precession, in order to better investigate the effects of precession on the surrounding winds, within the limited time-frame of the model run.

In scenario D, the jet is quite heavier than both winds, in order to consider the possibility of a dense jet beam, containing the estimated jet mass flow of SS433 while remaining

more focused and more both narrow. The heavier jet of this scenario crosses the winds with greater ease. Also the effects of its interaction with the winds appear decreased.

We note that another characteristic scenario would have been a jet much lighter than both winds, but this would have taken longer simulation time, and practically more difficult.

In both cases, the jet begins to expand into the accretion disk wind, but at a more limited pace, due to the increased density of that wind in the model. As soon as the jet head reaches the stellar wind region, however, the jet's expansion rate increases greatly (especially sideways), in the form of a side shock that accumulates ambient matter. At the same time, the accretion disk matter is expelled outwards, from the vicinity of the jet base, forming a "ring" around the jet. The accretion disk wind is swept in a prominent way, being denser than the stellar wind, leading to the creation of a halo around the jet base (see below).

The structure develops throughout the model run, therefore suggesting the possibility of its persistence later on, when the jet reaches its lobe in the W50 nebula. This is similar (to a certain extent) in structure to that discussed in [14]. The above scenarios are applied to the SS433 microquasar as described below.

4.1. Description of Runs for Scenarios C and D

4.1.1. Simulations of Scenario C. Scenario C (medium resolution, see Figures 1, 2, 3, and 4) has been chosen to cover the case of artificially fast precession of the jet. This way we may investigate the effects of precession on the system observables. The precessing jet sweeps across more of the ambient matter in a given period of time, as compared to an otherwise same but nonprecessing jet (run2-scenario), with both jet examples considered to be moving through identical surroundings. Consequently, the effects of the precessing jet on its surrounding environment are, in terms of affected volume, more prominent than when precession is absent. More ambient matter is displaced and part of it ends up being dragged along by the jet, albeit at a pace clearly slower than when precession is slower.

The precessing jet model was therefore run, at an accelerated precession rate, and that showed an enhanced effect of sweeping the accretion disk wind matter from the jet cone. This, in effect, caused the formation of an enhanced, outward moving, "halo", around the jet base (Figures 1 and 2). The precessing jet advances, first through the accretion disk wind, and then through the stellar wind, opening its path at an accelerating pace, due to meeting with progressively lower resistance, due to the falling density of the winds. The latter originated from both the accretion disk and the companion star. The gradient of the stellar wind, within the computational grid, is, however, not big, due to the increased distance from its origin, the companion star.

The jet precession pronounces the sweeping of the inner, denser part of the accretion disk wind, leading, later on, to the formation of an expanding approximately torus-shaped halo surrounding the jet whose axis roughly coincides with the axis around which the jet precesses. The torus

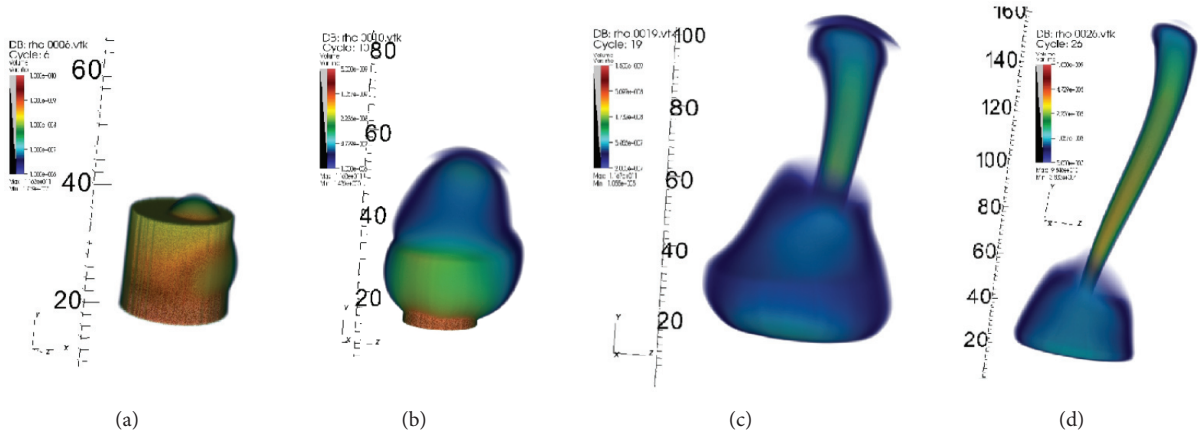


FIGURE 1: Scenario C: three-dimensional density snapshots obtained as in scenario A of [13], but now we added an accelerated precession of the jet that leads to the formation of a revolving jet flow. See the rightmost panel of Table 1, where the jet is the most evolved among the plots (parameters of run3, snapshot intervals 50/count). The jet’s behaviour resembles to that of scenario A (run1) of [13]. Also, now the jet sweeps a larger volume of ambient matter and propagates slower than in the nonprecession case, though now more ambient matter is further activated for emission. Matter piles up around the jet base, hinting on a halo of slower moving (outbound) material there, crudely reminiscent of the suggestion of [14] for a halo formed around SS433.

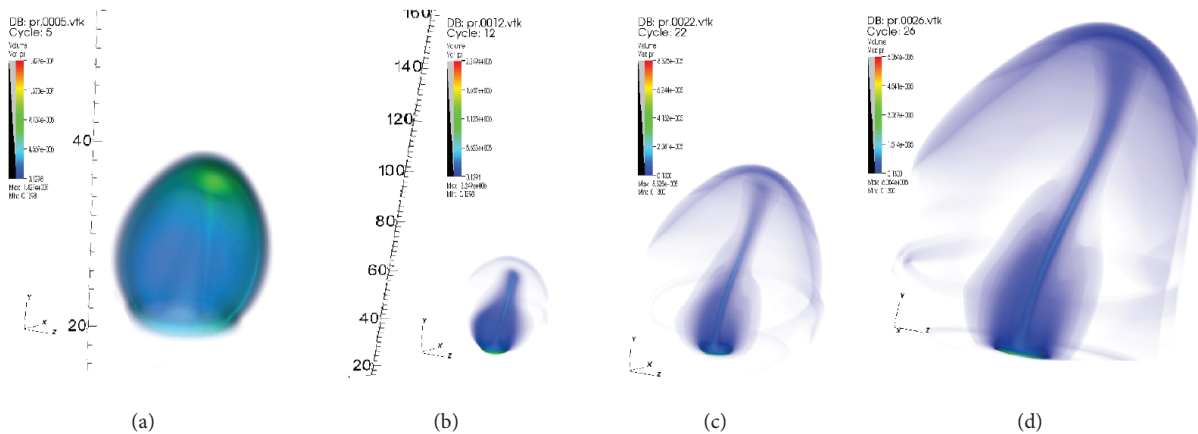


FIGURE 2: Scenario C: 3D illustrations of pressure evolution in the vicinity of the jet, as well as in the jet itself (in this case linear plots are produced, in order to better display the periphery of the system; see run3 parameters in Table 1). The three rightmost plots (b, c, d) share the same spatial size scale, whereas (a) has been magnified. The jet precession is visible, especially in (c) and (d), while a pressurized mass concentration can be found in the vicinity of the jet base, persisting throughout the model run and slowly advancing outwards. The front of the jet itself, due to precession, advances in an asymmetrical way.

consists mainly of accretion disk wind matter, forming a loose “barrel”, or hollow cylinder (Figures 1 and 2) around the jet, having a velocity component (clearly slower than the jet, i.e., subrelativistic) parallel to the jet’s precession axis, and a sideways expansion velocity component as well.

In the scale of the simulation, the companion star has a nonnegligible distance from the jet base, therefore in the immediate vicinity of the jet base, it is the more localized accretion disk wind that dominates over the stellar wind, in terms of density. It is, therefore, the accretion disk wind matter that is mainly expelled from the incoming jet and rushed outwards, swept over by the precessing jet. This finding might suggest a behaviour that over a much longer timescale leads to the formation of a “ruff” of material, around

the cone swept by the precessing jet, perhaps along the lines of the “bow-tie” structure recently observed in SS433 [14].

The jet precession makes it possible to drag an increased quantity of surrounding matter along the jet which is in contrast to a nonprecessing jet where the swept matter is significantly less. This happens because the precessing jet covers a cone with an opening angle much larger than the jet’s own. Therefore, more ambient matter is displaced than from a straight jet. Furthermore, the partially sideways motion of the precessing jet further disturbs the surrounding winds, pushing and dragging them in an outwards direction. However, the time scale for precession is much bigger than the jet crossing time of the model space. Therefore, a longer term simulation, perhaps including replenishment of the

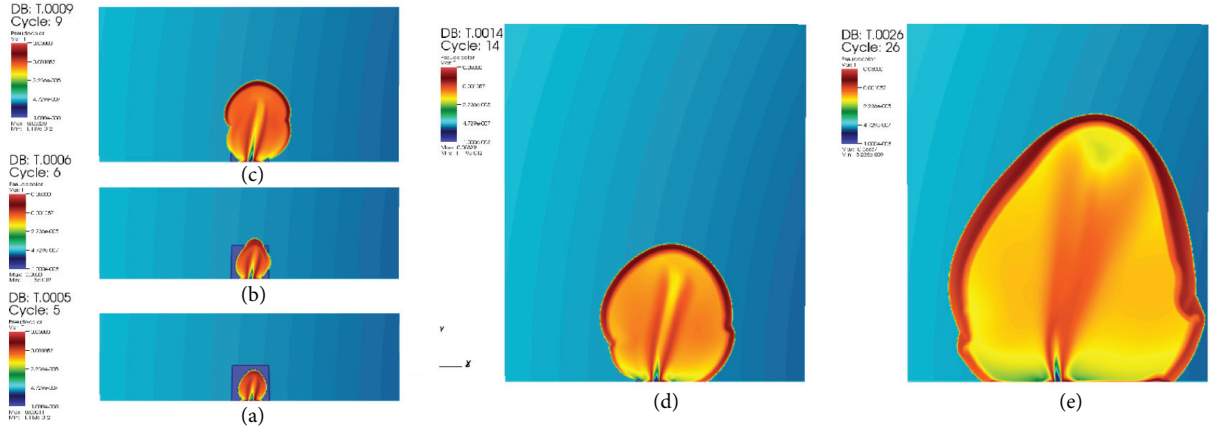


FIGURE 3: Scenario C: a series of slices representing the time evolution of temperature, as in scenario A of [13], but now assuming increased precession rate (see text). The temperature image depicts 2D slices cut along the jet, at a specific time instant. The precessing jet can be seen (d,e) to sweep across a larger (compared to scenario A [13]) portion of the surrounding wind volume, piling up additional matter around its head and sides (see run3 parameters in Table 1). The expansion rate is lower in the accretion disk wind region and increases in the stellar wind region, but afterwards it stays relatively constant, as the density gradient of the wind (visible in the images) is not too large along the jet path.

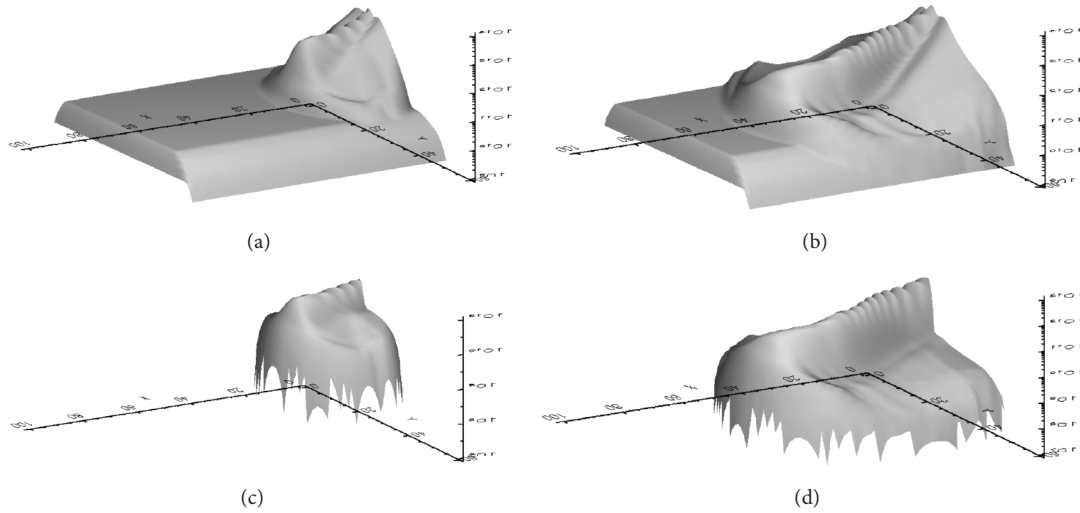


FIGURE 4: Scenario C (run3): illustration of the synthetic γ -ray images. In the plots the x - y plane defines the (synthetic) observation plane. z -axis represents the intensity at each pixel of the observation plane (arbitrary units). For each one of the latter, a line of sight (LOS) is drawn that crosses the computational domain volume and ends up at the aforementioned pixel. The radiative intensity along the LOS is calculated using the radiative transfer equation. We see two different cases for emission coefficient used, with two snapshots for each case. In the first row, ρ is used as emission coefficient (the intensity appears higher when the matter is denser). In the second row, ρ^2 is used as emission coefficient. The fast-moving jet matter now prevails in terms of γ -ray intensity, as compared to the clearly lower emission from slower moving surrounding material. In both configurations, we see the distinct signature of the precessing jet on the bent jet emission patterns formed, as well as on resolution effects at a faster pace than the rest of runs. In order to compare those images to actual observations, one would have to convolve them with the “beam” of the observing instrument, as it is provided by the operator. As a first step, it is possible to compare the sensitivity of an observing gamma-ray instrument to the “sensitivity” of the synthetic images, using a process similar to the one described in SK14.

winds as well, would be needed in order to study the effects of precession on the jet’s environment.

4.1.2. Simulations of Scenario D. In scenario D (medium resolution) discussed in this work (see Figures 5, 6, 7, and 8), the jet is assumed heavier than its surrounding winds, which in turn are also somewhat heavier than those of the

other cases, leading to a faster crossing of the computational domain (Figure 5). Sideways expansion is also swift as the increased jet mass density allows for a faster “sweep” of the wind matter. Leftovers from the displaced accretion disk wind matter can be seen piling up around the jet base (Figure 6).

The jet forms a funnel that transfers mass outwards at an increased flow rate. The properties of the jet’s surroundings

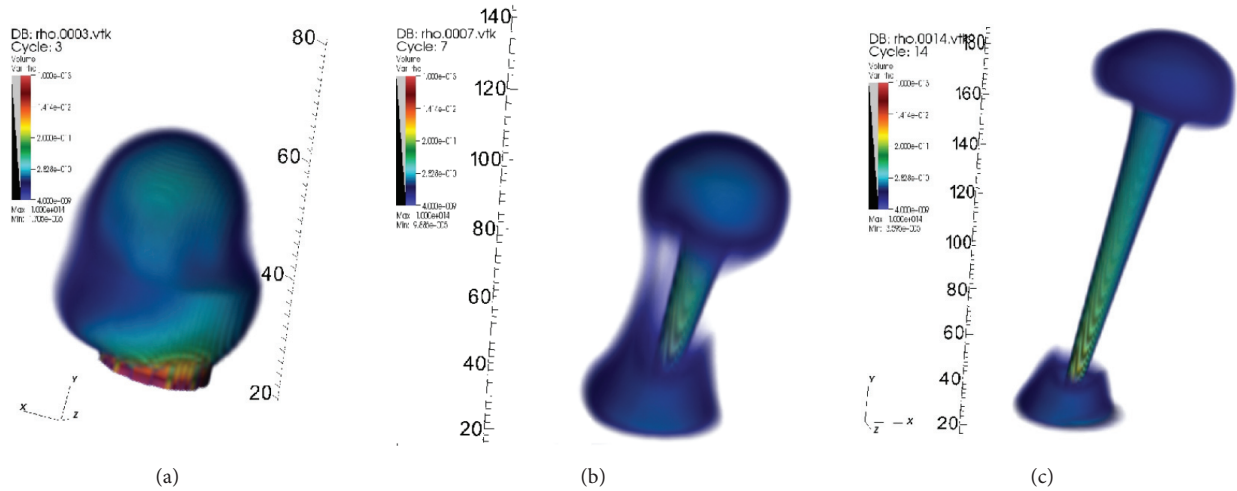


FIGURE 5: Scenario D: a series of snapshots depicting the density evolution (logarithmic plots) for the run4. Here we can see 3D plots of the jet proton density in space, at specific time instants of the simulation run. This time the jet is quite much heavier than both surrounding winds, leading to a decreased jet crossing time of the model space. The jet mass flow rate now rests closer to the estimates for SS433. The jet breaks through the accretion disk wind construct and soon crosses the stellar wind at a rapid pace (run4 parameters in Table 1, snapshot intervals of 50/count).

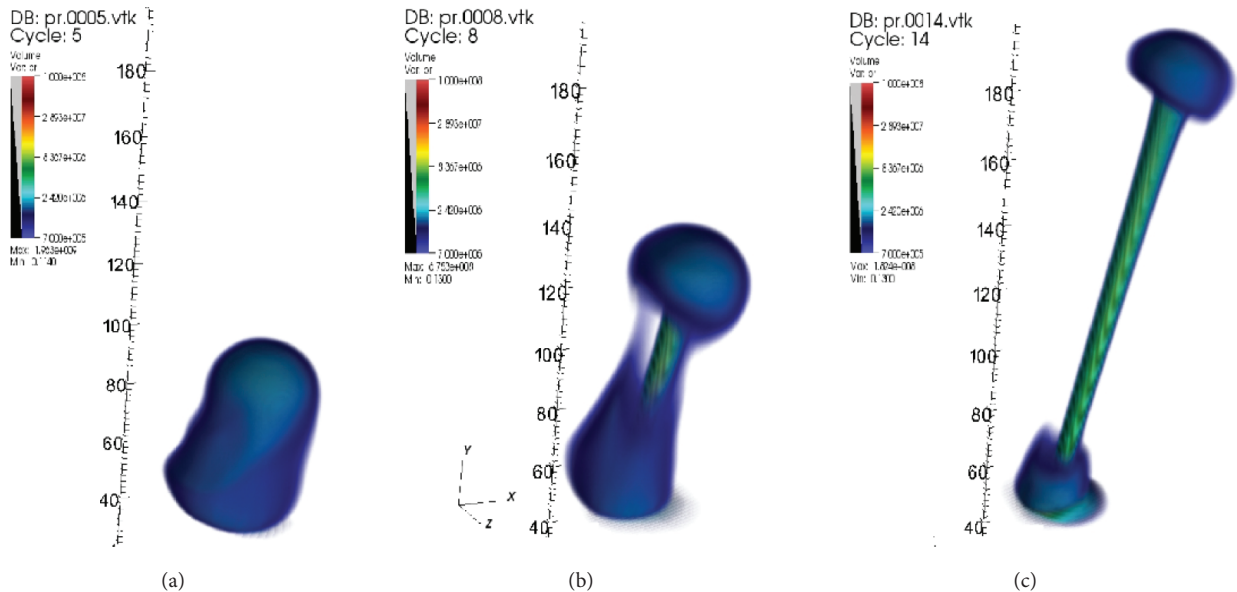


FIGURE 6: Scenario D: the pressure evolution for the model jet of run4. This plot is similar to the one for the jet density. The patterns are similar to those of the density for the same run. The higher jet's density dominates the system dynamics, leading to comparatively poorer features around the jet, in relation to other runs where the jet was lighter. The pressure distribution follows the above general pattern. A pressure increase is also seen around the jet base, due to the mass leftover from the disturbed accretion disk wind that used to be there (run4 parameters in Table 1).

are now less pronounced as the expansion meets with reduced resistance from ambient matter. The dynamic behaviour of the jet dominates the hydrosimulation, with the wind's matter giving way to the jet (Figures 7 and 8). This case covers the possibility of jet production as a very dense inflow at the source, thus enriching nearby interstellar matter with important mass outflow per time interval.

All of the hydrocode snapshots, of hydrodynamic parameters, have been created with the VisIt visualization

code (<https://wci.llnl.gov/simulation/computer-codes/visit>), whereas the synthetic γ -ray images have been produced using IDL (<https://www.harrisgeospatial.com/SoftwareTechnology/IDL.aspx>).

4.2. *Gamma-Ray Emission Synthetic Images.* The above discussed runs with the hydrocode PLUTO have been performed for a precessing jet model of SS433. As the simulation

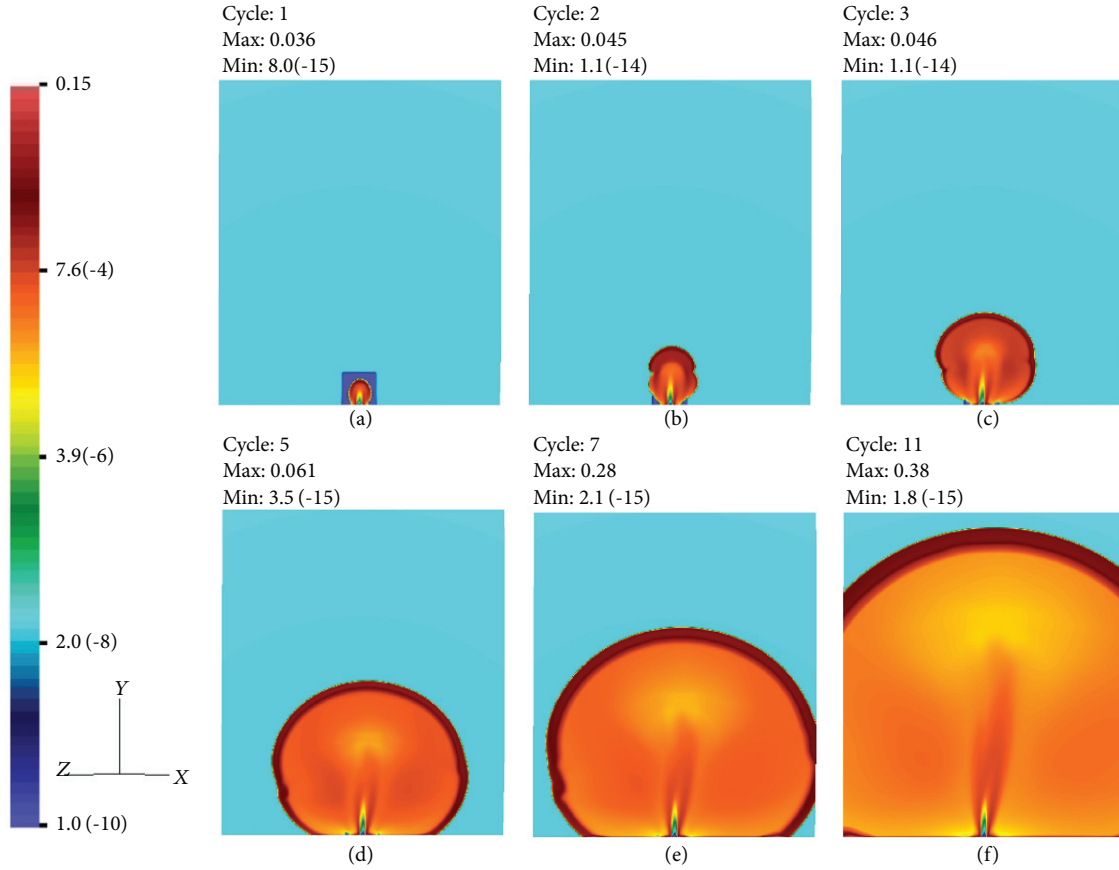


FIGURE 7: Scenario D: a series of plots for the jet temperature of run4 (run4 parameters in Table 1). This plot shows 2D slices cut along the jet, depicting the temperature on the slice, at a specific time instant. The, faster than previous runs, advance of the jet, through surrounding wind matter, is characterized by an expanding shock front. Said expansion is initially slower, till the jet crosses the simplified accretion disk wind construct. Then, a higher rate of expansion occurs, especially to the sides, as the stellar wind gradient is less pronounced, since we have $\Delta x < \Delta r$, where x is the jet crossing distance and r is the distance to the binary companion star.

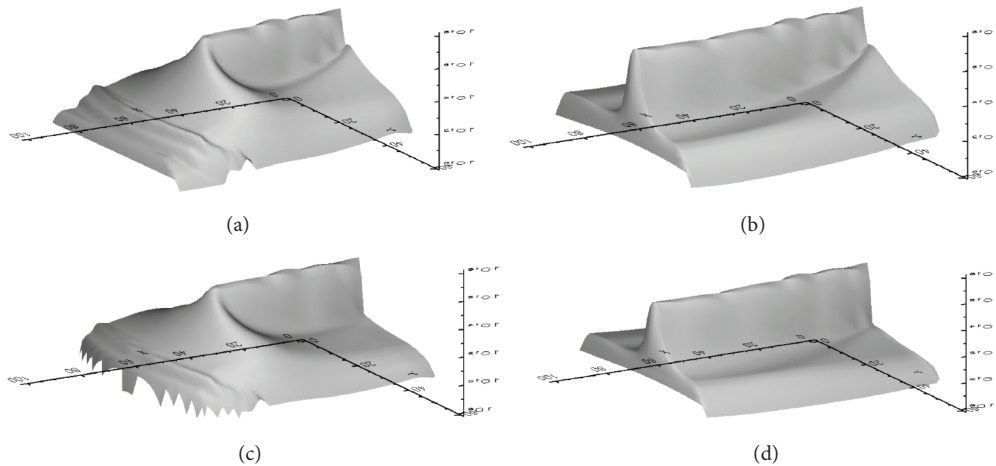


FIGURE 8: Scenario D: the top row shows two snapshots of the “heavy jet” run4 (run4 parameters in Table 1), using the hydrodynamical density ρ as the emission coefficient (arbitrary units). The jet makes its way through the surrounding winds, piling up matter ahead of its head and around the jet shock front, as well as around the jet base (remnants of the accretion disk wind). The bottom row shows the line of sight integration images of the same scenario (D), where now ρu^2 is the emission coefficient. This time only matter that is both fast and dense, simultaneously, does contribute to the emission. The jet base, therefore, now emits much less, since, only the jet flow there is both fast and dense, whereas the remnants of the wind constitute dense but slow matter. The impact of resolution effects, from near the jet base, can also be seen as humps on the back of the jet intensity ridge.

proceeds, at some point the computational model space data is transferred to an output file to be processed (with the available line of sight (LOS) code) for producing a synthetic γ -ray image of the system. The data of a snapshot from the PLUTO hydrocode is transferred, in the form of 3D data arrays (density, velocity vector, pressure: ρ, u_x, u_y, u_z, P) to a routine that performs the LOS integration [12, 13]. Along the LOS, γ -ray emission and absorption coefficients are provided at each point.

At this level, the orbital separation of the compact object and the donor star is taken to be about 4×10^{12} cm so the stellar wind origin does not coincide with the jet base. Also, the jet is taken to travel through a halo produced from the accretion disk (centred at the jet's base). This matter is commonly called the accretion disk wind [12, 13].

With our method we follow two separate steps of calculations. We first obtain the hydrodynamic quantities of density and velocity with the PLUTO hydrocode and second, the integration (with the LOS code) provides the intensity. This decoupling allows, in the calculation of emission, the LOS integration to be performed using either ρ (in CGS units) or ρv^2 (in speed of light dimensionless units, $c = 1$) as the emission coefficient. Then, the synthetic image is formed, and subsequently the values of all of its pixels are summed to provide the total intensity released from the studied object. Finally, the γ -ray emission calculation is performed separately in Mathematica (for unit proton number density).

In each of the above scenarios (runs), for γ -rays a synthetic image was produced, at a suitable model time, using the relevant radiative transfer code of [12] (only the emission coefficient was employed). As can be seen, in all the synthetic γ -ray images (Figures 4 and 8), at each point of the computational volume, the denser the matter, the higher the emission at that point is.

Furthermore, it is clear that the larger the number of significant emission points along a line of sight, the higher the total emission of the whole line of sight is. By adding the dependence on the local velocity, denser but slower matter cannot emit any significant amount of γ -rays. Therefore, emission from the jet body and its interaction zone with surrounding media can be seen to be stronger in the $\rho\beta^2$ maps. In addition, the rest of the (roughly inert) medium in the system contributes very little to γ -ray emission.

Before closing we note that currently we apply the above-mentioned method to carry out jet emission simulations for other microquasar systems like the Cygnus X-1 and Cygnus X-3. From the viewpoint of observations we should mention that, for lower energy γ -rays, orbital platforms, such as NASA's Fermi and ESA's INTEGRAL, already offered an important relevant body of observations for various systems [21, 35]. Very high energy γ -rays can also be studied using data provided by ground-based Cherenkov telescopes such as HESS, MAGIC and HEGRA. Hydrodynamical jet models, combined with artificial imaging, offer realistic estimates of the conditions in the jet and surrounding environments, adding insight to open questions about the γ -ray jet emission from a microquasar.

5. Summary and Conclusions

A precessing jet was modelled using relativistic hydrodynamic code (PLUTO). Furthermore, the results were processed using line of sight code, assuming that the flow velocity u is much smaller than the speed of light. The LOS code integrates along lines of sight the equation of radiative transfer without scattering. The emission coefficients are, in general, a function of hydrodynamical and radiative parameters.

The intensity result of each LOS is assigned to the pixel where the LOS meets the imaging plane of "observation". In this way, an image is formed which could be called a synthetic γ -ray image. Only emission is used for this paper, but absorption may both be incorporated.

The currently available resolution for γ -ray imaging is lower than the resolution of synthetic imaging. Yet the connections between the emission properties and the underlying system dynamics do offer useful constraints on a variety of system parameters, such as the jet kinetic luminosity energy L_k . The above occurs in the light of potential future observations, originating from orbital γ -ray telescopes, from terrestrial Cherenkov detector arrays and even from underground neutrino detectors.

Data Availability

All data are provided in full in the results section of this paper.

Conflicts of Interest

The authors declare that they have no conflicts of interest.

Acknowledgments

Dr. Odysseas Kosmas wishes to acknowledge the support of EPSRC via Grant EP/N026136/1 "Geometric Mechanics of Solids".

References

- [1] M. C. Begelman, S. P. Hatchett, C. F. McKee, C. L. Sarazin, and J. Arons, "Beam models for SS 433," *The Astrophysical Journal*, vol. 238, pp. 722–730, 1980.
- [2] B. Margon, "Observations of SS 433," *Annual Review of Astronomy and Astrophysics*, vol. 22, no. 1, pp. 507–536, 1984.
- [3] R. M. Hjellming and K. J. Johnston, "Radio emission from conical jets associated with X-ray binaries," *The Astrophysical Journal*, vol. 328, pp. 600–609, 1988.
- [4] A. Levinson and E. Waxman, "Probing microquasars with TeV neutrinos," *Physical Review Letters*, vol. 87, Article ID 171101, 2001.
- [5] C. Distefano, D. Guetta, E. Waxman, and A. Levinson, "Neutrino flux predictions for known galactic microquasars," *The Astrophysical Journal*, vol. 575, no. 1 I, pp. 378–383, 2002.
- [6] G. E. Romero, D. F. Torres, M. M. K. Bernadó, and I. F. Mirabel, "Hadronic gamma-ray emission from windy microquasars," *Astronomy & Astrophysics*, vol. 410, no. 2, pp. L1–L4, 2003.
- [7] M. M. Reynoso, G. E. Romero, and H. R. Christiansen, "Production of gamma rays and neutrinos in the dark jets of the

- microquasar SS433,” *Monthly Notices of the Royal Astronomical Society*, vol. 387, no. 4, pp. 1745–1754, 2008.
- [8] B. Cerutti, G. Dubus, J. Malzac et al., “Absorption of high-energy gamma rays in Cygnus X-3,” *Astronomy & Astrophysics*, vol. 529, 2011.
- [9] I. F. Mirabel and L. F. Rodríguez, “Sources of relativistic jets in the galaxy,” *Annual Review of Astronomy and Astrophysics*, vol. 37, pp. 409–443, 1999.
- [10] M. M. Reynoso and G. E. Romero, “Magnetic field effects on neutrino production in microquasars,” *Astronomy & Astrophysics*, vol. 493, no. 1, pp. 1–11, 2009.
- [11] P. Lipari, M. Lusignoli, and D. Meloni, “Flavor composition and energy spectrum of astrophysical neutrinos,” *Physical Review D: Particles, Fields, Gravitation and Cosmology*, vol. 75, Article ID 123005, 2007.
- [12] T. Smpsonias and T. S. Kosmas, “Modelling the equatorial emission in a microquasar,” *Monthly Notices of the Royal Astronomical Society*, vol. 412, no. 2, pp. 1320–1330, 2011.
- [13] T. Smpsonias and T. S. Kosmas, “Dynamical and radiative simulations of γ -ray jets in microquasars,” *Monthly Notices of the Royal Astronomical Society*, vol. 438, no. 2, pp. 1014–1026, 2014.
- [14] K. M. Blundell and P. Hirst, “Jet propulsion of wind ejecta from a major flare in the black hole microquasar SS433,” *The Astrophysical Journal Letters*, vol. 735, no. 1, 2011.
- [15] J. A. Hinton, “The status of the HESS project,” *New Astronomy Reviews*, vol. 48, no. 5–6, pp. 331–337, 2004.
- [16] C. Baixeras, D. Bastieribo, C. Bigongiari et al., “Commissioning and first tests of the MAGIC telescope,” *Nuclear Instruments and Methods in Physics Research Section A*, vol. 518, pp. 188–192, 2004.
- [17] M. Actis, G. Agnetta, and F. Aharonian, “Design concepts for the Cherenkov Telescope Array CTA: an advanced facility for ground-based high-energy gamma-ray astronomy,” *Experimental Astronomy*, vol. 32, pp. 193–316, 2011.
- [18] F. Aharonian, A. G. Akhperjanian, and K.-M. Aye, “Discovery of very high energy gamma rays associated with an X-ray binary,” *Science*, vol. 309, no. 5735, pp. 746–749, 2005.
- [19] T. Y. Saito, R. Zanin, P. Bordas et al., “Microquasar observations with the MAGIC telescope,” <https://arxiv.org/abs/0907.1017>.
- [20] A. A. Abdo, M. Ackermann et al., “Modulated high-energy gamma-ray emission from the microquasar Cygnus X-3,” *Science*, vol. 326, pp. 1512–1516, 2009.
- [21] S. Hayashi, F. Kajino, T. Naito et al., “Search for VHE gamma rays from SS433/W50 with the CANGAROO-II telescope,” *Astroparticle Physics*, vol. 32, pp. 112–119, 2009.
- [22] A. Mignone, G. Bodo, S. Massaglia et al., “PLUTO: a numerical code for computational astrophysics,” *The Astrophysical Journal Supplement Series*, vol. 170, no. 1, pp. 228–242, 2007.
- [23] O. T. Kosmas and D. S. Vlachos, “Local path fitting: a new approach to variational integrators,” *Journal of Computational and Applied Mathematics*, vol. 236, no. 10, pp. 2632–2642, 2012.
- [24] O. Kosmas and S. Leyendecker, “Analysis of higher order phase fitted variational integrators,” *Advances in Computational Mathematics*, vol. 42, no. 3, pp. 605–619, 2016.
- [25] O. T. Kosmas, “Charged particle in an electromagnetic field using variational integrators,” in *Proceedings of the International Conference on Numerical Analysis and Applied Mathematics: Numerical Analysis and Applied Mathematics, ICNAAM 2011*, pp. 1927–1931, Greece, September 2011.
- [26] S. R. Kelner, F. A. Aharonian, and V. V. Bugayov, “Energy spectra of gamma rays, electrons, and neutrinos produced at proton-proton interactions in the very high energy regime,” *Physical Review D*, vol. 79, Article ID 039901, 2009.
- [27] D. F. Torres and A. Reimer, “Hadronic beam models for quasars and microquasars,” *Astronomy & Astrophysics*, vol. 528, article L2, 2011.
- [28] T. Smpsonias and O. T. Kosmas, “High energy neutrino emission from astrophysical jets in the Galaxy,” *Advances in High Energy Physics*, vol. 2015, Article ID 921757, 7 pages, 2015.
- [29] T. Smpsonias and O. Kosmas, “Neutrino Emission from Magnetized Microquasar Jets,” *Advances in High Energy Physics*, vol. 2017, Article ID 4962741, 7 pages, 2017.
- [30] F. M. Rieger, V. Bosch-Ramon, and P. Duffy, “Fermi acceleration in astrophysical jets,” *Astrophysics and Space Science*, vol. 309, no. 1–4, pp. 119–125, 2007.
- [31] V. Bosch-Ramon, G. E. Romero, and J. M. Paredes, “A broadband leptonic model for gamma-ray emitting microquasars,” *Astronomy & Astrophysics*, vol. 447, no. 1, pp. 263–276, 2006.
- [32] D. Purmohammad and J. Samimi, “On the hadronic beam model of TeV γ -ray flares from blazars,” *Astronomy & Astrophysics*, vol. 371, no. 1, pp. 61–67, 2001.
- [33] A. Ferrari, “Modeling extragalactic jets,” *Annual Review of Astronomy and Astrophysics*, vol. 36, no. 1, pp. 539–598, 1998.
- [34] S. Fabrika, “The jets and supercritical accretion disk,” *Astrophysics and Space Physics Reviews*, vol. 12, pp. 1–152, 2004.
- [35] M. G. Aartsen, M. Ackermann, and J. Adams, “Search for prompt neutrino emission from gamma-ray bursts with Ice-Cube,” *The Astrophysical Journal Letters*, vol. 805, no. 1, article L5, 2015.

Research Article

Neutral-Current Neutrino-Nucleus Scattering off Xe Isotopes

P. Pirinen ¹, J. Suhonen ¹ and E. Ydrefors²

¹University of Jyväskylä, Department of Physics, P.O. Box 35, 40014, Finland

²Instituto Tecnológico de Aeronáutica, DCTA, 12228-900 São José dos Campos, Brazil

Correspondence should be addressed to P. Pirinen; pekka.a.pirinen@student.jyu.fi

Received 26 April 2018; Accepted 18 August 2018; Published 4 October 2018

Academic Editor: Athanasios Hatzikoutelis

Copyright © 2018 P. Pirinen et al. This is an open access article distributed under the Creative Commons Attribution License, which permits unrestricted use, distribution, and reproduction in any medium, provided the original work is properly cited. The publication of this article was funded by SCOAP³.

Large liquid xenon detectors aiming for dark matter direct detection will soon become viable tools also for investigating neutrino physics. Information on the effects of nuclear structure in neutrino-nucleus scattering can be important in distinguishing neutrino backgrounds in such detectors. We perform calculations for differential and total cross sections of neutral-current neutrino scattering off the most abundant xenon isotopes. The nuclear-structure calculations are made in the nuclear shell model for elastic scattering and also in the quasiparticle random-phase approximation (QRPA) and microscopic quasiparticle-phonon model (MQPM) for both elastic and inelastic scattering. Using suitable neutrino energy distributions, we compute estimates of total averaged cross sections for ⁸B solar neutrinos and supernova neutrinos.

1. Introduction

When the idea of neutrinos was first suggested by Pauli in 1930, it was thought that they would never be observed experimentally. Only two decades later interaction of neutrinos with matter was detected in the famous Cowan-Reines experiment [1]. More recently, detection and research of neutrinos have become more and more of an everyday commodity, and various more versatile ways to examine interactions of the little neutral one have emerged and are being tested in laboratories all over the world.

Coherent elastic neutrino-nucleus scattering (CE ν NS) is a process where the neutrino interacts with the target nucleus as a whole instead of a single nucleon. Although CE ν NS has been predicted since the 1970s [2], it was discovered only very recently by the COHERENT collaboration [3]. Due to the coherent enhancement, this experiment had the remarkable feature of detecting neutrinos with a compact 14.6 kg detector instead of a massive detector volume which is used in conventional neutrino experiments. Coherent neutrino-nucleus scattering is on one hand an important potential source of information for beyond-standard-model physics [4–11], but on the other hand it may also hinder new

discoveries as it will start disturbing dark matter detectors in the near future.

A great experimental effort has been put into directly detecting dark matter in the past few decades (see [12] for a review). The next-generation detectors are expected to be sensitive enough to probe cross sections low enough to start observing CE ν NS as an irreducible background [13, 14]. Solar neutrinos, atmospheric neutrinos, and diffuse supernova background neutrinos provide a natural source of background neutrinos, which for obvious reasons cannot be shielded against. As there are uncertainties in the fluxes of each of the aforementioned neutrino types, the sensitivity of WIMP (weakly interacting massive particle) detection is basically limited to the magnitude of this uncertainty. To make matters worse, it has been shown that for some specific WIMP masses and cross sections the recoil spectra of CE ν NS very closely mimic that of scattering WIMPs [14].

It is therefore of utmost importance to devise a way to go through this neutrino floor. One potential way of achieving this is having directional sensitivity in the detector [15, 16]. As solar and atmospheric neutrinos have a distinct source within the solar system, it is expected that their recoil direction would be different to that of WIMPs, which are typically

assumed to be gravitationally bound in a halo spanning the galaxy. Also arising from the different origin of neutrinos and WIMPs is the idea of using timing information to discriminate between neutrino and WIMP induced events in a detector [17]. Due to the motion of the Earth around the Sun, it is expected that the solar neutrino flux peaks around January, but the WIMP flux peaks in June when the velocities of the Sun and Earth are the most in phase. The recoil spectra of WIMPs and neutrinos could also be distinguished if the WIMP-nucleus interaction happens via a nonstandard operator emerging in the effective field theory framework [18, 19].

Some of the leading dark matter experiments use a liquid xenon target [20–24], which allows for easy scalability to larger detector volumes. It is expected that the xenon detectors are the first to hit the neutrino floor. In this article we compute cross sections for elastic and inelastic neutrino-nucleus scattering for the most abundant xenon isotopes. For the coherent scattering we use the quasiparticle random-phase approximation (QRPA) framework and the nuclear shell model to model the nuclear structure and we compare the results between the two models. The wave functions of the states of odd-mass xenon isotopes are obtained by using the microscopic quasiparticle-phonon model (MQPM) on top of a QRPA calculation. Inelastic scattering is computed in the QRPA/MQPM formalism. In our calculations we consider ^8B solar neutrinos and supernova neutrinos.

A similar QRPA calculation has been made in [25] for ^{136}Xe , where both charged-current and neutral-current inelastic scattering was examined. Similar computations of neutral-current neutrino-nucleus scattering cross sections have been made before for the stable cadmium isotopes in [26] and for molybdenum isotopes in [27]. Both calculations used the QRPA/MQPM approach. To our knowledge this article presents the first calculation of neutral-current neutrino-nucleus scattering within a complete microscopic nuclear framework for Xe isotopes other than ^{136}Xe .

This article is organized as follows. In Section 2 we outline the formalism used to compute neutral-current neutrino-nucleus scattering. In Section 3 we summarize the nuclear-structure calculations made for the target xenon isotopes. In Section 4 we discuss the results of our cross-section calculations and in Section 5 conclusions are drawn.

2. Neutral-Current Neutrino-Nucleus Scattering

In this section we summarize the formalism used to compute neutral-current neutrino-nucleus scattering processes. We examine standard-model reactions mediated by the neutral Z^0 boson, namely, the processes

$$\nu + (A, Z) \longrightarrow \nu + (A, Z), \quad (1)$$

$$\nu + (A, Z) \longrightarrow \nu + (A, Z)^*, \quad (2)$$

i.e., the elastic and inelastic scattering of neutrinos off a nucleus (with A nucleons and Z protons), respectively. In the elastic process the initial and final states of the target

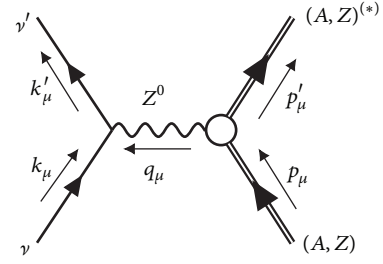


FIGURE 1: A diagram of the neutral-current scattering process. The four momenta of the involved particles are labeled in the figure.

nucleus are the same, while in the inelastic process excitation of the target nucleus takes place. The kinematics of the scattering process is illustrated in Figure 1. We label the four momenta of the incoming and outgoing neutrino as k_μ and k'_μ , respectively. The momenta of the target nucleus before and after interacting with the neutrino are p_μ and p'_μ . The momentum transfer to the nucleus is referred to as $q_\mu = k'_\mu - k_\mu = p_\mu - p'_\mu$. The neutrino kinetic energy before and after scattering is E_k and $E_{k'}$.

The neutral-current neutrino-nucleus scattering differential cross section to an excited state of energy E_{ex} can be written as [28]

$$\frac{d^2\sigma}{d\Omega dE_{\text{ex}}} = \frac{G_F^2 |\mathbf{k}'| E_{k'}}{\pi (2J_i + 1)} \left(\sum_{J \geq 0} \sigma_{\text{CL}}^J + \sum_{J \geq 1} \sigma_{\text{T}}^J \right), \quad (3)$$

which comprises the Coulomb-longitudinal (σ_{CL}^J) and transverse (σ_{T}^J) parts. They are defined as

$$\begin{aligned} \sigma_{\text{CL}}^J &= (1 + \cos \theta) \left| \langle J_f \| \mathcal{M}_J(q) \| J_i \rangle \right|^2 \\ &+ (1 + \cos \theta - 2b \sin^2 \theta) \left| \langle J_f \| \mathcal{L}_J(q) \| J_i \rangle \right|^2 \\ &+ \frac{E_{\text{ex}}}{q} (1 + \cos \theta) \\ &\times 2 \text{Re} \left\{ \langle J_f \| \mathcal{M}_J(q) \| J_i \rangle^* \langle J_f \| \mathcal{L}_J(q) \| J_i \rangle \right\}, \end{aligned} \quad (4)$$

and

$$\begin{aligned} \sigma_{\text{T}}^J &= (1 - \cos \theta + b \sin^2 \theta) \\ &\cdot \left[\left| \langle J_f \| \mathcal{T}_J^{\text{mag}}(q) \| J_i \rangle \right|^2 + \left| \langle J_f \| \mathcal{T}_J^{\text{el}}(q) \| J_i \rangle \right|^2 \right] \\ &\mp \frac{E_k + E_{k'}}{q} (1 - \cos \theta) \times 2 \\ &\cdot \text{Re} \left\{ \langle J_f \| \mathcal{T}_J^{\text{mag}}(q) \| J_i \rangle \langle J_f \| \mathcal{T}_J^{\text{el}} \| J_i \rangle^* \right\}, \end{aligned} \quad (5)$$

where the minus sign is taken for neutrino scattering and the plus sign for antineutrino scattering. J_i and J_f are the initial and final state angular momenta of the nucleus. We use the abbreviation

$$b = \frac{E_k E_{k'}}{q^2}, \quad (6)$$

and q is the magnitude of the three-momentum transfer. The formalism and various different operators involved are discussed in detail in [28, 29].

To compute the averaged cross section $\langle\sigma\rangle$, we need to fold the computed cross sections with the energy distribution of the incoming neutrinos. We take the supernova neutrino spectrum to be of a two-parameter Fermi-Dirac character

$$f_{\text{FD}}(E_k) = \frac{1}{F_2(\alpha_\nu) T_\nu} \frac{(E_k/T_\nu)^2}{1 + e^{E_k/(T_\nu - \alpha_\nu)}}, \quad (7)$$

where α_ν is the so-called pinching parameter and T_ν is the neutrino temperature. The normalization factor $F_2(\alpha_\nu)$ is defined by the formula

$$F_k(\alpha_\nu) = \int \frac{x^k dx}{1 + e^{x - \alpha_\nu}}, \quad (8)$$

and the temperature and mean energy of neutrinos are related by

$$\frac{\langle E_\nu \rangle}{T_\nu} = \frac{F_3(\alpha_\nu)}{F_2(\alpha_\nu)}. \quad (9)$$

We also examine solar neutrinos from ${}^8\text{B}$ beta decay. We use an ${}^8\text{B}$ neutrino energy spectrum from [30].

3. Nuclear Structure of the Target Nuclei

In this section we outline the nuclear-structure calculations performed for the investigated nuclei ${}^{128,129,130,131,132,134,136}\text{Xe}$. We have performed computations in the quasiparticle random-phase approximation (QRPA), microscopic quasiparticle-phonon model (MQPM), and the nuclear shell model.

3.1. QRPA/MQPM Calculations. The nuclear structure of even-even Xe isotopes was computed by using the charge-conserving QRPA framework. The QRPA is based on a BCS calculation [31], where quasiparticle creation and annihilation operators are defined via the Bogoliubov-Valatin transformation as

$$\begin{aligned} a_\alpha^\dagger &= u_\alpha c_\alpha^\dagger + v_\alpha \tilde{c}_\alpha, \\ \tilde{a}_\alpha &= u_\alpha \tilde{c}_\alpha - v_\alpha c_\alpha^\dagger, \end{aligned} \quad (10)$$

with the regular particle creation and annihilation operators c_α^\dagger and \tilde{c} defined in [32]. Here α contains the quantum numbers (a, m_α) with $a = (n_a, l_a, j_a)$. The excited states with respect to the QRPA vacuum are created with the phonon creation operator

$$Q_\omega^\dagger = \sum_{ab} \mathcal{N}_{ab}(J_\omega) \left(X_{ab}^\omega [a_a^\dagger a_b^\dagger]_{J_\omega M_\omega} + Y_{ab}^\omega [\tilde{a}_a \tilde{a}_b]_{J_\omega M_\omega} \right) \quad (11)$$

for an excited state $\omega = (J_\omega, M_\omega, \pi_\omega, k_\omega)$, where k_ω is a number labeling the excited states of given J^π . In the above equation

$$\mathcal{N}_{ab}(J_\omega) = \frac{\sqrt{1 + \delta_{ab} (-1)^{J_\omega}}}{1 + \delta_{ab}}, \quad (12)$$

and X_{ab}^ω and Y_{ab}^ω are amplitudes describing the wave function that are solved from the QRPA equation

$$\begin{bmatrix} A & B \\ -B^* & -A^* \end{bmatrix} \begin{bmatrix} X^\omega \\ Y^\omega \end{bmatrix} = E_\omega \begin{bmatrix} X^\omega \\ Y^\omega \end{bmatrix}, \quad (13)$$

where the matrix A is the basic Tamm-Dankoff matrix and B is the so-called correlation matrix, both defined in detail in [32].

We perform the QRPA calculations using large model spaces consisting of the entire $0s-0d$, $1p-0f-0g$, $2s-1d-0h$, and $1f-2p$ major shells, adding also the $0i_{13/2}$ and $0i_{11/2}$ orbitals. The single-particle bases are constructed by solving the Schrödinger equation for a Coulomb-corrected Woods-Saxon potential. We use the Woods-Saxon parameters given in [33]. We make an exception for ${}^{136}\text{Xe}$, adopting the set of adjusted values of single-particle energies from [25]. Due to the neutron-magic nature of ${}^{136}\text{Xe}$, adjusted single-particle energies are necessary to get agreement with experimental energy levels. The Bonn one-boson exchange potential [34] was used to estimate the residual two-body interaction.

The QRPA formalism involves several parameters that have to be fixed by fitting observables to experimental data. In the BCS calculation we fit the proton and neutron pairing strengths G_{pair}^p and G_{pair}^n so that the lowest quasiparticle energy matches the empirical pairing gap given by the three-point formula [35]:

$$\begin{aligned} \Delta_p(A, Z) &= \frac{1}{4} (-1)^{Z+1} \left[S_p(A+1, Z+1) - 2S_p(A, Z) \right. \\ &\quad \left. + S_p(A-1, Z-1) \right], \\ \Delta_n(A, Z) &= \frac{1}{4} (-1)^{A-Z+1} \left[S_n(A+1, Z) - 2S_n(A, Z) \right. \\ &\quad \left. + S_n(A-1, Z) \right]. \end{aligned} \quad (14)$$

It should be noted that for the neutron-magic ${}^{136}\text{Xe}$ this procedure cannot be done for the neutron pairing strength. We have instead used a bare value of $G_{\text{pair}} = 1.0$ for ${}^{136}\text{Xe}$.

The particle-particle and particle-hole terms of the two-body matrix elements are scaled by strength parameters G_{pp} and G_{ph} , respectively. The energies of the computed QRPA states are quite sensitive to these model parameters. We fit the lowest excited states of each J^π separately to experimental values from [36] by altering the values of G_{pp} and G_{ph} . The values used for the model parameters are given in Table 1.

The QRPA process is known to produce states that are spurious, namely, the first excited 0^+ state and the first 1^- state. The first 0^+ state has been deemed spurious in [26, 37]. The first 1^- state is spurious due to center-of-mass motion as described in [32]. We have fitted the energies of these states to zero, if possible, by using the model parameters G_{pp} and G_{ph} , and subsequently the states have been omitted from calculations for the even-mass isotopes and also from the MQPM calculations for the odd-mass isotopes. The contributions of these spurious states to the total neutrino-nucleus scattering cross section would be tiny in any case.

TABLE 1: Model parameters used in the BCS and QRPA calculations. For each nucleus (column 1) the values of G_{pp} and G_{ph} (column 2) are given for the important J^π phonons in columns 3 to 9.

Nucleus	G	0^+	1^-	2^+	3^-	4^+	5^-	6^+
^{128}Xe	pp	0.796	1.000	1.000	1.000	1.000	1.000	1.000
	ph	0.298	0.500	0.527	0.500	0.652	0.883	0.934
^{130}Xe	pp	0.730	1.000	1.000	1.000	1.000	1.000	1.000
	ph	0.303	0.500	0.531	0.500	0.581	0.833	0.788
^{132}Xe	pp	0.653	1.000	1.000	1.000	1.000	1.000	1.000
	ph	0.319	0.500	0.533	0.500	0.436	0.933	1.000
^{134}Xe	pp	0.500	1.000	1.000	1.000	1.000	1.000	1.000
	ph	0.370	0.500	0.511	0.500	0.596	1.000	0.891
^{136}Xe	pp	0.843	1.000	1.000	1.000	1.000	1.000	1.000
	ph	0.100	0.500	0.583	0.500	0.700	0.747	0.891

TABLE 2: The valence-space truncations made in the shell-model calculations. The first column labels the Xe isotope; the following five columns give the minimum/maximum number of neutrons on the single-particle orbitals $0g_{7/2}$, $1d_{5/2}$, $1d_{3/2}$, $2s_{1/2}$, and $1h_{11/2}$, respectively.

Nucleus	$0g_{7/2}$	$1d_{5/2}$	$1d_{3/2}$	$2s_{1/2}$	$1h_{11/2}$
^{128}Xe	8/8	6/6	0/4	0/2	4/12
^{129}Xe	8/8	6/6	0/4	0/2	4/12
^{130}Xe	8/8	4/6	0/4	0/2	0/12
^{131}Xe	8/8	6/6	0/4	0/2	0/12
^{132}Xe	0/8	0/8	0/4	0/2	0/12
^{134}Xe	0/8	0/8	0/4	0/2	0/12
^{136}Xe	0/8	0/8	0/4	0/2	0/12

Odd-mass xenon isotopes $^{129,131}\text{Xe}$ are then computed by using the MQPM formalism, in which we use a combination of one- and three-quasiparticle states by coupling a quasiparticle with a QRPA phonon to form the three-quasiparticle configurations. The MQPM basic excitation can be written in terms of quasiparticle and QRPA-phonon creation operators as [38]

$$\Gamma_k^\dagger(jm) = \sum_n C_n^k a_{njm}^\dagger + \sum_{a,\omega} D_{a\omega}^k [a_a^\dagger Q_\omega^\dagger]_{jm}. \quad (15)$$

The amplitudes C and D are computed by solving the MQPM equations of motion. The detailed description of the process can be found in [38]. No additional model parameters are required for the MQPM calculation aside for the parameters fitted for the BCS/QRPA calculation described above. We do the MQPM calculations of ^{129}Xe and ^{131}Xe using ^{130}Xe and ^{132}Xe as reference nuclei, respectively. We select all QRPA phonons of $J \leq 6$ with an energy less than 10 MeV to be used in the calculation.

3.2. Shell-Model Calculations. We perform shell-model calculations for Xe isotopes using the shell-model code NuShellX@MSU [39]. We use the $0g_{7/2}$, $1d_{5/2}$, $1d_{3/2}$, $2s_{1/2}$, and $0h_{11/2}$ valence space and the SN100PN interaction [40]. The single-particle energies associated with the aforementioned orbitals in the SN100PN interaction are 0.8072, 1.5623, 3.3160, 3.2238, and 3.6051 MeV, respectively, for protons, and -10.6089 , -10.2893 , -8.7167 , -8.6944 , and -8.8152 MeV for neutrons.

The matrix dimension in the shell-model calculation increases rapidly when moving away from the $N = 82$ shell closure of ^{136}Xe . For $^{132,134,136}\text{Xe}$ we were able to do a full calculation with no truncations, but for $^{128-131}\text{Xe}$ we had to put restrictions on the neutron valence space. The truncations made for each isotope are shown in detail in Table 2. For the isotopes $^{128-131}\text{Xe}$ we assume a completely filled $0g_{7/2}$ orbital and for $^{128,129,131}\text{Xe}$ we also assume the $1d_{5/2}$ orbital to be full. These should be reasonable approximations when aiming to describe the ground state and low-lying excited states in the xenon nuclei. The orbitals $0g_{7/2}$ and $1d_{5/2}$ have the lowest single-particle energies and the excitations are likely to take place from higher orbitals when the neutron number of the nuclei is quite large.

The computed energy levels of the even-mass xenon isotopes are given in Figure 2 and the odd-mass isotopes in Figure 3. For the even-mass isotopes the experimental energy spectra are very well reproduced by the shell-model calculations. The accuracy is somewhat diminished when moving to lower masses from the closed neutron major shell of ^{136}Xe , but a decent correspondence between experimental and theoretical levels can be found. For the odd-mass isotopes the situation is more complex, but the positive-parity states are well reproduced by the calculations. However, the negative-parity states $11/2^-$ and $9/2^-$ are computed to be much lower than in the experimental spectrum. This effect has been observed in earlier calculations using the SN100PN interaction in this mass region [41]. The experimental data for the xenon isotopes was obtained from [36].

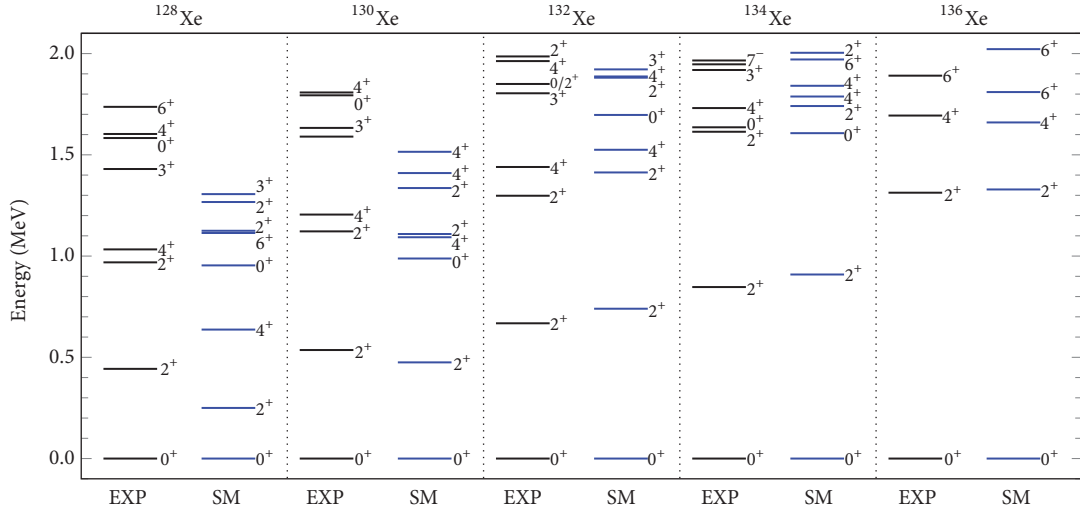


FIGURE 2: Experimental and shell-model energy spectra of even-mass xenon isotopes. A maximum of eight lowest energy levels are shown for each isotope. From left to right: ^{128}Xe , ^{130}Xe , ^{132}Xe , ^{134}Xe , and ^{136}Xe .

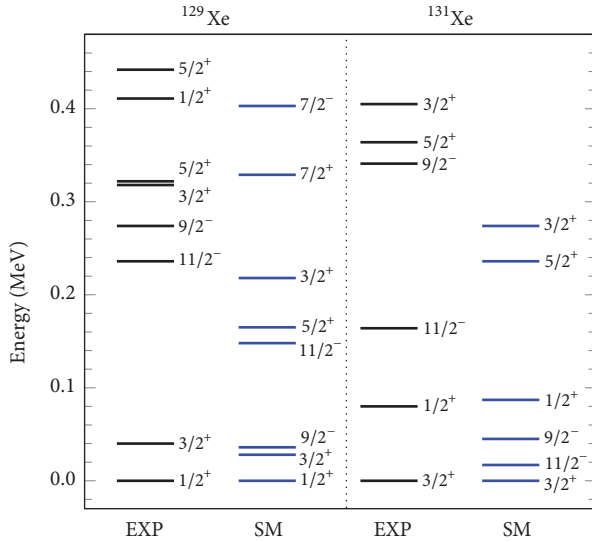


FIGURE 3: Experimental and shell-model energy spectra of odd-mass xenon isotopes ^{129}Xe (left) and ^{131}Xe (right).

To give a further measure of accuracy of our calculation, we computed the ground state magnetic moments for ^{129}Xe and ^{131}Xe . For ^{129}Xe the experimental magnetic moment of the $1/2^+$ ground state is $\mu_{\text{exp}} = -0.7779763(84)\mu_N$ while the shell-model calculated value is $\mu_{\text{sm}} = -1.360\mu_N$. For ^{131}Xe $3/2^+$ ground state the numbers are $\mu_{\text{exp}} = +0.691862(4)\mu_N$ and $\mu_{\text{sm}} = +1.059\mu_N$ for experiment and shell model, respectively. The sign of the magnetic moment in both cases is correct, but the magnitude of both of our calculated values is somewhat larger than that of the experimental ones.

4. Neutrino Scattering Results

In this section we present the results of our calculations for neutrino-nucleus scattering cross sections by methods

described in Section 2. We have computed total cross sections for coherent and inelastic neutrino-nucleus scattering as a function of the neutrino energy and also averaged total cross sections for solar ^8B neutrinos and supernova neutrinos scattering off the most abundant xenon isotopes. In the following calculations of averaged supernova neutrino cross sections we have used two different neutrino temperatures corresponding to different neutrino flavors. We follow the choices of [26, 37] and have the electron neutrinos described by parameters $\alpha = 3.0$, $\langle E_\nu \rangle = 11.5$ MeV, and $T_\nu = 2.88$ MeV, and the muon and tau neutrinos by $\alpha = 3.0$, $\langle E_\nu \rangle = 16.3$ MeV, and $T_\nu = 4.08$ MeV. Whenever we refer to supernova neutrinos in the following text these parameter values are used in the calculations.

4.1. Coherent Elastic Scattering. In Table 3 we present the total cross section for coherent neutrino-nucleus scattering off the target xenon isotopes as a function of neutrino energy. In Table 3 we only show calculations in the nuclear shell model, but the values for the QRPA/MQPM formalism are very similar, which is reflected on the total averaged cross sections shown later. The cross sections rise rapidly for small neutrino energies and start to saturate when approaching 100 MeV. The cross sections are larger for the higher- A isotopes, following the N^2 coherent enhancement.

We present the total averaged cross section for supernova neutrinos as well as solar ^8B neutrinos in Table 4. Results for coherent scattering are shown for the shell model and QRPA/MQPM calculations. The results between the shell model and quasiparticle approaches are very similar. Some small differences can be observed in the results for the odd-mass isotopes, but those are still not very significant. The cross sections for the supernova neutrinos are larger than for ^8B neutrinos by roughly a factor of 3 or 5 depending on the neutrino flavor. This is due to the average energy of the supernova neutrinos being larger at 11.5 MeV or 16.3 MeV, while the ^8B spectrum peaks at around 7 MeV.

TABLE 3: Coherent elastic neutral-current scattering cross section for neutrinos scattering off xenon targets as a function of neutrino energy. The cross sections for each isotope are given in units of cm^2 in columns 2-8 as a function of the neutrino energy (column 1). The computations were made in the nuclear shell model.

E_ν (MeV)	σ (cm^2)						
	^{128}Xe	^{129}Xe	^{130}Xe	^{131}Xe	^{132}Xe	^{134}Xe	^{136}Xe
5	5.16×10^{-40}	5.31×10^{-40}	5.46×10^{-40}	5.61×10^{-40}	5.76×10^{-40}	6.08×10^{-40}	6.40×10^{-40}
10	2.02×10^{-39}	2.08×10^{-39}	2.14×10^{-39}	2.20×10^{-39}	2.26×10^{-39}	2.38×10^{-39}	2.50×10^{-39}
20	7.44×10^{-39}	7.65×10^{-39}	7.86×10^{-39}	8.07×10^{-39}	8.29×10^{-39}	8.73×10^{-39}	9.19×10^{-39}
30	1.47×10^{-38}	1.51×10^{-38}	1.55×10^{-38}	1.59×10^{-38}	1.63×10^{-38}	1.71×10^{-38}	1.80×10^{-38}
40	2.19×10^{-38}	2.25×10^{-38}	2.31×10^{-38}	2.37×10^{-38}	2.43×10^{-38}	2.55×10^{-38}	2.67×10^{-38}
50	2.80×10^{-38}	2.88×10^{-38}	2.94×10^{-38}	3.02×10^{-38}	3.09×10^{-38}	3.24×10^{-38}	3.39×10^{-38}
60	3.25×10^{-38}	3.33×10^{-38}	3.40×10^{-38}	3.49×10^{-38}	3.57×10^{-38}	3.73×10^{-38}	3.91×10^{-38}
70	3.55×10^{-38}	3.64×10^{-38}	3.72×10^{-38}	3.81×10^{-38}	3.89×10^{-38}	4.07×10^{-38}	4.25×10^{-38}
80	3.75×10^{-38}	3.84×10^{-38}	3.92×10^{-38}	4.02×10^{-38}	4.10×10^{-38}	4.28×10^{-38}	4.48×10^{-38}

TABLE 4: Total averaged cross section for ^8B solar neutrinos and electron and muon/tau supernova neutrinos ($\text{SN}\nu_e/\text{SN}\nu_x$) scattering off xenon targets. The results are shown for calculations in the nuclear shell model (SM) and the QRPA/MQPM formalisms. Cross sections for coherent scattering are given in units of 10^{-39} cm^2 and for inelastic scattering in 10^{-43} cm^2 .

Nucleus	Model	$\langle \sigma \rangle_{\text{coh}, ^8\text{B}}$	$\langle \sigma \rangle_{\text{coh}, \text{SN}\nu_e}$	$\langle \sigma \rangle_{\text{coh}, \text{SN}\nu_x}$	$\langle \sigma \rangle_{\text{inel}, ^8\text{B}}$	$\langle \sigma \rangle_{\text{inel}, \text{SN}\nu_e}$	$\langle \sigma \rangle_{\text{inel}, \text{SN}\nu_x}$
		(10^{-39} cm^2)	(10^{-39} cm^2)	(10^{-39} cm^2)	(10^{-43} cm^2)	(10^{-43} cm^2)	(10^{-43} cm^2)
^{128}Xe	SM	1.064	3.051	5.692	-	-	-
	QRPA	1.065	3.052	5.696	1.567	38.10	152.0
^{129}Xe	SM	1.095	3.138	5.853	-	-	-
	MQPM	1.105	3.166	5.903	2.208	45.11	173.4
^{130}Xe	SM	1.125	3.223	6.008	-	-	-
	QRPA	1.126	3.225	6.013	1.564	40.94	161.0
^{131}Xe	SM	1.157	3.313	6.173	-	-	-
	MQPM	1.167	3.336	6.215	3.699	54.14	195.4
^{132}Xe	SM	1.188	3.401	6.335	-	-	-
	QRPA	1.189	3.403	6.339	2.341	48.21	180.4
^{134}Xe	SM	1.253	3.585	6.671	-	-	-
	QRPA	1.253	3.585	6.673	3.107	56.10	201.7
^{136}Xe	SM	1.320	3.773	7.016	-	-	-
	QRPA	1.320	3.773	7.016	2.102	53.43	200.5

4.2. *Inelastic Scattering.* Due to the limitations of the shell model in describing high-lying excited states, we compute inelastic scattering properties using only the QRPA/MQPM formalism, which is known to depict well the collective properties of excited nuclear states. The total cross section as a function of neutrino energy is given in Table 5 for each xenon isotope. For smaller neutrino energies, 0 to 30 MeV, the cross sections are slightly larger for the odd-mass isotopes than for their neighboring isotopes. The energies of solar neutrinos fit completely into this range, which leads to the averaged cross sections for solar neutrinos to be larger for the odd-mass isotopes.

The total averaged inelastic cross sections are listed in Table 4. The inelastic scattering cross sections are some orders of magnitude smaller than the coherent cross sections, as expected. Here the cross sections of the supernova neutrinos are an order of magnitude or two larger than of ^8B solar neutrinos, again due to the supernova neutrinos having on average a higher energy. The effect of neutrino energy

appears more pronounced in inelastic scattering than in coherent scattering, however. The cross sections of the odd-mass isotopes are again slightly larger than those of the neighboring isotopes.

We can compare our inelastic scattering results with those calculated in [26] for Cd isotopes using the same supernova neutrino parameters. The results for Cd isotopes in [26] in the case of electron neutrino range from $4.38 \times 10^{-42} \text{ cm}^2$ for ^{106}Cd to $4.96 \times 10^{-42} \text{ cm}^2$ for ^{111}Cd , with a general decreasing trend with increasing mass number for even-mass nuclei. Our results for Xe isotopes in Table 4 are very similar in magnitude, but the trend is rather rising than decreasing with increasing mass number. This could be a shell effect, as adding neutrons to Cd isotopes takes the nucleus further away from a closed major shell, but for the xenon nuclei it gets closer to a shell closure. Same conclusions can be made for the other neutrino flavors.

We show the contributions from different multipole channels to the total averaged cross sections in Figure 4

TABLE 5: Inelastic neutral-current scattering cross section for neutrinos scattering off xenon targets as a function of neutrino energy. The cross sections are given in units of cm^2 . The computations were made in the QRPA/MQPM formalism.

E_ν (MeV)	σ (cm^2)						
	^{128}Xe	^{129}Xe	^{130}Xe	^{131}Xe	^{132}Xe	^{134}Xe	^{136}Xe
5	1.71×10^{-45}	2.10×10^{-45}	1.29×10^{-46}	2.74×10^{-44}	7.74×10^{-45}	1.28×10^{-44}	2.00×10^{-47}
10	3.56×10^{-43}	5.27×10^{-43}	3.54×10^{-43}	8.49×10^{-43}	5.49×10^{-43}	7.57×10^{-43}	4.75×10^{-43}
20	1.41×10^{-41}	1.71×10^{-41}	1.53×10^{-41}	2.00×10^{-41}	1.78×10^{-41}	2.06×10^{-41}	2.02×10^{-41}
30	6.50×10^{-41}	7.45×10^{-41}	6.85×10^{-41}	8.18×10^{-41}	7.53×10^{-41}	8.29×10^{-41}	8.41×10^{-41}
40	1.85×10^{-40}	1.94×10^{-40}	1.91×10^{-40}	2.05×10^{-40}	2.02×10^{-40}	2.16×10^{-40}	2.20×10^{-40}
50	3.99×10^{-40}	3.85×10^{-40}	4.05×10^{-40}	3.95×10^{-40}	4.20×10^{-40}	4.38×10^{-40}	4.47×10^{-40}
60	7.17×10^{-40}	6.41×10^{-40}	7.20×10^{-40}	6.45×10^{-40}	7.35×10^{-40}	7.55×10^{-40}	7.66×10^{-40}
70	1.14×10^{-39}	9.51×10^{-40}	1.14×10^{-39}	9.44×10^{-40}	1.15×10^{-39}	1.16×10^{-39}	1.18×10^{-39}
80	1.66×10^{-39}	1.30×10^{-39}	1.64×10^{-39}	1.28×10^{-39}	1.65×10^{-39}	1.66×10^{-39}	1.67×10^{-39}

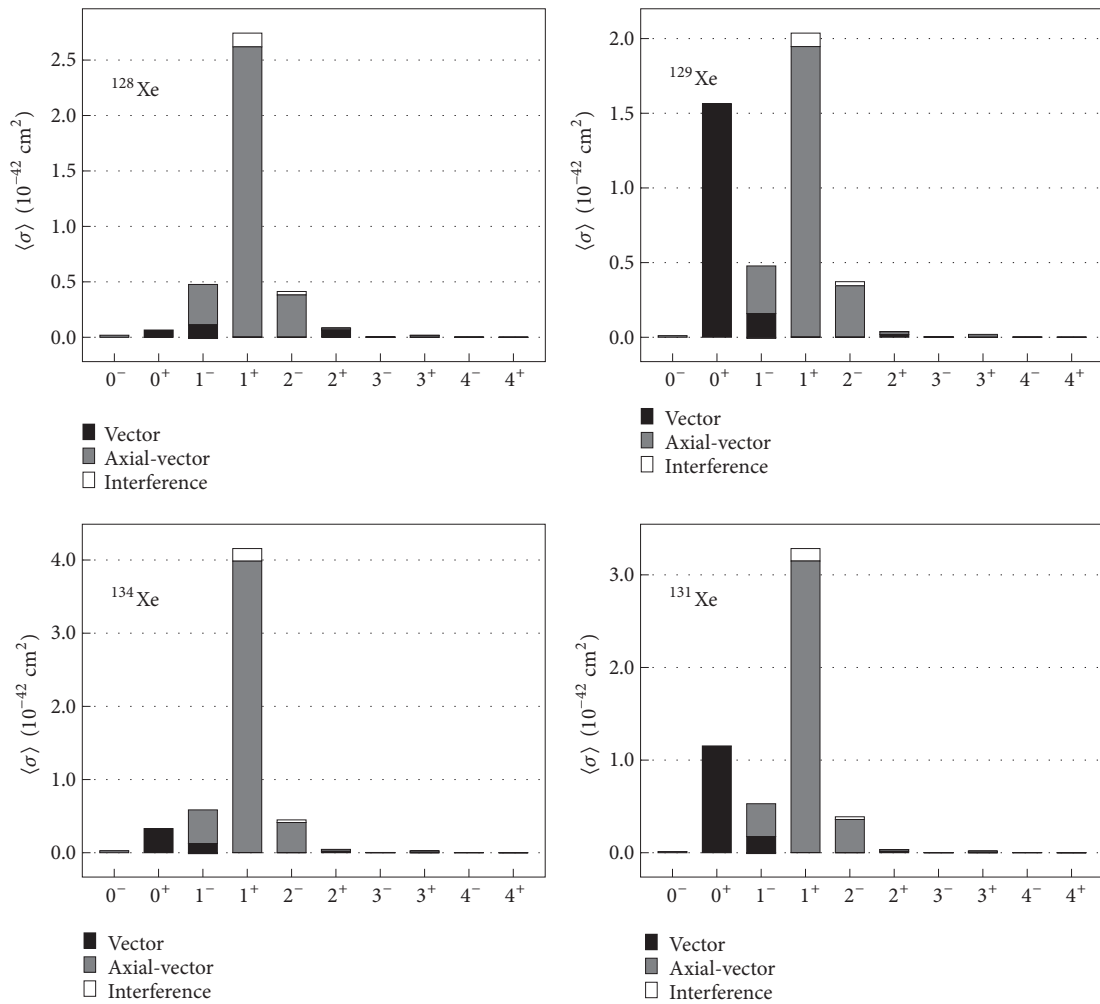


FIGURE 4: The contributions of multipole channels $J \leq 4$ to the total averaged cross section for inelastic scattering of supernova electron neutrinos. Bar plots are shown for a representative sample of ^{128}Xe (top left), ^{129}Xe (top right), ^{134}Xe (bottom left), and ^{131}Xe (bottom right). A division to vector, axial-vector, and interference parts of the interaction is shown. Cross sections are given in units of 10^{-42} cm^2 .

for supernova electron neutrinos and Figure 5 for solar neutrinos. It is evident that the most dominant contribution comes from an axial-vector 1^+ multipole transition in all cases but one. Smaller, yet still important contributions arise from the axial-vector 1^- and 2^- channels for higher

neutrino energies. This is characteristic behavior for neutral-current scattering, which has been observed in [26] for Cd isotopes and in [27] for Mo isotopes. The contributions get more evenly distributed among the different multipoles with increasing neutrino energy.

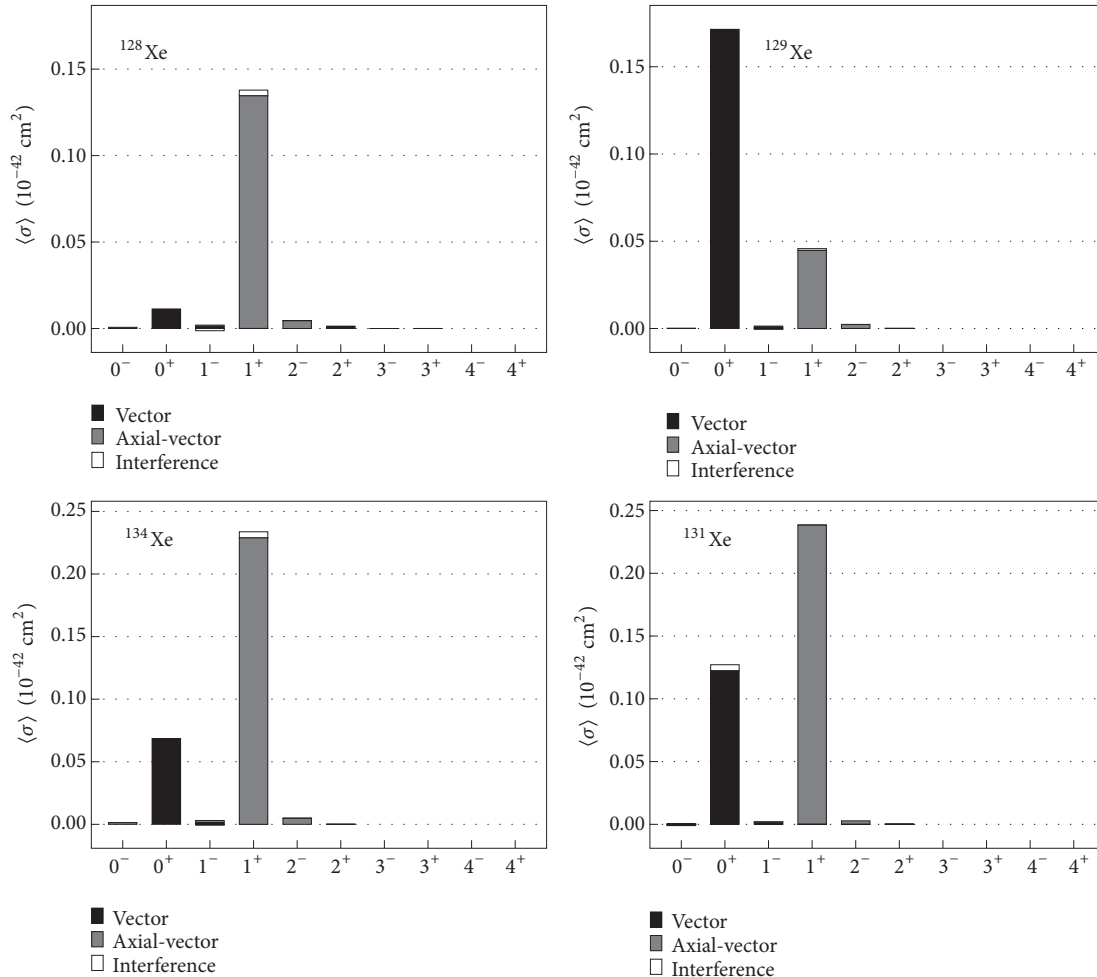


FIGURE 5: The contributions of multipole channels $J \leq 4$ to the total averaged cross section for inelastic scattering of solar ^8B neutrinos. Bar plots are shown for a representative sample of ^{128}Xe (top left), ^{129}Xe (top right), ^{134}Xe (bottom left), and ^{131}Xe (bottom right). A division to vector, axial-vector, and interference parts of the interaction is shown. Cross sections are given in units of 10^{-42} cm^2 .

For the odd-mass nuclei our calculations also show a significant contribution from a vector 0^+ channel, and for solar neutrinos scattering off ^{129}Xe this channel in fact becomes the strongest. For the even-mass isotopes this channel is more suppressed, but it becomes more significant for the lower energy solar neutrinos. Similar large 0^+ contributions were observed in [26] for Cd isotopes. This is problematic as, in principle, the 0^+ contribution is expected to be small because it vanishes at the limit $q \rightarrow 0$. The particle-number violation of the quasiparticle framework can be an explanation for the large computed 0^+ contribution. A detailed examination on the origins of the 0^+ anomaly will be conducted in a later study. At this time one should regard the 0^+ contributions with caution as they are probably at least partially spurious.

In Figures 6 and 7 we show the dominating contributions to the inelastic scattering cross section from various final states of ^{128}Xe and ^{131}Xe , respectively. We notice that the major contributions are very similar for the solar and supernova electron neutrinos for the even-mass ^{128}Xe , where the leading contributions come from 1^+ states at 8.4 MeV, 5.0 MeV, and 6.7 MeV. For solar neutrinos there is also a

notable contribution from a 0^+ state at 2.4 MeV. The situation is very much different for the odd-mass ^{131}Xe , where for supernova neutrinos there is a pile-up of $5/2^+$, $3/2^+$, and $1/2^+$ states at roughly 8 MeV giving large contributions to the total cross section in addition to the large contributions from lower-lying $5/2^+$ and $3/2^+$ states. However, for solar ^8B neutrinos this peak at 8 MeV is much smaller, and the leading contributions are more localized to the $5/2^+$ state at 1.8 MeV and the $3/2^+$ state at 2.9 MeV. It is interesting that a relatively small change in the average neutrino energy can lead to the higher-lying states to give much larger contributions to the total cross section.

Following the discussion on the anomalously large 0^+ multipole contribution in ^{129}Xe we show the dominant final states for neutrinos scattering off ^{129}Xe in Figure 8. As expected from the large 0^+ multipole, the largest contributions here come from $1/2^+$ states at energies of roughly 2 – 3 MeV. Something in the nuclear-structure calculation seems to favor the 0^+ multipole transition to $1/2^+$ final states over the 1^+ multipole transition to $3/2^+$ states. Otherwise similar conclusions can be made for ^{129}Xe as for ^{131}Xe above about

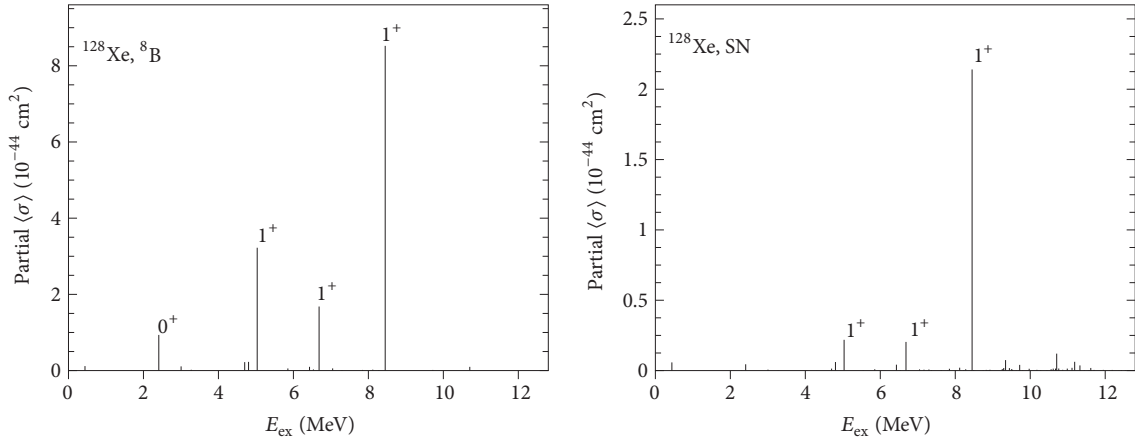


FIGURE 6: Contributions to the inelastic scattering averaged cross section arising from various final states of ^{128}Xe at energies E_{ex} . Results are shown for ^8B solar neutrinos (left panel) and supernova electron neutrinos (right panel). Cross sections are given in units of 10^{-44} cm 2 for solar neutrinos and 10^{-42} cm 2 for supernova neutrinos.

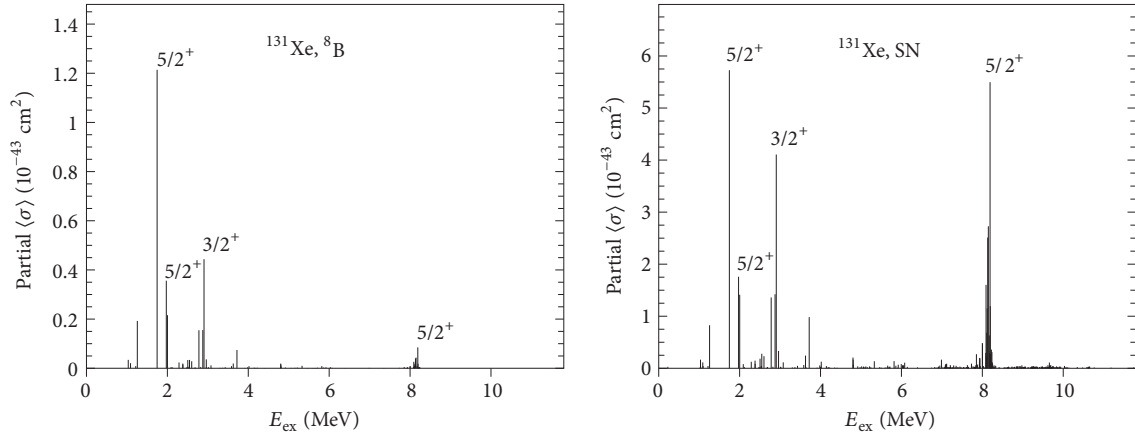


FIGURE 7: Contributions to the inelastic scattering averaged cross section arising from various final states of ^{131}Xe at energies E_{ex} . Results are shown for ^8B solar neutrinos (left panel) and supernova electron neutrinos (right panel). In both panels cross sections are given in units of 10^{-43} cm 2 .

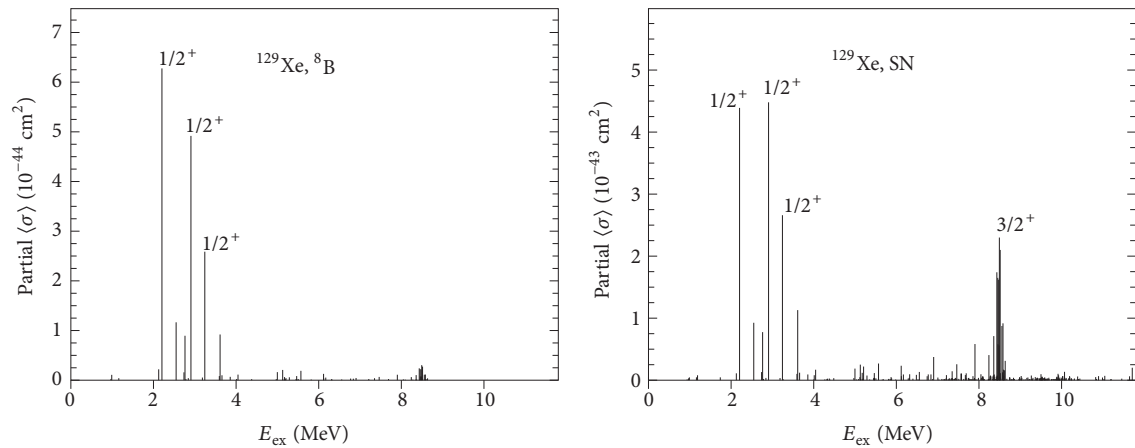


FIGURE 8: Contributions to the inelastic scattering averaged cross section arising from various final states of ^{129}Xe at energies E_{ex} . Results are shown for ^8B solar neutrinos (left panel) and supernova electron neutrinos (right panel). Cross sections are given in units of 10^{-44} cm 2 for solar neutrinos and 10^{-43} cm 2 for supernova neutrinos.

the location of the peaks in energy and differences between solar and supernova neutrinos.

5. Conclusions

We have computed various properties of cross sections of neutral-current neutrino-nucleus scattering off the most abundant Xe isotopes. The nuclear structure of our target Xe nuclei was computed in the nuclear shell model for elastic scattering and in the QRPA framework for both elastic and inelastic scattering. For the odd-mass nuclei ^{129}Xe and ^{131}Xe an MQPM calculation was performed based on the QRPA calculation for ^{130}Xe and ^{132}Xe , respectively. We used realistic neutrino energy distributions for solar neutrinos from ^8B beta decay and supernova neutrinos to compute the averaged cross sections for each neutrino scenario.

The total averaged cross sections for supernova neutrinos are dependent on the values of the parameters α_ν and $\langle E_{\nu_e} \rangle$. We have shown results of only one set of parameters for electron neutrinos and one for muon/tau neutrinos. The dependence of the cross sections on the parameter α_ν is typically quite mild, unless the change is large [25, 26]. The values $\alpha_\nu = 3.0$, $\langle E_{\nu_e} \rangle = 11.5$ MeV, and $\langle E_{\nu_\mu} \rangle = 16.3$ MeV used in this work are reasonable estimates and allow comparison of results with the ^8B solar neutrinos, for which the energy distribution is better known. A mapping of cross sections for various supernova neutrino parameters is out of scope of this work. However, we have tabulated total cross section as a function of neutrino energy, which can be used to obtain estimates of total averaged cross sections for any neutrino energy profile.

The scattering process in even-even nuclei is dominated by transitions to high-lying 1^+ states and for odd-mass nuclei typically by states differing from the initial state by one unit of angular momentum. We found that in even-mass nuclei the leading contributions from various final states are quite similar between solar neutrinos and supernova neutrinos. In odd-mass nuclei, however, the smaller energy of the solar neutrinos does not allow large contributions to the total cross section to arise from high-lying states. We also noted that the smaller energies of solar neutrinos lead into an enhancement in the vector 0^+ multipole channel in comparison to the otherwise dominating 1^+ axial-vector channel, especially in the odd-mass Xe nuclei. However, the large contribution from the 0^+ multipole can be mostly spurious, possibly due to the particle-number violation of the quasiparticle framework. This matter will be investigated further and subsequently reported elsewhere.

Data Availability

All relevant data used to support the findings of this study are included or cited within the article.

Conflicts of Interest

The authors declare that there are no conflicts of interest regarding the publication of this paper.

Acknowledgments

This work has been partially supported by the Academy of Finland under the Finnish Centre of Excellence Programme 2012-2017 (Nuclear and Accelerator Based Programme at JYFL). P. Pirinen was supported by a graduate student stipend from the Magnus Ehrnrooth Foundation. E. Ydrefors acknowledges the financial support of Grant no. 2016/25143-7 from the Sao Paulo Research Foundation (FAPESP).

References

- [1] C. L. Cowan Jr, F. Reines, F. B. Harrison, H. W. Kruse, and A. D. McGuire, "Detection of the Free Neutrino: a Confirmation," *Science*, vol. 124, p. 103, 1956.
- [2] D. Z. Freedman, "Coherent effects of a weak neutral current," *Physical Review D: Particles, Fields, Gravitation and Cosmology*, vol. 9, no. 5, pp. 1389–1392, 1974.
- [3] D. Akimov, J. B. Albert, P. Awe et al., "Observation of coherent elastic neutrino-nucleus scattering," *Science*, vol. 357, p. 1123, 2017.
- [4] A. J. Anderson, J. M. Conrad, E. Figueroa-Feliciano et al., "Measuring active-to-sterile neutrino oscillations with neutral current coherent neutrino-nucleus scattering," *Physical Review D: Particles, Fields, Gravitation and Cosmology*, vol. 86, no. 1, Article ID 013004, 2012.
- [5] B. Dutta, Y. Gao, A. Kubik et al., "Sensitivity to oscillation with a sterile fourth generation neutrino from ultralow threshold neutrino-nucleus coherent scattering," *Physical Review D*, vol. 94, Article ID 093002, 2016.
- [6] T. Kosmas, D. Papoulias, M. Tórtola, and J. Valle, "Probing light sterile neutrino signatures at reactor and Spallation Neutron Source neutrino experiments," *Physical Review D: Particles, Fields, Gravitation and Cosmology*, vol. 96, no. 6, Article ID 063013, 2017.
- [7] T. S. Kosmas, O. G. Miranda, D. K. Papoulias, M. Tórtola, and J. W. F. Valle, "Probing neutrino magnetic moments at Spallation Neutron Source facility," *Physical Review D*, vol. 92, no. 1, Article ID 013011, 2015.
- [8] J. Barranco, O. G. Miranda, and T. I. Rashba, "Sensitivity of low energy neutrino experiments to physics beyond the standard model," *Physical Review D: Particles, Fields, Gravitation and Cosmology*, vol. 76, Article ID 073008, 2007.
- [9] P. deNiverville, M. Pospelov, and A. Ritz, "Light new physics in coherent neutrino-nucleus scattering experiments," *Physical Review D*, vol. 92, Article ID 095005, 7 pages, 2015.
- [10] B. Dutta, R. Mahapatra, L. E. Strigari, and J. W. Walker, "Sensitivity to Z-prime and nonstandard neutrino interactions from ultralow threshold neutrino-nucleus coherent scattering," *Physical Review D*, vol. 93, Article ID 013015, 2016.
- [11] M. Lindner, W. Rodejohann, and X. Xu, "Coherent neutrino-nucleus scattering and new neutrino interactions," *Journal of High Energy Physics*, vol. 2017, no. 3, article no. 97, 2017.
- [12] T. M. Undagoitia and L. Rauch, "Dark matter direct-detection experiments," *Journal of Physics G: Nuclear and Particle Physics*, vol. 43, Article ID 013001, 78 pages, 2016.
- [13] J. Monroe and P. Fisher, "Neutrino Backgrounds to Dark Matter Searches," *Phys. Rev. D - Physical Review Journals - American Physical Society*, vol. 76, Article ID 033007, 6 pages, 2007.
- [14] J. Billard and E. Figueroa-Feliciano, "Implication of neutrino backgrounds on the reach of next generation dark matter direct

- detection experiments,” *Physical Review D*, vol. 89, Article ID 023524, 2014.
- [15] C. A. J. OHare, A. M. Green, J. Billard, E. Figueroa-Feliciano, and L. E. Strigari, “Readout strategies for directional dark matter detection beyond the neutrino background,” *Physical Review D*, vol. 92, Article ID 063518, 2015.
- [16] P. Grothaus and M. Fairbairn, “Aspects of WIMP Dark Matter Searches at Colliders and Other Probes,” *Physical Review D*, vol. 90, Article ID 055018, 2014.
- [17] J. H. Davis, “Dark matter vs. neutrinos: the effect of astrophysical uncertainties and timing information on the neutrino floor,” *Journal of Cosmology and Astroparticle Physics*, vol. 2015, no. 3, article no. 12, 2015.
- [18] J. B. Dent, B. Dutta, J. L. Newstead, and L. E. Strigari, “Effective field theory treatment of the neutrino background in direct dark matter detection experiments,” *Physical Review D*, vol. 93, Article ID 075018, 2016.
- [19] J. B. Dent, B. Dutta, J. L. Newstead, and L. E. Strigari, “Dark matter, light mediators, and the neutrino floor,” *Physical Review D: Particles, Fields, Gravitation and Cosmology*, vol. 95, Article ID 051701(R), 20 pages, 2017.
- [20] E. Aprile, “First Dark Matter Search Results from the XENON1T Experiment,” *Physical Review Letters*, vol. 119, Article ID 181301, 2017.
- [21] K. Abe, K. Hieda, K. Hiraide, S. Hirano et al., “XMASS detector,” *Nuclear Instruments and Methods in Physics Research*, vol. 716, no. 11, pp. 78–85, 2013.
- [22] V. A. Kudryavtsev and LZ Collaboration, “Expected background in the LZ experiment,” in *Proceedings of the AIP Conference*, vol. 1672, Article ID 060003, 2015.
- [23] D. S. Akerib and LUX Collaboration, “Results from a Search for Dark Matter in the Complete LUX Exposure,” *Physical Review Letters*, vol. 118, Article ID 021303, 2017.
- [24] J. Aalbers, F. Agostini, M. Alfonsi et al., “DARWIN: towards the ultimate dark matter detector,” *Journal of Cosmology and Astroparticle Physics*, vol. 2016, no. 11, article no. 017, 2016.
- [25] E. Ydrefors, J. Suhonen, and Y. M. Zhao, “Neutrino-nucleus scattering off ^{136}Xe ,” *Physical Review C*, vol. 91, Article ID 014307, 2015.
- [26] W. Almosly, E. Ydrefors, and J. Suhonen, “Neutrino scattering off the stable cadmium isotopes: neutral-current processes,” *Journal of Physics G: Nuclear and Particle Physics*, vol. 42, no. 2, Article ID 025106, 2014.
- [27] E. Ydrefors, K. G. Balasi, T. S. Kosmas, and J. Suhonen, “Detailed study of the neutral-current neutrino–nucleus scattering off the stable Mo isotopes,” *Nuclear Physics A*, vol. 896, pp. 1–23, 2012.
- [28] E. Ydrefors, K. G. Balasi, J. Suhonen, and T. S. Kosmas, “Nuclear responses to supernova neutrinos for the stable molybdenum isotopes,” in *Neutrinos: Properties, Sources and Detection, Physics Research and Technology*, pp. 151–175, Nova Science Publishers, 2011.
- [29] T. W. Donnelly and R. D. Peccei, “Neutral current effects in nuclei,” *Physics Reports*, vol. 50, pp. 1–85, 1979.
- [30] J. N. Bahcall, E. Lisi, D. E. Alburger, L. De Braekeleer, S. J. Freedman, and J. Napolitano, “Standard neutrino spectrum from B-8 Decay,” *Physical Review C: Nuclear Physics*, vol. 54, no. 1, pp. 411–422, 1996.
- [31] A. Bohr, B. R. Mottelson, and D. Pines, “Possible Analogy between the Excitation Spectra of Nuclei and Those of the Superconducting Metallic State,” *Physical Review*, vol. 110, no. 4, pp. 936–938, 1958.
- [32] J. Suhonen, *From Nucleons to Nucleus: Concepts of Microscopic Nuclear Theory*, Theoretical and Mathematical Physics, Springer, Berlin, Germany, 2007.
- [33] A. Bohr and B. R. Mottelson, “Nuclear Structure: Volume 1,” in *Nuclear Structure*, Benjamin, New York, NY, USA, 1969.
- [34] K. Holinde, “Two-nucleon forces and nuclear matter,” *Physics Reports*, vol. 68, no. 3, pp. 121–188, 1981.
- [35] A. H. Wapstra and G. Audi, “The 1983 atomic mass evaluation: (I). Atomic mass table,” *Nuclear Physics A*, vol. 432, pp. 1–54, 1985.
- [36] “National Nuclear Data Center: Evaluated Nuclear Structure Data File,” <http://www.nndc.bnl.gov/ensdf/>.
- [37] W. Almosly, E. Ydrefors, and J. Suhonen, “Neutral- and charged-current supernova-neutrino scattering off ^{116}Cd ,” *Journal of Physics G: Nuclear and Particle Physics*, vol. 40, no. 9, Article ID 095201, 2013.
- [38] J. Toivanen and J. Suhonen, “Microscopic quasiparticle-phonon description of odd-mass $^{127-133}\text{Xe}$ isotopes and their β decay,” *Physical Review C: Nuclear Physics*, vol. 57, no. 3, pp. 1237–1245, 1998.
- [39] B. A. Brown and W. D. M. Rae, “The Shell-Model Code NuShellX@MSU,” *Nuclear Data Sheets*, vol. 120, pp. 115–118, 2014.
- [40] B. A. Brown, N. J. Stone, J. R. Stone, I. S. Towner, and M. Hjorth-Jensen, “Magnetic moments of the 2_1^+ states around ^{132}Sn ,” *Physical Review C*, vol. 71, no. 4, Article ID 044317, 2005.
- [41] P. Pirinen, P. C. Srivastava, J. Suhonen, and M. Kortelainen, “Shell-model study on event rates of lightest supersymmetric particles scattering off ^{83}Kr and ^{125}Te ,” *Physical Review D*, vol. 93, Article ID 095012, 2016.

Research Article

Degeneracy Resolution Capabilities of NO ν A and DUNE in the Presence of Light Sterile Neutrino

Akshay Chatla ¹, Sahithi Rudrabhatla ² and Bindu A. Bambah¹

¹*School of Physics, University of Hyderabad, Hyderabad 500046, India*

²*Department of Physics, University of Illinois at Chicago, Chicago, IL 60607, USA*

Correspondence should be addressed to Akshay Chatla; chatlaakshay@gmail.com

Received 10 April 2018; Accepted 15 August 2018; Published 6 September 2018

Academic Editor: Hiroyasu Ejiri

Copyright © 2018 Akshay Chatla et al. This is an open access article distributed under the Creative Commons Attribution License, which permits unrestricted use, distribution, and reproduction in any medium, provided the original work is properly cited. The publication of this article was funded by SCOAP³.

We investigate the implications of a sterile neutrino on the physics potential of the proposed experiment DUNE and future runs of NO ν A using latest NO ν A results. Using combined analysis of the disappearance and appearance data, NO ν A reported preferred solutions at normal hierarchy (NH) with two degenerate best-fit points: one in the lower octant (LO) and $\delta_{13} = 1.48\pi$ and the other in higher octant (HO) and $\delta_{13} = 0.74\pi$. Another solution of inverted hierarchy (IH), which is 0.46σ away from best fit, was also reported. We discuss chances of resolving these degeneracies in the presence of sterile neutrino.

1. Introduction

Sterile neutrinos are hypothetical particles that do not interact via any of the fundamental interactions other than gravity. The term sterile is used to distinguish them from active neutrinos, which are charged under weak interaction. The theoretical motivation for sterile neutrino explains the active neutrino mass after spontaneous symmetry breaking, by adding a gauge singlet term (sterile neutrino) to the Lagrangian under $SU(3)_c \otimes SU(2)_L \otimes U(1)_f$, where the Dirac term appears through the Higgs mechanism, and Majorana mass term is a gauge singlet and hence appears as a bare mass term [1]. The diagonalization of the mass matrix gives masses to all neutrinos due to the See-Saw mechanism.

Some experimental anomalies also point towards the existence of sterile neutrinos. Liquid Scintillator Neutrino Detector (LSND) detected $\bar{\nu}_\mu \rightarrow \bar{\nu}_e$ transitions indicating $\Delta m^2 \approx 1eV^2$ which is inconsistent with $\Delta m_{32}^2, \Delta m_{21}^2$ (LSND anomaly) [2]. Measurement of the width of Z boson by LEP gave number of active neutrinos to be 2.984 ± 0.008 [3]. Thus the new neutrino introduced to explain the anomaly has to be a sterile neutrino. MiniBooNE, designed to verify the LSND anomaly, observed an unexplained excess of events in low-energy region of $\bar{\nu}_e, \nu_e$ spectra, consistent with LSND

[4]. SAGE and GALLEX observed lower event rate than expected, explained by the oscillations of ν_e due to $\Delta m^2 \geq 1eV^2$ (Gallium anomaly) [5–7]. Recent precise predictions of reactor antineutrino flux have increased the expected flux by 3% over old predictions. With the new flux evaluation, the ratio of observed and predicted flux deviates at 98.6% C.L (Confidence level) from unity; this is called “reactor antineutrino anomaly” [8]. This anomaly can also be explained using sterile neutrino model.

Short-baseline (SBL) experiments are running to search for sterile neutrinos. SBL experiments are the best place to look for sterile neutrino, as they are sensitive to new expected mass-squared splitting $\Delta m^2 \approx 1eV^2$. However, SBL experiments cannot study all the properties of sterile neutrinos, mainly new CP phases introduced by sterile neutrino models. These new CP phases need long distances to become measurable [9, 10] and thus can be measured using long baseline (LBL) experiments. With the discovery of relatively large value for θ_{13} by Daya Bay [11], the sensitivity of LBL experiments towards neutrino mass hierarchy and CP phases increased significantly. In this context, some phenomenological studies regarding the sensitivity of LBL experiments can be found in recent works [12–16]. Using recent global fits of oscillation parameters in the 3+1 scenario

[17], current LBL experiments can extract two out of three CP phases (one of them being standard δ_{13}) [10]. The phenomenological studies of LBL experiments in presence of sterile neutrino is studied by several groups [18–23]. Now, the sensitivity of LBL experiments towards their original goals decreases due to sterile neutrinos. It is seen in case of the CPV measurement; new CP phases will decrease the sensitivity towards standard CP phase (δ_{13}). This will reduce degeneracy resolution capacities of LBL experiments. In this paper, we study hierarchy- θ_{23} - δ_{13} degeneracies using contours in θ_{23} - δ_{13} plane and how they are affected by the introduction of sterile neutrinos. We attempt to find the extent to which these degeneracies can be resolved in future runs of NO ν A and DUNE.

The outline of the paper is as follows. In Section 2, we present the experimental specifications of NO ν A and DUNE used in our simulation. We introduce the effect of sterile neutrino on parameter degeneracies resolution in Section 3. Section 4 contains the discussion about the degeneracy resolving capacities of future runs of NO ν A and DUNE assuming latest NO ν A results—NH- (normal hierarchy-) LO (lower octant); NH-HO (higher octant); and IH- (inverted hierarchy-) HO—as true solutions for both 3 and 3+1 models. Finally, Section 5 contains concluding comments on our results.

2. Experiment Specifications

We used GLOBES (General Long Baseline Experiment Simulator) [24, 25] to simulate the data for different LBL experiments including NO ν A and DUNE. The neutrino oscillation probabilities for the 3+1 model are calculated using the new physics engine available from [26].

NO ν A [27, 28] is an LBL experiment which started its full operation from October 2014. NO ν A has two detectors: the near detector is located at Fermilab (300 ton, 1 km from NuMI beam target) while the far detector (14 Kt) is located at Northern Minnesota 14.6 mrad off the NuMI beam axis at 810 km from NuMI beam target, justifying “off-axis” in the name. This off-axis orientation gives us a narrow beam of flux, peak at 2 GeV [29]. For simulations, we used NO ν A setup from [30]. We used the full projected exposure of 3.6×10^{21} p.o.t (protons on target) expected after six years of runtime at 700 kW beam power. Assuming the same runtime for neutrino and antineutrino modes, we get 1.8×10^{21} p.o.t for each mode. Following [31] we considered 5% normalization error for the signal and 10% error for the background for appearance and disappearance channels.

DUNE (Deep Underground Neutrino Experiment) [32, 33] is the next generation LBL experiment. Long Base Neutrino Facility (LBNF) of Fermilab is the source for DUNE. Near detector of DUNE will be at Fermilab. Liquid Argon detector of 40 kt to be constructed at Sanford Underground Research Facility, situated 1300 km from the beam target, will act as the far detector. DUNE uses the same source as of NO ν A; we will observe beam flux peak at 2.5 GeV. We used DUNE setup give in [34] for our simulations. Since DUNE is still in its early stages, we used simplified systematic

treatment, i.e., 5% normalization error on signal and 10% error on the background for both appearance and disappearance spectra. We give experimental details described above in tabular form in Tables 1 and 2.

Oscillation parameters are estimated from the data by comparing observed and predicted ν_e and ν_μ interaction rates and energy spectra. GLOBES calculates event rates of neutrinos for energy bins taking systematic errors, detector resolutions, MSW effect due to earth’s crust, etc. into account. The event rates generated for true and test values are used to plot χ^2 contours. GLOBES uses its inbuilt algorithm to calculate χ^2 values numerically considering parameter correlations as well as systematic errors. In our calculations we used χ^2 as

$$\chi^2 = \sum_{i=1}^{\text{\#ofbins}} \sum_{E_n=E_1, E_2, \dots} \frac{(O_{E_n, i} - (1 + a_F + a_{E_n}) T_{E_n, i})^2}{O_{E_n, i}} + \frac{a_F^2}{\sigma_F^2} + \frac{a_{E_n}^2}{\sigma_{E_n}^2} \quad (1)$$

where $O_{E_n, i}, O_{E_2, i} \dots$ are the event rates for the i^{th} bin in the detectors of different experiments, calculated for true values of oscillation parameters; $T_{E_n, i}$ are the expected event rates for the i^{th} bin in the detectors of different experiments for the test parameter values; a_F, a_{E_n} are the uncertainties associated with the flux and detector mass; and σ_F, σ_{E_n} are the respective associated standard deviations. The calculated χ^2 function gives the confidence level in which tested oscillation parameter values can be ruled out with referenced data. It provides an excellent preliminary evaluation model to estimate the experiment performance.

3. Theory

In a 3+1 sterile neutrino model, the flavour and mass eigenstates are connected through a 4×4 mixing matrix. A convenient parametrization of the mixing matrix is [36]

$$U = R_{34} \widetilde{R}_{24} \widetilde{R}_{14} R_{23} \widetilde{R}_{13} R_{12}. \quad (2)$$

Here R_{ij} and \widetilde{R}_{ij} represent real and complex 4×4 rotation in the plane containing the 2×2 subblock in (i, j) subblock

$$R_{ij}^{2 \times 2} = \begin{pmatrix} c_{ij} & s_{ij} \\ -s_{ij} & c_{ij} \end{pmatrix} \quad \widetilde{R}_{ij}^{2 \times 2} = \begin{pmatrix} c_{ij} & \widetilde{s}_{ij} \\ -\widetilde{s}_{ij}^* & c_{ij} \end{pmatrix} \quad (3)$$

where, $c_{ij} = \cos \theta_{ij}$, $s_{ij} = \sin \theta_{ij}$, $\widetilde{s}_{ij} = s_{ij} e^{-i\delta_{ij}}$, and δ_{ij} are the CP phases.

There are three mass-squared difference terms in 3+1 model: Δm_{21}^2 (solar) $\approx 7.5 \times 10^{-5} \text{eV}^2$, Δm_{31}^2 (atmospheric) $\approx 2.4 \times 10^{-3} \text{eV}^2$, and Δm_{41}^2 (sterile) $\approx 1 \text{eV}^2$. The mass-squared difference term towards which the experiment is sensitive depends on L/E of the experiment. Since SBL experiments have a very small L/E, $\sin^2(\Delta m_{ij}^2 L/4E) \approx 0$ for Δm_{21}^2 and Δm_{31}^2 . Δm_{41}^2 term survives. Hence, SBL experiments

TABLE 1: Details of experiments.

Name of Exp	NO ν A	DUNE
Location	Minnesota	South Dakota
POT(yr^{-1})	6.0×10^{20}	1.1×10^{21}
Baseline(Far/Near)	812 km/1km	1300 km/500 m
Target mass(Far/Near)	14 kt/290 t	40 kt/8 t
Exposure(years)	6	10
Detector type	Tracking Calorimeters	LArTPCs

TABLE 2: Systematic errors associated with NO ν A and DUNE.

Name of Exp	Rule	Normalization error	
		signal(%)	background(%)
NO ν A	ν_e appearance	5	10
	ν_μ disappearance	2	10
	$\bar{\nu}_e$ appearance	5	10
	$\bar{\nu}_\mu$ disappearance	2	10
DUNE	ν_e appearance	5	10
	ν_μ disappearance	5	10
	$\bar{\nu}_e$ appearance	5	10
	$\bar{\nu}_\mu$ disappearance	5	10

depend only on sterile mixing angles and are insensitive to the CP phases. The oscillation probability, $P_{\mu e}$ for LBL experiments in 3+1 model, after averaging Δm_{41}^2 oscillations and neglecting MSW effects, [37] is expressed as sum of the four terms

$$P_{\mu e}^{4\nu} \simeq P_1 + P_2 (\delta_{13}) + P_3 (\delta_{14} - \delta_{24}) + P_4 (\delta_{13} - (\delta_{14} - \delta_{24})). \quad (4)$$

These terms can be approximately expressed as follows:

$$P_1 = \frac{1}{2} \sin^2 2\theta_{\mu e}^{4\nu} + \left[a^2 \sin^2 2\theta_{\mu e}^{3\nu} - \frac{1}{4} \sin^2 2\theta_{13} \sin^2 2\theta_{\mu e}^{4\nu} \right] \cdot \sin^2 \Delta_{31} + \left[a^2 b^2 - \frac{1}{4} \sin^2 2\theta_{12} \right] \cdot \left(\cos^4 \theta_{13} \sin^2 2\theta_{\mu e}^{4\nu} + a^2 \sin^2 2\theta_{\mu e}^{3\nu} \right) \sin^2 \Delta_{21}, \quad (5)$$

$$P_2 (\delta_{13}) = a^2 b \sin 2\theta_{\mu e}^{3\nu} \left(\cos 2\theta_{12} \cos \delta_{13} \sin^2 \Delta_{21} - \frac{1}{2} \cdot \sin \delta_{13} \sin 2\Delta_{21} \right), \quad (6)$$

$$P_3 (\delta_{14} - \delta_{24}) = ab \sin 2\theta_{\mu e}^{4\nu} \cos^2 \theta_{13} \left[\cos 2\theta_{12} \cdot \cos (\delta_{14} - \delta_{24}) \sin^2 \Delta_{21} - \frac{1}{2} \sin (\delta_{14} - \delta_{24}) \cdot \sin 2\Delta_{21} \right], \quad (7)$$

$$P_4 (\delta_{13} - (\delta_{14} - \delta_{24})) = a \sin 2\theta_{\mu e}^{3\nu} \sin 2\theta_{\mu e}^{4\nu} \left[\cos 2\theta_{13} \cdot \cos (\delta_{13} - (\delta_{14} - \delta_{24})) \sin^2 \Delta_{31} + \frac{1}{2} \cdot \sin (\delta_{13} - (\delta_{14} - \delta_{24})) \sin 2\Delta_{31} - \frac{1}{4} \sin^2 2\theta_{12} \cdot \cos^2 \theta_{13} \cos (\delta_{13} - (\delta_{14} - \delta_{24})) \sin^2 \Delta_{21} \right], \quad (8)$$

with the parameters defined as

$$\Delta_{ij} \equiv \frac{\Delta m_{ij}^2 L}{4E}, \text{ a function of baseline (L) and neutrino energy (E)}$$

$$a = \cos \theta_{14} \cos \theta_{24}, \quad (9)$$

$$b = \cos \theta_{13} \cos \theta_{23} \sin 2\theta_{12},$$

$$\sin 2\theta_{\mu e}^{3\nu} = \sin 2\theta_{13} \sin \theta_{23},$$

$$\sin 2\theta_{\mu e}^{4\nu} = \sin 2\theta_{14} \sin \theta_{24}.$$

The CP phases introduced due to sterile neutrinos persist in the $P_{\mu e}$ even after averaging out Δm_{41}^2 lead oscillations. Last two terms of (4) give the sterile CP phase dependence terms. $P_3 (\delta_{14} - \delta_{24})$ depends on the sterile CP phases δ_{14} and δ_{24} , while P_4 depends on a combination of δ_{13} and $\delta_{14} - \delta_{24}$. Thus, we expect LBL experiments to be sensitive to sterile phases. We note that the probability $P_{\mu e}$ is independent θ_{34} . One can see that θ_{34} will effect $P_{\mu e}$ if we consider earth mass effects. Since matter effects are relatively small for

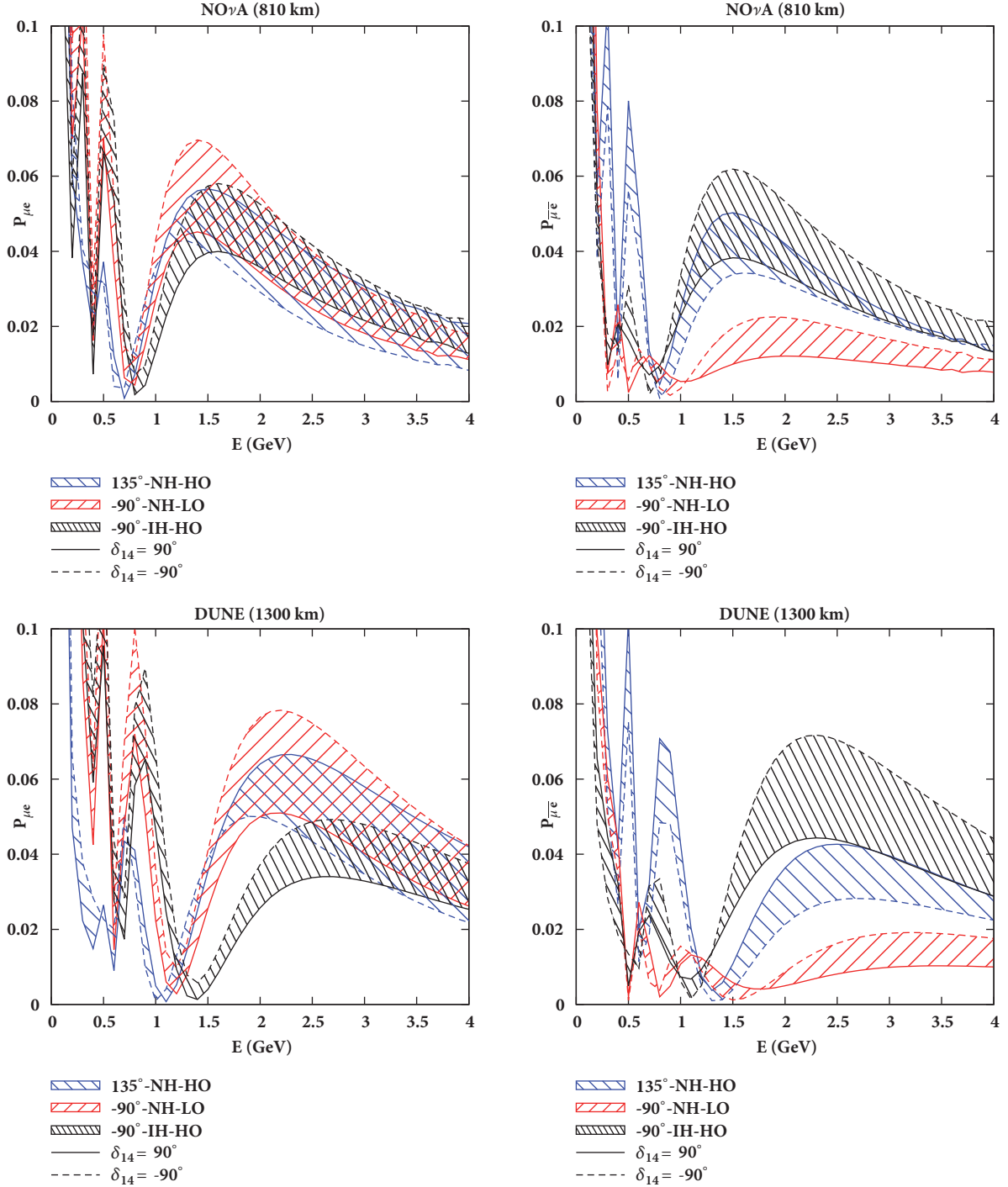


FIGURE 1: The oscillation probability $P_{\mu e}$ as a function of energy. The top (bottom) panel is NO ν A (DUNE). The bands correspond to different values of δ_{14} , ranging from -180° to 180° when $\delta_{24} = 0^\circ$. Inside each band, the probability for $\delta_{14} = 90^\circ$ ($\delta_{14} = -90^\circ$) case is shown as the solid (dashed) line. The left (right) panel corresponds to neutrinos (antineutrinos).

NO ν A and DUNE, their sensitivity towards θ_{34} is negligible. The amplitudes of atmospheric-sterile interference term (8) and solar-atmospheric interference term (6) are of the same order. This new interference term reduces the sensitivity of experiments to the standard CP phase (δ_{13}).

In Figure 1, we plot the oscillation probability ($P_{\mu e}$) as a function of energy while varying δ_{14} (-180° to 180°) and keeping $\delta_{24} = 0$ for the three best-fit values of latest NO ν A results [35], i.e., NH-LO- $1.48\pi[\delta_{13}]$, NH-HO- 0.74π , and IH-HO- 1.48π , where HO implies $\sin^2\theta_{23} = 0.62$ and LO implies

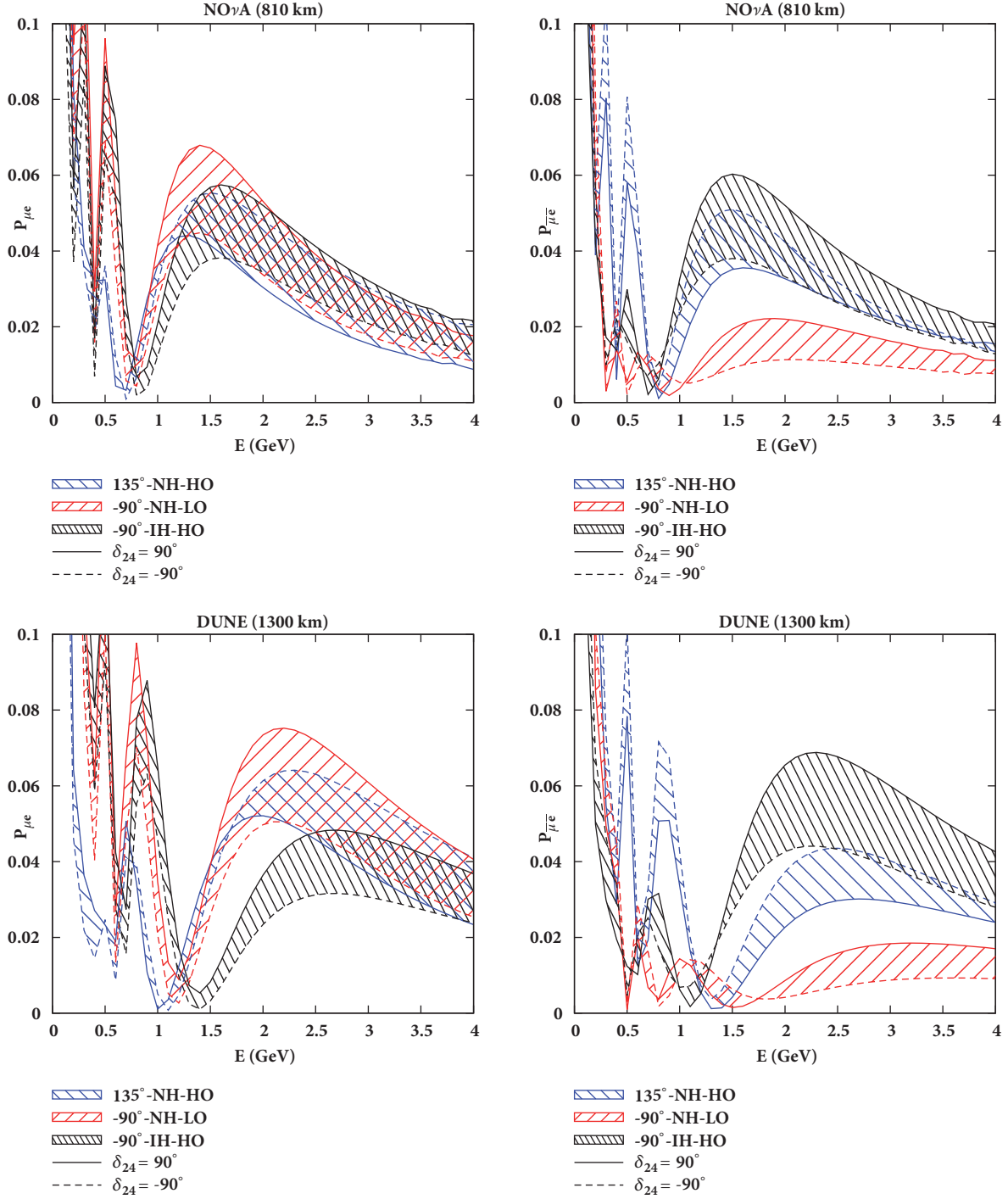


FIGURE 2: The oscillation probability $P_{\mu e}$ as a function of energy. The top (bottom) panel is NO ν A (DUNE). The bands correspond to different values of δ_{24} , ranging from -180° to 180° when $\delta_{14} = 0^\circ$. Inside each band, the probability for $\delta_{24} = 90^\circ$ ($\delta_{24} = -90^\circ$) case is shown as solid (dashed) line. The left (right) panel is for neutrinos (antineutrinos).

$\sin^2\theta_{23} = 0.40$. For the flux peak of NO ν A, $E \approx 2\text{GeV}$, we observe a degeneracy between all best-fit values due to the presence of δ_{14} band for neutrino case, while only NH-HO and IH-HO bands overlap in antineutrino case. We see that δ_{14} phase decreases both octant and hierarchy resolution capacity for neutrino case and only mass hierarchy resolution

capacity for antineutrino case. The second row plots $P_{\mu e}$ for DUNE at baseline 1300 km. We observe smaller overlap between bands compared to NO ν A. Thus, the decrease of degeneracy resolution capacity for DUNE is less than NO ν A. Similarly we plot $P_{\mu e}$ while varying δ_{24} (-180° to 180°) in Figure 2 and keeping $\delta_{14} = 0^\circ$. We see that δ_{24} has similar

TABLE 3: Oscillation parameters considered in numerical analysis. The $\sin^2\theta_{23}$ and δ_{13} are taken from latest NO ν A results [35].

Parameter	True value	Marginalization Range
$\sin^2\theta_{12}$	0.304	Not Marginalized
$\sin^2 2\theta_{13}$	0.085	[0.075,0.095]
$\sin^2\theta_{23}$	0.623(HO),0.404(LO)	[0.32,0.67]
$\sin^2\theta_{14}$	0.025	Not Marginalized
$\sin^2\theta_{24}$	0.025	Not Marginalized
$\sin^2\theta_{34}$	0.025	Not Marginalized
δ_{13}	135(NH-HO),-90(NH-LO,IH)	[-180,180]
δ_{14}	[-180,180]	[-180,180]
δ_{24}	[-180,180]	[-180,180]
Δm_{21}^2	$7.50 \times 10^{-5} \text{ eV}^2$	Not Marginalized
Δm_{31}^2 (NH)	$2.40 \times 10^{-3} \text{ eV}^2$	Not Marginalized
Δm_{31}^2 (IH)	$-2.33 \times 10^{-3} \text{ eV}^2$	Not Marginalized
Δm_{41}^2	1 eV^2	Not Marginalized

effect to that of δ_{14} ; the only change is reversal of δ_{24} band extrema; i.e., $\delta_{24} = -90^\circ$ gives the same result as $\delta_{14} = 90^\circ$ and vice versa. This can be explained using (4) in which we see δ_{14} and δ_{24} are always together with opposite signs. Overall from the probability plots, we observe that the addition of new CP phases decreases octant and mass hierarchy resolution capacities.

In the next section, we explore how parameter degeneracies are affected in the 3+1 model and the extent to which these degeneracies can be resolved in future runs of NO ν A and DUNE.

4. Results for NO ν A and DUNE

We explore allowed regions in $\sin^2\theta_{23}$ - δ_{cp} plane from NO ν A and DUNE simulation data with different runtimes, considering latest NO ν A results as true values. Using combined analysis of the disappearance and appearance data, NO ν A reported preferred solutions [35] at normal hierarchy (NH) with two degenerate best-fit points: one in the lower octant (LO) and $\delta_{cp} = 1.48\pi$ and the other in higher octant (HO) and $\delta_{cp} = 0.74\pi$. Another solution of inverted hierarchy (IH), 0.46σ away from best fit, is also reported. Table 3 shows true values of oscillation parameters and their marginalization ranges we used in our simulation. By studying the allowed regions, we understand the extent to which future runs of NO ν A and DUNE will resolve these degeneracies, if the best-fit values are true values.

In the first row of Figure 3, we show allowed areas for NO ν A[3+0]. In first plot of first row, we show 90% C.L allowed regions for true values of $\delta_{13} = 135^\circ$ and $\theta_{23} = 52^\circ$ and normal hierarchy. We plot test values for both NH and IH, of 3 and 3+1 neutrino models. We observe that introducing sterile neutrino largely decreases the precision of θ_{23} . The WO-RH region, for 3 ν case confined between 45° and -180° of δ_{13} , confines the whole δ_{13} region for 4 ν case. The WH-RO region of 3 ν case doubles, covering the entire region of δ_{13} for 4 ν case. The 3+1 model also introduces a small WH-WO region, which was absent in 3 ν model. In the second plot

of first row (true value $\delta_{13} = -90^\circ$, $\theta_{23} = 40^\circ$ and normal hierarchy), for the 3 ν case, we see RH-RO region excluding 45° to 150° of δ_{13} , while RH-WO region covers the whole of the δ_{13} region. In 3+1 model, both RH-RO and RH-WO regions cover the whole of the δ_{13} region. WH-RO solution occupies a small region for 3 ν case, covering half of δ_{13} region for 4 ν case. WH-WO region covers the whole of the δ_{13} region for 4 ν case. In the third plot of first row, true values are taken as $\delta_{13} = -90^\circ$, $\theta_{23} = 52^\circ$ and inverted hierarchy. The RH-RO region covers the entire range of δ_{13} for both 3 ν and 4 ν case, whereas RH-WO region almost doubles from 3 ν case to 4 ν case. A small range of δ_{13} excluded from WH-RO for 3 ν case is covered in 4 ν case. WH-WO region of 3 ν case excludes 60° to 150° of δ_{13} while full δ_{13} range is covered for 4 ν case.

In the second row of the figure, we plot allowed regions for NO ν A[3+1]. We take true values as best-fit points obtained by NO ν A. We observe an increase in precision of parameter measurement, due to an increase in statistics, from added 1 yr of antineutrino run. In the first plot of the second row, the RH-RO octant region covers entire δ_{13} range for both 3 ν and 4 ν case. RH-WO region includes -180° to 45° of δ_{13} for 3 ν case, while the whole range of δ_{13} is covered in 4 ν case. A slight increase in the area of WH-RO is observed from 3 ν to 4 ν case. 4 ν introduces WH-WO region which was resolved for 3 ν case. In the second plot, RH-RO region allows full range of δ_{13} for 4 ν case, while it was restricted to lower half of CP range in 3 ν case. We see that WH-RO solution, which was resolved in 3 ν case, is reintroduced in 4 ν case. We also see a slight increase in the size of WH-WO solution from 3 ν to 4 ν . In third plot, RH-RO region covers the whole CP range for 4 ν while 35° to 125° of δ_{13} are excluded in 3 ν case. The almost resolved RH-WO solution for 3 ν doubles for 4 ν case. WH-RO and WH-WO cover the entire region of δ_{13} for 4 ν case.

In the third row, we show allowed regions for NO ν A[3+3]. In the first plot, it can be seen that small area of RH-WO in case of 3 ν now covers the whole of δ_{13} region for 4 ν case. While the 3 ν case has WH-WO δ_{13} degeneracy, 4 ν case introduces equal sized WH-WO-WO δ_{13} degeneracy. In second plot, for 3 ν case most of δ_{13} values above 0° are excluded, but

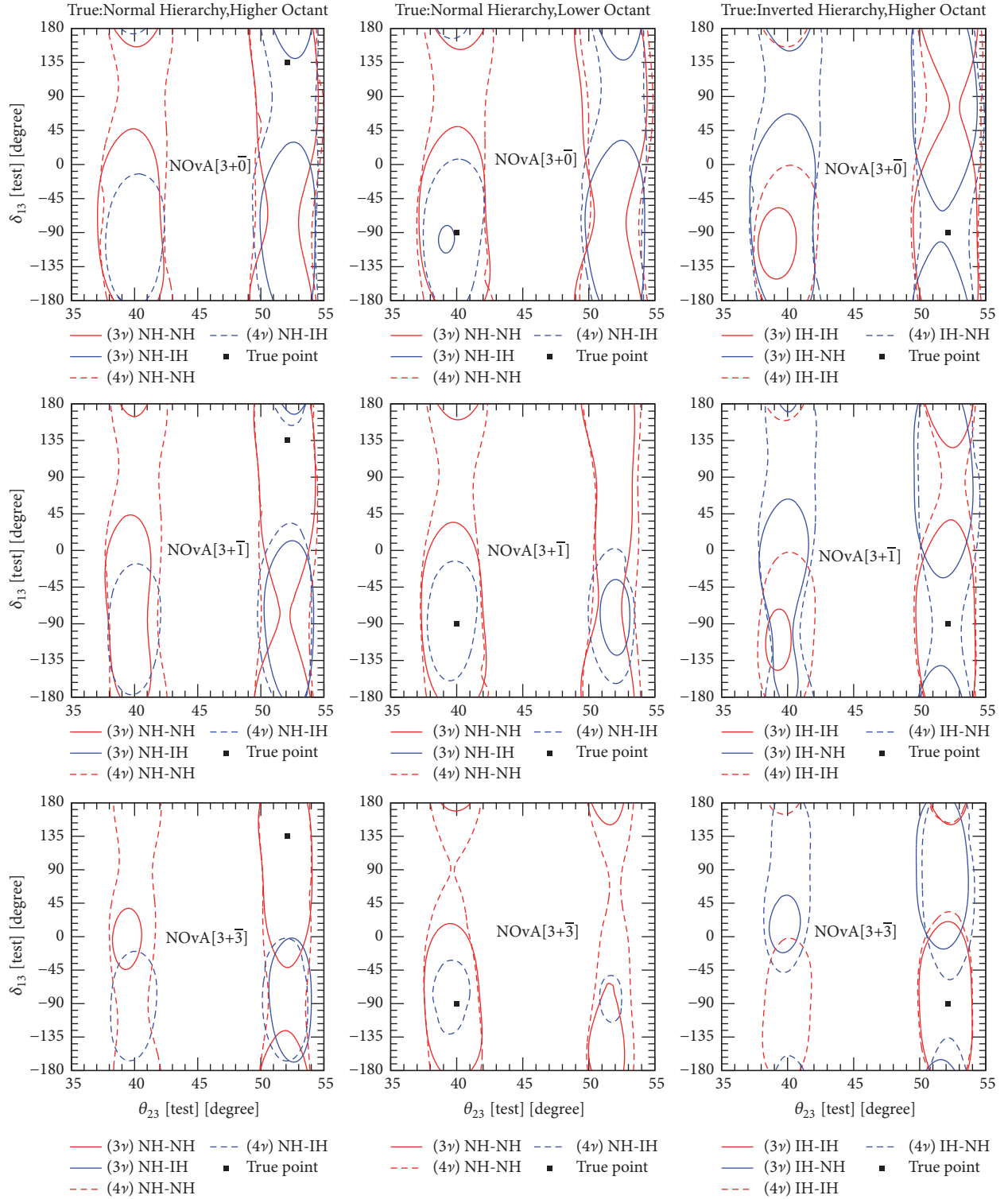


FIGURE 3: Contour plots of allowed regions in the test plane, θ_{23} versus δ_{13} , at 90% C.I. with top, middle, and bottom rows for NO ν A runs of 3 + 0, 3 + 1, and 3 + 3 years, respectively.

for 4 ν case we see that contour covers the whole of δ_{13} range. Already present small area of RH-WO of 3 ν is also increased for 4 ν case. 4 ν case also introduces a small region of WH solutions which were not present in 3 ν case. In the third plot,

we see that 4 ν introduces RH-WO region of the almost equal size of RH-RO region of 3 ν case. We observed a slight increase in WH-RO region for 4 ν over 3 ν case, while the WH-WO region almost triples for 4 ν case.

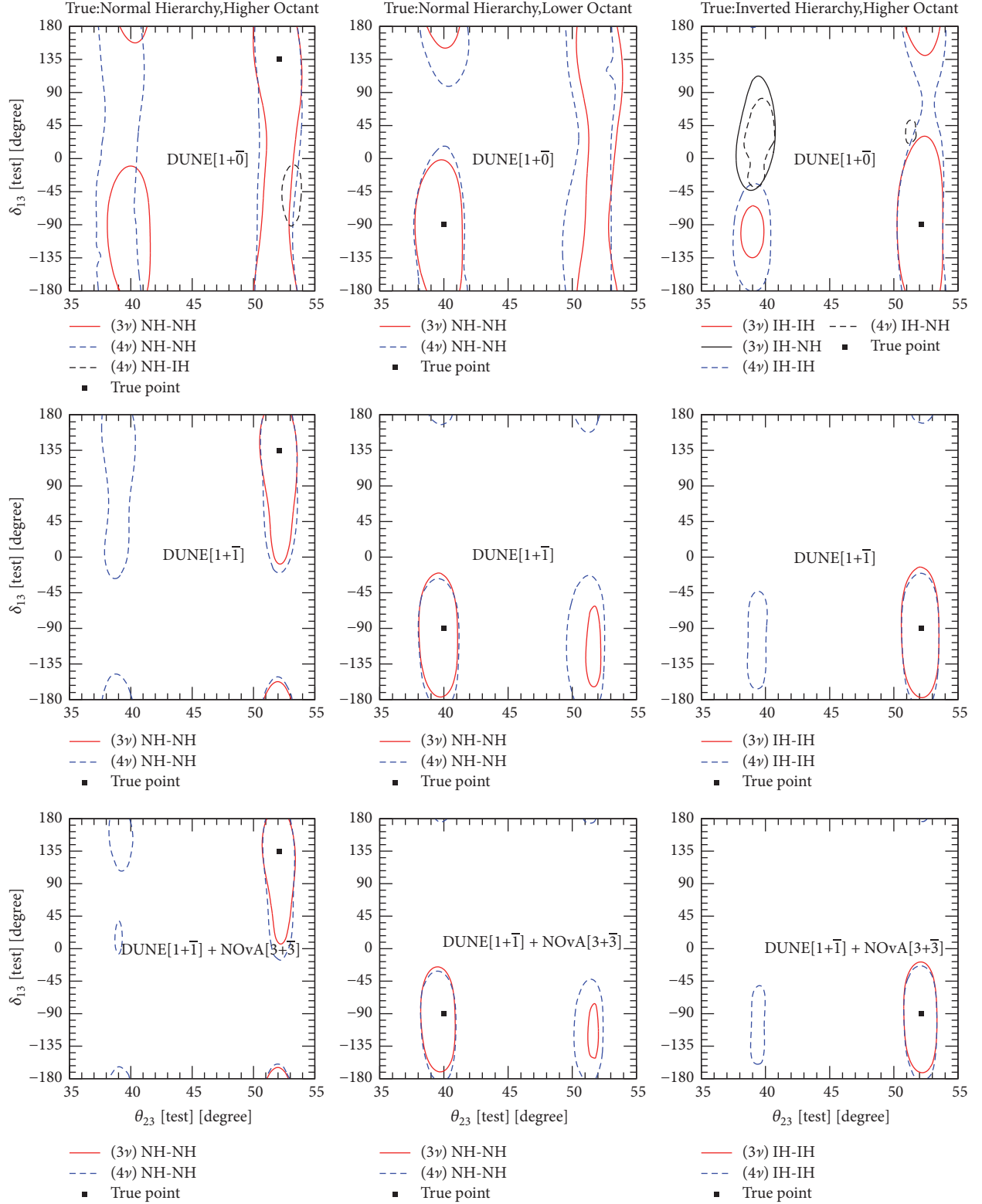


FIGURE 4: Contour plots of allowed regions in the test plane θ_{23} versus δ_{13} at 99% C.L. with top, middle, and bottom rows for DUNE runs of $1 + \bar{0}$, $1 + \bar{1}$ years and DUNE[$1 + \bar{1}$]+NOvA[$3 + \bar{3}$], respectively.

In Figure 4, we show allowed parameter regions for DUNE experiment for different runtimes. DUNE, being the next generation LBL experiment, is expected to have excellent statistics. Hence, we plot 99% C.L. regions for DUNE. In the

first row of Figure 4, we show 99% C.L. for DUNE[$1 + \bar{0}$]. In the first plot, RH-RO region covers the entire δ_{13} range for both 3ν and 4ν case. The RH-WO region which covers only lower half of δ_{13} region for 3ν case covers the whole range

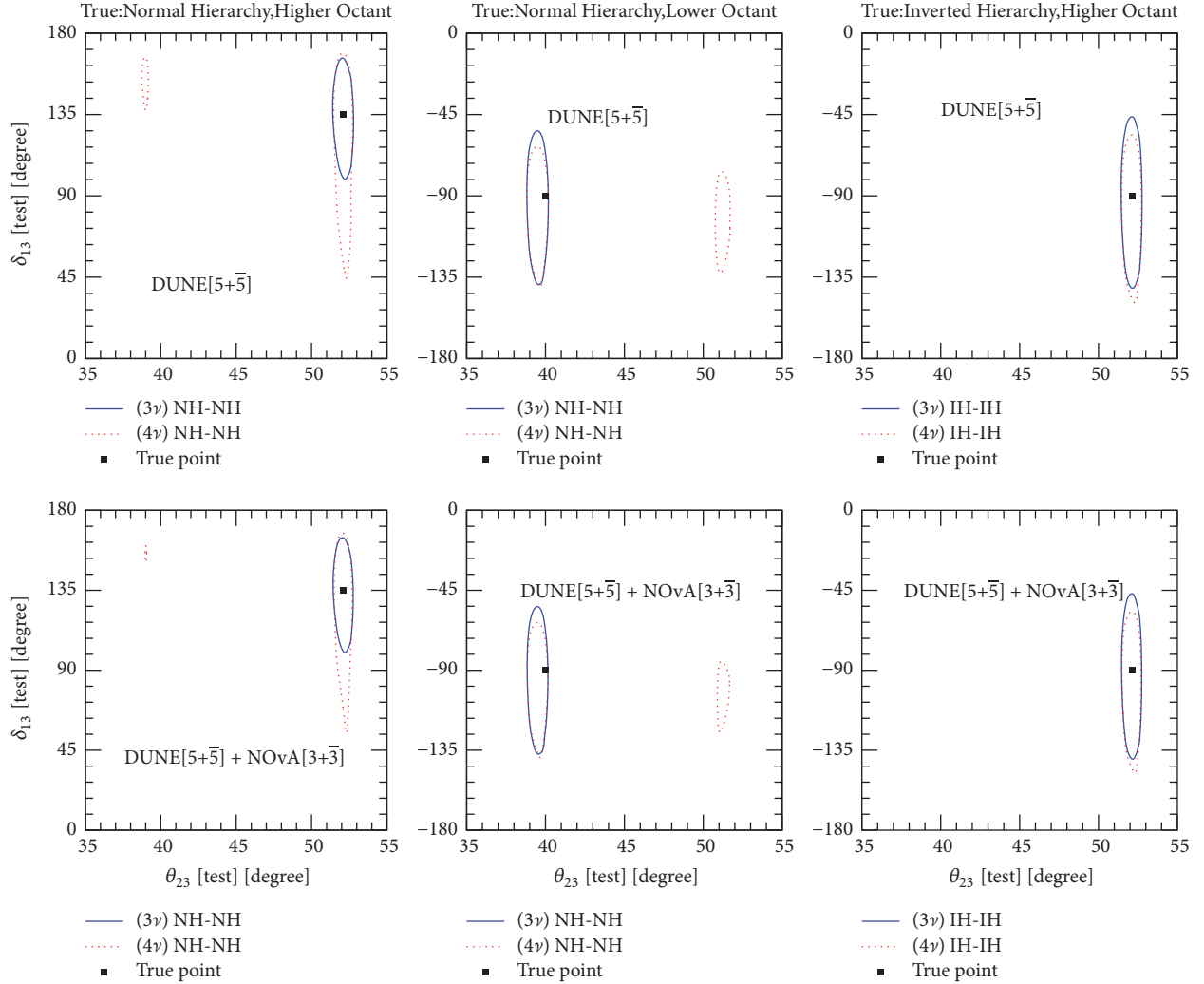


FIGURE 5: Contour plots of allowed regions in the test plane θ_{23} versus δ_{13} at 99% C.L with top and bottom rows for DUNE[5 + $\bar{5}$] and NO ν A[3 + $\bar{3}$] + DUNE[5 + $\bar{5}$], respectively.

for 4ν case. A small region of WH is also observed. In the second plot we see that all WH solutions are resolved. RH-WO covers the whole range of δ_{13} for both 3ν and 4ν case. RH-RO solutions exclude 0° to 155° of δ_{13} for 3ν case, while 20° to 100° of δ_{13} are excluded for 4ν case. In third plot, we see that 4ν case extends RH-RO to the whole range of δ_{13} while 30° to 140° of δ_{13} were excluded for 3ν case. We can see that DUNE clearly has better precision than NO ν A experiment. In the second row, we show allowed regions for DUNE[1 + $\bar{1}$]. We see the WH solutions are resolved for both 3ν and 4ν cases for all the best-fit values. In the first plot, 4ν case introduces RH-WO solution of similar size as RH-RO region of 3ν case. In the second plot, there is no considerable change in 4ν , compared to 3ν case for RH-RO region, while RH-WO octant is approximately doubled for 4ν case compared to 3ν case. In the third plot, 4ν case introduces small region of RH-WO which covers -45° to -170° of δ_{13} . In the third row, we combine statistics of DUNE[1 + $\bar{1}$] and NO ν A[3 + $\bar{3}$]. There is a small improvement in precision from the combined result over the result from DUNE[1 + $\bar{1}$] alone. In the first plot, we

see that a small RH-WO region is introduced by 4ν case. In the second plot, there is no considerable change between 3ν and 4ν case for RH-RO region, while RH-WO octant almost doubles over 3ν case for 4ν case. In the third plot, 4ν case introduces small region of RH-WO which covers -35° to -160° of δ_{13} .

In Figure 5, we show allowed parameter regions for DUNE experiment, at 99% C.L for DUNE[5 + $\bar{5}$]. We see that WH regions completely disappear for all the true value assumptions. In the first plot, RH-RO region covers a small δ_{13} range for both 3ν and 4ν case indicating high precision measurement capacity of DUNE. We see that δ_{13} range for 4ν case is approximately doubled as compared to the 3ν case. A small region of RH-WO is observed for 4ν case. In the second plot, RH-RO region covers small δ_{13} range of equal area for both 3ν and 4ν case. A small region of RH-WO is observed for 4ν case. In the third plot, the RH-WO solution is resolved. There is an increase in precision due to an increase in statistics. DUNE[5 + $\bar{5}$] clearly has a better precision compared to the NO ν A[3 + $\bar{3}$] experiment. In the

second row, we combine full run of NO ν A and DUNE to check their degeneracy resolution capacity. The WH solutions are resolved for both 3 ν and 4 ν cases for all the best-fit values. In the first plot, RH-WO solution is almost resolved for 4 ν case. In the second plot, RH-RO region covers small δ_{13} range of equal area for both 3 ν and 4 ν case. A small region of RH-WO is observed for 4 ν case. We observe a slight improvement in degeneracy resolution, on consideration of combined statistics of full run DUNE and NO ν A, over DUNE[5+5].

5. Conclusions

We have discussed how the presence of a sterile neutrino will affect the physics potential of the proposed experiment DUNE and future runs of NO ν A, in the light of latest NO ν A results [35]. The best-fit parameters reported by NO ν A still contain degenerate solutions. We attempt to see the extent to which these degeneracies could be resolved in future runs for the 3+1 model. Latest NO ν A best-fit values are taken as our true values. First, we show the degeneracy resolution capacity, for future runs of NO ν A. We conclude that NO ν A[3+3] could resolve WH-WO solutions for first two true value cases, at 90% C.L for 3 ν case, but not for 4 ν case. DUNE[1+1] could resolve WH and RH-W δ_{cp} solutions for both 3 ν and 4 ν case. WO degeneracy is resolved for 3 ν case at 99% C.L except for small RH-WO region for the second case of true values. DUNE[1+1] combined with NO ν A[3+3] shows increased sensitivity towards degeneracy resolution. Finally, for the full planned run of DUNE[5+5], all the degeneracies are resolved at 99% C.L for 3 ν case while a tiny region of WO lingers on for 4 ν case. For combined statistics of DUNE[5+5] and NO ν A[3+3], we observe that all the degeneracies are resolved at 99% C.L for both 3 ν and 4 ν case except for the NH-LO case. Thus, we conclude that NO ν A and DUNE experiments together can resolve all the degeneracies at 99% C.L even in the presence of sterile neutrino, if one of the current best-fit values of NO ν A is the true value.

Data Availability

The data used to support the findings of this study are based on published data and licensed open access software.

Conflicts of Interest

The authors declare that they have no conflicts of interest.

Acknowledgments

Akshay Chatla would like to thank *the Council of Scientific & Industrial Research, Government of India*, for financial support. The work of Sahithi Rudrabhatla was supported by *the Department of Science & Technology, Government of India*. We would like to thank Dr. Monojit Ghosh, Dr. C Soumya, and K Siva Prasad for their valuable help.

References

- [1] R. R. Volkas, "Introduction to sterile neutrinos," *Progress in Particle and Nuclear Physics*, vol. 48, no. 1, pp. 161–174, 2002.
- [2] C. Athanassopoulos et al., "Candidate events in a search for $\bar{\nu}_\mu \rightarrow \bar{\nu}_e$ oscillations," *Physical Review Letters*, vol. 75, p. 2650, 1995.
- [3] S. Schael et al., "ALEPH and DELPHI and L3 and OPAL and SLD collaborations and LEP electroweak working group and SLD electroweak group and SLD heavy flavour group," *Physics Reports*, vol. 427, p. 257, 2006.
- [4] A. A. Aguilar-Arevalo et al., "MiniBooNE collaboration," *Physical Review Letters*, vol. 102, Article ID 101802, 2009, arXiv:0812.2243.
- [5] J. N. Abdurashitov et al., "Measurement of the response of a Ga solar neutrino experiment to neutrinos from an ^{37}Ar source," *Physical Review C: Nuclear Physics*, vol. 73, Article ID 045805, 2006.
- [6] M. A. Acero, C. Giunti, and M. Laveder, "Limits on ν_e and $\bar{\nu}_e$ disappearance from Gallium and reactor experiments," *Physical Review D: Particles, Fields, Gravitation and Cosmology*, vol. 78, no. 7, 2008.
- [7] C. Giunti and M. Laveder, "Statistical significance of the gallium anomaly," *Physical Review C: Covering Nuclear Physics*, vol. 83, no. 6, p. 065504, 2011.
- [8] G. Mention, M. Fechner, T. Lasserre et al., "Reactor antineutrino anomaly," *Physical Review D: Particles, Fields, Gravitation and Cosmology*, vol. 83, no. 7, Article ID 073006, 2011.
- [9] N. Klop and A. Palazzo, "Imprints of CP violation induced by sterile neutrinos in T2K data," *Physical Review D: Particles, Fields, Gravitation and Cosmology*, vol. 91, no. 7, 2015.
- [10] A. Palazzo, "3-flavor and 4-flavor implications of the latest T2K and NO ν A electron (anti-)neutrino appearance results," *Physics Letters B*, vol. 757, p. 142, 2016.
- [11] F. P. An et al., "Independent measurement of the neutrino mixing angle θ_{13} via neutron capture on hydrogen at Daya Bay," *Physical Review Letters*, vol. 90, no. 7, 2014.
- [12] C. Soumya and R. Mohanta, "Towards extracting the best possible results from NO ν A," *European Physical Journal C*, vol. 76, no. 6, p. 302, 2016, arXiv:1605.00523.
- [13] C. Soumya, K. N. Deepthi, and R. Mohanta, "A Comprehensive Study of the Discovery Potential of NO ν A, T2K, and T2HK Experiments," *Advances in High Energy Physics*, vol. 2016, Article ID 9139402, 15 pages, 2016.
- [14] K. N. Deepthi, C. Soumya, and R. Mohanta, "Revisiting the sensitivity studies for leptonic CP violation and mass hierarchy with T2K, NO ν A and LBNE experiments," *New Journal of Physics*, vol. 17, no. 2, Article ID 023035, 2015, arXiv:1409.2343.
- [15] M. Ghosh, P. Ghoshal, S. Goswami, N. Nath, and S. K. Raut, "New look at the degeneracies in the neutrino oscillation parameters, and their resolution by T2K, NO ν A and ICAL," *Physical Review D: Particles, Fields, Gravitation and Cosmology*, vol. 93, no. 1, Article ID 013013, 2016.
- [16] S. Goswami and N. Nath, "Implications of the latest NO ν A results," *High Energy Physics - Phenomenology*, 2017, arXiv:1705.01274.
- [17] J. Kopp, P. A. Machado, M. Maltoni, and T. Schwetz, "Sterile neutrino oscillations: the global picture," *High Energy Physics - Phenomenology*, vol. 1305, p. 050009, 2013.
- [18] M. Ghosh, S. Gupta, Z. M. Matthews, P. Sharma, and A. G. Williams, "Study of parameter degeneracy and hierarchy

- sensitivity of NO ν A in presence of sterile neutrino,” *Physical Review D: Particles, Fields, Gravitation and Cosmology*, vol. 96, no. 7, 2017.
- [19] S. K. Agarwalla, S. S. Chatterjee, and A. Palazzo, “Physics reach of DUNE with a light sterile neutrino,” *High Energy Physics - Phenomenology*, vol. 016, 2016, arXiv:1603.03759.
- [20] D. Dutta, R. Gandhi, B. Kayser, M. Masud, and S. Prakash, “Capabilities of long-baseline experiments in the presence of a sterile neutrino,” *Journal of High Energy Physics*, vol. 122, 2016.
- [21] S. K. Agarwalla, S. S. Chatterjee, and A. Palazzo, “Signatures of a light sterile neutrino in T2HK,” *High Energy Physics - Phenomenology*, vol. 1804, no. 091, 2018, arXiv:1801.04855.
- [22] S. K. Agarwalla, S. S. Chatterjee, and A. Palazzo, “Octant of θ_{23} in danger with a light sterile neutrino,” *Physical Review Letters*, vol. 118, no. 3, 2017.
- [23] S. Choubey, D. Dutta, and D. Pramanik, “Measuring the sterile neutrino CP phase at DUNE and T2HK,” *The European Physical Journal C*, vol. 78, no. 4, 2018.
- [24] P. Huber, M. Lindner, and W. Winter, “Simulation of long-baseline neutrino oscillation experiments with GLOBES: (General Long Baseline Experiment Simulator),” *Computer Physics Communications*, vol. 167, no. 3, pp. 195–202, 2005.
- [25] P. Huber, J. Kopp, M. Lindner, M. Rolinec, and W. Winter, “New features in the simulation of neutrino oscillation experiments with GLOBES 3.0. (General Long Baseline Experiment Simulator),” *Computer Physics Communications*, vol. 177, p. 432, 2007.
- [26] J. Kopp, “New physics engine for the inclusion sterile neutrinos and non-standard interactions in GLOBES,” <https://www.mpi-hd.mpg.de/personalhomes/globes/tools.html>, 2011.
- [27] P. Adamson et al., “First measurement of muon-neutrino disappearance in NO ν A,” *Physical Review Letters D*, vol. 93, no. 5, 2016.
- [28] P. Adamson, “First Measurement of Electron Neutrino Appearance in NO ν A,” *Physical Review Letters*, vol. 116, no. 5, 2016.
- [29] D. S. Ayres et al., “The NO ν A technical design report,” *INIS*, vol. 39, no. 38, 2007, [NO ν A Collaboration], doi:10.2172/, doi.
- [30] S. K. Agarwalla, S. Prakash, S. K. Raut, and S. U. Sankar, “Potential of optimized NO ν A for large θ_{13} & combined performance with a LArTPC & T2K,” *High Energy Physics - Phenomenology*, vol. 1212, 2012, arXiv:1208.3644.
- [31] D. S. Ayres et al., “NO ν A proposal to build a 30 kiloton Off-axis detector to study neutrino oscillations in the fermilab NuMI beamline,” *High Energy Physics - Experiment*, 2005.
- [32] R. Acciarri, “Long-baseline neutrino facility (LBNF) and deep underground neutrino experiment (DUNE) conceptual design report volume 2: The physics program for DUNE at LBNF,” *High Energy Physics - Experiment*, 2016, arXiv:1512.06148.
- [33] R. Acciarri et al., “Long-baseline neutrino facility (LBNF) and deep underground neutrino experiment (DUNE) conceptual design report volume 1: The LBNF and DUNE projects,” *High Energy Physics - Experiment*, 2016, arXiv:1601.05471.
- [34] T. Alion et al., “Experiment simulation configurations used in DUNE CDR,” *High Energy Physics - Phenomenology*, 2016, arXiv:1606.09550.
- [35] P. Adamson et al., “Constraints on Oscillation Parameters from ν_e appearance and ν_μ disappearance in NO ν A,” *Physical Review Letters*, vol. 118, 2017.
- [36] P. Adamson et al., “Search for active-sterile neutrino mixing using neutral-current interactions in NO ν A,” *Physical Review Letters*, vol. 96, no. 7, Article ID 072006, 2017.
- [37] A. Y. Smirnov, “The MSW effect and matter effects in neutrino oscillations,” *Physica Scripta*, vol. T121, pp. 57–64, 2005.

Research Article

Novel Neutrino-Floor and Dark Matter Searches with Deformed Shell Model Calculations

D. K. Papoulias ¹, R. Sahu,² T. S. Kosmas ³, V. K. B. Kota,⁴ and B. Nayak²

¹*Institute of Nuclear and Particle Physics, NCSR 'Demokritos', 15310 Agia Paraskevi, Greece*

²*National Institute of Science and Technology, Palur Hills, Berhampur, Odisha 761008, India*

³*Theoretical Physics Section, University of Ioannina, 45110 Ioannina, Greece*

⁴*Physical Research Laboratory, Ahmedabad 380 009, India*

Correspondence should be addressed to D. K. Papoulias; dimpap@cc.uoi.gr

Received 15 May 2018; Revised 16 July 2018; Accepted 9 August 2018; Published 26 August 2018

Academic Editor: Enrico Lunghi

Copyright © 2018 D. K. Papoulias et al. This is an open access article distributed under the Creative Commons Attribution License, which permits unrestricted use, distribution, and reproduction in any medium, provided the original work is properly cited. The publication of this article was funded by SCOAP³.

Event detection rates for WIMP-nucleus interactions are calculated for ^{71}Ga , ^{73}Ge , ^{75}As , and ^{127}I (direct dark matter detectors). The nuclear structure form factors, which are rather independent of the underlying physics beyond the Standard Model particle physics scenario assumed, are evaluated within the context of the deformed nuclear shell model (DSM) based on Hartree-Fock nuclear states. Along with the previously published DSM results for ^{73}Ge , the neutrino-floor due to coherent elastic neutrino-nucleus scattering (CE ν NS), an important source of background to dark matter searches, is extensively calculated. The impact of new contributions to CE ν NS due to neutrino magnetic moments and Z' mediators at direct dark matter detection experiments is also examined and discussed. The results show that the neutrino-floor constitutes a crucial source of background events for multi-ton scale detectors with sub-keV capabilities.

1. Introduction

In the last few decades, the measurements of the cosmic microwave background (CMB) radiation offered a remarkably powerful way of modelling the origin of cosmic-ray anisotropies and constraining the geometry, the evolution, and the matter content of our universe. Such observations have in general indicated the consistency of the standard cosmological model [1] and the fact that our universe hardly contains $\sim 5\%$ luminous matter, whereas the remainder consists of nonluminous dark matter ($\sim 23\%$) and dark energy ($\sim 72\%$) [2]. After the discovery of the CMB fluctuations by the Cosmic Background Explorer (COBE) satellite [3], the extremely high precision of the WMAP satellite and especially of the Planck third-generation space mission has helped us to produce maps for the CMB anisotropies and other cosmological parameters (see [4] for details). We also mention that high-resolution ground-based CMB data, like those of the Atacama Cosmology Telescope (ACT) [5] and the

South Pole Telescope (SPT) [6] have recovered the underlying CMB spectra observed by the space missions.

Focusing on the topic we address in this work, it is worth noting that the CMB data, the Supernova Cosmology project [7], and so on suggest that most of the dark matter of the universe is cold. Furthermore, the baryonic cold dark matter (CDM) component can be considered to consist of either massive compact halo objects (MACHOs) like neutron stars, white dwarfs, Jupiters, etc. or Weakly Interacting Massive Particles (WIMPs) that constantly bombard Earth's atmosphere. Several results of experimental searches suggest that the MACHO fraction should not exceed a portion of about 20% [1]. On the theoretical side, within the framework of new physics beyond the Standard Model (SM), supersymmetric (SUSY) theories provide promising nonbaryonic candidates for dark matter [8] (for a review see [9]). In the simple picture, the dark matter in the galactic halo is assumed to be Weakly Interacting Massive Particles (WIMPs). The most appealing WIMP candidate for nonbaryonic CDM is the

lightest supersymmetric particle (LSP) which is expected to be a neutral Majorana fermion traveling with nonrelativistic velocities [10].

In recent years, there have been considerable theoretical and experimental efforts towards WIMP detection through several nuclear probes [11–13]. Popular target nuclei include among others the ^{71}Ga , ^{73}Ge , ^{75}As , ^{127}I , ^{134}Xe , and ^{208}Pb isotopes [14, 15]. Towards the first ever dark matter detection, a great number of experimental efforts take place aiming at measuring the energy deposited after the galactic halo WIMPs scatter off the nuclear isotopes of the detection material. Because of the low count rates, due to the fact that the WIMP-nucleus interaction is remarkably weak, the choice of the detector plays very important role and for this reason spin-dependent interactions require the use of targets with nonzero spin. The Cryogenic Dark Matter Search (CDMS) experimental facility [16] has been designed to directly detect the dark matter by employing a ^{73}Ge as the target nucleus, setting the most sensitive limits on the interaction of WIMP with terrestrial materials to date. The development of upgrades is under way and will be located at SNOLAB. Another prominent dark matter experiment is the EDELWEISS facility in France [17] which uses high purity germanium cryogenic bolometers at milli-Kelvin temperatures. There are also other experimental attempts using detectors like ^{127}I , $^{129,131}\text{Xe}$, ^{133}Cs , etc. (see [18–20]).

Inevitably, direct detection experiments are exposed to various neutrino emissions, such as those originating from astrophysical sources (e.g., Solar [21], Atmospheric [22, 23], and diffuse Supernova [24] neutrinos), Earth neutrinos (Geoneutrinos [25]), and in other cases even artificial terrestrial neutrinos (e.g., neutrinos from nearby reactors [26]). The subsequent neutrino interactions with the material of dark matter detectors, namely, the neutrino-floor, may perfectly mimic possible WIMP signals [27]. Thus, the impacts of the neutrino-floor on the relevant experiments looking for CDM as well as on the detector responses to neutrino interactions need be comprehensively investigated. Since Geoneutrino fluxes are relatively low, astrophysical neutrinos are recognised as the most significant background source that remains practically irreducible [28]. The recent advances of direct detection dark matter experiments, mainly due to the development of low threshold technology and high detection efficiency, are expected to reach the sensitivity frontiers in which astrophysical neutrino-induced backgrounds are expected to limit the observation potential of the WIMP signal [29].

In this work, we explore the impact of the most important neutrino background source on the relevant direct dark matter detection experiments by concentrating on the dominant neutrino-matter interaction channel, e.g., the coherent elastic neutrino-nucleus scattering (CE ν NS) [30, 31]. It is worthwhile to mention that events of this process were recently measured for the first time by the COHERENT experiment at the Spallation Neutrino Source [32], completing the SM picture of electroweak interactions at low energies. Such a profound discovery motivated our present work and we will make an effort to shed light on the nuclear physics

aspects. Neutrino nonstandard interactions (NSIs) [33] may constitute an important source of neutrino background and have been investigated recently in [34, 35]. Thus, apart from addressing the SM contributions to CE ν NS [36], we also explore the impact of new physics contributions that arise in the context of electromagnetic (EM) neutrino properties [37, 38] as well as of those emerging in the framework of $U(1)'$ gauge interactions [39] due to the presence of new light Z' mediators [40, 41]. The aforementioned interaction channels may lead to a novel neutrino-floor as demonstrated by [42]. The latter could be detectable in view of the constantly increasing sensitivity of the upcoming direct detection experiments with multi-ton mass scale and sub-keV capabilities [43].

Direct detection dark matter experiments are currently entering a precision era, and nuclear structure effects are expected to become rather important and should be incorporated in astroparticle physics applications [45]. For this reason, our nuclear model is at first tested in its capabilities to adequately describe the nuclear properties before being applied to problems like dark matter detection. This work considers the deformed shell model (DSM), on the basis of Hartree-Fock (HF) deformed intrinsic states with angular momentum projection and band mixing [46], all with a realistic effective interaction and a set of single-particle states and single-particle energies, which is established to be rather successful in describing the properties of nuclei in the mass range $A = 60\text{--}90$ (see [47] for details regarding DSM and its applications). In particular, the DSM is employed for calculating the required nuclear structure factors entering the dark matter and neutrino-floor expected event rates by focusing on four interesting nuclei regarding dark matter investigations such as ^{71}Ga , ^{73}Ge , ^{75}As , and ^{127}I . Let us add that details of nuclear structure and dark matter event rates for ^{73}Ge obtained using DSM have been reported recently [48].

The paper has been organised as follows. Section 2 gives the main ingredients of WIMP-nucleus scattering, while Section 3 provides the formulation for neutrino-nucleus scattering (neutrino-floor) within and beyond the SM. Then in Section 4 we describe briefly the methodology of the DSM, and the main results of the present work are presented and discussed in Section 5. Finally, the concluding remarks are drawn in Section 6.

2. Searching WIMP Dark Matter

The Earth is exposed to a huge number of WIMPs originating from the galactic halo. Their direct detection through nuclear recoil measurements after scattering off the target nuclei at the relevant dark matter experiments is of fundamental interest in modern physics and is expected to have a direct impact on astroparticle physics and cosmology. In this section we discuss the mathematical formulation of WIMP-nucleus scattering. The formalism introduces an appropriate separation of the SUSY and nuclear parts entering the event rates of WIMP-nucleus interactions in our effort to emphasise the important role played by the nuclear physics aspects. In particular we perform reliable nuclear structure calculations within the context of DSM based on Hartree-Fock states.

2.1. WIMP-Nucleus Scattering. For direct detection dark matter experiments, the differential event rate of a WIMP with mass m_χ scattering off a nucleus (A, Z) with respect to the momentum transfer q can be cast in the form [1]

$$\frac{dR(u, v)}{dq^2} = N_t \phi \frac{d\sigma}{dq^2} f(v) d^3 v, \quad (1)$$

where $N_t = 1/(Am_p)$ denotes the number of target nuclei per unit mass, A stands for the mass number of the target nucleus, and m_p is the proton mass. In the above expression the WIMP flux is $\phi = \rho_0 v / m_\chi$, with ρ_0 being the local WIMP density. The distribution of WIMP velocity relative to the detector (or Earth) and also the motion of the Sun and Earth, $f(v)$, is taken into account and assumed to resemble a Maxwell-Boltzmann distribution to ensure consistency with the LSP velocity distribution. Note that, by neglecting the rotation of Earth in its own axis, $v = |v|$ accounts for the relative velocity of WIMP with respect to the detector. For later convenience a dimensionless variable $u = q^2 b^2 / 2$ is introduced with b denoting the oscillator length parameter, and the corresponding WIMP-nucleus differential cross section in the laboratory frame reads [10, 15, 48–50]

$$\frac{d\sigma(u, v)}{du} = \frac{1}{2} \sigma_0 \left(\frac{1}{m_p b} \right)^2 \frac{c^2}{v^2} \frac{d\sigma_A(u)}{du}, \quad (2)$$

with

$$\begin{aligned} \frac{d\sigma_A}{du} &= [f_A^0 \Omega_0(0)]^2 F_{00}(u) \\ &+ 2 f_A^0 f_A^1 \Omega_0(0) \Omega_1(0) F_{01}(u) \\ &+ [f_A^1 \Omega_1(0)]^2 F_{11}(u) + \mathcal{M}^2(u). \end{aligned} \quad (3)$$

The first three terms account for the spin contribution due to the axial current, while the fourth term accounts for the coherent contribution arising from the scalar interaction. The coherent contribution is expressed in terms of the nuclear form factors given as

$$\begin{aligned} \mathcal{M}^2(u) &= (f_S^0 [ZF_Z(u) + NF_N(u)] \\ &+ f_S^1 [ZF_Z(u) - NF_N(u)])^2. \end{aligned} \quad (4)$$

The coherent part in the approximation of nearly equal proton and neutron nuclear form factors $F_Z(u) \approx F_N(u)$ is given as

$$\mathcal{M}^2(u) = A^2 \left(f_S^0 - f_S^1 \frac{A-2Z}{A} \right)^2 |F(u)|^2. \quad (5)$$

The respective values of the nucleonic-current parameters f_V^0 , f_V^1 for the isoscalar and isovector parts of the vector current (not shown here), f_A^0 , f_A^1 for the isoscalar and isovector parts of the axial-vector current, and f_S^0 , f_S^1 for the isoscalar and isovector parts of the scalar current depend on the specific SUSY model employed [51]. The spin structure functions

$F_{\rho\rho'}(u)$ with $\rho, \rho' = 0, 1$ for the isoscalar and isovector contributions, respectively, take the form

$$F_{\rho\rho'}(u) = \sum_{\lambda, \kappa} \frac{\Omega_\rho^{(\lambda, \kappa)}(u) \Omega_{\rho'}^{(\lambda, \kappa)}(u)}{\Omega_\rho(0) \Omega_{\rho'}(0)}, \quad (6)$$

with

$$\begin{aligned} \Omega_\rho^{(\lambda, \kappa)}(u) &= \sqrt{\frac{4\pi}{2J_\lambda + 1}} \times \langle J_f | | \\ &\sum_{j=1}^A [Y_\lambda(\Omega_j) \otimes \sigma(j)]_\kappa j_\lambda(\sqrt{u} r_j) \omega_\rho(j) | | J_i \rangle. \end{aligned} \quad (7)$$

Here, $\omega_0(j) = 1$ and $\omega_1(j) = \tau(j)$ with $\tau = +1$ for protons and $\tau = -1$ for neutrons, while Ω_j represents the solid angle for the position vector of the j -th nucleon and j_λ stands for the well-known spherical Bessel function. The quantities $\Omega_\rho(0) = \Omega_\rho^{(0,1)}(0)$ are the static spin matrix elements (see, e.g., [8]). In this context, the WIMP-nucleus event rate per unit mass of the detector is conveniently written as

$$\begin{aligned} \langle R \rangle &= (f_A^0)^2 D_1 + 2 f_A^0 f_A^1 D_2 + (f_A^1)^2 D_3 \\ &+ A^2 \left(f_S^0 - f_S^1 \frac{A-2Z}{A} \right)^2 |F(u)|^2 D_4. \end{aligned} \quad (8)$$

The functions D_i enter the definition of the WIMP-nucleus event rate through the three-dimensional integrals, given by

$$D_i = \int_{-1}^1 d\xi \int_{\psi_{\min}}^{\psi_{\max}} d\psi \int_{u_{\min}}^{u_{\max}} G(\psi, \xi) X_i du, \quad (9)$$

with

$$\begin{aligned} X_1 &= [\Omega_0(0)]^2 F_{00}(u), \\ X_2 &= \Omega_0(0) \Omega_1(0) F_{01}(u), \\ X_3 &= [\Omega_1(0)]^2 F_{11}(u), \\ X_4 &= |F(u)|^2. \end{aligned} \quad (10)$$

In the latter expression, D_1 , D_2 , and D_3 account for the spin-dependent parts of (3), while D_4 is associated with the coherent contribution.

In this work, the nuclear wave functions $\langle J_f |$ and $| J_i \rangle$ entering (7) are calculated within the nuclear DSM of [46, 47]. For a comprehensive discussion on the explicit form of the function $G(\psi)$, the integration limits of (9) and the various parameters entering into these, the reader is referred to [48].

3. Neutrino-Nucleus Scattering

The neutrino-floor stands out as an important source of irreducible background to WIMP searches at a direct detection experiment. In this work we explore the neutrino-floor due to neutrino-nucleus scattering since the corresponding floor

TABLE 1: Solar neutrino fluxes and uncertainties in the framework of the employed high metallicity SSM (for details, see the text).

type	$E_{\nu_{\max}}$ [MeV]	flux [$\text{cm}^{-2}\text{s}^{-1}$]
pp	0.423	$(5.98 \pm 0.006) \times 10^{10}$
pep	1.440	$(1.44 \pm 0.012) \times 10^8$
hep	18.784	$(8.04 \pm 1.30) \times 10^3$
${}^7\text{Be}_{\text{low}}$	0.3843	$(4.84 \pm 0.48) \times 10^8$
${}^7\text{Be}_{\text{high}}$	0.8613	$(4.35 \pm 0.35) \times 10^9$
${}^8\text{B}$	16.360	$(5.58 \pm 0.14) \times 10^6$
${}^{13}\text{N}$	1.199	$(2.97 \pm 0.14) \times 10^8$
${}^{15}\text{O}$	1.732	$(2.23 \pm 0.15) \times 10^8$
${}^{17}\text{F}$	1.740	$(5.52 \pm 0.17) \times 10^6$

coming from neutrino-electron scattering is relatively low [52]. Motivated by the novel neutrino interaction searches using reactor neutrinos of [42], here we consider various astrophysical neutrino sources in our calculations that involve the conventional and beyond the SM interactions channels (see below).

3.1. Differential Event Rate at Dark Matter Detectors. For a given interaction channel $x = \text{SM}, \text{EM}, Z'$, the differential event rate dR_ν/dT_N of CE ν NS processes at a dark matter detector is obtained through the convolution of the normalised neutrino energy distribution $\lambda_\nu(E_\nu)$ of the background neutrino source in question (i.e., Solar, Atmospheric and Diffuse Supernova Neutrinos, as seen below) with the CE ν NS cross section, as follows [53]:

$$\left(\frac{dR_\nu}{dT_N}\right)_x = \mathcal{K} \int_{E_\nu^{\min}}^{E_\nu^{\max}} \lambda_\nu(E_\nu) \frac{d\sigma_x}{dT_N}(E_\nu, T_N) dE_\nu, \quad (11)$$

where E_ν^{\max} is the maximum neutrino energy of the source in question (for the case of Solar neutrinos see, e.g., Table 1) and $E_\nu^{\min} = \sqrt{MT_N/2}$ is the minimum neutrino energy that is required to yield a nuclear recoil with energy T_N . In the latter expression $\mathcal{K} = t_{\text{run}} N_{\text{targ}} \Phi_\nu$ with t_{run} being the exposure time, N_{targ} is the number of target nuclei and Φ_ν is the assumed neutrino flux.

3.1.1. Standard Model Interactions. Assuming SM interactions only, at low and intermediate neutrino energies $E_\nu \ll M_W$, the weak neutral-current CE ν NS process is adequately described by the four-fermion effective interaction Lagrangian [33, 36]

$$\mathcal{L}_{\text{SM}} = -2\sqrt{2}G_F \sum_{\substack{f=u,d \\ \alpha=e,\mu,\tau}} g_{\alpha\alpha}^{f,P} [\bar{\nu}_\alpha \gamma_\rho L \nu_\alpha] [\bar{f} \gamma^\rho P f], \quad (12)$$

where $P = \{L, R\}$ denote the chiral projectors, $\alpha = \{e, \mu, \tau\}$ represents the neutrino flavour, and $f = \{u, d\}$ is a first generation quark. By including the radiative corrections of

[54], the P -handed couplings of the f quarks to the Z -boson are expressed as

$$\begin{aligned} g_{\alpha\alpha}^{u,L} &= \rho_{\nu N}^{\text{NC}} \left(\frac{1}{2} - \frac{2}{3} \hat{\kappa}_{\nu N} \hat{s}_Z^2 \right) + \lambda^{u,L}, \\ g_{\alpha\alpha}^{d,L} &= \rho_{\nu N}^{\text{NC}} \left(-\frac{1}{2} + \frac{1}{3} \hat{\kappa}_{\nu N} \hat{s}_Z^2 \right) + \lambda^{d,L}, \\ g_{\alpha\alpha}^{u,R} &= \rho_{\nu N}^{\text{NC}} \left(-\frac{2}{3} \hat{\kappa}_{\nu N} \hat{s}_Z^2 \right) + \lambda^{u,R}, \\ g_{\alpha\alpha}^{d,R} &= \rho_{\nu N}^{\text{NC}} \left(\frac{1}{3} \hat{\kappa}_{\nu N} \hat{s}_Z^2 \right) + \lambda^{d,R}, \end{aligned} \quad (13)$$

with $\hat{s}_Z^2 = \sin^2 \theta_W = 0.2312$, $\rho_{\nu N}^{\text{NC}} = 1.0086$, $\hat{\kappa}_{\nu N} = 0.9978$, $\lambda^{u,L} = -0.0031$, $\lambda^{d,L} = -0.0025$, and $\lambda^{d,R} = 2\lambda^{u,R} = 7.5 \times 10^{-5}$.

In this work we restrict our study only to low momentum transfer in order to satisfy the coherent condition $|\mathbf{q}| \leq 1/R_A$, where R_A is the nuclear size and $|\mathbf{q}|$ is the magnitude of the three-momentum transfer [31]. Focusing on the dominant CE ν NS channel, the relevant SM differential cross section with respect to the nuclear recoil energy T_N takes the form [41]

$$\begin{aligned} \frac{d\sigma_{\text{SM}}}{dT_N}(E_\nu, T_N) &= \frac{G_F^2 M}{\pi} \left[(\mathcal{Q}_W^V)^2 \left(1 - \frac{MT_N}{2E_\nu^2} \right) \right. \\ &\quad \left. + (\mathcal{Q}_W^A)^2 \left(1 + \frac{MT_N}{2E_\nu^2} \right) \right], \end{aligned} \quad (14)$$

with E_ν denoting the neutrino energy and M the mass of the target nucleus. The relevant vector (\mathcal{Q}_W^V) and axial-vector (\mathcal{Q}_W^A) weak charges entering the CE ν NS cross section are given by the relations [55]

$$\begin{aligned} \mathcal{Q}_W^V(Q^2) &= [g_p^V Z F_Z^V(Q^2) + g_n^V N F_N^V(Q^2)], \\ \mathcal{Q}_W^A(Q^2) &= [g_p^A (Z_+ - Z_-) + g_n^A (N_+ - N_-)] F_A(Q^2). \end{aligned} \quad (15)$$

Here, Z_\pm (N_\pm) stands for the number of protons (neutrons) with spin up (+) and spin down (-), respectively, while g_p^A

(g_n^A) represent the axial-vector couplings of protons (neutrons) to the Z^0 boson. At the nuclear level, the relevant vector (axial-vector) couplings of protons g_p^V (g_p^A) and neutrons g_n^V (g_n^A) take the form

$$\begin{aligned} g_p^V &= 2(g_{\alpha\alpha}^{u,L} + g_{\alpha\alpha}^{u,R}) + (g_{\alpha\alpha}^{d,L} + g_{\alpha\alpha}^{d,R}), \\ g_n^V &= (g_{\alpha\alpha}^{u,L} + g_{\alpha\alpha}^{u,R}) + 2(g_{\alpha\alpha}^{d,L} + g_{\alpha\alpha}^{d,R}), \\ g_p^A &= 2(g_{\alpha\alpha}^{u,L} - g_{\alpha\alpha}^{u,R}) + (g_{\alpha\alpha}^{d,L} - g_{\alpha\alpha}^{d,R}), \\ g_n^A &= (g_{\alpha\alpha}^{u,L} - g_{\alpha\alpha}^{u,R}) + 2(g_{\alpha\alpha}^{d,L} - g_{\alpha\alpha}^{d,R}). \end{aligned} \quad (16)$$

The axial-vector nucleon form factor takes into account the spin structure of the nucleon and is defined as [56]

$$F_A(Q^2) = g_A \left(1 + \frac{Q^2}{M_A^2} \right)^{-2}, \quad (17)$$

where $g_A = 1.267$ is the free axial-vector coupling constant and the axial mass is taken to be $M_A = 1$ GeV, while strange quark effects have been neglected.

We note that for spin-zero nuclei the axial-vector contribution vanishes, while for the odd- A nuclei considered in the present study \mathcal{Q}_W^A it is negligible and of the order of $\mathcal{Q}_W^A/\mathcal{Q}_W^V \sim 1/A$. The weak charges in (15) encode crucial information regarding the finite nuclear size through the proton $F_Z^V(Q^2)$ and neutron $F_N^V(Q^2)$ nuclear form factors, which in our work are obtained within the context of the DSM (see below), as functions of the momentum transfer $-q^\mu q_\mu = Q^2 = 2MT_N$. Contrary to similar studies assuming the conventional Helm-type form factors, the present work also takes into account the nuclear effects due to the nonspherical symmetric nuclei employed in dark matter searches.

3.1.2. Electromagnetic Neutrino Contributions. Turning our attention to new physics phenomena we now address potential contributions to CE ν NS in the framework of nontrivial neutrino EM interactions that may lead to a new neutrino-floor at low detector thresholds. In this framework, the presence of an effective neutrino magnetic moment μ_ν leads to an EM contribution of the differential cross section that has been written as [41]

$$\left(\frac{d\sigma}{dT_N} \right)_{\text{SM+EM}} = \mathcal{E}_{\text{EM}}(E_\nu, T_N) \frac{d\sigma_{\text{SM}}}{dT_N}. \quad (18)$$

Neglecting axial effects, the EM contribution to CE ν NS at a direct detection dark matter is encoded in the factor

$$\mathcal{E}_{\text{EM}} = 1 + \frac{1}{G_F^2 M} \left(\frac{\mathcal{Q}_{\text{EM}}}{\mathcal{Q}_W^V} \right)^2 \frac{(1 - T_N)/E_\nu/T_N}{1 - MT_N/2E_\nu^2}, \quad (19)$$

where the relevant EM charge \mathcal{Q}_{EM} is written in terms of the electron mass m_e , the fine-structure constant a_{EM} , and the effective neutrino magnetic moment as [57]

$$\mathcal{Q}_{\text{EM}} = \frac{\pi a_{\text{EM}} \mu_\nu}{m_e} Z. \quad (20)$$

In contrast to the $\sim N^2$ dependence of the SM case, (19) and (20) imply the existence of a Z^2 coherence along with a characteristic $\sim 1/T_N$ enhancement of the total cross section. This implies a potential distortion of the expected recoil spectrum at very low recoil energies that may be detectable at future direct dark matter detection with sub-keV operation thresholds.

For the sake of completeness, we stress that the effective neutrino magnetic moment μ_ν is expressed through neutrino amplitudes of positive and negative helicity states, e.g., the 3-vectors a_+ and a_- and the neutrino transition magnetic moment matrix, λ , in flavour basis, as [37, 58]

$$\mu_\nu^2 = a_+^\dagger \lambda \lambda^\dagger a_+ + a_-^\dagger \lambda \lambda^\dagger a_-. \quad (21)$$

Then, the effective neutrino magnetic moment is written in mass basis through a proper rotation; for a detailed description of this formalism see [59].

3.1.3. Novel Mediator Contribution. We now explore novel mediator fields that could be accommodated in the context of simplified $U(1)'$ scenarios [60, 61] predicting the existence of a new Z' vector mediator with mass $M_{Z'}$ [62]. Such beyond the SM interactions may constitute a new neutrino-floor at direct detection dark matter experiments [39].

The presence of a Z' mediator gives rise to subleading contributions to the SM CE ν NS rate, described by the Lagrangian [63]

$$\mathcal{L}_{\text{vec}} = Z'_\mu \left(g_{Z'}^{qV} \bar{q} \gamma^\mu q + g_{Z'}^{\nu V} \bar{\nu}_L \gamma^\mu \nu_L \right) + \frac{1}{2} M_{Z'}^2 Z'_\mu Z'^\mu, \quad (22)$$

where only left-handed neutrinos are assumed (right-handed neutrinos in the theory would lead to vector-axial-vector cancellations). The resulting cross section reads [41]

$$\left(\frac{d\sigma}{dT_N} \right)_{\text{SM+Z}'} = \mathcal{E}_{Z'}^2(Q) \frac{d\sigma_{\text{SM}}}{dT_N}, \quad (23)$$

with the factor $\mathcal{E}_{Z'}$ being written in terms of the neutrino-vector coupling $g_{Z'}^{\nu V}$, as

$$\mathcal{E}_{Z'}(Q) = 1 - \frac{1}{2\sqrt{2}G_F} \frac{\mathcal{Q}_{Z'}}{\mathcal{Q}_W^V} \frac{g_{Z'}^{\nu V}}{Q^2 + M_{Z'}^2}. \quad (24)$$

The relevant charge in this case is expressed through the vector quark couplings $g_{Z'}^{qV}$ to the Z' boson, as [39]

$$\mathcal{Q}_{Z'} = \left(2g_{Z'}^{uV} + g_{Z'}^{dV} \right) Z + \left(g_{Z'}^{uV} + 2g_{Z'}^{dV} \right) N. \quad (25)$$

Let us mention that emerging degeneracies can be either reduced through multidetector measurements [61] or broken in the framework of NSIs [64]. For completeness we note that, despite being not present for the low energies considered here, these couplings could be changed by currently unknown in-medium effects (see, e.g., [23] and references therein).

3.2. Neutrino Sources

3.2.1. Solar Neutrinos. In terrestrial searches for dark matter candidates at low energies, the Solar neutrinos emanating from the interior of the Sun generated through various fusion reactions produce a dominant background for direct CDM detection experiments. Assuming WIMP masses less than 10 GeV, an estimated total Solar neutrino flux of about $6.5 \times 10^{11} \text{ cm}^{-2} \text{ s}^{-1}$ [65] hitting the Earth is expected to appreciably limit the sensitivity of such experiments [27]. On the other hand, the theoretical uncertainties of Solar neutrinos are presently quite large and depend strongly on the assumed Solar neutrino model. To maintain consistency with existing Solar data, in this work we consider the high metallicity Standard Solar Model (SSM) [21]. We note however that the dominant Solar neutrino component coming from the primary proton-proton channel (pp neutrinos) that accounts for about 86% the Solar neutrinos flux has been recently measured by the Borexino experiment with an uncertainty of 1% [66]. Through CE ν NS, the direct detection dark matter experiments are mainly sensitive to two sources of Solar neutrinos, namely, the ^8B and the hep neutrinos which cover the highest energy range of the Solar neutrino spectrum. Since ^8B neutrinos are generated from the decay $^8\text{B} \rightarrow ^7\text{Be}^* + e^+ + \nu_e$, while hep neutrinos from $^3\text{He} + p \rightarrow ^4\text{He} + e^+ + \nu_e$, both sources occur in the aftermath of the pp chain. Following previous similar studies [28], in this work, we explore the neutrino-floor extending our analysis to the lowest neutrino energies, by considering the pep neutrino line which belongs to the pp chain and the e^- -capture reaction on ^7Be that leads to two monochromatic beams at 384.3 and 861.3 keV as well as the well-known CNO cycle. The latter neutrinos appear as three continuous spectra (^{13}N , ^{15}O , and ^{17}F) with end point energies close to the pep neutrinos.

3.2.2. Atmospheric Neutrinos. Atmospheric neutrinos are decay products of the particles (mostly pions and kaons) produced as a result of cosmic-ray scattering in the Earth's atmosphere. The generated secondary particles decay to ν_e , $\bar{\nu}_e$, ν_μ , and $\bar{\nu}_\mu$ constituting a significant background to dark matter searches especially for WIMP masses above 100 GeV. In particular, the effect is crucial on the discovery potential of WIMPs with spin-independent cross section of the order of 10^{-48} cm^2 . The direct detection dark matter experiments, due to the lack of directional sensitivity, are in principle sensitive to the lowest energy (less than ~ 100 MeV) atmospheric neutrinos. For this reason, in our present work atmospheric neutrinos are considered by employing the low-energy flux coming out of the FLUKA code simulations [22].

3.2.3. Diffuse Supernova Neutrinos. The weak glow of MeV neutrinos emitted from the total number of core-collapse supernovae, known as the Diffuse Supernova Neutrino Background (DSNB), creates an important source of neutrino background specifically for the WIMPs mass range 10–30 GeV [24]. Despite the appreciably lower flux compared to Solar neutrinos, DSNB neutrino energies are higher than those of the Solar neutrino spectrum. In our simulations,

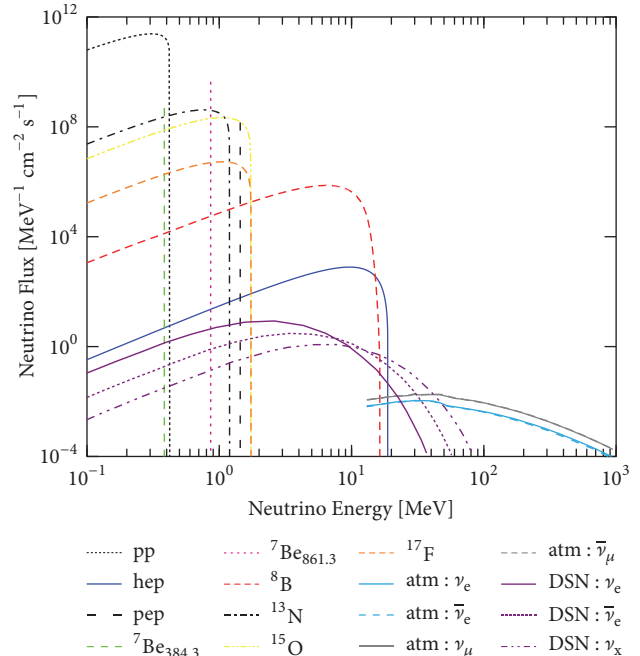


FIGURE 1: Unoscillate neutrino flux considered in the present study, including the Solar, Atmospheric, and DSNB spectra.

the adopted DSNB distributions (usually of Fermi-Dirac or power-law type) correspond to temperatures 3 MeV for ν_e , 5 MeV for $\bar{\nu}_e$, and 8 MeV for the other neutrino flavours denoted as ν_x or $\bar{\nu}_x$, $x = \mu, \tau$.

Figure 1 shows the unoscillate neutrino flux considered in the present study, illustrating the Solar neutrino spectra of the dominant neutrino sources assuming the high metallicity Standard Solar Model (SSM) as defined in [21]. Also shown is the low-energy atmospheric neutrino flux as obtained from the FLUKA simulation [22] as well as the DSNB spectrum [67]. The corresponding neutrino types, maximum energies, and fluxes are listed in Table 1.

4. Deformed Shell Model

In the formalism of the WIMP-nucleus or neutrino-nucleus event rates of Sections 2 and 3, both for the case of elastic or inelastic interaction channels, the nuclear physics and particle physics (SUSY model) parts appear almost completely separated. In the present work our main focus drops on the nuclear physics aspects which are contained in the nuclear structure factors discussed in Section 2. Special attention is paid on the factors D_i of (9) that depend on the spin structure functions and the nuclear form factors. These quantities have been calculated using the DSM method [48] (for a comprehensive discussion of DSM see [47]) given the kinematics and the assumptions describing the WIMP particles.

The construction of the many-body wave functions for the initial $|J_i^\pi\rangle$ and final $|J_f^\pi\rangle$ nuclear states in the framework of DSM involves performance of the following steps. (i) At first, one chooses a model space consisting of a given set of spherical single-particle (sp) orbits, sp energies, and the

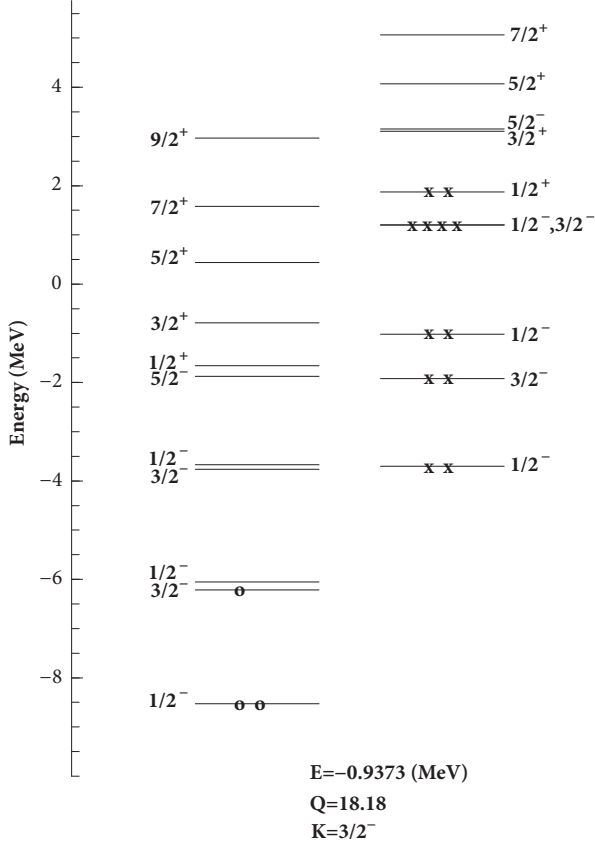


FIGURE 2: HF single-particle spectra for ^{71}Ga corresponding to the lowest prolate configuration. In the figure, circles represent protons and crosses represent neutrons. The HF energy E in MeV, the mass quadrupole moment Q in units of the square of the oscillator length parameter, and the total azimuthal quantum number K are given in the figure.

appropriate two-body effective interaction matrix elements. For ^{71}Ga and ^{75}As , the spherical sp orbits are $1p_{3/2}$, $0f_{5/2}$, $1p_{1/2}$, and $0g_{9/2}$ with energies 0.0, 2.20, 2.28, and 5.40 MeV and 0.0, 0.78, 1.08, and 3.20 MeV, respectively, while the assumed effective interaction is the modified Kuo interaction [68]. Similarly for ^{127}I , the sp orbits, their energies, and the effective interaction are taken from a recent paper [69]. (ii) Assuming axial symmetry and solving the HF single-particle equations self-consistently, the lowest-energy prolate (or oblate) intrinsic state for the nucleus in question is obtained. An example is shown in Figure 2 for ^{71}Ga . (iii) The various excited intrinsic states then are obtained by making particle-hole (p - h) excitations over the lowest-energy intrinsic state (lowest configuration). (iv) Then, because the HF intrinsic nuclear states $|\chi_K(\eta)\rangle$ (K is azimuthal quantum number and η distinguishes states with the same K) do not have definite angular momentum, angular momentum projected states $|\phi_{MK}^J(\mu)\rangle$ are constructed as

$$\begin{aligned} & |\phi_{MK}^J(\eta)\rangle \\ &= \frac{2J+1}{8\pi^2\sqrt{N_{JK}}} \int d\Omega D_{MK}^{J*}(\Omega) R(\Omega) |\chi_K(\eta)\rangle. \end{aligned} \quad (26)$$

In the previous expression, $\Omega = (\alpha, \beta, \gamma)$ represents the Euler angles, $R(\Omega)$ denotes the known general rotation operator, and the Wigner D -matrices are defined as $D_{MK}^J(\Omega) = \langle JM | R(\Omega) | JK \rangle$. Here, N_{JK} is the normalisation constant which by assuming axial symmetry is defined as

$$N_{JK} = \frac{2J+1}{2} \int_0^\pi d\beta \sin \beta d_{KK}^J(\beta) \langle \chi_K(\eta) | e^{-i\beta J_y} | \chi_K(\eta) \rangle, \quad (27)$$

where the functions $d_{KK}^J(\beta)$ are the diagonal elements of the matrix $d_{MK}^J(\beta) = \langle JM | e^{-i\beta J_y} | JK \rangle$. (v) Finally, the good angular momentum states ϕ_{MK}^J are orthonormalised by band mixing calculations and then, in terms of the index η , it is possible to distinguish between different states having the same angular momentum J ,

$$|\Phi_M^J(\eta)\rangle = \sum_{K,\alpha} S_{K\eta}^J(\alpha) |\phi_{MK}^J(\alpha)\rangle. \quad (28)$$

Within the DSM method, for the evaluation of the reduced nuclear matrix element entering (6) and (7), we first calculate the single-particle matrix elements of the relevant operators $t_v^{(l,s)J}$, as

$$\begin{aligned} & \langle n_i l_i j_i | \hat{t}^{(l,s)J} | n_k l_k j_k \rangle \\ &= \sqrt{(2j_k+1)(2j_i+1)(2J+1)(s+1)(s+2)} \\ & \times \begin{Bmatrix} l_i & \frac{1}{2} & j_i \\ l_k & \frac{1}{2} & j_k \\ l & s & J \end{Bmatrix} \langle l_i | \sqrt{4\pi Y^l} | l_k \rangle \langle n_i l_i | j_i(kr) | n_l l_k \rangle, \end{aligned} \quad (29)$$

where $\{-\}$ is the 9- j symbol. For more details, the reader is referred to [70–72]. It should be noted that in the DSM method one considers an adequate number of intrinsic states in the band mixing calculations.

DSM calculations are performed in the same spirit as in spherical shell model where one takes a model space and a suitable effective interaction (single-particle orbitals, single-particle energies, and a two-body effective interaction). This procedure has been found to be quite successful in describing the spectroscopic properties and electromagnetic properties of many nuclei in the mass region $A = 60$ – 90 and has also been applied to double beta decay nuclear transition matrix elements [47]. In addition, this model has been used recently in calculating the event rates for dark matter detection [48]. With the proper choice of effective interaction, one will not be considering core excitations. This is a standard prescription in shell model as well as in DSM. To go beyond this, one has to use no-core shell model or DSM with much larger set of single-particle orbitals (inclusion of core orbitals), such refinements are planned to be employed in future calculations.

We note that the many-body nuclear calculations performed take into account in the usual way the inert core orbits

TABLE 2: $2k$ values of the occupied proton and neutron single particle deformed orbits of the HF intrinsic states used in the calculation for each nucleus. The second column gives the serial no. of the HF intrinsic states used. All the $2k$ values are of negative parity unless explicitly shown. The (+), (-), or (\pm) sign before the $2k$ values implies that either the time-like, time-reversed, or both orbits are occupied. In columns 3 and 4, 3_1 means the first $3/2^-$ HF deformed sp orbit, 3_2 means the second $3/2^-$ deformed HF orbit, and so on (see also Figure 2). Detailed information regarding the structure each of the deformed HF sp orbits, their energies, and the parentage of each of the HF intrinsic state in the Φ^J states (e.g., the linear combination of ϕ_{MK}^J obtained in the band mixing diagonalisation) can be obtained from the authors.

Nucleus	Serial No.	proton orbits				neutron orbits					
^{71}Ga	1	$\pm 1_1$	$+3_1$	$\pm 1_1$	$\pm 1_2$	$\pm 3_1$	$\pm 3_2$	$\pm 1_3$	$\pm 1_1^+$		
	2	$\pm 1_1$	$+1_2$	$\pm 1_1$	$\pm 1_2$	$\pm 3_1$	$\pm 3_2$	$\pm 1_3$	$\pm 1_1^+$		
	3	$\pm 1_1$	-3_1	$\pm 1_1$	$\pm 1_2$	$\pm 3_1$	$\pm 3_2$	$\pm 1_3$	$+1^+$	$+3^+$	
	4	$\pm 1_1$	$+3_1$	$\pm 1_1$	$\pm 1_2$	$\pm 3_1$	$\pm 3_2$	$\pm 1_3$	$\pm 5_1$		
^{73}Ge	1	$\pm 1_1$	$\pm 1_2$	$\pm 1_1$	$\pm 1_2$	$\pm 3_1$	$\pm 3_2$	$\pm 1_3$	$\pm 1_1^+$	$+3_1^+$	
	2	$\pm 1_1$	$\pm 1_2$	$\pm 1_1$	$\pm 1_2$	$\pm 3_1$	$\pm 3_2$	$\pm 1_3$	$\pm 3_1^+$	$+1_1^+$	
	3	$\pm 1_1$	$\pm 3_1$	$\pm 1_1$	$\pm 1_2$	$\pm 3_1$	$\pm 3_2$	$\pm 1_3$	$\pm 1_1^+$	$+3_1^+$	
^{75}As	1	$\pm 1_1$	$\pm 1_2$	$+3_1$	$\pm 1_1$	$\pm 1_2$	$\pm 3_1$	$\pm 1_1^+$	$\pm 3_1^+$	$\pm 3_2$	$\pm 1_3$
	2	$\pm 1_1$	$\pm 3_1$	$+1_2$	$\pm 1_1$	$\pm 1_2$	$\pm 3_1$	$\pm 1_1^+$	$\pm 3_1^+$	$\pm 3_2$	$\pm 1_3$
	3	$\pm 1_1$	$\pm 1_2$	$+3_1$	$\pm 1_1$	$\pm 1_2$	$\pm 3_1$	$\pm 1_1^+$	$\pm 3_1^+$	$\pm 3_2$	$\pm 5_1^+$
	4	$\pm 1_1$	$\pm 3_1$	$+1_3$	$\pm 1_1$	$\pm 1_2$	$\pm 3_1$	$\pm 1_1^+$	$\pm 3_1^+$	$\pm 3_2$	$\pm 5_1^+$
	5	$\pm 1_1$	$\pm 1_2$	$+3_1$	$\pm 1_1$	$\pm 1_2$	$\pm 3_1$	$\pm 1_1^+$	$\pm 3_1^+$	$\pm 3_2$	$\pm 5_1$
	6	$\pm 1_1$	$\pm 3_1$	$+1_2$	$\pm 1_1$	$\pm 1_2$	$\pm 3_1$	$\pm 1_1^+$	$\pm 3_1^+$	$\pm 3_2$	$\pm 5_1$
^{127}I	1	$\pm 7_1^+$	$+5_1^+$	$\pm 7_1^+$	$\pm 5_1^+$	$\pm 3_1^+$	$\pm 11_1$	$\pm 1_1^+$	$\pm 5_2^+$	$\pm 9_1$	
				$\pm 3_2^+$	$\pm 1_2^+$	$\pm 7_1$	$\pm 5_1$	$\pm 3_1$			
	2	$\pm 7_1^+$	$+5_1^+$	$\pm 7_1^+$	$\pm 5_1^+$	$\pm 3_1^+$	$\pm 11_1$	$\pm 1_1^+$	$\pm 5_2^+$	$\pm 9_1$	
				$\pm 3_2^+$	$\pm 1_2^+$	$\pm 7_1$	$\pm 5_1$	$\pm 3_3^+$			
	3	$\pm 7_1^+$	$+3_1^+$	$\pm 7_1^+$	$\pm 5_1^+$	$\pm 3_1^+$	$\pm 11_1$	$\pm 1_1^+$	$\pm 5_2^+$	$\pm 9_1$	
				$\pm 3_2^+$	$\pm 1_2^+$	$\pm 7_1$	$\pm 5_1$	$\pm 3_1$			
4	$\pm 7_1^+$	$+3_1^+$	$\pm 7_1^+$	$\pm 5_1^+$	$\pm 3_1^+$	$\pm 11_1$	$\pm 1_1^+$	$\pm 5_2^+$	$\pm 9_1$		
			$\pm 3_2^+$	$\pm 1_2^+$	$\pm 7_1$	$\pm 5_1$	$\pm 3_3^+$				
5	$\pm 7_1^+$	$+1_1^+$	$\pm 7_1^+$	$\pm 5_1^+$	$\pm 3_1^+$	$\pm 11_1$	$\pm 1_1^+$	$\pm 5_2^+$	$\pm 9_1$		
			$\pm 3_2^+$	$\pm 1_2^+$	$\pm 7_1$	$\pm 5_1$	$\pm 3_1$				
6	$\pm 7_1^+$	$+1_1^+$	$\pm 7_1^+$	$\pm 5_1^+$	$\pm 3_1^+$	$\pm 11_1$	$\pm 1_1^+$	$\pm 5_2^+$	$\pm 9_1$		
			$\pm 3_2^+$	$\pm 1_2^+$	$\pm 7_1$	$\pm 5_1$	$\pm 3_3^+$				

(completely filled by the protons and neutrons) and the extra-core nucleons moving in the assumed model space under the influence of an effective interaction. The explicit $2k$ values of the occupied nucleon single-particle deformed orbits of the HF intrinsic states considered in our calculations are listed in Table 2.

5. Results and Discussion

5.1. Nuclear Physics Aspects. To maximise the significance of our WIMP-nucleus and neutrino-floor calculations, the reliability of the obtained nuclear wave functions is tested by comparing the extracted energy level spectrum and magnetic moments with available experimental data. The consistency of this method obtained for ^{73}Ge has been already presented in [48]. Furthermore, in the DSM calculations for ^{71}Ga and ^{75}As , we restrict ourselves to prolate solutions only, since the oblate solution does not reproduce the energy spectra and electromagnetic properties of these nuclei. It also does not mix with the prolate solution. Hence, we neglect the oblate solutions in the calculations. For each of these nuclei, we consider only four intrinsic prolate states which should be

sufficient to explain the systematics of the ground state and close lying excited state. Due to size restrictions, in Figure 3 we illustrate only the calculated spectrum for ^{71}Ga .

For ^{75}As , the ground state is $3/2^-$ and there are also two $1/2^-$ and $3/2^-$ levels around 0.12 MeV. In addition, there is a collective band consisting of $5/2^-$, $9/2^-$, and $13/2^-$ $17/2^-$ levels at 0.279, 1.095, 2.150, and 3.091 MeV, respectively. All these levels are well reproduced by the DSM method. Turning to the ^{127}I spectrum, there are four observed collective bands with band heads $5/2^+$, $(7/2^+)_{1,2}$, and $9/2^+$. There are evidences suggesting that low-lying states in ^{127}I have oblate deformation [73]. Hence, for this nucleus, we consider only oblate configurations and take the six lowest oblate intrinsic states in the band mixing calculation. These intrinsic states are found to provide adequate description of the energy spectrum and electromagnetic properties for this nucleus. The calculations for this nucleus utilise a new effective interaction developed by an Italian group very recently [69]. The new effective interaction is seen to reproduce well the ^{127}I spectrum; details will be presented elsewhere.

We thus conclude that concerning the evaluation of the WIMP-nucleus and CE ν NS event rates we are interested in

TABLE 3: List of potential dark matter detectors considered in the present study. The calculated magnetic moments for the ground states of ^{71}Ga , ^{73}Ge , ^{75}As , and ^{127}I are shown. The results involve the bare gyromagnetic ratios and experimental data are from [44]. The ground state J^π and the harmonic oscillator size b are also shown.

Nucleus	A	Z	J^π	$\langle I_p \rangle$	$\langle S_p \rangle$	$\langle I_n \rangle$	$\langle S_n \rangle$	μ (nm)	Exp	b [fm^{-1}]
Ga	71	31	$3/2^-$	0.863	0.257	0.369	0.011	2.259	2.562	1.90
Ge	73	32	$9/2^+$	0.581	-0.001	3.558	0.362	-0.811	-0.879	1.91
As	75	33	$(3/2^-)_1$	0.667	0.164	0.626	0.042	1.422	1.439	1.92
I	127	53	$5/2^+$	2.395	-0.211	0.313	2.343	1.207	2.813	2.09

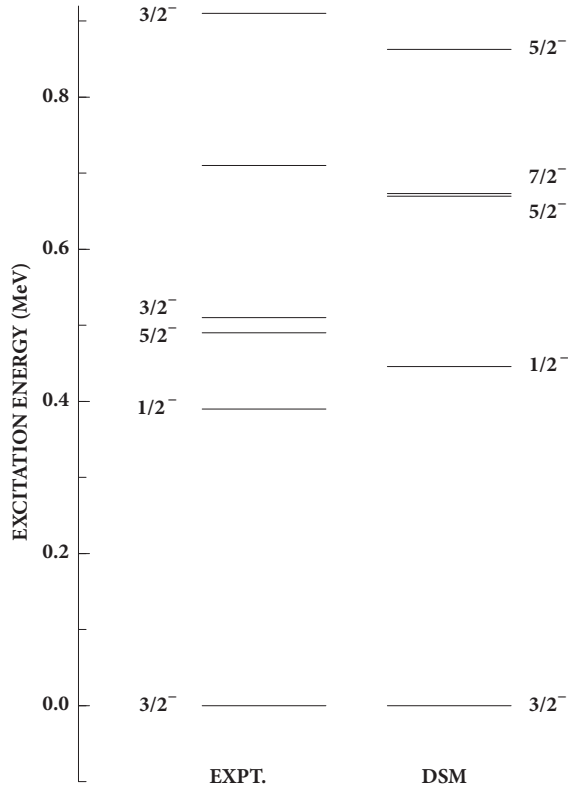


FIGURE 3: Comparison of deformed shell model results with experimental data for ^{71}Ga for low-lying states. The experimental values are taken from [44].

this work, the required ground state wave functions obtained through the DSM method are reliable and the intrinsic states used in the subsequent analysis are considered sufficient. From the perspective of nuclear physics, spin contributions constitute significant ingredients in the evaluation of WIMP-nucleus event rates. For this reason, the first stage of our work involves the calculation of the magnetic moment, which is decomposed into an orbital and spin part. The relevant results for the proton and neutron contributions to the orbital and spin parts concerning the ground states of the four nuclear isotopes studied in this paper are given in Table 3. A comparison between the obtained magnetic moments and the respective experimental data is also provided. Despite the fact that these calculations adopt bare values of g -factors neglecting quenching effects, the obtained DSM results of the ground state magnetic moments are consistent with the experimental values.

Having successfully reproduced the energy spectrum and the magnetic moments within the context of the DSM wave functions, we evaluate important nuclear physics inputs entering the WIMP-nucleus and $\text{CE}\nu\text{NS}$ cross sections. Figures 4 and 5 present a comparison between the DSM nuclear form factors and the effective Helm-type ones employed in various similar studies, where, as can be seen, the DSM results differ from the Helm-type ones. The behaviour of the proton form factor for ^{71}Ga is found to be different from those of the other nuclei and this may be due to the nearby proton shell closure and the neutron subshell closure. Calculations with several different effective interactions are under way to rule out the possibility of any deficiency of the effective two-body interaction used. We furthermore illustrate the spin structure functions of WIMP- ^{71}Ga elastic scattering calculated using (6) and (7). The variation of F_{00} , F_{01} , and F_{11} with respect to the parameter u is shown in Figure 6, while similar results are obtained for ^{75}As and ^{127}I (for the ^{73}Ge case see [48]).

The consistency of our nuclear physics DSM calculations has been extensively explored in this work and compared with existing experimental data (see Figures 2 and 3 and Table 3) making the considered form factors reliable. Specifically we have tested the reliability of this model to describe nuclear structure properties such as excitation spectra and nuclear magnetic moments. We mention that DSM has been tested in the past in many nuclei in the $A = 60\text{--}90$ region [47] (see above).

5.2. WIMP-Nucleus Rates and the Neutrino-Floor. The WIMP-nucleus event rates and the neutrino-floor due to neutrino-nucleus scattering are calculated for a set of interesting nuclear targets such as ^{71}Ga , ^{73}Ge , ^{75}As , and ^{127}I (see Table 3). In evaluating the neutrino-induced backgrounds, we consider only the dominant $\text{CE}\nu\text{NS}$ channel, since neutrino-electron events are expected to produce less events by about one order of magnitude [27]. For the case of a ^{71}Ga target, in Figure 7 we provide the coefficients D_i associated with the spin dependent and coherent interactions given in (9) as functions of the WIMP mass m_χ by assuming three typical values of the detector threshold energy $T_N = 0, 5, 10$ keV. For the special case of $T_N = 0$, all plots peak at $m_\chi \sim 35$ GeV, while for higher threshold energies D_i are shifted towards higher values of the WIMP mass. The calculations take also into account the annual modulation which is represented by the curve thickness. As can be seen from the figure, the modulation signal varies with respect to the WIMP mass, being larger for $m_\chi \leq 50$ GeV, while its magnitude is slightly different for the spin dependent and coherent channels.

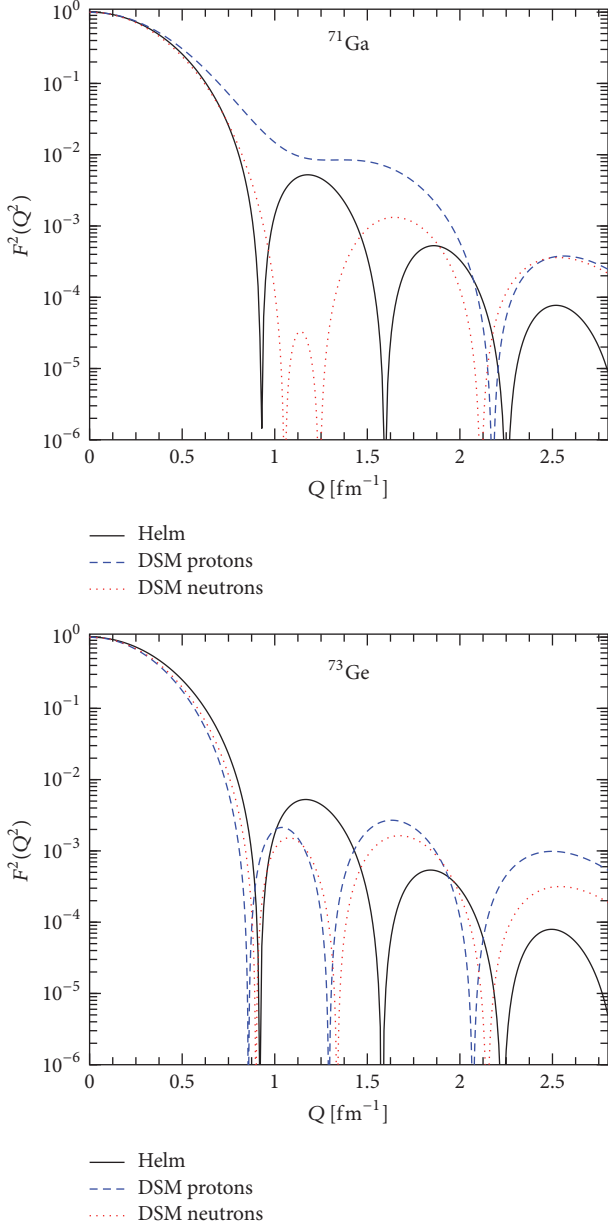


FIGURE 4: Comparison of the DSM nuclear form factors of the ^{71}Ga and ^{73}Ge isotopes, obtained in the present work with the corresponding effective Helm form factors.

Proceeding further, in Figure 8 we evaluate the expected event rates for the four target nuclei assuming elastic WIMP scattering for WIMP candidates with mass $m_\chi = 110$ GeV, by adopting the nucleonic-current parameters $f_A^0 = 3.55 \times 10^{-2}$, $f_A^1 = 5.31 \times 10^{-2}$, $f_S^0 = 8.02 \times 10^{-4}$, and $f_S^1 = -0.15 \times f_S^0$. As in the previous discussion, the thickness of the graph accounts for the annual modulation. We find that there is a strong dependence of the event rate on the studied nuclear isotope. Again the modulation is found to decrease for heavier mass. Among the four studied nuclei, we come out with a larger event rate for the case of a ^{71}Ga nuclear detector, since D_1 , D_2 , and D_3 are all positive and have similar values. For ^{73}Ge ,

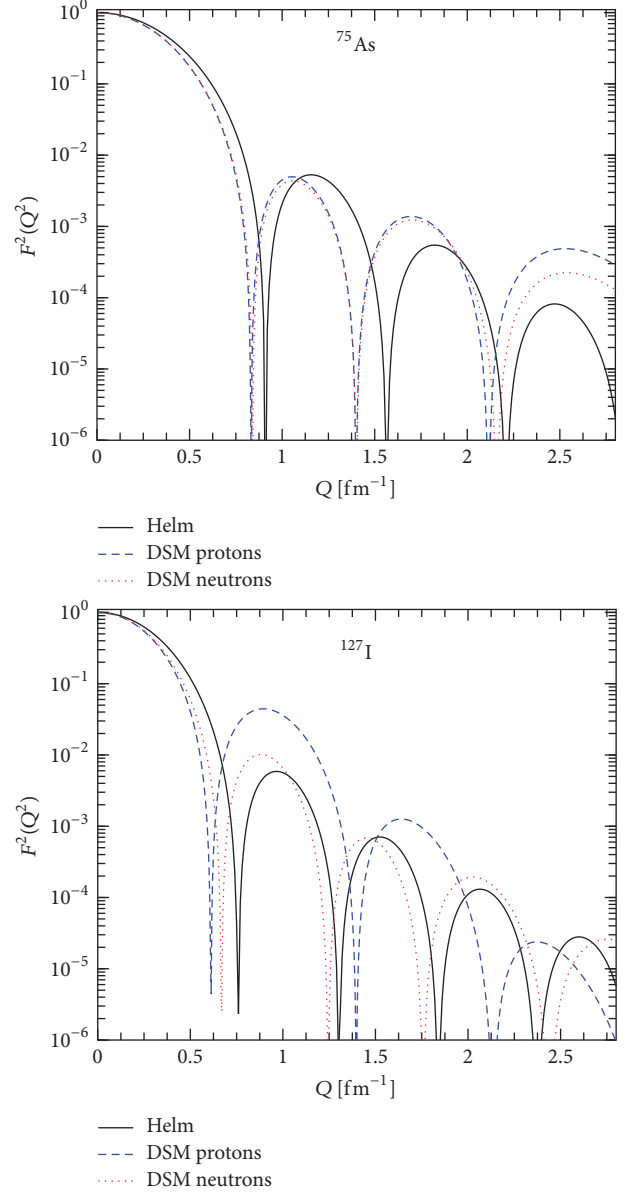


FIGURE 5: Same as in Figure 4 but for the ^{75}As and ^{127}I isotopes.

D_2 is negative and its magnitude is comparable to D_1 and D_3 , while for ^{75}As , D_3 is positive but small, and finally for ^{127}I , D_2 and D_3 are relatively smaller and D_1 is large. The coherent contribution D_4 has more or less similar values for all nuclei considered.

For each component of the Solar, Atmospheric, and DSNB neutrino distributions we calculate the expected neutrino-floor due to $\text{CE}\nu\text{NS}$, by considering the target nuclei presented in Table 3. In our calculations, we neglect possible recoil events arising from Geoneutrinos as they are expected to be at least one order of magnitude less than the aforementioned neutrino sources (see, e.g., [25, 26]). In order to make a quantitative estimate of the neutrino-floor, here we do not consider neutrino oscillations and we assume that $\text{CE}\nu\text{NS}$ is a flavour blind process in the SM. The

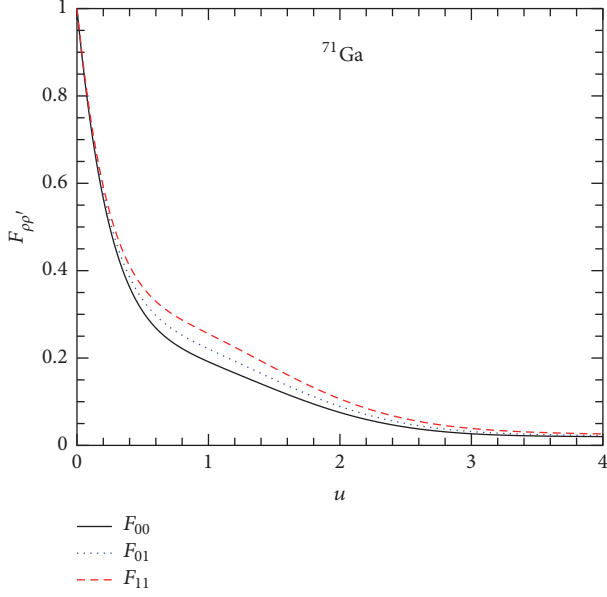


FIGURE 6: Normalised spin structure functions of ^{71}Ga for the ground state.

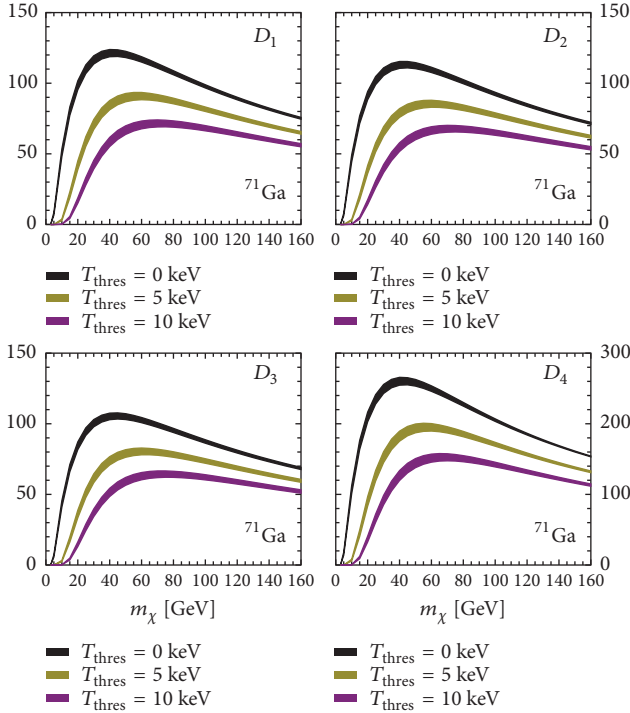


FIGURE 7: Nuclear structure coefficients D_i for ^{71}Ga plotted as a function of the WIMP mass. The graphs are plotted for three values of the detector threshold 0, 5, and 10 keV. The thickness of the graphs represents annual modulation.

differential event rate due to $\text{CE}\nu\text{NS}$, for the various dark matter detectors considered in the present study, is presented in Figure 9. It can be noticed that the neutrino background is dominated by Solar neutrinos at very low recoil energies. We stress that, for the typical keV-recoil thresholds of the

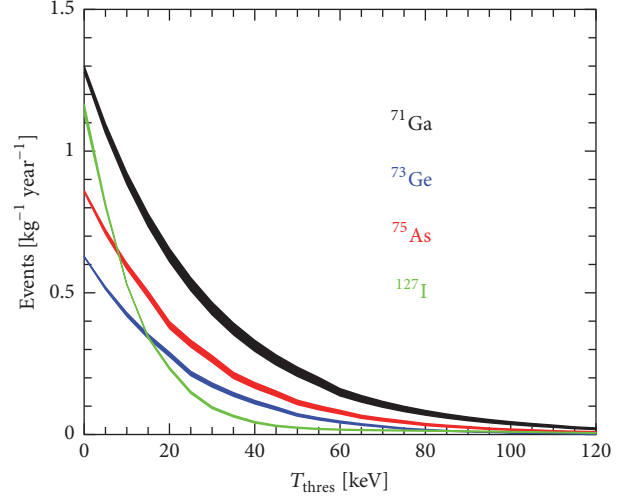


FIGURE 8: The WIMP event rates for ^{71}Ga , ^{73}Ge , ^{75}As , and ^{127}I detectors in units of $\text{kg}^{-1}\text{year}^{-1}$ as a function of the detector threshold T_N . The nuclear threshold T_N energy through the limit of the integration in (9). The thickness of the curve represents the annual modulation which decreases with increasing nuclear mass.

current direct detection dark matter experiments only the hep and ^8B sources constitute a possibly detectable background. From our results we conclude that, for recoil energies above about 10 keV, Atmospheric neutrinos dominate the neutrino background event rates, having a tiny contribution coming from the DSNB spectrum.

The number of expected background events due to $\text{CE}\nu\text{NS}$ for each component of the Solar, Atmospheric, and DSNB neutrino fluxes is illustrated in Figure 10. Similar to the differential event case, at low energies the neutrino background is dominated by the Solar neutrino spectrum with the dominant components being the hep and ^8B neutrino sources. The results imply that future multi-ton scale detectors with sub-keV sensitivities may be also sensitive to ^7Be and pp neutrinos. We comment however that such sensitivities will be further limited due to the quenching effect of the nuclear recoil spectrum which is not taken into account here. Moreover, it is worth mentioning that neutrino-induced and WIMP-nucleus scattering processes provide similar recoil spectra; e.g., the recoil spectrum of ^8B neutrinos may mimic that of a WIMP with mass 6 GeV (100 MeV) [28].

At this point, we consider additional interactions in the context of new physics beyond the SM that may enhance the $\text{CE}\nu\text{NS}$ rate at a direct detection dark matter experiment. Specifically we study the impact of neutrino EM properties as well as the impact of new interactions due to a Z' mediator, on the neutrino floor. In our calculations we assume the existence of a neutrino magnetic moment $\mu_\nu = 4.3 \times 10^{-9} \mu_B$, extracted from $\text{CE}\nu\text{NS}$ data in [41] as well as the corresponding limit from $\bar{\nu}_e - e^-$ scattering data of the GEMMA experiment, e.g., $\mu_{\bar{\nu}_e} = 2.9 \times 10^{-11} \mu_B$ [74]. Regarding the Z' interaction we consider typical values such as $M'_{Z'} = 10 \text{ MeV}$, $g'^2_{Z'} = 10^{-6}$, and $M'_{Z'} = 1 \text{ GeV}$, $g'^2_{Z'} = 10^{-6}$

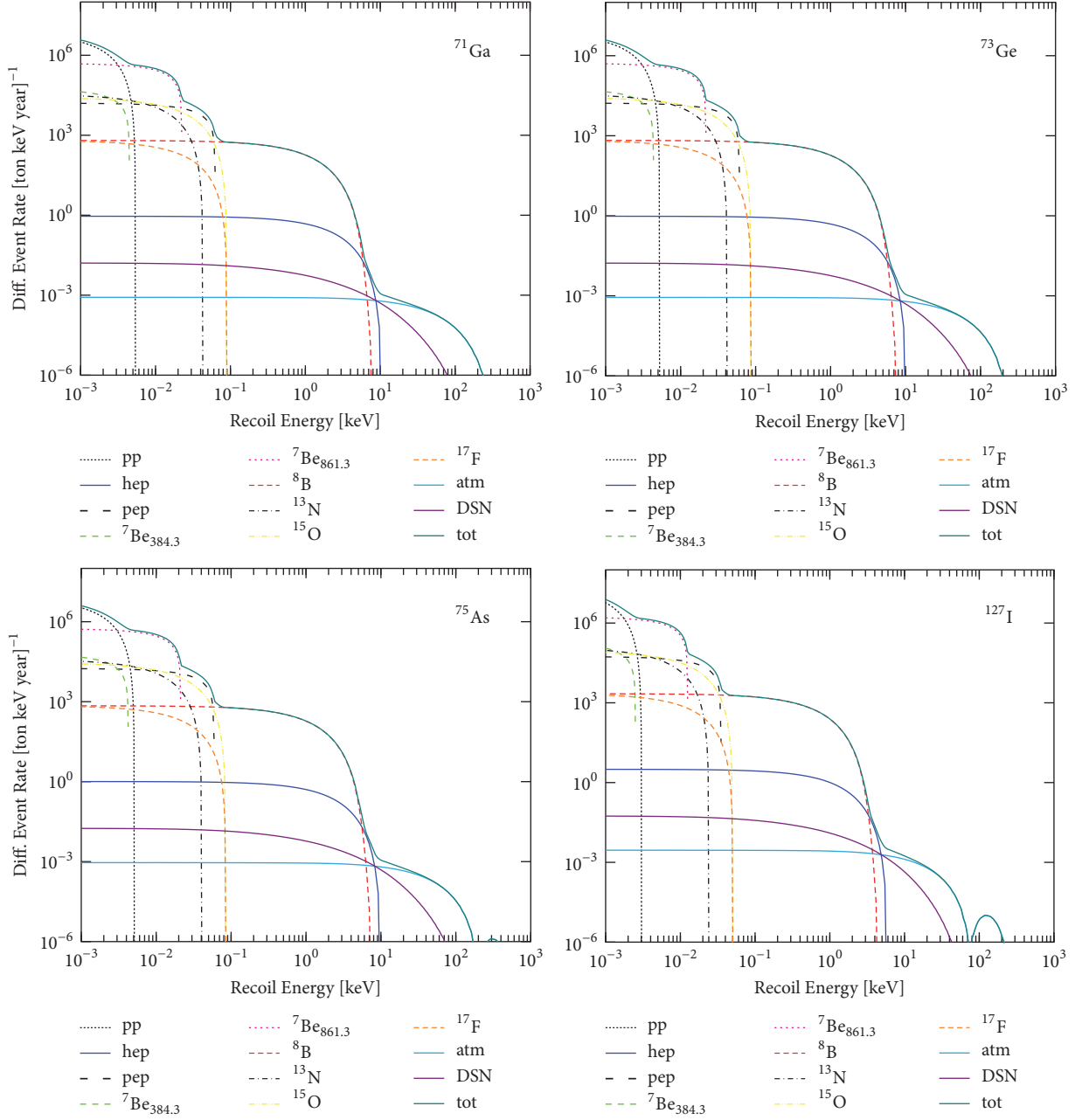


FIGURE 9: Differential event rate of the neutrino-floor assuming ^{71}Ga , ^{73}Ge , ^{75}As , and ^{127}I as cold dark matter detectors. The individual components coming from the Solar, Atmospheric, and DSNB flux are also shown.

[75]. Following [64], by assuming universal couplings, our calculations involve the product of neutrino and quark Z' couplings defined as (for a comprehensive study involving the flavour dependence of the Z' couplings the reader is referred to [76])

$$g_{Z'}^2 = \frac{g_{Z'}^{\nu} Q_{Z'}}{3A}. \quad (30)$$

The corresponding results are presented in Figure 11, indicating that such new physics phenomena may constitute a crucial source of background even for multi-ton scale detectors with sub-keV capabilities. We stress, however, that the

latter conclusion depends largely on the assumed parameters, which currently are unknown.

Before closing, we estimate the difference in the calculated number of neutrino-floor events between the conventional Helm-type and DSM predictions by defining the ratio

$$\mathcal{R} = \frac{\text{DSM}_{\text{events}}}{\text{Helm}_{\text{events}}}. \quad (31)$$

For each nuclear system, the corresponding results are presented in Figure 12 indicating that the differences can become significant, especially in the high energy tail of the detected recoil spectrum.

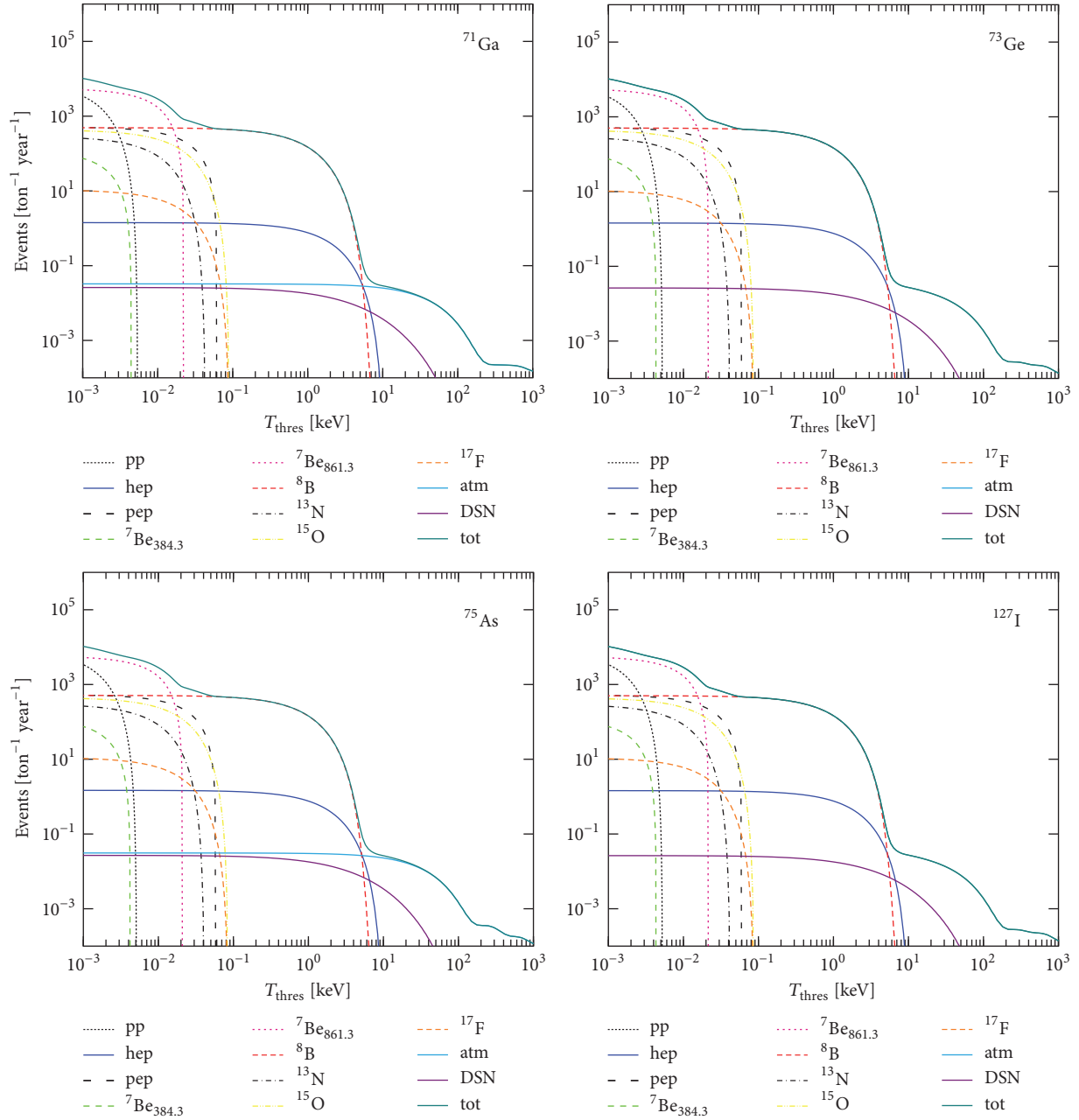


FIGURE 10: Same as in Figure 9 but for the number of events above the detector threshold.

6. Conclusions

In this work, we studied comprehensively the expected event rates in WIMP-nucleus and neutrino-floor processes by performing reliable calculations for a set of prominent nuclear materials of direct dark matter detection experiments. The detailed calculations involve crucial nuclear physics inputs in the framework of the deformed shell model based on Hartree-Fock nuclear states. This way, the nuclear deformation and the spin structure effects of odd- A isotopes that play significant role in searching for dark matter candidates are incorporated. The chosen nuclear detectors involve popular nuclear isotopes in dark matter investigations such as the ^{71}Ga , ^{73}Ge ,

^{75}As , and ^{127}I isotopes. The DSM results indicate that ^{71}Ga needs further investigation by employing another effective two-body interaction than the one used in the chosen set of nuclear isotopes.

The deformed shell model (DSM) employed for the nuclear structure calculations in this work is very well tested in many examples in the past [47] for nuclei with $A=60-90$. Therefore, in our study we have chosen the dark matter candidates ^{71}Ga , ^{73}Ge , and ^{75}As . In addition, to extend DSM to heavier nuclei of interest in dark matter detection, we have considered ^{127}I and the results, reported in the present paper, are quite encouraging. In the near future we will consider Xe isotopes that are also of current interest. For lighter candidate

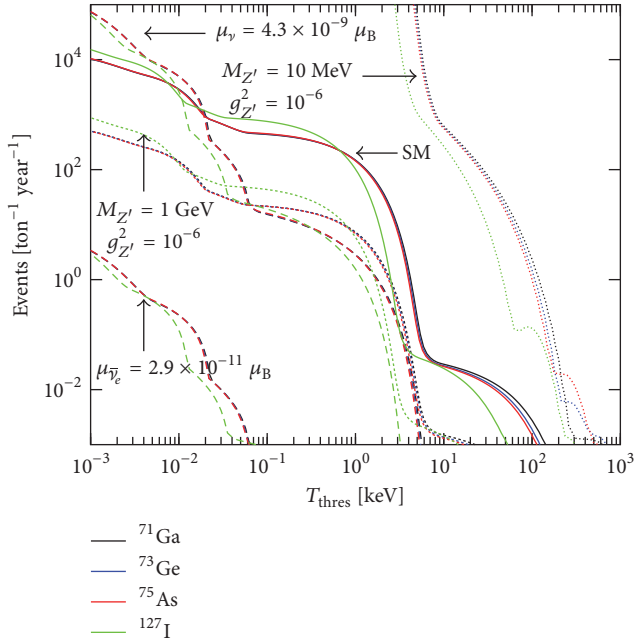


FIGURE 11: The neutrino-floor for various interaction channels. Solid, dashed, and dotted lines correspond to SM, EM, and Z' contributions, respectively.

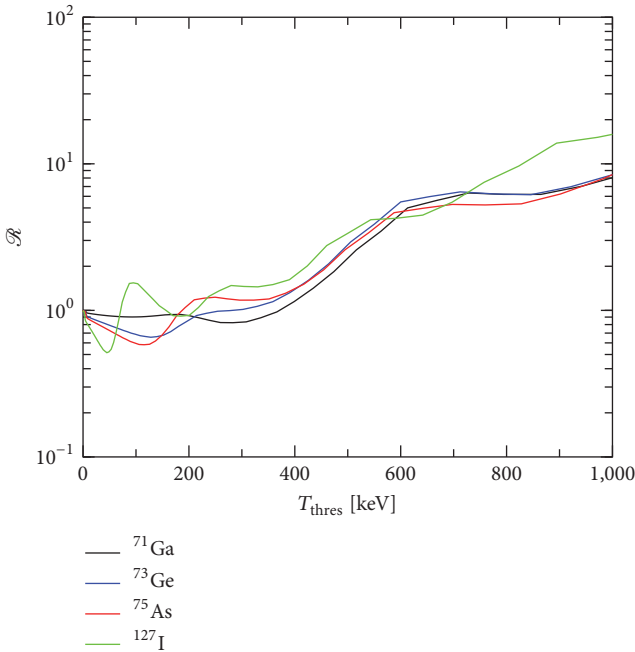


FIGURE 12: The ratio \mathcal{R} as a function of the detector threshold.

nuclei, such as Na, Si, and Ar, clearly shell model will be better choice and DSM may also be tested for these isotopes.

More importantly, by exploiting the expected neutrino-floor due to Solar, Atmospheric, and DSNB neutrinos, which constitute an important source of background to dark matter searches, the impacts of new physics CE ν NS contributions based on novel electromagnetic neutrino properties and Z'

mediator bosons have been estimated and discussed. Our results also indicate that the addressed novel contributions may lead to a distortion of the expected recoil spectrum that could limit the sensitivity of upcoming WIMP searches. Such aspects could also provide key information concerning existing anomalies in B -meson decay at the LHCb experiment [77] and offer new insights into the LMA-Dark solution [78, 79].

Finally, the present results indicate that the addressed nuclear effects may become significant, leading to alterations especially in the high energy tail of the expected neutrino-floor as described by effective nuclear calculations, thus motivating further studies in the context of advanced nuclear physics methods such as the deformed shell model or the Quasiparticle Random Phase approximations and others. Such a comprehensive study using available data of the COHERENT experiment is under way and will be presented elsewhere.

Data Availability

The data used to support the findings of this study are available from the corresponding author upon request.

Conflicts of Interest

The authors declare that they have no conflicts of interest.

Acknowledgments

R. Sahu is thankful to SERB of Department of Science and Technology (Government of India) for financial support. D. K. Papoulias is grateful to Professor Naumov for stimulating discussions.

References

- [1] G. Jungman, M. Kamionkowski, and K. Griest, "Supersymmetric dark matter," *Physics Reports*, vol. 267, no. 5-6, pp. 195–373, 1996.
- [2] G. Hinshaw, D. Larson, E. Komatsu et al., "Nine-Year Wilkinson Microwave Anisotropy Probe (WMAP) Observations: Cosmological Parameter Results," *The Astrophysical Journal Supplement Series*, vol. 208, p. 19, 2013.
- [3] G. F. Smoot, C. L. Bennett, and A. Kogut, "Structure in the COBE differential microwave radiometer first-year maps," *The Astrophysical Journal*, vol. 396, no. 1, pp. L1–L5, 1992.
- [4] P. A. R. Ade, N. Aghanim, M. Arnaud et al., "Planck 2015 results. XIII. Cosmological parameters," *Astronomy & Astrophysics*, vol. A13, p. 594, 2016.
- [5] S. Das, T. Louis, M. R. Nolta et al., "The Atacama Cosmology Telescope: Temperature and Gravitational Lensing Power Spectrum Measurements from Three Seasons of Data," *Journal of Cosmology and Astroparticle Physics*, vol. 2014, no. 04, p. 14, 2014.
- [6] E. M. George, C. L. Reichardt, K. A. Aird et al., "A measurement of secondary cosmic microwave background anisotropies from the 2500-square-degree SPT-SZ survey," *The Astrophysical Journal*, vol. 799, p. 177, 2015, <https://arxiv.org/abs/1408.3161>.

- [7] E. Gawiser, “Extracting Primordial Density Fluctuations,” *Science*, vol. 280, no. 5368, pp. 1405–1411.
- [8] T. S. Kosmas and J. D. Vergados, “Cold dark matter in SUSY theories: the role of nuclear form factors and the folding with the LSP velocity,” *Physical Review D: Particles, Fields, Gravitation and Cosmology*, vol. 55, no. 4, pp. 1752–1764, 1997.
- [9] G. Bertone, D. Hooper, and J. Silk, “Particle dark matter: evidence, candidates and constraints,” *Physics Reports*, vol. 405, no. 5–6, pp. 279–390, 2005.
- [10] M. Kortelainen, T. Kosmas, J. Suhonen, and J. Toivanen, “Event rates for CDM detectors from large-scale shell-model calculations,” *Physics Letters B*, vol. 632, no. 2–3, pp. 226–232, 2006.
- [11] J. L. Feng, “Dark Matter Candidates from Particle Physics and Methods of Detection,” *Annual Review of Astronomy and Astrophysics*, vol. 48, p. 495, 2010, <https://arxiv.org/abs/1003.0904>.
- [12] A. L. Fitzpatrick, W. Haxton, E. Katz, N. Lubbers, and Y. Xu, “The effective field theory of dark matter direct detection,” *Journal of Cosmology and Astroparticle Physics*, vol. 2013, no. 02, pp. 004–004, 2013.
- [13] J. Vergados, F. Avignone, P. Pirinen, P. Srivastava, M. Kortelainen, and J. Suhonen, “Theoretical direct WIMP detection rates for transitions to the first excited state in,” *Physical Review D: Particles, Fields, Gravitation and Cosmology*, vol. 92, no. 1, 2015.
- [14] P. C. Divari, T. S. Kosmas, J. D. Vergados, and L. D. Skouras, “Shell model calculations for light supersymmetric particle scattering off light nuclei,” *Physical Review C: Nuclear Physics*, vol. 61, no. 5, 2000.
- [15] E. Holmlund, M. Kortelainen, T. S. Kosmas, J. Suhonen, and J. Toivanen, “Microscopic calculation of the LSP detection rates for the ^{71}Ga , ^{73}Ge and ^{127}I dark-matter detectors,” *Physics Letters B*, vol. 584, no. 1–2, pp. 31–39, 2004.
- [16] D. S. Akerib and CDMS Collaboration, “Exclusion Limits on the WIMP-Nucleon Cross-Section from the First Run of the Cryogenic Dark Matter Search in the Soudan Underground Lab,” *Physical Review D*, vol. 72, Article ID 052009, 2005, <https://arxiv.org/abs/astro-ph/0507190>.
- [17] A. Broniatowski and EDELWEISS Collaboration, “A new high-background-rejection dark matter Ge cryogenic detector,” *Physics Letters B*, vol. 681, no. 4, pp. 305–309, 2009.
- [18] K. Freese, M. Lisanti, and C. Savage, “Annual Modulation of Dark Matter: A Review,” *Reviews of Modern Physics*, vol. 85, no. 4, pp. 1561–1581, 2013.
- [19] D. S. Akerib, S. Alsum, H. M. Araújo et al., “Results from a search for dark matter in the complete LUX exposure,” *Physical Review Letters*, vol. 118, Article ID 021303, 2017, <https://arxiv.org/abs/1608.07648>.
- [20] C. Fu and PandaX-II Collaboration, “Spin-Dependent Weakly-Interacting-Massive-Particle-Nucleon Cross Section Limits from First Data of PandaX-II Experiment,” *Physical Review Letters*, vol. 118, Article ID 071301, 2017, [Erratum: *Physical Review Letters*, vol. 120, no.4, Article ID 049902, 2018].
- [21] W. C. Haxton, R. G. Hamish Robertson, and A. M. Serenelli, “Solar Neutrinos: Status and Prospects,” *Annual Review of Astronomy and Astrophysics*, vol. 51, p. 21, 2013, <https://arxiv.org/abs/1208.5723>.
- [22] G. Battistoni, A. Ferrari, T. Montaruli, and P. R. Sala, “The atmospheric neutrino flux below 100 MeV: The FLUKA results,” *Astroparticle Physics*, vol. 23, no. 5, pp. 526–534, 2005.
- [23] K. C. Y. Ng, J. F. Beacom, A. H. G. Peter, and C. Rott, “Solar atmospheric neutrinos: A new neutrino floor for dark matter searches,” *Physical Review D: Particles, Fields, Gravitation and Cosmology*, vol. 96, Article ID 103006, 2017.
- [24] J. F. Beacom, “The Diffuse Supernova Neutrino Background,” *Annual Review of Nuclear and Particle Science*, vol. 60, pp. 439–462, 2010.
- [25] J. Monroe and P. Fisher, “Neutrino backgrounds to dark matter searches,” *Physical Review D*, vol. 76, Article ID 033007, 2007.
- [26] G. B. Gelmini, V. Takhistov, and S. J. Witte, “Casting a wide signal net with future direct dark matter detection experiments,” *Journal of Cosmology and Astroparticle Physics*, 2018.
- [27] J. Billard, E. Figueroa-Feliciano, and L. Strigari, “Implication of neutrino backgrounds on the reach of next generation dark matter direct detection experiments,” *Physical Review D: Particles, Fields, Gravitation and Cosmology*, vol. 89, no. 2, Article ID 023524, 2014.
- [28] C. A. O’Hare, “Dark matter astrophysical uncertainties and the neutrino floor,” *Physical Review D*, vol. 94, Article ID 063527, 2016.
- [29] J. B. R. Battat et al., “Readout technologies for directional WIMP Dark Matter detection,” *Physics Reports*, vol. 662, pp. 1–46, 2016.
- [30] D. Z. Freedman, “Coherent effects of a weak neutral current,” *Physical Review D: Particles, Fields, Gravitation and Cosmology*, vol. 9, no. 5, pp. 1389–1392, 1974.
- [31] V. A. Bednyakov and D. V. Naumov, “Coherency and incoherency in neutrino-nucleus elastic and inelastic scattering,” <https://arxiv.org/abs/1806.08768>.
- [32] D. Akimov et al., “Observation of coherent elastic neutrino-nucleus scattering,” *Science*, vol. 357, pp. 1123–1126, 2017.
- [33] D. K. Papoulias and T. S. Kosmas, “Nuclear aspects of neutral current non-standard ν -nucleus reactions and the role of the exotic $\mu^- \rightarrow e^-$ transitions experimental limits,” *Physics Letters B*, vol. 728, p. 482, 2014.
- [34] P. Coloma, M. C. Gonzalez-Garcia, M. Maltoni, and T. Schwetz, “A COHERENT enlightenment of the neutrino Dark Side,” *Physical Review D*, vol. 96, Article ID 115007, 2017.
- [35] D. Aristizabal Sierra, N. Rojas, and M. H. G. Tytgat, “Neutrino non-standard interactions and dark matter searches with multi-ton scale detectors,” <https://arxiv.org/abs/1712.09667>.
- [36] D. Papoulias and T. Kosmas, “Standard and Nonstandard Neutrino-Nucleus Reactions Cross Sections and Event Rates to Neutrino Detection Experiments,” *Advances in High Energy Physics*, vol. 2015, Article ID 763648, 17 pages, 2015.
- [37] T. S. Kosmas, O. G. Miranda, D. K. Papoulias, M. Tortola, and J. W. F. Valle, “Probing neutrino magnetic moments at the Spallation Neutron Source facility,” *Physical Review D*, vol. 92, Article ID 013011, 2015.
- [38] T. S. Kosmas, O. G. Miranda, D. K. Papoulias, M. Tortola, and J. W. F. Valle, “Sensitivities to neutrino electromagnetic properties at the TEXONO experiment,” *Physics Letters B*, vol. 750, p. 459, 2015.
- [39] E. Bertuzzo, F. F. Deppisch, S. Kulkarni, Y. F. Perez Gonzalez, and R. Z. Funchal, “Dark matter and exotic neutrino interactions in direct detection searches,” *Journal of High Energy Physics*, vol. 2017, no. 4, 2017.
- [40] J. B. Dent, B. Dutta, J. L. Newstead, and L. E. Strigari, “Dark matter, light mediators, and the neutrino floor,” *Physical Review D: Particles, Fields, Gravitation and Cosmology*, vol. 95, no. 5, 2017.

- [41] D. Papoulias and T. Kosmas, “COHERENT constraints to conventional and exotic neutrino physics,” *Physical Review D: Particles, Fields, Gravitation and Cosmology*, vol. 97, no. 3, 2018.
- [42] A. Cisterna, T. Delsate, L. Ducobu, and M. Rinaldi, “Sensitivity to Z-prime and nonstandard neutrino interactions from ultralow threshold neutrino-nucleus coherent scattering,” *Physical Review D*, vol. 93, Article ID 013015, 2016.
- [43] L. E. Strigari, “Neutrino floor at ultralow threshold,” *Physical Review D*, vol. 93, Article ID 103534, 2016.
- [44] <http://www.nndc.bnl.gov/ensdf>.
- [45] S. Gardner and G. Fuller, “Dark matter studies entrain nuclear physics,” *Progress in Particle and Nuclear Physics*, vol. 71, pp. 167–184, 2013.
- [46] T. S. Kosmas, A. Faessler, and R. Sahu, “Transition matrix elements for,” *Physical Review C: Nuclear Physics*, vol. 68, no. 5, 2003.
- [47] V. K. B. Kota and R. Sahu, *Structure of Medium Mass Nuclei: Deformed Shell Model and Spin-Isospin Interacting Boson Model*, CRC Press, 2016.
- [48] R. Sahu and V. K. Kota, “Deformed shell model study of event rates for WIMP-73Ge scattering,” *Modern Physics Letters A*, vol. 32, no. 38, p. 1750210, 2017.
- [49] P. Pirinen, P. Srivastava, J. Suhonen, and M. Kortelainen, “Shell-model study on event rates of lightest supersymmetric particles scattering off,” *Physical Review D: Particles, Fields, Gravitation and Cosmology*, vol. 93, no. 9, 2016.
- [50] P. Toivanen, M. Kortelainen, J. Suhonen, and J. Toivanen, “Large-scale shell-model calculations of elastic and inelastic scattering rates of lightest supersymmetric particles (LSP) on I-127, Xe-129, Xe-131, and Cs-133 nuclei,” *Physical Review C*, vol. 79, Article ID 044302, 2009.
- [51] J. D. Vergados and T. S. Kosmas, “Searching for Cold Dark Matter. A case of coexistence of Supersymmetry and Nuclear Physics,” *Physics of Atomic Nuclei*, vol. 61, p. 1066, 1998, <https://arxiv.org/abs/hep-ph/9802270>.
- [52] J. Wyenberg and I. M. Shoemaker, “Mapping The Neutrino Floor For Dark Matter-Electron Direct Detection Experiments,” *Physical Review D*, vol. 79, Article ID 115026, 2018.
- [53] D. K. Papoulias and T. S. Kosmas, “Neutrino transition magnetic moments within the non-standard neutrino-nucleus interactions,” *Physics Letters B*, vol. 747, pp. 454–459, 2015.
- [54] J. Beringer, J. F. Arguin, and R. M. Barnett, “Review of particle physics,” *Physical Review D: Particles, Fields, Gravitation and Cosmology*, vol. 86, no. 1, Article ID 010001, 2012.
- [55] J. Barranco, O. G. Miranda, and T. I. Rashba, “Probing new physics with coherent neutrino scattering off nuclei,” *Journal of High Energy Physics*, vol. 2005, article 021, 14 pages, 2005.
- [56] W. M. Alberico, S. M. Bilenky, and C. Maieron, “Strangeness in the nucleon: neutrino–nucleon and polarized electron–nucleon scattering,” *Physics Reports*, vol. 358, no. 4, pp. 227–308, 2002.
- [57] K. Scholberg, “Prospects for measuring coherent neutrino-nucleus elastic scattering at a stopped-pion neutrino source,” *Physical Review D: Particles, Fields, Gravitation and Cosmology*, vol. 73, Article ID 033005, 2006.
- [58] W. Grimus, M. Maltoni, T. Schwetz, M. A. Tortola, and J. W. F. Valle, “Constraining Majorana neutrino electromagnetic properties from the LMA-MSW solution of the solar neutrino problem,” *Nuclear Physics B*, vol. 648, no. 1-2, pp. 376–396, 2003.
- [59] B. Cañas, O. Miranda, A. Parada, M. Tórtola, and J. Valle, “Addendum to “Updating neutrino magnetic moment constraints,” *Physics Letters B*, vol. 757, p. 568, 2016.
- [60] J. B. Dent, B. Dutta, S. Liao, J. L. Newstead, L. E. Strigari, and J. W. Walker, “Probing light mediators at ultralow threshold energies with coherent elastic neutrino-nucleus scattering,” *Physical Review D: Particles, Fields, Gravitation and Cosmology*, vol. 96, no. 9, 2017.
- [61] I. M. Shoemaker, “A COHERENT Search Strategy for Beyond Standard Model Neutrino Interactions,” *Physical Review D: Particles, Fields, Gravitation and Cosmology*, vol. 95, Article ID 115028, 2017.
- [62] M. Lindner, W. Rodejohann, and X.-J. Xu, “Coherent Neutrino-Nucleus Scattering and new Neutrino Interactions,” *Journal of High Energy Physics*, vol. 3, no. 97, 2017.
- [63] D. G. Cerdeño, M. Fairbairn, T. Jubb, P. A. Machado, A. C. Vincent, and C. Boehm, “Erratum to: Physics from solar neutrinos in dark matter direct detection experiments,” *Journal of High Energy Physics*, vol. 2016, no. 9, 2016.
- [64] J. Liao and D. Marfatia, “COHERENT constraints on nonstandard neutrino interactions,” *Physics Letters B*, vol. 775, pp. 54–57, 2017.
- [65] V. Antonelli, L. Miramonti, C. Pena Garay, and A. Serenelli, “Solar Neutrinos,” <https://arxiv.org/abs/1208.1356>.
- [66] G. Bellini, J. Benziger, and D. Bick, “Neutrinos from the primary proton-proton fusion process in the Sun,” *Nature*, vol. 512, no. 7515, pp. 383–386, 2014.
- [67] S. Horiuchi, J. F. Beacom, and E. Dwek, “Diffuse supernova neutrino background is detectable in Super-Kamiokande,” *Physical Review D: Particles, Fields, Gravitation and Cosmology*, vol. 79, no. 8, 2009.
- [68] D. P. Ahalpara, K. H. Bhatt, and R. Sahu, “Collective bands in 81Sr,” *Journal of Physics G: Nuclear and Particle Physics*, vol. 11, no. 6, pp. 735–743, 1985.
- [69] L. Coraggio, L. De Angelis, T. Fukui, A. Gargano, and N. Itaco, “Calculation of Gamow-Teller and two-neutrino double- β decay properties for 130Te and 136Xe with a realistic nucleon-nucleon potential,” *Physical Review C*, vol. 59, Article ID 064324, 2018.
- [70] R. Sahu and V. K. B. Kota, “Deformed shell model for T=0 and T=1 bands in 62Ga and 66As,” *Physical Review C*, vol. 66, Article ID 024301, 2002.
- [71] R. Sahu and V. K. B. Kota, “Deformed shell model for collective T=0 and T=1 bands in 46V and 50Mn,” *Physical Review C*, vol. 67, Article ID 054323, 2003.
- [72] P. C. Srivastava, R. Sahu, and V. K. B. Kota, “Shell model and deformed shell model spectroscopy of 62Ga,” *The European Physical Journal A*, vol. 51, no. 3, 2015.
- [73] B. Ding et al., “High-spin states in ^{127}I ,” *Physical Review C*, vol. 85, Article ID 044306, 2012.
- [74] A. Beda, V. Brudanin, V. Egorov et al., “The results of search for the neutrino magnetic moment in GEMMA experiment,” *Advances in High Energy Physics*, vol. 2012, Article ID 350150, 12 pages, 2012.
- [75] J. Billard, J. Johnston, and B. J. Kavanagh, “Prospects for exploring New Physics in Coherent Elastic Neutrino-Nucleus Scattering,” <https://arxiv.org/abs/1805.01798>.
- [76] M. Abdullah, J. B. Dent, B. Dutta, G. L. Kane, S. Liao, and L. E. Strigari, “Coherent Elastic Neutrino Nucleus Scattering ($\text{CE}\nu\text{NS}$) as a probe of Z' through kinetic and mass mixing effects,” *Physical Review D*, vol. 98, Article ID 015005, 2018.
- [77] M. Abdullah, M. Dalchenko, B. Dutta et al., “Bottom-quark Fusion Processes at the LHC for Probing Z' Models and B-meson Decay Anomalies,” *Physical Review D*, vol. 97, Article ID 075035, 2018.

- [78] Y. Farzan, “A model for large non-standard interactions of neutrinos leading to the LMA-Dark solution,” *Physics Letters B*, vol. 748, pp. 311–315, 2015.
- [79] P. Coloma, P. B. Denton, M. C. Gonzalez-Garcia, M. Maltoni, and T. Schwetz, “Curtailling the dark side in non-standard neutrino interactions,” *Journal of High Energy Physics*, vol. 2017, no. 4, 2017.

Research Article

Deep Learning the Effects of Photon Sensors on the Event Reconstruction Performance in an Antineutrino Detector

Chang-Wei Loh, Zhi-Qiang Qian, Rui Zhang, You-Hang Liu, De-Wen Cao, Wei Wang, Hai-Bo Yang, and Ming Qi 

Physics Department, Nanjing University, 22 Hankou Road, Nanjing, Jiangsu, China

Correspondence should be addressed to Ming Qi; mqi@cern.ch

Received 3 January 2018; Revised 3 April 2018; Accepted 15 April 2018; Published 9 July 2018

Academic Editor: Hiroyasu Ejiri

Copyright © 2018 Chang-Wei Loh et al. This is an open access article distributed under the Creative Commons Attribution License, which permits unrestricted use, distribution, and reproduction in any medium, provided the original work is properly cited. The publication of this article was funded by SCOAP³.

We provide a fast approach incorporating the usage of deep learning for studying the effects of the number of photon sensors in an antineutrino detector on the event reconstruction performance therein. This work is a first attempt to harness the power of deep learning for detector designing and upgrade planning. Using the Daya Bay detector as a case study and the vertex reconstruction performance as the objective for the deep neural network, we find that the photomultiplier tubes (PMTs) at Daya Bay have different relative importance to the vertex reconstruction. More importantly, the vertex position resolutions for the Daya Bay detector follow approximately a multiexponential relationship with respect to the number of PMTs and, hence, the coverage. This could also assist in deciding on the merits of installing additional PMTs for future detector plans. The approach could easily be used with other objectives in place of vertex reconstruction.

1. Introduction

The choice of photon sensors such as photomultiplier tubes (PMTs), be it their expected sizes, locations, and the total number of sensors in antineutrino detectors, including Daya Bay [1], Double Chooz [2], RENO [3], and JUNO [4], are of interest as these sensors are the information gatherers through which we can identify antineutrino interaction events. This work is an attempt in using machine learning, in particular deep learning [5–7] as a way to understand how the number of PMTs in the detector influences the event reconstruction performance and extract lessons to be learned therefrom for areas such as detector designing and upgrade planning. To the best of our knowledge, this work is the first study on the efficacy of deep learning in detector designing and planning. For this work, we ask the following: suppose we are given N possible number of locations for the installation of k number of PMTs ($k \leq N$), where should the PMTs be installed such that the event interaction vertex reconstruction is optimal or near-optimal given only these k PMTs in the detector and N possible locations? Of course, N and k could be infinite, but this is technically impossible as it would not

meet the budget of a detector construction. In this work, we use deep learning on a model of the Daya Bay detector as a case study to understand the impact of PMTs on event position vertex reconstructions in a detector. The vertex is useful for studies on signal-background discriminations and the correction to the position-dependent energy response in the detector. The reconstruction of the vertices has been studied in-depth in the Daya Bay experiment using non-machine learning methods. As such, this allows us to cross-check our vertex reconstruction with deep learning with other methods in the Daya Bay before studying its potential in detector designing. Moreover, the vertex reconstruction performance is chosen as the objective since it is relatively simple for deep learning to handle for a clear understanding of the approach without involving too much experimental details. Nonetheless, experimentalists can easily substitute the vertex reconstruction performance with other objectives of interest. Beyond antineutrino detectors, sensor placements have been studied in areas ranging from water network distributions [8] to fault detections [9].

The Daya Bay antineutrino detectors are liquid scintillator detectors with a physics program focusing on the

precision measurement of the neutrino mixing angle θ_{13} with reactor antineutrinos. Each Daya Bay detector consists of three concentric cylindrical tanks: an inner acrylic vessel (IAV) containing gadolinium- (Gd-) doped liquid scintillator, an outer acrylic vessel (OAV) containing undoped liquid scintillator which surrounds the IAV, and a stainless steel vessel (SSV) which surrounds the IAV and OAV. With this design, the detectors could detect the interaction of the antineutrinos and the scintillator via inverse beta decay (IBD) reactions:

$$\bar{\nu}_e + p \longrightarrow e^+ + n. \quad (1)$$

The emitted positron then undergoes ionization processes in the liquid scintillator before annihilating with an electron producing a prompt signal with an energy deposition in the range of 1 - 8 MeV. The deposited energy is converted to scintillation photons which are then collected by the PMTs. As the positron displacement prior to the annihilation is negligible, the interaction vertex of the prompt signal can be assumed to be the antineutrino IBD interaction vertex. However, the neutron thermalizes and diffuses before being captured on either a proton or Gd with a mean capture time of $\sim 30 \mu\text{s}$ in the Gd-doped liquid scintillator and $\sim 200 \mu\text{s}$ in the undoped liquid scintillator, giving rise to a delayed signal. A total of 192 Hamamatsu R5912 8-inch PMTs [10], arranged in a layout with 8 rows and 24 columns, are installed on the vertical wall of the SSV pointing inward towards the OAV and IAV forming a total of 6% photodetector coverage. Located above and below the OAV are reflective panels that serve to redirect scintillation light towards the PMTs thereby increasing the photon collection efficiency to 12% effectively.

As aforementioned, we used deep learning to perform the IBD vertex reconstruction in order to study the effects of PMTs on an event reconstruction. Deep learning is a class of machine learning, which is especially adept at leveraging large datasets to compute human-comprehensible quantities by learning the various degrees of correlations within. Notably, it can, on its own, learn to discover functional relationships from the data without *a priori* given, effectively forming a mapping from the inputs to a quantity of interest. In other words, deep learning seeks to model the quantity of interest y using a vector of inputs x with $DL(x, p) = y$, where p are parameters of the deep network; their numerical values were found by minimizing the error between the predicted y' and y . Deep learning machine architectures, commonly known as deep neural networks (DNN), are based on artificial neural networks [11] but deeper in terms of the number of hidden layers and are more flexible in terms of how each neuron is connected to other neurons.

The ubiquity of deep learning and its significant success over traditional methods across disparate fields [12–14] in discovering patterns is surprising. However, this may well be due, in part, to that our universe operates on simple physical properties [15]. In high-energy physics, deep learning has demonstrated its prospective use in jets [16, 17], as part of the signal-background discrimination toolkit in the search for beyond the Standard Model particles [18] and Higgs bosons [19] and in neutrino physics experiments [20–24].

2. Recursive Search

As mentioned in Section 1, we wish to search for the k most important locations corresponding to k PMTs installed therein from the N total possible locations in the detector in determining the vertex position V of events collected from the detector. N is a free parameter which could be chosen during the detector design and simulation stage. Denoting the set containing the k number of most important locations as the set S_k^* , this implies that we should find the set S_k^* such that the vertex reconstruction error is minimized. However, finding such k locations simultaneously is a task confounded by a computation that grows exponentially with k . Alternatively, we could search for an approximation to S_k^* by recursively finding the important PMT location one at a time, which can be achieved using deep learning. Since searching for the most important location is equivalent to searching for the most important PMT at that particular location, the phrase “ k -th important PMT” will be used in this work as a shorthand for “ k -th important PMT location”.

Let the true position of the IBD prompt events be $V_{true} = \{x_{true}, y_{true}, z_{true}\}$; the predicted position using DNN as $V_{pred} = \{x_{pred}, y_{pred}, z_{pred}\}$, then in a recursive search, the k -th important PMT, PMT_k^* , will be the one that maximizes the improvement in the resolution σ of the residual distribution given that the $(k - 1)$ other PMTs have already been found through the recursive search, i.e., $\{PMT_{k-1}^*, PMT_{k-2}^*, \dots, PMT_1^*\}$, and where the residual is $V_{pred} - V_{true}$. Namely,

$$PMT_k^* = \arg \min_{P_k \in N \setminus S_{k-1}^{recu}} \sigma(PMT_k, S_{k-1}^{recu}), \quad (2)$$

where $S_{k-1}^{recu} = \{PMT_{k-1}^*, \dots, PMT_1^*\}$ and N is the set containing all the PMTs. Using (2), PMTs could be progressively added into a larger and larger subset S defining the best set found by the algorithm. Alternatively, one could perform a backward elimination: starting from the set with all PMTs and progressively eliminating the most “unimportant” PMT. At the conclusion of this recursive search, we obtain a curve of the event reconstruction resolution versus the number of PMTs used for the reconstruction thereof.

3. Deep Neural Network

In our approach utilizing DNNs, we used a Monte Carlo dataset comprising 2 million IBD prompt events obtained from a Daya Bay detector model which were randomly partitioned into a training set (1.4 million), a validation set (0.3 million), and a test set (0.3 million). The validation set is used for the early stopping of the DNN training to prevent overfitting or underfitting of the data [25]. The parameter N as defined in Section 2 would be 192 corresponding to the 192 PMT locations in the Daya Bay detector model. The charge information of the 192 PMTs is fed into the DNN as its inputs, and the output is the predicted vertex location V_{pred} . To train the DNN, we used the mean square error (*MSE*) loss function

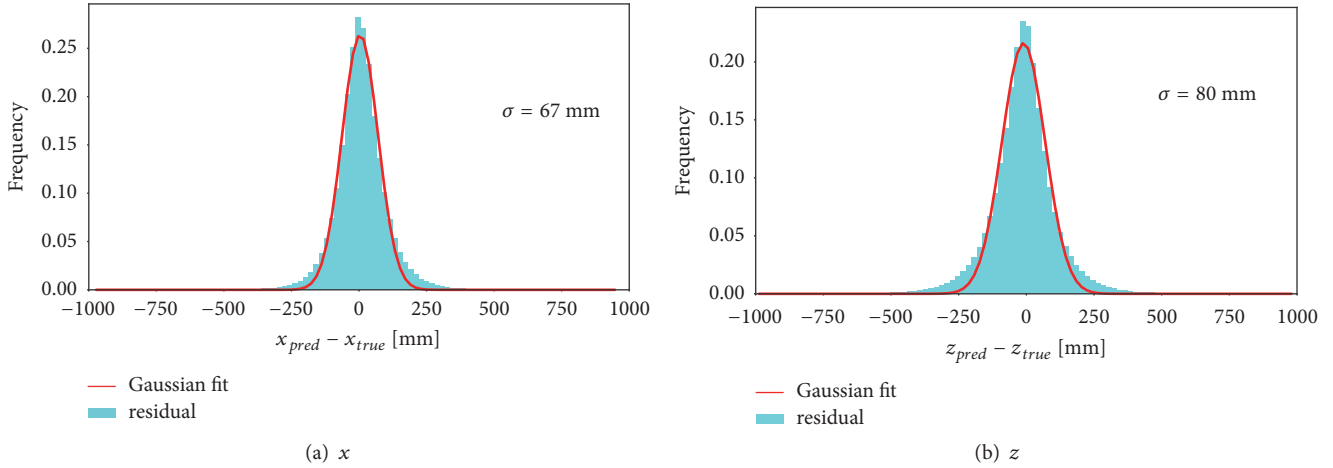


FIGURE 1: Residual distributions for x and z using all 192 PMT charge information.

to measure the error between the predicted, and the truth vertex positions:

$$MSE = \frac{1}{T} \sum_{j=1}^T \left(v_{ij_{pred}} - v_{ij_{true}} \right)^2, \quad (3)$$

where T is the number of events, $v_{ij_{pred}}$ and $v_{ij_{true}}$ are the predicted and truth values for the i -th coordinate of the j -th event vertex, respectively ($i = x, y, z$). The MSE was minimized to obtain the optimal DNN parameters. The minimization is typically done with a gradient descent method [26] involving the gradient of the loss function with respect to the DNN parameters, including the weights of each neuron; i.e., at each training iteration, the parameters w are updated via

$$w_i = w_i - \gamma \cdot \frac{\partial MSE}{\partial w_i}, \quad (4)$$

where γ is the learning rate determined by the user that controls the step length in the negative gradient direction during the training stage. When the MSE reaches minima, $\partial MSE / \partial w_i = 0$. At this point, the DNN has found the needed parameter values to best reconstruct the vertex position. To train the DNN, γ starts with a value of 0.001 and is progressively multiplied a factor of 0.5 whenever the value of the loss function metric stops improving. In this manner, the DNN training will descent quickly in the direction of the minima in the early stage; with a smaller learning rate at a later stage, the training will not overshoot the minima but will descent steadily towards it. An early stopping is made during the training, whereby the training is terminated when no further improvements could be observed from the loss function value after a predetermined number of training rounds, in this case ten. Without such early stopping, the loss function value can rise again indicating that an overfitting has occurred.

The efficacy of deep learning to predict the position of the IBD prompt events can be demonstrated by the residual distributions shown in Figure 1 where the charge

information of the 192 PMTs is fed into a DNN as its inputs. The DNN used here to obtain V_{pred} consists of multiple fully connected layers with ReLU [27] hidden neurons. The optimal number of layers and neurons were obtained using a tree-structured Parzen estimator [28]. The resulting network comprises three hidden layers containing 180, 148, and 148 neurons, respectively. The resolutions as obtained from the Gaussian fit to the residual distributions are 67 mm and 80 mm for $(x_{pred} - x_{true})$ and $(z_{pred} - z_{true})$, respectively.

A straightforward and brute force use of (2) in a recursive search using a DNN to identify PMT_k^* would be to check over all the remaining PMTs not in the optimal set S_{k-1}^* and separately construct the residual distributions, picking the one giving the best resolution for a particular coordinate in V_{true} . For this brute force search, we used a DNN architecture similar to the aforementioned DNN. The input layer will contain neurons with charge information from the already-chosen PMTs, i.e., those in S_{k-1}^{recu} , plus a candidate PMT, i.e., PMT_k . The computation time for such a search grows quadratically with the total number of PMTs in the detector. Such a brute force search is clearly not scalable. Hence, in this work, we have also used a fast approach to approximate the brute force search but which mitigates the nonscalability of the latter.

This fast approach integrates a DNN component from the autoencoder architecture [29]: a bottleneck layer with a single neuron, as shown in Figure 2. In this bottleneck DNN architecture, the remaining candidate PMTs not in S_{k-1}^{recu} are forced to connect to the bottleneck neuron before being given to the fully connected layers as inputs, effectively demanding the DNN to search for the best weights associated with each of these PMTs. At the bottleneck region, the DNN computes the sum $\sum w_i PMT_i$, where i runs over the candidate PMTs, the quantity PMT_i is the i -th PMT input to the DNN in the form of charge information, and the weight w_i of the i -th PMT is a parameter in the DNN. When the training stage of the DNN ends, the w_i s would have reached their best values corresponding to a minima of the MSE . The PMT with the largest weight in magnitude indicates that the reconstruction

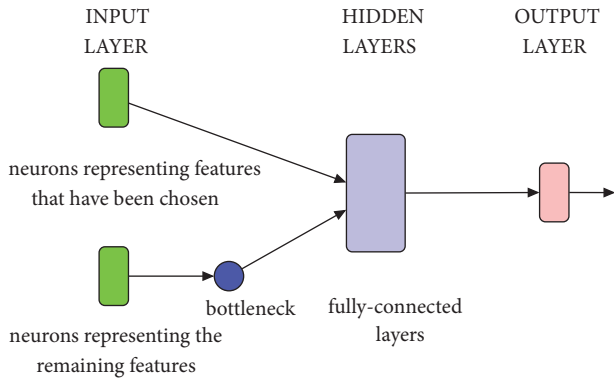


FIGURE 2: DNN architecture consisting of a bottleneck neuron.

of the position of the IBD prompt events relies the heaviest on this PMT compared to the rest of the candidate PMTs. Hence, this PMT would be our k -th important PMT, PMT_k^* . Crucially, this type of DNN only needs to be trained once to identify PMT_k^* no matter the value of k , whereas the brute force DNN needs to be trained $(N - k)$ times, once for each remaining candidate PMT.

4. Results

The heatmap in Figure 3 shows the resolutions as obtained from the residual distributions corresponding to using only one PMT for training and determining the vertex location of the antineutrino IBD interaction using the brute force search. Specifically, the resolution pertaining to using each PMT is indicated by a value from the color scale. Clearly, some PMTs contain more information about the vertex position than others. The first most important PMT from the brute force search, i.e., PMT_1^{brute*} , is chosen as the one having the smallest color value in the heatmap. The variation in resolution for the x -direction by column is due to the use of σ_x rather than σ_r . The reconstruction shows that the most important PMT is different for the x -direction and the z -direction. The heatmap pattern for the y -direction is similar to the x -direction, but with the dark region in the x -direction being the light region in the y -direction and vice versa, reflecting that x and y depend on $\cos \phi$ and $\sin \phi$, respectively in a cylindrical coordinate system, i.e., a $\pi/2$ shift in difference between x and y .

In Figure 4, the heatmap shows the weight corresponding to each PMT as obtained from the bottleneck neuron when searching for the first most important PMT. A higher weight indicates that the PMT has a larger impact on the vertex reconstruction. The PMT with the largest weight is identified as the most important PMT, PMT_1^{bneck*} . Ideally, we would like to constrain the weights to be discrete at the bottleneck, i.e., to be either 0 or 1, where weight is 1 for the most important PMT and 0 for the rest during the training of the DNN. However, such a constraint is nondifferentiable and noncontinuous with respect to the loss function which would render DNN parameter optimization using gradient

descent algorithms unfeasible. Comparing Figures 3 and 4, the brute force and the bottleneck DNN have chosen different PMTs as their most important PMTs possibly due to degeneracies in the detector. For example, in the z -direction, the PMTs at the top and bottom rings should produce the same resolution. Our suspect is that, during the training of the bottleneck DNN, some information sharing between a subset of PMTs, in which the DNN thinks their information values are similar, is unavoidable. Hence, the bottleneck neuron contains information from not one but a subset of PMTs; i.e., the importance by weights of each PMT could be partially “shared” amongst several PMTs. Further understanding of these are being conducted. Figures 5 and 6 are the results as obtained from the brute force and bottleneck DNN approach, respectively, while searching for the second most important PMT after having found the first most important PMT.

Figure 7 shows the residual curve for x and z as a function of the number of PMTs used in the reconstruction. Using an Nvidia Tesla P40 GPU, we estimated that it would take about 60 days to complete the entire residual curve with the brute force search, whereas it took about one day to complete with the bottleneck DNN. Resolutions from random choice of PMTs are also included in the figures as a comparison to the result from the bottleneck DNN. An empirical fit to the bottleneck DNN results is done with a triple exponential fit. It can be clearly seen that there is a diminishing return on the improvement in the vertex resolution when adding additional PMTs to an existing set of PMTs, which is an implication of the submodular [30] nature of the Gaussian standard deviation and its relationship to the information entropy, $H = \log \sigma + 0.5 \log(2\pi e)$. Succinctly, the submodularity of the Gaussian standard deviation, i.e., the resolution in this case shows that there is less new information that could be gained from adding a new PMT to a larger set of already-chosen PMTs than to a smaller set. As all the PMTs in the Daya Bay detector are of the same size and model, Figure 7 could also be interpreted as the residual curve being a function of the detector coverage.

5. Summary

In this work, we provide a fast approach using a deep neural network with a bottleneck neuron to uncover the effects of the number of photon sensors such as PMTs on the vertex resolutions in an antineutrino detector. The results have been compared with a random PMT search and a brute force search which yields the ideal result. Our inputs are the simulated charge information of the Daya Bay PMTs. The fast approach produces results close to those from the brute force search and fares much better than a random search. We find that the vertex resolution of the event reconstruction at the Daya Bay is approximately a multiexponentially decreasing function with respect to the number of PMTs and hence, also, the coverage. In future work, we envisage the possibility of incorporating the temporal information, i.e., the time of arrival of each photon in addition to the charge information to reconstruct the vertices. In addition, one could also study the size of the PMT needed alongside its installation location corresponding to the best event vertex reconstruction

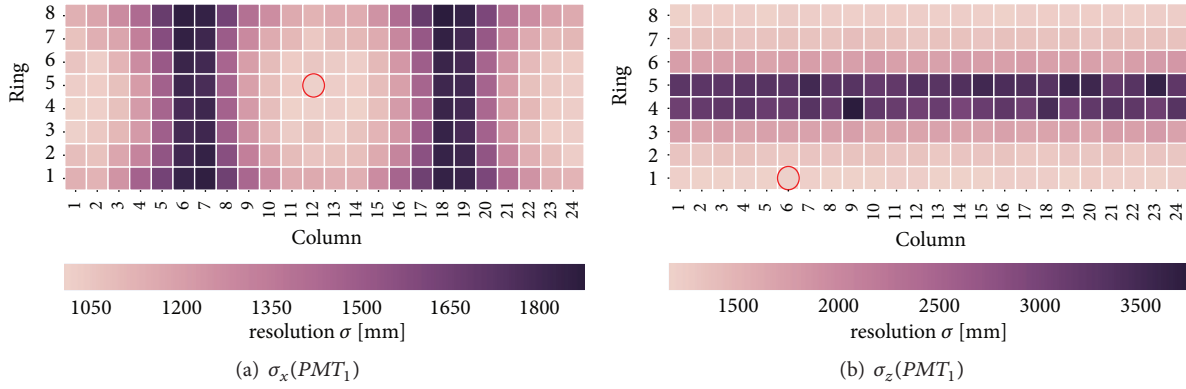


FIGURE 3: Resolution σ corresponding to using each individual PMT for (a) x and (b) z , using the brute force search. In each heatmap, the circled PMT corresponds to the best resolution amongst all the 192 PMTs.

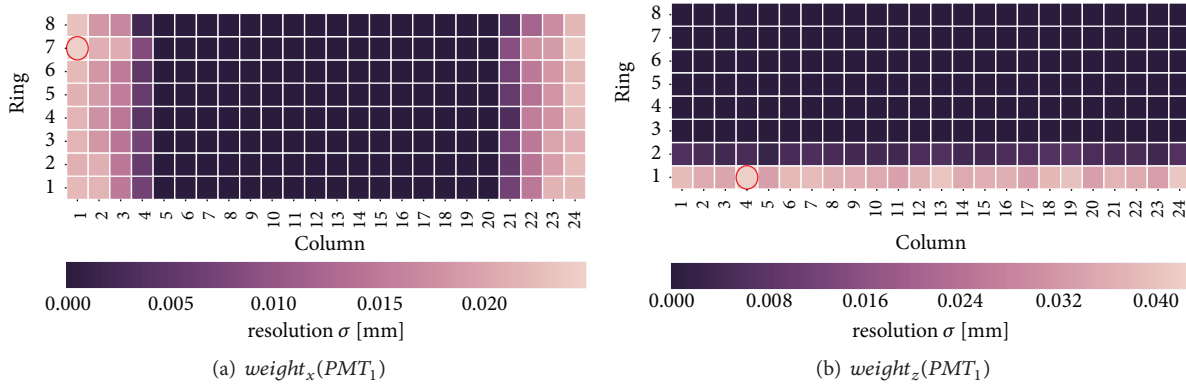


FIGURE 4: Weights as given by the bottleneck neuron corresponding to each PMT for (a) x and (b) z using the bottleneck DNN. In each heatmap, the circled PMT corresponds to the largest weight in the heatmap amongst all the 192 PMTs, indicating that it is the most heavily used PMT in the DNN during the vertex reconstruction.

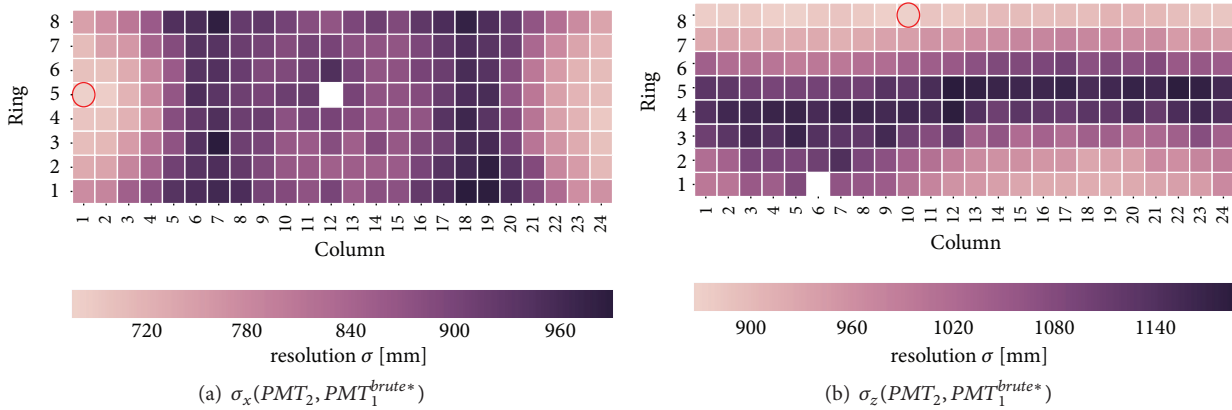


FIGURE 5: Resolution σ corresponding to using the charge information from the most important PMT as identified previously and a second candidate PMT for (a) x and (b) z . The first PMT as found by the previous round, PMT_1^{brute*} , using the brute force search is whitened in each figure. In each of the heatmap, the circled PMT, PMT_2^* , corresponds to the best resolution when considering the said PMT and the first important PMT found previously for the vertex reconstruction.

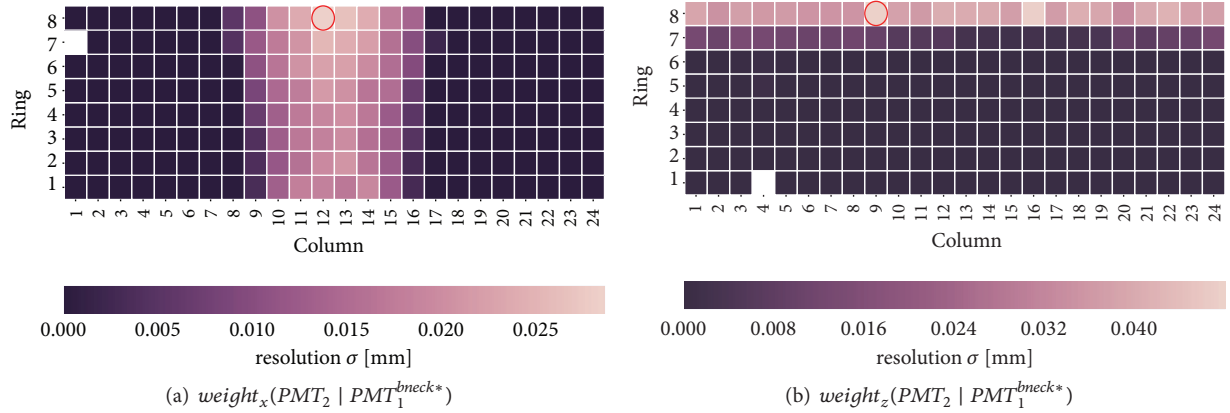


FIGURE 6: Weights as given by the bottleneck neuron corresponding to using a second candidate PMT, and the most important PMT, PMT_1^{bneck*} , as identified previously for (a) x and (b) z . PMT_1^{bneck*} is whitened in each figure. In each of the heatmap, the circled PMT, PMT_2^* , corresponds to the largest weight amongst the remaining 191 PMTs given that the first important PMT has been identified with the bottleneck DNN.

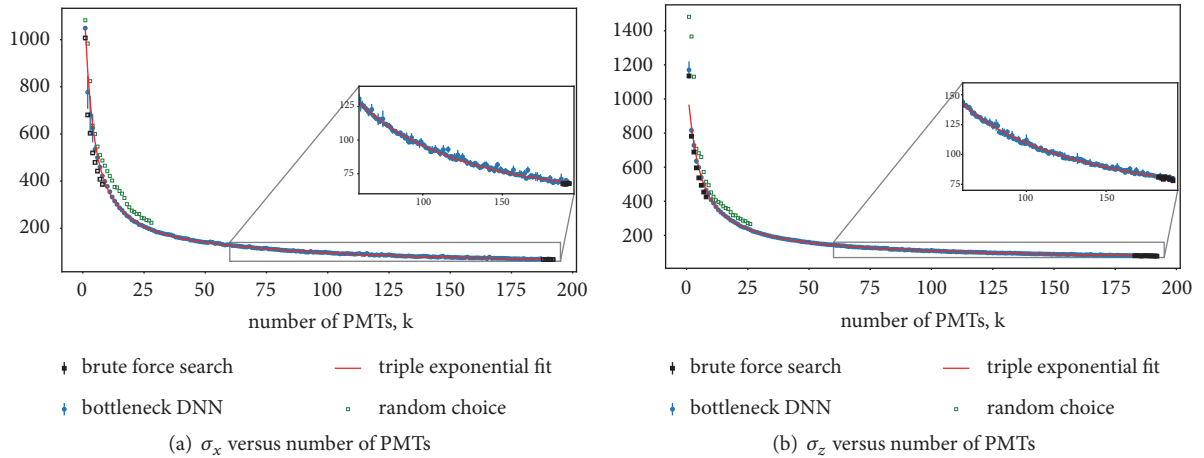


FIGURE 7: Residual curves for x (a) and z (b) as a function of the number of PMTs used in the reconstruction. The results plotted as solid squares are those from the brute force search. An empirical fit to the bottleneck DNN results was done with a triple exponential. Resolutions from random choice of PMTs are shown as empty squares. A zoom-in on the residual curves is also shown in the figures.

resolution. Also, a subsequent work from here would be the study of the effect of PMTs based on the event energy upon obtaining the vertex positions. Although studying the energy might need modifications to the deep network as the energy is a positive-definite quantity, the energy resolution is important when considering physics sensitivity and thereby also impacting the design of future antineutrino detectors including JUNO.

In order to use the bottleneck DNN approach for new detectors in designing phases, we suggest Monte Carlo simulations using various N . Then, one can obtain the (P, N, k) surface in the hyperspace, where P is some detector performance metric; N and k are as described in this work. Experimentalists can then decide on the (P, N, k) working point for their detector in accordance with their construction budget and the desired detector performance.

Data Availability

The data used to support the findings of this study are available from the corresponding author upon request.

Disclosure

Zhi-Qiang Qian is co-first author.

Conflicts of Interest

The authors declare that there are no conflicts of interest regarding the publication of this paper.

Acknowledgments

The authors thank Shen-Jian Chen and Zuo-Wei Liu for their computing facilities and helpful discussions. They would

also like to thank Chao Zhang, Zhe Wang, Samuel Kohn, the Daya Bay ACC, and the Collaboration for their time and comments. This work was supported by the National 973 Project Foundation of the Ministry of Science and Technology of China (Contract no. 2013CB834300) and the International Science & Technology Cooperation Program of China (Contract No. 2015DFG02100).

References

- [1] J. Cao and K.-B. Luk, “An overview of the Daya Bay reactor neutrino experiment,” *Nuclear Physics B*, vol. 908, pp. 62–73, 2016.
- [2] Double Chooz collaboration, Y. Abe et al., “Improved measurements of the neutrino mixing angle θ_{13} with the Double Chooz detector,” *Journal of High Energy Physics*, vol. 2014, no. 86, 2014.
- [3] RENO Collaboration, J. Choi et al., “Observation of Energy and Baseline Dependent Reactor Antineutrino Disappearance in the RENO Experiment,” *Physical Review Letters*, vol. 116, 2016.
- [4] JUNO collaboration, F. An et al., “Neutrino physics with JUNO,” *Journal of Physics G: Nuclear and Particle Physics*, vol. 43, Article ID 030401, 2016.
- [5] Y. LeCun, Y. Bengio, and G. Hinton, “Deep learning,” *Nature*, vol. 521, no. 7553, pp. 436–444, 2015.
- [6] Y. Bengio, “Deep Learning of Representations: Looking Forward,” in *Statistical Language and Speech Processing*, A. Dediu, C. Martín-Vide, R. Mitkov, and B. Truthe, Eds., p. 37, Springer Berlin Heidelberg, Berlin, Heidelberg, 2013.
- [7] J. Schmidhuber, “Deep learning in neural networks: an overview,” *Neural Networks*, vol. 61, pp. 85–117, 2015.
- [8] A. Krause, J. Leskovec, C. Guestrin, J. VanBriesen, and C. Faloutsos, “Efficient sensor placement optimization for securing large water distribution networks,” *Journal of Water Resources Planning and Management*, vol. 134, no. 6, pp. 516–526, 2008.
- [9] K. Worden and A. P. Burrows, “Optimal sensor placement for fault detection,” *Engineering Structures*, vol. 23, no. 8, pp. 885–901, 2001.
- [10] S. Jetter, D. Dwyer, W.-Q. Jiang et al., “PMT waveform modeling at the Daya Bay experiment,” *Chinese Physics C*, vol. 36, no. 8, pp. 733–741, 2012.
- [11] W. S. McCulloch and W. Pitts, “A logical calculus of the ideas immanent in nervous activity,” *Bulletin of Mathematical Biology*, vol. 5, no. 4, pp. 115–133, 1943.
- [12] A. Krizhevsky, I. Sutskever, and G. E. Hinton, “Imagenet classification with deep convolutional neural networks,” in *Advances in Neural Information Processing Systems*, F. Pereira, C. J. C. Burges, L. Bottou, and K. Q. Weinberger, Eds., vol. 25, pp. 1097–1105, 2012.
- [13] D. Silver, A. Huang, C. J. Maddison et al., “Mastering the game of Go with deep neural networks and tree search,” *Nature*, vol. 529, no. 7587, pp. 484–489, 2016.
- [14] F. Buggenthin, F. Buettner, P. S. Hoppe et al., “Prospective identification of hematopoietic lineage choice by deep learning,” *Nature Methods*, vol. 14, no. 4, pp. 403–406, 2017.
- [15] H. W. Lin, M. Tegmark, and D. Rolnick, “Why does deep and cheap learning work so well?” *Journal of Statistical Physics*, vol. 168, no. 6, pp. 1223–1247, 2017.
- [16] D. Guest, J. Collado, P. Baldi, S. Hsu, G. Urban, and D. Whiteson, “Jet flavor classification in high-energy physics with deep neural networks,” *Physical Review D: Particles, Fields, Gravitation and Cosmology*, vol. 94, no. 11, 2016.
- [17] P. T. Komiske, E. M. Metodiev, and M. D. Schwartz, “Deep learning in color: towards automated quark/gluon jet discrimination,” *Journal of High Energy Physics*, vol. 2017, no. 1, 2017.
- [18] P. Baldi, P. Sadowski, and D. Whiteson, “Searching for exotic particles in high-energy physics with deep learning,” *Nature Communications*, vol. 5, 2014.
- [19] P. Baldi, P. Sadowski, and D. Whiteson, “Enhanced Higgs Boson to Tau+ Tau- Search with Deep Learning,” *Physical Review Letters*, vol. 114, no. 11, 2015.
- [20] S. Kohn, “Understanding Backgrounds using Deep Learning at the Daya Bay Experiment,” in *Proceedings of the Work presented at the 28th International Symposium on Lepton Photon Interactions at High Energies*, 2017.
- [21] MiniBoone collaboration, R. Acciarri et al., “Convolutional neural networks applied to neutrino events in a liquid argon time projection chamber,” *Journal of Instrumentation*, vol. 12, 2017.
- [22] A. Aurisano, A. Radovic, D. Rocco et al., “A convolutional neural network neutrino event classifier,” *Journal of Instrumentation*, vol. 11, no. 09, pp. P09001–P09001, 2016.
- [23] NEXT collaboration, J. Renner et al., “Background rejection in NEXT using deep neural networks,” *Journal of Instrumentation*, vol. 12, Article ID T01004, 2017.
- [24] E. Racah, S. Ko, P. Sadowski et al., “Revealing fundamental physics from the Daya Bay Neutrino Experiment using deep neural networks,” in *Proceedings of the 15th IEEE International Conference on Machine Learning and Applications, ICMLA 2016*, pp. 892–897, USA, December 2016.
- [25] L. Prechelt, “Early Stopping - But When?” in *Neural Networks: Tricks of the Trade*, vol. 1524 of *Lecture Notes in Computer Science*, pp. 55–69, Springer Berlin Heidelberg, Berlin, Heidelberg, 1998.
- [26] D. E. Rumelhart, G. E. Hinton, and R. J. Williams, “Learning representations by back-propagating errors,” *Nature*, vol. 323, no. 6088, pp. 533–536, 1986.
- [27] V. Nair and G. Hinton, “Rectified Linear Units Improve Restricted Boltzmann Machines,” in *Proceedings of the 27th International Conference on Machine Learning (ICML-10)*, J. Furnkranz and T. Joachims, Eds., pp. 807–814, Omnipress, 2010.
- [28] J. Bergstra, R. Bardenet, B. Yoshua, and K. Balázs, “Algorithms for Hyper-parameter Optimization,” in *Proceedings of the 24th International Conference on Neural Information Processing Systems, NIPS11*, pp. 2546–2554, Curran Associates Inc, USA, 2011.
- [29] G. E. Hinton and R. S. Zemel, “Autoencoders, Minimum Description Length and Helmholtz Free Energy,” in *Advances in Neural Information Processing Systems 6*, J. D. Cowan, G. Tesauro, and J. Alspector, Eds., pp. 3–10, Morgan-Kaufmann, 1994.
- [30] G. L. Nemhauser, L. A. Wolsey, and M. L. Fisher, “An analysis of approximations for maximizing submodular set functions—I,” *Mathematical Programming*, vol. 14, no. 1, pp. 265–294, 1978.

Research Article

Effects of Leptonic Nonunitarity on Lepton Flavor Violation, Neutrino Oscillation, Leptogenesis, and Lightest Neutrino Mass

Gayatri Ghosh  and Kalpana Bora 

Department Of Physics, Gauhati University, Guwahati, Assam 781014, India

Correspondence should be addressed to Gayatri Ghosh; gayatrighsh@gmail.com

Received 19 January 2018; Revised 20 March 2018; Accepted 2 April 2018; Published 25 June 2018

Academic Editor: Theocharis Kosmas

Copyright © 2018 Gayatri Ghosh and Kalpana Bora. This is an open access article distributed under the Creative Commons Attribution License, which permits unrestricted use, distribution, and reproduction in any medium, provided the original work is properly cited. The publication of this article was funded by SCOAP³.

Neutrino physics is a mature branch of science with all the three neutrino mixing angles and two mass squared differences determined with high precision. In spite of several experimental verifications of neutrino oscillations and precise measurements of two mass squared differences and the three mixing angles, the unitarity of the leptonic mixing matrix is not yet established, leaving room for the presence of small nonunitarity effects. Deriving the bounds on these nonunitarity parameters from existing experimental constraints, on cLFV decays such as $\mu \rightarrow e\gamma$, $\mu \rightarrow \tau\gamma$, and $\tau \rightarrow e\gamma$, we study their effects on the generation of baryon asymmetry through leptogenesis and neutrino oscillation probabilities. We consider a model where see-saw is extended by an additional singlet S which is very light but can give rise to nonunitarity effects without affecting the form on see-saw formula. We do a parameter scan of a minimal see-saw model in a type I see-saw framework satisfying the Planck data on baryon to photon ratio of the Universe, which lies in the interval $5.8 \times 10^{-10} < Y_B < 6.6 \times 10^{-10}$ (BBN). We predict values of lightest neutrino mass and Dirac and Majorana CP-violating phases δ_{CP} , α , and β , for normal hierarchy and inverted hierarchy for one-flavor leptogenesis. It is worth mentioning that all these four quantities are unknown yet, and future experiments will be measuring them.

1. Introduction

Neutrinos have nonzero masses. There are 3 known flavors of neutrinos, ν_e , ν_μ , and ν_τ , each of which couples only to the charged lepton of the same flavor. ν_e , ν_μ , and ν_τ are superpositions of three mass eigenstates, $|\nu_\alpha\rangle = \sum U_{\alpha i}^* |\nu_i\rangle$, where $\alpha = e, \mu, \tau$ and ν_i is the neutrino of definite mass m_i . The cosmological constraints of the sum of the ν masses bound are $\sum_i m(\nu_i) < 0.23$ eV from CMB, Planck 2015 data (CMB15+LRG+ lensing + H_0) [1]. We note that the lepton mixing matrix U has a big mixing and we know almost nothing about the phases. The discoveries of neutrino mass and leptonic mixing have come from the observation of neutrino flavor change, $\nu_\alpha \rightarrow \nu_\beta$. CP violation interchanges every particle in a process by its antiparticle. This CP violation can be produced by the phase δ_{CP} in U . Neutrinos can have two types of mass term in the Lagrangian—Dirac and Majorana mass terms. To determine whether Majorana masses occur in nature, so that $\bar{\nu}_i = \nu_i$, the favorable approach to seek is Neutrinoless Double Beta Decay ($0\nu\beta\beta$).

In the conventional type I see-saw framework, there are Dirac and Majorana mass matrices m_D and M_R in the Lagrangian:

$$L = \frac{1}{2} \bar{N}_R M_R N_R^c + N_R m_D \nu_L + h.c. \quad (1)$$

The low-energy mass matrix is given by

$$m_\nu = -m_D^T M_R^{-1} m_D. \quad (2)$$

In the usual unitarity scenario, the three active neutrinos, the flavor eigenstates ν_e , ν_μ , and ν_τ are connected to the mass eigenstates ν_1 , ν_2 , and ν_3 via $\nu_\alpha = N_{\alpha i} \nu_i$, where $N^\dagger N = 1$. Here N is the generalized neutrino mixing matrix which could be either unitary or nonunitary. In the diagonal charged lepton basis, m_ν is diagonalized by a unitary matrix as

$$UPm_\nu P^\dagger U^\dagger = m_\nu^D. \quad (3)$$

The Pontecorvo-Maki-Nakagawa-Sakata (PMNS) matrix is UP, where U is

$$U = \begin{pmatrix} c_{12}c_{13} & s_{12}c_{13} & s_{13}e^{-i\delta} \\ -s_{12}c_{23} - c_{12}s_{23}s_{13}e^{i\delta} & c_{12}c_{23} - s_{12}s_{23}s_{13}e^{i\delta} & s_{23}c_{13} \\ s_{12}s_{23} - c_{12}c_{23}s_{13}e^{i\delta} & -c_{12}s_{23} - s_{12}c_{23}s_{13}e^{i\delta} & c_{23}c_{13} \end{pmatrix}. \quad (4)$$

Here $\theta_{12} = 33.56^\circ$, $\theta_{23} = 41.6^\circ (50^\circ)$, $\theta_{13} = 8.46^\circ (8.49^\circ)$ [3] (see [3] for recent global fit values) are the solar, atmospheric, and reactor angles for Normal Ordering (Inverted Ordering), respectively. The Majorana phases reside in P, where

$$P = \text{diag} \left(1 \quad e^{i\alpha} \quad e^{i(\alpha+\beta)} \right). \quad (5)$$

Cosmologists suggest that, just after the Big Bang, the Universe contained equal amounts of matter and antimatter. Today the Universe contains matter but almost no antimatter. This change needs that matter and antimatter act differently (CP violation). The CP-violating scenario to explain this change is leptogenesis. Leptogenesis is a natural outcome of the see-saw mechanism. In the see-saw picture, we assume that, just as there are 3 light neutrinos ν_1, ν_2, ν_3 , there are 3 heavy right-handed neutrinos M_1, M_2, M_3 , where $M_R \sim 10^{9-14}$ GeV, $M_R \sim M_1, M_2, M_3$ which were there in the Hot Big Bang. The M_R decays modes are

$$\begin{aligned} M &\longrightarrow l^- + H^+, \\ M &\longrightarrow l^+ + H^-, \\ M &\longrightarrow \nu + H^0, \\ M &\longrightarrow \bar{\nu} + \bar{H}^0, \end{aligned} \quad (6)$$

where l^- are e^-, μ^-, τ^- and H^+, H^-, H^0 are SM Higgs. CP violation effects in the M_R decays may result from phases in the decay coupling constants. This leads to unequal numbers of leptons (l^- and ν) and antileptons (l^+ and $\bar{\nu}$) in the Universe:

$$\Gamma(M \longrightarrow l^+ + H^-) \neq \Gamma(M \longrightarrow l^- + H^+). \quad (7)$$

In leptogenesis, CP-violating decays of heavy Majorana neutrinos create a lepton-antilepton asymmetry [4] and then B+L violating sphaleron processes [5] at and above the electroweak symmetry breaking scale convert part of this asymmetry into the observed baryon-antibaryon asymmetry. The heavy neutrinos are see-saw partners of the observed light ones.

Depending on mass of the lightest heavy RH Majorana neutrinos (whose decay causes leptogenesis) the leptogenesis can be of three types: unflavored (or one-flavor), two-flavored, and three-flavored leptogenesis. For unflavored leptogenesis, valid for $M_1 \geq 10^{11}$ GeV, we have taken here $M_1 \sim 10^{12}$ GeV where the flavor of the final state leptons plays no role. It can be shown that for lower values of M_1 it depends on the flavor of the final state leptons and hence is called flavored leptogenesis [6]. Here we consider unflavored leptogenesis.

For unflavored leptogenesis, the decay asymmetry in the case of hierarchical heavy neutrinos is given by [7]

$$\varepsilon_1 = \frac{1}{8\pi v^2} \frac{1}{(m_D m_D^\dagger)_{11}} \sum_{2,3} \text{Im} (m_D m_D^\dagger)_{1j}^2 f \left(\frac{M_j}{M_1} \right), \quad (8)$$

where $f(x) = -3/2\sqrt{x}$ for $x > 1$, i.e., for hierarchical heavy neutrinos. The baryon asymmetry of the Universe is proportional to the decay asymmetry ε_1 . The Dirac mass matrix m_D in terms of a complex and orthogonal matrix R is [8]

$$m_D = i\sqrt{M_R} R \sqrt{m_\nu^{diag}} U^\dagger. \quad (9)$$

The compatible quantity for leptogenesis is then

$$\begin{aligned} m_D m_D^\dagger &= \sqrt{M_R} R \sqrt{m_\nu^{diag}} U^\dagger U \sqrt{m_\nu^{diag}} R^\dagger \sqrt{M_R} \\ &= \sqrt{M_R} R m_\nu^{diag} R^\dagger \sqrt{M_R} \end{aligned} \quad (10)$$

If R is real then there is no leptogenesis at all. Here, we have taken $R = U$ (see (4)). R consists of the low-energy mixing elements and the CP phases. Since unitarity of neutrino mixing matrix has not been proved yet, if it is nonunitary, then, for the neutrino mixing matrix N to be nonunitary, we have

$$\nu_\alpha = N_{\alpha i} \nu_i, \quad (11)$$

connecting the flavor and mass states. The nonunitary matrix N can be written as

$$N = (1 + \eta) U_0, \quad (12)$$

where $U_0 = U * P$. If m_ν , which is diagonalized by a non-unitary mixing matrix, originates from the see-saw mechanism, we have

$$m_D = i\sqrt{M_R} R \sqrt{m_\nu^{diag}} N^\dagger. \quad (13)$$

And, thereupon, we have

$$m_D m_D^\dagger = \sqrt{M_R} R \sqrt{m_\nu^{diag}} N^\dagger N \sqrt{m_\nu^{diag}} R^\dagger \sqrt{M_R}. \quad (14)$$

For nonunitary U_{PMNS} matrix, $N^\dagger N = 1 + 2U_0^\dagger \eta U_0 \neq 1$. Leptogenesis is no longer independent of the low-energy phases. It depends on the phases in U_0 as well as the phases in η . Leptogenesis [9] is one of the exceedingly well-inspired frameworks which produces baryon asymmetry of the Universe through B + L violating electroweak sphaleron process [5, 10].

In the conventional type I see-saw mechanism, due to the mixing of the left-handed and right-handed neutrinos the PMNS matrix is nonunitary. Nevertheless this nonunitarity is too small to have any observable effects in lepton flavor violation (LFV) or neutrino oscillation (see [7, 11, 12]). If we want to connect the lepton mixing matrix to leptogenesis via the Casas-Ibarra parametrization, then there should not be

any significant sizeable contribution to m_ν and leptogenesis other than the usual see-saw terms. Hence we must decouple the origin of unitarity violation from these terms. Mixing of the light neutrinos with new physics creates nonunitarity in the low-energy mixing matrix. We consider here a model as used in [7] where the see-saw mechanism is enlarged by an additional singlet sector, which leads to a 9×9 mass matrix. Here

$$L = \frac{1}{2} \begin{pmatrix} \overline{\nu}_L^c & \overline{N}_R & \overline{X} \end{pmatrix} \begin{pmatrix} 0 & m_D^T & m^T \\ m_D & M_R & 0 \\ m & 0 & M_s \end{pmatrix} \begin{pmatrix} \nu_L \\ N_R^c \\ X^c \end{pmatrix}, \quad (15)$$

where the upper left block is the one corresponding to usual type I see-saw mechanism. It can be diagonalized with a unitary matrix F , such that

$$F^T \begin{pmatrix} 0 & m_D^T & m^T \\ m_D & M_R & 0 \\ m & 0 & M_s \end{pmatrix} F = \begin{pmatrix} m_\nu^{diag} & 0 & 0 \\ 0 & M_R & 0 \\ 0 & 0 & M_s^{diag} \end{pmatrix}. \quad (16)$$

The form of F is as given in [7]. As discussed in [7] with proper choice of various elements in F and of M_s , it can be shown that

$$m_\nu^{diag} = -\widetilde{N}^T m_\nu^D M_R^{-1} m_\nu^D \widetilde{N}, \quad (17)$$

which shows that $N = (\widetilde{N}^\dagger)^{-1}$ is the lepton mixing matrix, as there is no other significant contribution to the mass term of the light neutrinos. Thus in this model the usual see-saw mechanism remains unaltered with unmodified leptogenesis. Here M_R does not couple to the new singlets but a sizeable nonunitary lepton mixing matrix N can be induced, thus providing us with a framework where we can apply (14).

We consider here that lepton asymmetry is generated by out-of-equilibrium decay of heavy right-handed Majorana neutrinos into Higgs and lepton within the framework of type I see-saw mechanism. In a hierarchical case of three right-handed heavy Majorana neutrinos $M_{2,3} > M_1$, with the lepton asymmetry created by the decay of M_1 , the lightest one of three heavy right-handed neutrinos is [13]

$$\begin{aligned} \epsilon_1^\alpha &= \frac{1}{8\pi v^2} \\ &\cdot \frac{1}{(m_D^\dagger m_D)_{11}} \left[\sum_{2,3} \text{Im} \left[(m_D^*)_{\alpha 1} (m_D^\dagger m_D)_{1j} (m_D)_{\alpha j} \right] \right. \\ &\cdot g(x_j) + \sum_{2,3} \text{Im} \left[(m_D^*)_{\alpha 1} (m_D^\dagger m_D)_{j1} (m_D)_{\alpha j} \right] \\ &\left. \cdot \frac{1}{1-x_j} \right]. \end{aligned} \quad (18)$$

Here $v = 174$ GeV is the vacuum expectation value of the SM Higgs and $g(x) = \sqrt{x}(1 + 1/(1-x) - (1+x) \ln((1+x)/x))$, where $x_j = M_j^2/M_1^2$.

At temperatures, $T \geq 10^{12}$ GeV, all the charged leptons are in equilibrium because the direct and inverse decays are very frequent and wash out any asymmetry. At moderate temperatures $T < 10^{12}$ GeV ($T < 10^9$ GeV), some particles decouple and thus flavor effects play an important role in the calculation of lepton asymmetry [6, 14–18]. The regions of temperatures belonging to $10^9 < T/\text{GeV} < 10^{12}$ and $T/\text{GeV} < 10^9$ are, respectively, denoted as two and three flavor regimes of leptogenesis [19].

The building blocks of matter are the quarks, the charged leptons, and the neutrinos. The discovery and study of the Higgs boson at the Large Hadron Collider (LHC) have provided strong evidence that the quarks and charged leptons derive their masses from a coupling to the Higgs field. Most theorists strongly believe that the origin of the neutrino masses is different from the origin of the quark and charged lepton masses. Neutrino oscillation has proved that neutrinos have nonzero masses. We and all matter may have descended from heavy neutrinos. We list the values of $m_{lightest}$ for one-flavor for different hierarchies and unitarity and nonunitarity of U_{PMNS} in Table 2 and check whether our values of $m_{lightest}$ are consistent with the constraints on the absolute scale of ν masses. The new results presented in this work are as follows:

(i) We have calculated new values of nonunitarity parameters of U_{PMNS} matrix from the bounds on rare cLFV decays.

(ii) Hence we predicted the absolute value of lightest ν mass in this regard. The values of lightest ν mass lie in the ranges of 0.0018 eV to 0.0023 eV, 0.048 eV to 0.056 eV, 0.05 eV to 0.054 eV, and 0.053 eV to 0.062 eV in one-flavor leptogenesis regime.

(iii) All these values satisfy the constraint $\sum_i m(\nu_i) < 0.23$ eV.

(iv) The predicted values of CP-violating phases, δ_{CP} , and Majorana phases α and β are $36^\circ, 72^\circ, 108^\circ, 144^\circ, 180^\circ, 216^\circ, 252^\circ, 288^\circ, 324^\circ$, and 360° . Here the calculated values of each of them, i.e., the Dirac CP-violating phase, δ_{CP} , and the Majorana phases α and β , are found to be same.

The paper is organized as follows. In Section 2, we show the effect of low-energy phenomenology of nonunitarity on charged lepton flavor violating decays in type I see-saw theories and present the values of various parameters used in our analysis for the generation of baryon asymmetry of the Universe through the mechanism of leptogenesis. Section 3 contains our calculations and results. Section 4 contains analysis and discussions. Section 5 summarizes the work.

2. Low-Energy Phenomenology of Nonunitarity and Leptogenesis

One interesting feature of nonunitarity of the PMNS matrix can be studied in rare charged lepton flavor violation (LFV) decay processes. In the light of unitarity violation in decays such as $\alpha \rightarrow \beta\gamma$, $(\alpha, \beta) = (\tau, \mu), (\tau, e)$ or (μ, e) , the branching ratio is [7]

$$\frac{BR(\alpha \rightarrow \beta + \gamma)}{BR(\alpha \rightarrow \beta + \overline{\nu\nu})} = \frac{100\alpha}{96\pi} \left| (NN^\dagger)_{\alpha\beta} \right|^2. \quad (19)$$

TABLE 1: Our calculated constraints on nonunitarity parameters $\eta_{\tau e}$, $\eta_{\tau\mu}$, and $\eta_{\mu e}$ using branching ratios of latest cLFV decays taken from [2].

Serial No.	Latest updated Branching Ratios on cLFV Decays	Calculated bounds on $ \eta _{\alpha\beta}$
1	$BR(\mu \rightarrow e + \gamma) = 4.2 \times 10^{-13}$	$ \eta_{\mu e} = 6.64733013 \times 10^{-6}$
2	$BR(\tau \rightarrow \mu + \gamma) = 4.4 \times 10^{-8}$	$ \eta_{\tau\mu} = 5.11766 \times 10^{-3}$
3	$BR(\tau \rightarrow e + \gamma) = 3.3 \times 10^{-8}$	$ \eta_{\tau e} = 7.021 \times 10^{-3}$

Also

$$\frac{BR(\tau \rightarrow \mu + \gamma)}{BR(\tau \rightarrow \mu + \nu\bar{\nu})} \simeq \frac{25\alpha}{6\pi} |\eta_{\mu\tau}|^2; \quad (20)$$

$$\frac{BR(\tau \rightarrow \mu + \gamma)}{4.2 \times 10^{-10}} \simeq \frac{|\eta_{\mu\tau}|^2}{25 \times 10^{-8}}.$$

Using the latest updated constraint on $BR(\tau \rightarrow \mu + \gamma) = 4.4 \times 10^{-8}$ [2], one can derive bounds on $|\eta_{\mu\tau}|$ from (23). It can be shown that

$$\frac{BR(\tau \rightarrow \mu + \gamma)}{BR(\mu \rightarrow e + \gamma)} = \frac{BR(\tau \rightarrow \mu + \nu_{\tau}\bar{\nu}_{\mu})}{BR(\mu \rightarrow e + \nu_{\mu}\bar{\nu}_{e})} \times \frac{|\eta_{\mu\tau}|^2}{|\eta_{\mu e}|^2}. \quad (21)$$

Now, we calculate the ratio

$$\frac{BR(\tau \rightarrow \mu + \nu_{\tau}\bar{\nu}_{\mu})}{BR(\mu \rightarrow e + \nu_{\mu}\bar{\nu}_{e})} = 0.176745. \quad (22)$$

Thus we find constraints on $|\eta_{\mu e}|$ from (24), using the latest constraint on $BR(\mu \rightarrow e + \gamma)$, where $BR(\mu \rightarrow e + \gamma) = 4.2 \times 10^{-13}$ [2]. Again we have

$$\frac{BR(\tau \rightarrow \mu + \gamma)}{BR(\tau \rightarrow e + \gamma)} = \frac{BR(\tau \rightarrow \mu + \nu_{\tau}\bar{\nu}_{\mu})}{BR(\tau \rightarrow e + \nu_{\mu}\bar{\nu}_{e})} \times \frac{|\eta_{\mu\tau}|^2}{|\eta_{\tau e}|^2}. \quad (23)$$

From our calculation, the ratio $BR(\tau \rightarrow \mu + \nu_{\tau}\bar{\nu}_{\mu})/BR(\tau \rightarrow e + \nu_{\mu}\bar{\nu}_{e})$ is

$$\frac{BR(\tau \rightarrow \mu + \nu_{\tau}\bar{\nu}_{\mu})}{BR(\tau \rightarrow e + \nu_{\mu}\bar{\nu}_{e})} = 2.509. \quad (24)$$

And then we calculate the latest updated bounds on $|\eta_{\tau e}|$. The calculations are summarized in Table 1. The study of the effects of leptonic nonunitarity on two- and three-flavored leptogenesis is presented in [20]. We note that interesting results on cLFV $\mu \rightarrow e\gamma$ in NUSM, NUHM, NUGM, and mSUGRA models are presented in [21] in which we have predicted some values of new SUSY particles that may be detected at next run of LHC.

Returning to leptogenesis, the baryon asymmetry should lie in the interval $5.8 \times 10^{-10} < Y_B < 6.6 \times 10^{-10}$ [22]. In general, we have taken complex and orthogonal matrix $R = U_{PMNS}$, but R can be taken as $R = V_{CKM} \times U_{PMNS}$ in non-SUSY SO(10) models [18] (see [18] for detailed discussion) as studied in the context of breaking entanglement of octant of

θ_{23} and δ_{CP} in the light of baryon asymmetry of the Universe through the mechanism of leptogenesis.

For the normally ordered light neutrino masses, we have

$$M_R^{diag} = \text{diag}(M_1, M_2, M_3) = M_1 \text{diag}\left(1, \frac{M_2}{M_1}, \frac{M_3}{M_1}\right) \quad (25)$$

$$= M_1 \text{diag}\left(1, \frac{m_1}{m_2}, \frac{m_1}{m_3}\right),$$

with $m_1 \in [10^{-6}eV, 10^{-1}eV]$, and $m_2^2 - m_1^2 = 7.60 \times 10^{-5}eV^2$, $m_3^2 - m_1^2 = 2.48 \times 10^{-3}eV^2$ as is evident from the neutrino oscillation data [3], with m_1 being the lightest one of three neutrino masses. For the inverted ordered light neutrino masses, we have

$$M_R^{diag} = \text{diag}(M_1, M_2, M_3) = M_1 \text{diag}\left(1, \frac{M_2}{M_1}, \frac{M_3}{M_1}\right) \quad (26)$$

$$= M_1 \text{diag}\left(1, \frac{m_1 * m_3}{m_2^2}, \frac{m_1}{m_2}\right),$$

with m_3 being the lightest one of the three neutrino masses. Next, we do the parameter scan for one-flavored leptogenesis of a minimal see-saw model satisfying the Planck data on baryon to photon ratio of the Universe for four cases:

- (i) Normal hierarchical structure neutrino masses, nonunitarity of PMNS matrix
- (ii) Normal hierarchical structure neutrino masses, unitarity of PMNS matrix
- (iii) Inverted hierarchical structure of neutrino masses, nonunitarity of PMNS matrix
- (iv) Inverted hierarchical structure neutrino masses, unitarity of PMNS matrix.

We perform random scan of the parameter space for NH and IH in the light of recent ratio of the baryon to photon density bounds $5.8 \times 10^{-10} < \eta_B < 6.6 \times 10^{-10}$ in the following ranges:

$$m_1(m_3) \in [10^{-6}eV, 0.1eV] ([10^{-6}eV, 0.1eV]),$$

$$\delta_{CP} \in [0, 2\pi], \quad (27)$$

$$\alpha \in [0, 2\pi],$$

$$\beta \in [0, 2\pi].$$

While doing parameter scan, we find values of lightest neutrino mass, Majorana phases α , β , and Dirac CPV phase δ_{CP} , for which baryon to photon ratio Y_B lies in the given range, for above four cases. This is done for one-flavor/unflavored leptogenesis regime.

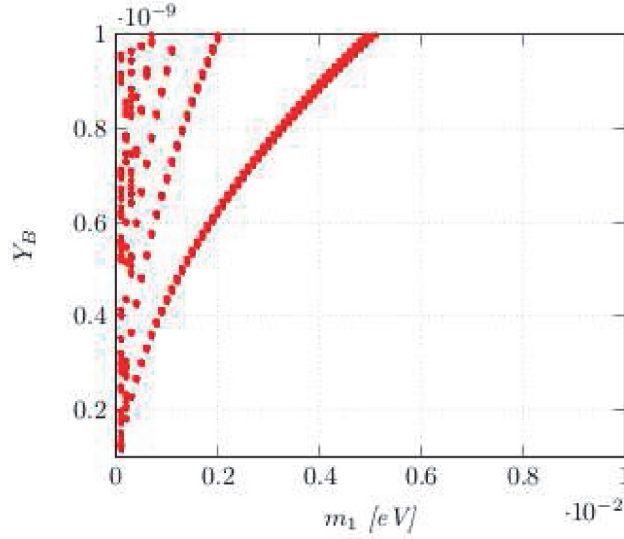


FIGURE 1: Scatter plot of the lightest neutrino mass m_1 against the baryon asymmetry of the Universe with normal hierarchy, nonunitarity case in one-flavor leptogenesis regime. The values of m_1 [eV] along the x-axis are multiplied by 10^{-2} .

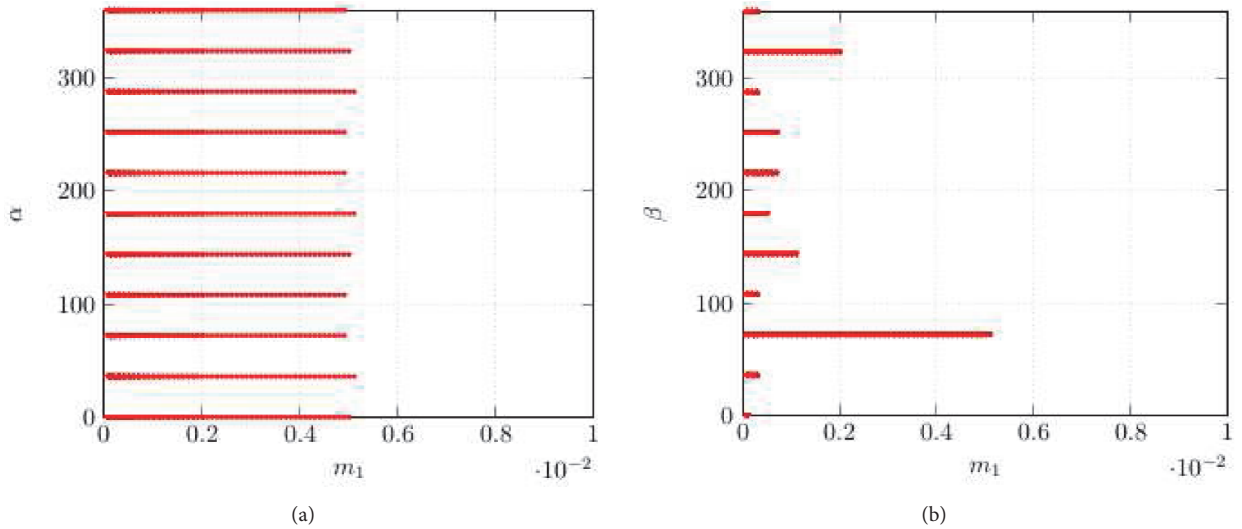


FIGURE 2: Variation of lightest neutrino mass m_1 with Majorana phases α and β in case of NH, nonunitarity case in one-flavor leptogenesis regime. m_1 is in eV. The values of m_1 [eV] in (a) and (b) along the x-axis are multiplied by 10^{-2} .

3. Calculations and Results

Results of our analysis have been presented in Figures 1–9. It can be seen from Figure 1 that in the one-flavor regime NH structure of neutrino masses and nonunitarity textures of PMNS matrix can give rise to correct baryon asymmetry of the Universe, $5.8 \times 10^{-10} < Y_B < 6.6 \times 10^{-10}$, if the lightest ν mass lies around 0.0018 eV to 0.0023 eV. A close numerical inspection of the situation reveals that for a lightest neutrino mass of 0.0024 eV–0.005 eV one can exceed the upper bound on Y_B . The dependence of lightest neutrino mass m_1 on Majorana phases α , β is shown in (a), (b) of Figure 2, respectively, Y_B being constrained in the order 10^{-10} .

We find that $M_1 = 10^{12}$ GeV is favored in the light of baryon asymmetry of the Universe for one-flavor regime.

Figure 3 shows the scatter plot of the lightest neutrino mass m_1 against the baryon asymmetry of the Universe with Normal hierarchy and unitary U_{PMNS} in one-flavor regime. For Y_B to be in the range, $5.8 \times 10^{-10} < \eta_B < 6.6 \times 10^{-10}$, m_1 lies between 0.048 eV and 0.056 eV. For Y_B in the order 10^{-10} , the lightest neutrino mass m_1 is mostly concentrated in the region 0.043 eV to 0.06 eV.

In Figure 4 we have shown the variation of lightest neutrino mass m_1 with Dirac CP phase δ_{CP} and Majorana phase α for NH (normal hierarchy) and unitarity texture. For Y_B to be in the consistent BAU range $5.8 \times 10^{-10} < Y_B < 6.6 \times 10^{-10}$,

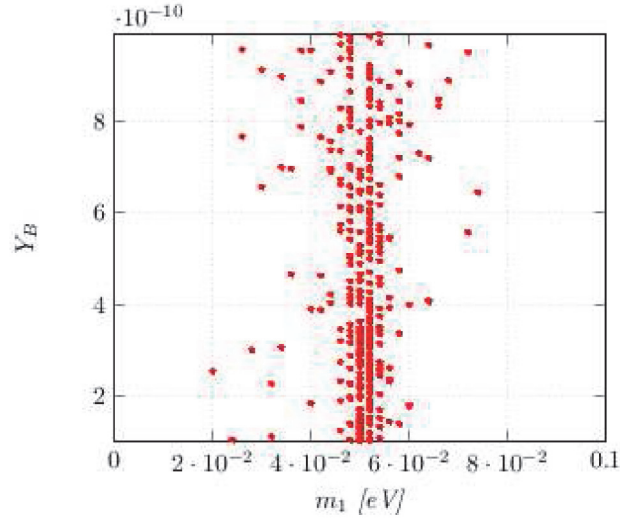


FIGURE 3: Scatter plot of the lightest neutrino mass m_1 against the baryon asymmetry of the Universe with normal hierarchy, unitarity case in one-flavor leptogenesis regime.

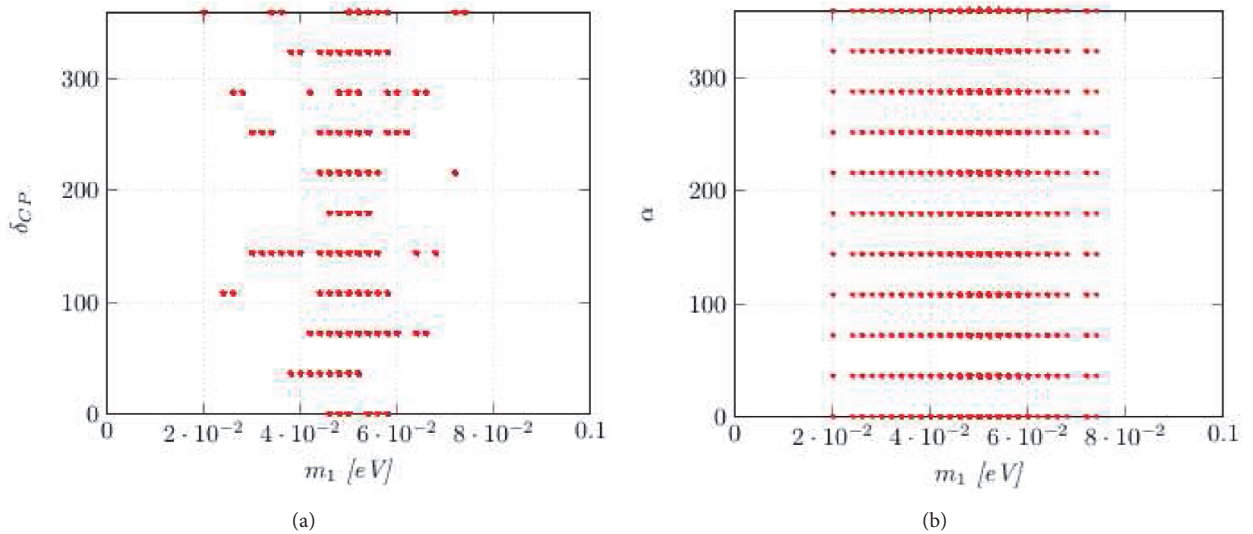


FIGURE 4: Variation of lightest neutrino mass m_1 on Dirac CP phase δ_{CP} and Majorana phases α in case of NH unitarity case in one-flavor leptogenesis regime.

one of the values of δ_{CP} predicted by us, i.e., $\delta_{CP} = 252.9^\circ$ is also favored in the recent global fit values, $\delta_{CP} = 253.8^\circ$ for normal hierarchy. It can be seen from Figure 5 that, in the one-flavor regime, IH structure of neutrino masses and nonunitarity textures of PMNS matrix can give rise to baryon asymmetry of the Universe, of the order of 10^{-10} , if the lightest neutrino mass lies around 0.05 eV to 0.054 eV. Few points lie in the region, $5.8 \times 10^{-10} < Y_B < 6.6 \times 10^{-10}$.

Figure 6 shows the scattered plot of lightest neutrino mass m_3 against Dirac CPV phase δ_{CP} and Majorana phase α in IH of neutrino mass and nonunitarity case of one-flavor leptogenesis regime. Figure 7 shows the variation of the lightest neutrino mass against the baryon asymmetry of the Universe and Dirac CP phase δ_{CP} with inverted hierarchy

and unitarity case in one-flavor leptogenesis regime. For Y_B in the order 10^{-10} , the lightest ν mass m_3 is concentrated in the region 0.053 eV to 0.062 eV. In Figure 8 we have shown the scatter plot of m_3 with Majorana phases α and β for IH and unitarity texture of U_{PMNS} in one-flavor leptogenesis regime.

In Figure 9, we have shown the effect of nonunitarity on probability $P(\nu_\mu \rightarrow \nu_e)$ for a particular case of Long Baseline Neutrino Experiments (DUNE, FNAL, USA). We have used the value of baseline to be $L = 1300$ Km and values of other oscillation parameters are taken from latest global fit [3]. It can be seen that nonunitarity affects the probability, which means that its effect could be studied in neutrino oscillation experiments provided we reach the required precision level.

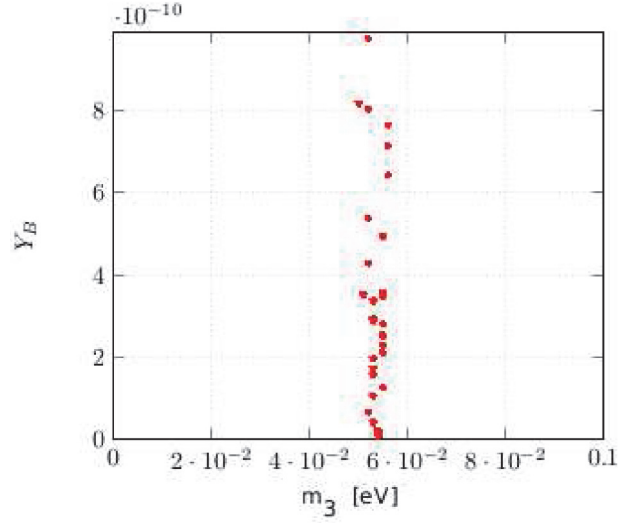


FIGURE 5: Scatter plot of the lightest neutrino mass m_3 against the baryon asymmetry of the Universe with inverted hierarchy, nonunitarity case in one-flavor leptogenesis regime.

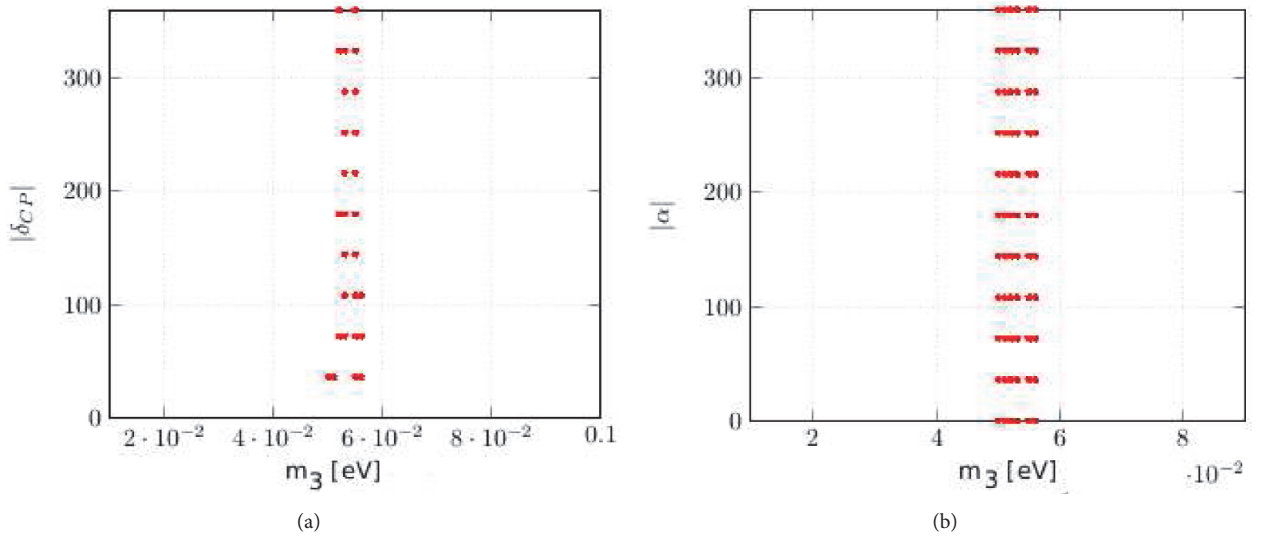


FIGURE 6: Variation of lightest neutrino mass m_3 against Dirac CP phase δ_{CP} and Majorana phase α in case of IH, nonunitarity case in one-flavor leptogenesis regime. The values of m_3 [eV] in (b) along the x-axis are multiplied by 10^{-2} .

4. Analysis and Discussion

We present here some comments that reflect the main inference of this work. From the results presented in Table 2 we see that in all the four cases there exist values of lightest neutrino mass, satisfying the constraint $\sum_i m(\nu_i) < 0.23\text{eV}$ and those of present day baryon asymmetry of the Universe. The analysis of our results can be summarized as follows:

(i) One-flavor leptogenesis: The value of lightest neutrino mass shifts to higher value in IH case, as compared to NH. Nonunitarity effects decrease the value of lightest neutrino mass in both NH and IH and the diminishing effect is more severe in NH.

(ii) We also found that nonunitarity affects the probability of ν oscillation $P(\nu_\mu \rightarrow \nu_e)$.

TABLE 2: Our calculated results for m_{lightest} with inverted hierarchy, normal hierarchy, and one-flavor leptogenesis. The symbol \checkmark (\times) is used when Y_B is within (not within) updated BAU range.

Case	m_{lightest}	One Flavor
NH, non-unitarity	0.0018 eV to 0.0023 eV	\checkmark
NH, unitarity	0.048 eV to 0.056 eV	\checkmark
IH, non-unitarity	0.05 eV to 0.054 eV	\checkmark
IH, unitarity	0.053 eV to 0.062 eV	\checkmark

(iii) The predicted values of CP-violating phases, δ_{CP} , and Majorana phases α and β are $36^\circ, 72^\circ, 108^\circ, 144^\circ, 180^\circ, 216^\circ, 252^\circ, 288^\circ, 324^\circ,$ and 360° . Here the calculated values of

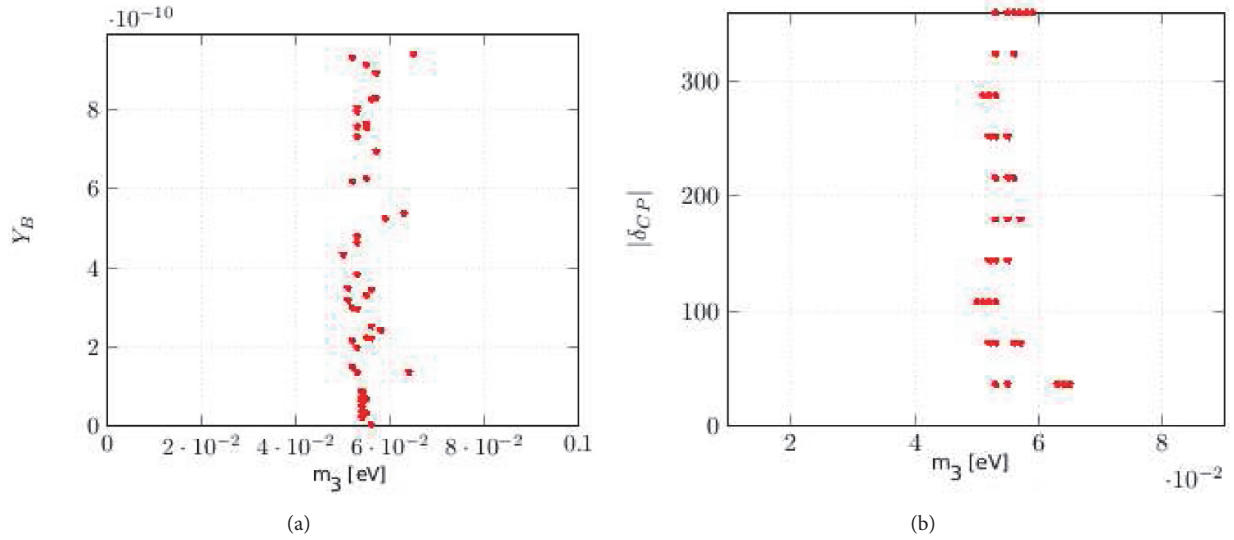


FIGURE 7: Scatter plot of the lightest neutrino mass against the baryon asymmetry of the Universe and Dirac CP phase δ_{CP} with inverted hierarchy, unitarity case in one-flavor leptogenesis regime. For Y_B in the order 10^{-10} , the lightest ν mass m_3 is concentrated in the region 0.053eV to 0.062 eV. The values of m_3 [eV] in (b) along the x-axis are multiplied by 10^{-2} .

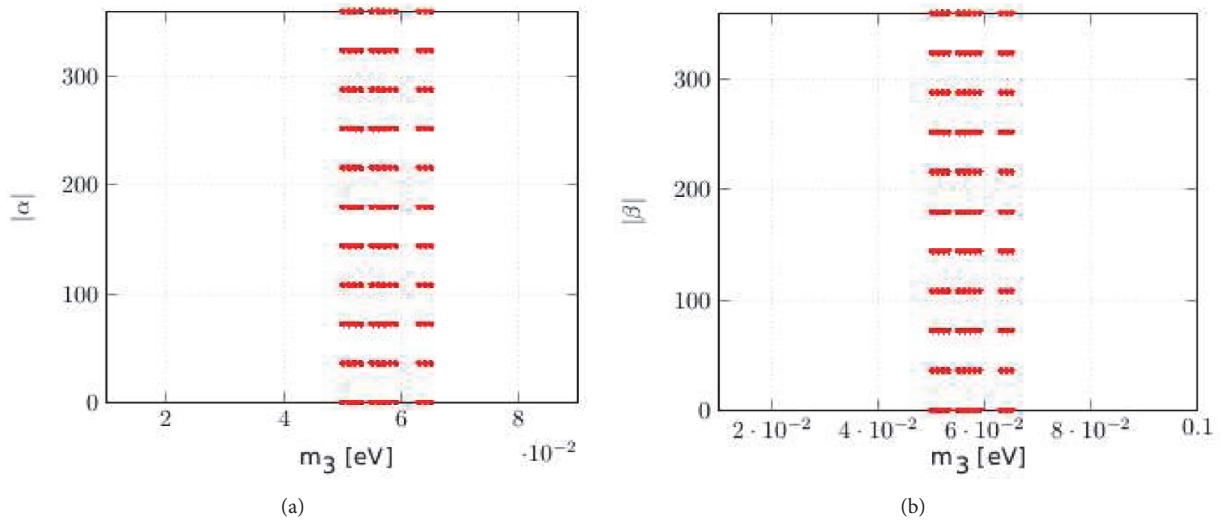


FIGURE 8: Variation of lightest neutrino mass m_3 with Majorana phases α and β for IH, unitarity texture of U_{PMNS} in one-flavor leptogenesis regime. The values of m_3 [eV] in (a) along the x-axis are multiplied by 10^{-2} .

each of the Dirac CP-violating phase, δ_{CP} , and the Majorana phases α and β are found to have the same set of values, i.e., $36^\circ, 72^\circ, 108^\circ, 144^\circ, 180^\circ, 216^\circ, 252^\circ, 288^\circ, 324^\circ$, and 360° .

5. Conclusion

In conclusion, in this work, we have considered the possibility that the neutrino mixing matrix (considering charged lepton mass matrix to be diagonal), U_{PMNS} , could be nonunitary and then calculated the limits on nonunitary parameters $\eta_{\mu e}$, $\eta_{\tau e}$, and $\eta_{\tau \mu}$ (see Table 1) from latest constraints on branching ratios of cLFV decays. It is well known that in usual type I see-saw mechanism, mixing of left- and right-handed neutrinos may lead to nonunitarity but it has been

found that [11] its effect is not significant for processes like lepton flavor violation and neutrino oscillation. Therefore we consider here a model (see [7]) where see-saw is extended by an additional singlet (very light) which, although inducing nonunitarity of the U_{PMNS} matrix, leaves formula for see-saw mechanism unmodified. This nonunitarity however may affect leptogenesis. Baryogenesis through leptogenesis is believed to be responsible for producing the matter-antimatter asymmetry present in the present day Universe, which can be expressed through parameter Y_B (baryon to photon ratio). We then analysed how the nonunitarity of U_{PMNS} can affect leptogenesis and hence calculated the values of lightest ν mass, Dirac CPV phase δ_{CP} , and Majorana phases α and β , such that Y_B lies in the present day constraints

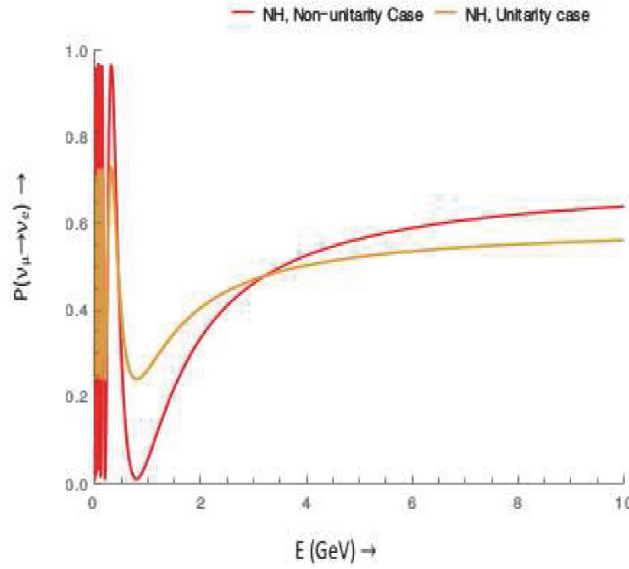


FIGURE 9: Variation of $P(\nu_\mu \rightarrow \nu_e)$ against energy E in Long Baseline Neutrino Experiments with value of Dirac CP phase, $\delta_{CP} = 1.45\pi$, equal to the best fit value [3]. The yellow (red) curve in the figure corresponds to unitarity (nonunitarity) of PMNS matrix.

TABLE 3: The results for Dirac CPV phase δ_{CP} and two Majorana phases α , β of all the four cases mentioned above in one flavor leptogenesis regime in this work. Here the calculated values of each of them (the Dirac CP-violating phase, δ_{CP} , and the Majorana phases α and β) are found to have the same set of values, i.e., 36° , 72° , 108° , 144° , 180° , 216° , 252° , 288° , 324° , and 360° .

$\delta_{CP}, \alpha, \beta$
$36^\circ, 72^\circ, 108^\circ,$
$144^\circ, 180^\circ, 216^\circ,$
$252^\circ, 288^\circ, 324^\circ,$
360°

($5.8 \times 10^{-10} < Y_B < 6.6 \times 10^{-10}$). This was done using type I see-saw mechanisms for producing light neutrino masses.

Above analysis was done for different cases: NH neutrino masses, unitary U_{PMNS} ; NH neutrino masses, nonunitary U_{PMNS} ; IH neutrino masses, unitary U_{PMNS} ; IH neutrino masses, nonunitary U_{PMNS} . We discussed these issues for unflavored leptogenesis regimes, for which $M_1 \geq 10^{12}$ GeV, where M_1 is the lightest one of the three heavy right-handed Majorana neutrinos, whose out-of-equilibrium decay produces lepton asymmetry (which in turn can be converted to BAU).

In this work, we have calculated new limits on nonunitarity parameters using latest bounds on cLFV decays and thus predicted values of lightest neutrino mass (Table 2) for both the hierarchies, which is still unknown experimentally. We also have predicted values of CPV phases – δ_{CP} (Dirac phase) and α and β (Majorana phases), which are also unknown so far (Table 3). Though Majorana phases do not affect neutrino oscillation probability, they may affect neutrino mass measurements in $0\nu\beta\beta$ experiments. Hence the results

in this work are important, keeping in view that in future experiments will be endeavoring to measure the values of absolute value of neutrino mass and CP-violating phase δ_{CP} and α , β (Majorana phases). Future measurements related to Dirac CPV phase in neutrino experiments will validate or contradict some of the results presented here. Our analysis in this work only provides a benchmark for consistent works affiliated to model building.

Disclosure

This paper is a talk presented at the XXII DAE BRNS High Energy Physics Symposium, 12–16 December 2016, Delhi University, India.

Conflicts of Interest

The authors declare that they have no conflicts of interest.

Acknowledgments

Gayatri Ghosh and Kalpana Bora would like to thank Debashish Borah for fruitful discussions and suggestions. Gayatri Ghosh would like to acknowledge UGC, Government of India, for providing RFSMS fellowship to her, during which this work was done. Gayatri Ghosh also acknowledges the fruitful discussions carried out on the constraints of the absolute neutrino mass scale sum at the XXII DAE BRNS High Energy Physics Symposium, 12–16 December 2016, Delhi University, India.

References

- [1] A. J. Cuesta, V. Niro, and L. Verde, “Neutrino mass limits: robust information from the power spectrum of galaxy surveys,” *Astrophysics: Cosmology and Nongalactic Astrophysics*, vol. 13, 2016.

- [2] A. M. Baldini et al., “Search for the lepton flavour violating decay $\mu^+ \rightarrow e^+ \gamma$ with the full dataset of the MEG experiment,” *The European Physical Journal C*, vol. 76, no. 8, p. 434, 2016.
- [3] I. Esteban, M. C. Gonzalez-Garcia, M. Maltoni, I. Martinez-Soler, and T. Schwetz, “Updated fit to three neutrino mixing: exploring the accelerator-reactor complementarity,” *Journal of High Energy Physics*, vol. 2017, p. 87, 2017.
- [4] S. Davidson, E. Nardi, and Y. Nir, “Leptogenesis,” *Physics Reports*, vol. 466, no. 4-5, pp. 105–177, 2008.
- [5] V. Kuzmin, V. Rubakov, and M. Shaposhnikov, “On the anomalous electroweak baryon number nonconservation in the early universe,” *Physics Letters B*, vol. 155, p. 36, 1985.
- [6] A. Abada, S. Davidson, F. Josse-Michaux, M. Losada, and A. Riotto, “Flavour issues in leptogenesis,” *Journal of Cosmology and Astroparticle Physics*, vol. 2006, 2006.
- [7] W. Rodejohann, “Non-unitary lepton mixing matrix, leptogenesis and low-energy CP violation,” *EPL (Europhysics Letters)*, vol. 88, no. 5, 2009.
- [8] J. A. Casas and A. Ibarra, “Oscillating neutrinos and muon $\rightarrow e, \gamma$,” *Nuclear Physics B*, vol. 618, no. 1-2, pp. 171–204, 2001.
- [9] S. Davidson, E. Nardi, and Y. Nir, “Leptogenesis,” *Physics Reports*, vol. 466, no. 105, pp. 105–177, 2008.
- [10] A. Sakharov, “Violation of CP invariance, C asymmetry, and baryon asymmetry of the universe,” *Pisma V Zhurnal Éksperimental'noi i Teoreticheskoi Fiziki*, vol. 5, no. 32, 1967.
- [11] Z. Z. Xing and S. Zhou, “Implications of leptonic unitarity violation at neutrino telescopes,” *Physics Letters B*, vol. 666, no. 2, pp. 166–172, 2008.
- [12] M. Malinsky, T. Ohlsson, and H. Zhang, “Nonunitarity effects in a realistic low-scale seesaw model,” *Physical Review D: Particles, Fields, Gravitation and Cosmology*, vol. 79, no. 7, Article ID 073009, 2009.
- [13] A. S. Joshipura, E. A. Paschos, and W. Rodejohann, “Leptogenesis in left–right symmetric theories,” *Nuclear Physics B*, vol. 611, pp. 227–238, 2001.
- [14] R. Barbieri, P. Creminelli, A. Strumia, and N. Tetradis, “Baryogenesis through leptogenesis,” *Nuclear Physics B*, vol. 575, no. 1-2, pp. 61–77, 2000.
- [15] A. Abada, S. Davidson, A. Ibarra, F. Josse-Michaux, M. Losada, and A. Riotto, “Flavour matters in leptogenesis,” *Journal of High Energy Physics*, vol. 2006, 2006.
- [16] E. Nardi, Y. Nir, E. Roulet, and J. Racker, “The importance of flavor in leptogenesis,” *Journal of High Energy Physics*, vol. 164, no. 1, pp. 4123–4149, 2006.
- [17] P. S. Dev, P. Millington, A. Pilaftsis, and D. Teresi, “Flavour covariant transport equations: an application to resonant leptogenesis,” *Nuclear Physics B*, vol. 886, pp. 569–664, 2014.
- [18] K. Bora, G. Ghosh, and D. Dutta, “Octant Degeneracy and Quadrant of Leptonic CPV Phase at Long Baseline,” *Advances in High Energy Physics*, vol. 2016, 11 pages, 2016, [talk presented at Simplicity II, Fermilab Theory Workshop, Fermilab USA, Sep 6- 9, 2016].
- [19] M. Borah, D. Borah, and M. K. Das, “Discriminating Majorana neutrino textures in light of the baryon asymmetry,” *Physical Review D: Particles, Fields, Gravitation and Cosmology*, vol. 91, no. 11, Article ID 113008, 2015.
- [20] G. Ghosh and K. Bora, “Effects of Leptonic Non-unitarity on Charged Lepton Flavor Violation, Leptogenesis and Lightest Neutrino Mass,” in *XXII DAE High Energy Physics Symposium*, vol. 203 of *Springer Proceedings in Physics*, pp. 309–311, Springer International Publishing, Cham, Switzerland, 2018.
- [21] K. Bora and G. Ghosh, “Charged lepton flavor violation $\mu \rightarrow e \gamma$ in $\mu - \tau$ symmetric SUSY SO(10) mSUGRA, NUHM, NUGM, and NUSM theories and LHC,” *The European Physical Journal C*, vol. 75, no. 428, 2015.
- [22] B. D. Fields, P. Molaro, and S. Sarkar, “Big bang nucleosynthesis,” in *Review of PDG-2014 (Astrophysical Constants and Parameters)*, 2014.

Review Article

Neutrino Emission from Cooper Pairs at Finite Temperatures

Lev B. Leinson 

Pushkov Institute of Terrestrial Magnetism, Ionosphere and Radiowave Propagation of the Russian Academy of Science (IZMIRAN), Troitsk, Moscow 108840, Russia

Correspondence should be addressed to Lev B. Leinson; leinson@yandex.ru

Received 27 December 2017; Revised 5 March 2018; Accepted 22 March 2018; Published 10 May 2018

Academic Editor: Theocharis Kosmas

Copyright © 2018 Lev B. Leinson. This is an open access article distributed under the Creative Commons Attribution License, which permits unrestricted use, distribution, and reproduction in any medium, provided the original work is properly cited. The publication of this article was funded by SCOAP³.

A brief review is given of the current state of the problem of neutrino pair emission through neutral weak currents caused by the Cooper pairs breaking and formation (PBF) in superfluid baryon matter at thermal equilibrium. The cases of singlet-state pairing with isotropic superfluid gap and spin-triplet pairing with an anisotropic gap are analyzed with allowance for the anomalous weak interactions caused by superfluidity. It is shown that taking into account the anomalous weak interactions in both the vector and axial channels is very important for a correct description of neutrino energy losses through the PBF processes. The anomalous contributions lead to an almost complete suppression of the PBF neutrino emission in spin-singlet superfluids and strong reduction of the PBF neutrino losses in the spin-triplet superfluid neutron matter, which considerably slows down the cooling rate of neutron stars with superfluid cores.

1. Introduction

At the long cooling era, the evolution of a neutron star (NS) surface temperature crucially depends on the overall rate of neutrino emission out of the star. The cooling dynamics below the superfluid transition temperature is governed primarily by the superfluid component of nucleon matter. The superfluidity of nucleons in NSs strongly suppresses most mechanisms of neutrino emission operating in the nonsuperfluid nucleon matter (the bremsstrahlung at nucleon collisions, modified Urca processes, etc. [1, 2]) but simultaneously strongly reduces the heat capacity and triggers the emission of neutrino pairs through neutral weak currents caused by the nucleon Cooper pair breaking and formation (PBF) processes in thermal equilibrium. Neutrino emission from Cooper pairs is currently thought to be the dominant cooling mechanism of baryon matter, for some ranges of the temperature and/or matter density. The total energy $\omega = \omega_1 + \omega_2$ and momentum $\mathbf{k} = \mathbf{k}_1 + \mathbf{k}_2$ of an escaping (massless) neutrino pair form a time-like four-momentum $K = (\omega, \mathbf{k})$, so the process is kinematically allowed only because of the existence of a superfluid energy gap Δ , which admits the nucleon transitions with $\omega > 2\Delta$ and $k < \omega$. (We use the Standard Model of weak interactions,

the system of units $\hbar = c = 1$, and the Boltzmann constant $k_B = 1$.)

The simplest case for baryon pairing corresponds to two particles correlated in the 1S_0 state with the total spin $S = 0$ and orbital momentum $L = 0$. The neutrino emissivity due to the PBF processes in the spin-singlet superfluid nucleon matter was first suggested and calculated by Flowers et al. [3]. The result of this calculation was recovered later by other authors [4–6]. Similar mechanism for the neutrino energy losses due to spin-singlet pairing of hyperons was suggested in [7–9]. For more than three decades these ideas were a key ingredient in numerical simulations of NS evolution (e.g., [10–12]). However, after such a long period, it was unexpectedly found that the PBF emission of neutrino pairs is practically absent in a nonrelativistic spin-singlet superfluid liquid [13]. Later this result was confirmed in other calculations [14–16]. (Note also the controversial work [17].)

The importance of the suppression of the PBF neutrino emission from the 1S_0 superfluid was first understood in [18] in connection with the fact that the previous theory predicted a too rapid cooling of the NS's crust, which dramatically contradicts the observed data of superbursts [19].

The 1S_0 neutron pairing in NS is essentially restricted to the crust. As a result, in the NS evolution, effects of

the suppression are mostly observed during the thermal relaxation of the crust [20–22]. The significant revision of PBF neutrino emission from this relatively thin layer does not change substantially the total energy losses from the star. The most neutrino losses occur from the NS core, which occupies more than 90% of the star’s volume and contains the superfluid neutrons paired in the $^3\text{P}_2$ state with $S = 1$, $L = 1$, and $J = 2$ [23, 24].

In the commonly used version of the minimal cooling paradigm, the emission of $^3\text{P}_2$ pairing was reduced by only about 30% due to the suppression of the vector channel of weak interactions [22, 25, 26]. This approach does not take into account the anomalous axial-vector weak interactions, existing due to spin fluctuations in the spin-triplet superfluid neutron matter [27]. Some simulations of the NS evolution accounting for the anomalous contributions predict a raising of its surface temperature and argue that a full exploration of this effect is necessary [28] (also see [29, 30]).

A correct description of the efficiency of neutrino emission in the PBF processes allows for a better understanding of observations [31–33]. This review is devoted to the current state of this problem. Since the complete calculations have been published repeatedly (e.g., [13, 27, 34]), I will briefly sketch the main steps of the derivation, referring the reader to the original papers for more detailed information.

2. Preliminary Notes

The low-energy Hamiltonian of the weak interaction may be described in a point-like approximation. For interactions mediated by neutral weak currents, it can be written as follows (e.g., [1]):

$$\mathcal{H}_{\text{vac}} = -\frac{G_F}{2\sqrt{2}} J_B^\mu l_\mu. \quad (1)$$

Here G_F is the Fermi coupling constant, and the neutrino weak current is given by $l_\mu = \bar{\nu}\gamma_\mu(1 - \gamma_5)\nu$, where γ_μ are Dirac matrices ($\mu = 0, 1, 2, 3$) and $\gamma_5 = -i\gamma_0\gamma_1\gamma_2\gamma_3$. The neutral weak current of the baryon, $J_\mu = C_V J_\mu^V - C_A J_\mu^A$, represents the combination of the vector and axial-vector terms, $J_\mu^V = \bar{\psi}\gamma_\mu\psi$ and $J_\mu^A = \bar{\psi}\gamma_\mu\gamma_5\psi$, respectively. Here ψ represents the baryon field. The weak coupling constants C_V and C_A are determined by quark composition of the baryons. For the reactions with neutrons, one has $C_V = 1$ and $C_A = g_A$, while, for those with protons, $C_V \approx -0.08$ and $C_A = -g_A$, where $g_A \approx 1.26$ is the axial-vector constant. Notice that similar interaction Hamiltonian, but with other coupling constants, describes the neutrino weak interaction of hyperons in NS matter (e.g., [35]).

In the nonrelativistic nucleon system, the vector part of the weak current can be approximated by its temporal component

$$J_0^V = \psi^\dagger \hat{1} \psi, \quad (2)$$

where $\hat{1} = \delta_{\alpha\beta}$. Throughout the text, a hat means a 2×2 matrix in spin space and $\alpha, \beta = \uparrow, \downarrow$. The axial weak current is given dominantly by its space component

$$J^A = \psi^\dagger \hat{\sigma} \psi, \quad (3)$$

where $\hat{\sigma} = (\hat{\sigma}_1, \hat{\sigma}_2, \hat{\sigma}_3)$ are Pauli spin matrices.

It is important to notice that the vector weak current is conserved in the standard theory. The conservation law implies that the transition matrix element in the vector channel of the reaction obeys the relation

$$\omega (J_0^V)_{fi} = \mathbf{k} (\mathbf{J}^V)_{fi}. \quad (4)$$

The transferred momentum \mathbf{k} enters into the medium response function through the quasiparticle energy, which for $k \ll p_F$ in a degenerate Fermi liquid takes the form $\xi_{\mathbf{p}+\mathbf{k}} \approx v_F(\mathbf{p} - \mathbf{p}_F) + \mathbf{k}\mathbf{v}_F$. Thus, in the absence of external fields, the momentum transfer \mathbf{k} enters the response function of the medium only in combination with the Fermi velocity, which is small in the nonrelativistic system, $v_F \ll 1$. Therefore, for the PBF processes the relation $k v_F \ll \omega, \Delta$ is always satisfied. This allows one to evaluate the medium response function in the long-wave limit $\mathbf{k} \rightarrow 0$. Together with the conservation law (4) this immediately yields $(J_0^V)_{fi} = 0$ for $\omega > 2\Delta$, which means that the neutrino pair emission through the vector channel of weak interactions is strongly suppressed in the nonrelativistic system. This important fact was overlooked for a long time, since a direct calculation shows that the matrix element $(J_0^V)_{fi}$ for the recombination of two Bogolons into the condensate does not vanish, which erroneously leads to a large neutrino emissivity through the vector channel.

First calculations of the PBF neutrino energy losses were performed using a vacuum-type weak interactions assuming that the medium effects can be taken into account by introducing effective masses of participating quasiparticles [3, 6]. This resulted in a substantial overestimate of the PBF neutrino energy losses from the superfluid core and inner crust of NSs. Only three decades later has it been understood that the calculation of neutrino radiation from a superfluid Fermi liquid requires a more delicate approach.

Within the Nambu-Gor’kov formalism the effective vertex of nucleon interactions with an external neutrino field represents a 2×2 matrix in the particle-hole space. This matrix is diagonal for nucleons in the normal Fermi liquid but it gets the off-diagonal entries in superfluid systems [36–39]. The diagonal elements represent the ordinary (dressed) vertices of the field interaction with quasiparticles and holes, respectively, while the off-diagonal elements of the matrix represent the effective vertices for a virtual breaking and formation of Cooper pairs in the external field. In other words, the off-diagonal components of the vertex matrix describe a coupling of the external field with fluctuations of the order parameter in the superfluid Fermi liquid. These so-called “anomalous weak interactions” should be necessarily taken into account when calculating the neutrino energy losses from superfluid cores of NSs.

In particular, the anomalous weak interactions are crucial for the neutrino emission caused by the PBF processes. For example, in nonrelativistic systems, the ordinary and anomalous contributions into the matrix element of the weak vector transition current are mutually cancelled in the long-wave limit, leading to a strong suppression of the PBF neutrino emission [13]. The more accurate calculation [14, 16] has shown that the neutrino pair emission owing to the density fluctuations is suppressed proportionally to v_F^4 . This

reflects the well known fact that the dipole radiation is not possible in the vector channel in the collision of two identical particles. Thus, exactly due to the anomalous contributions, the PBF neutrino emission in the vector channel of weak interactions is practically absent.

In the case of 1S_0 pairing this has far-reaching consequences. The total spin $\mathbf{S} = 0$ of the nonrelativistic Cooper pair is conserved. Therefore the neutrino emission through the axial-vector channel of weak interactions could arise only due to small relativistic effects and is proportional to v_F^2 [3, 15]. Thus the PBF neutrino energy losses due to singlet-state pairing of baryons can, in practice, be neglected in simulations of NS cooling. This makes the neutrino radiation from 1S_0 pairing of protons or hyperons unimportant.

The minimal cooling paradigm [22] suggests that, below the critical temperature for a triplet pairing of neutrons, the dominant neutrino energy losses occur from the superfluid neutron liquid in the inner core of a NS. It is commonly believed [23, 24, 40–42] that, in this case, the 3P_2 pairing (with a small admixture of 3F_2 state) takes place with a preferred magnetic quantum number $M_J = 0$. Since the spin of a Cooper pair in the 3P_2 state is $S = 1$ the spin fluctuations are possible and the PBF neutrino energy losses from the neutron superfluid occur through the axial channel of weak interactions.

The pairing interaction, in the most attractive 3P_2 channel, can be written as [23]

$$\begin{aligned} \Gamma_{\alpha\beta,\gamma\delta}(\mathbf{p}, \mathbf{p}') \\ = \frac{\pi^2}{p_F m^*} V(p, p') [\bar{\mathbf{b}}(\mathbf{n}) \hat{\sigma}_i \hat{\sigma}_j]_{\alpha\beta} [i\hat{\sigma}_2 \hat{\sigma} \bar{\mathbf{b}}(\mathbf{n}')]_{\gamma\delta}, \end{aligned} \quad (5)$$

where $V(p, p')$ is the corresponding interaction amplitude; p_F and $m^* = p_F/v_F$ are the Fermi momentum and the neutron effective mass, respectively, so that $p_F m^*/\pi^2$ is the density of states near the Fermi surface. The angular dependence of the interaction is represented by Cartesian components of the unit vector $\mathbf{n} = \mathbf{p}/p$ which involves the polar angles on the Fermi surface,

$$\begin{aligned} n_1 &= \sin \theta \cos \varphi, \\ n_2 &= \sin \theta \sin \varphi, \\ n_3 &= \cos \theta. \end{aligned} \quad (6)$$

Further, $\bar{\mathbf{b}}(\mathbf{n})$ is a real vector in the spin space, normalizable by condition

$$\langle \bar{b}^2(\mathbf{n}) \rangle = 1. \quad (7)$$

Hereafter we use the angle brackets to denote angle averages,

$$\langle \dots \rangle \equiv \frac{1}{4\pi} \int d\mathbf{n} \dots = \frac{1}{2} \int_{-1}^1 dn_3 \int_0^{2\pi} \frac{d\varphi}{2\pi} \dots \quad (8)$$

For spin-triplet pairing, the order parameter $\hat{D} \equiv D_{\alpha\beta}(\mathbf{n})$ is a symmetric matrix in the spin space, which near the Fermi surface can be written as follows (see, e.g., [43]):

$$\hat{D}(\mathbf{n}, T) = \Delta \bar{\mathbf{b}} \hat{\sigma}_i \hat{\sigma}_2, \quad (9)$$

where the temperature-dependent gap amplitude $\Delta(T)$ is a real constant.

The vector $\bar{\mathbf{b}}$ defines the angle anisotropy of energy gap which depends on the phase state of the superfluid condensate. In general, this vector can be written in the form $\bar{b}_i = \bar{A}_{ij} n_j$, where \bar{A}_{ij} is a 3×3 matrix. In the case of a unitary 3P_2 condensate the matrix \bar{A}_{ij} must be a real symmetric traceless tensor. It may be specified by giving the orientation of its principal axes and its two independent diagonal elements in its principal-axis coordinate system. Within the preferred coordinate system, the ground state with $M_J = 0$ is described by the matrix

$$\bar{A}_{ij} = \frac{1}{\sqrt{2}} \text{diag}(-1, -1, 2) \quad (10)$$

and $\bar{b}^2(\mathbf{n}) = 1/2(1 + 3\cos^2\theta)$.

3. General Approach to Neutrino Energy Losses

Thermal fluctuations of the neutral weak currents in nucleon matter are closely related to the imaginary, dissipative part of the response function of the medium onto the external neutrino field. According to the fluctuation-dissipation theorem, the total energy loss per unit volume and time caused by thermal fluctuations of the neutral weak current in the nucleon matter is given by the following formula:

$$\begin{aligned} Q &= \frac{G_F^2}{8} \sum_{\nu} \int \omega \\ &\cdot \frac{2 \text{Im} \Pi_{\mu\nu}(\omega, \mathbf{k}) \text{Tr}(l^\mu l^{\nu*})}{1 - \exp(\omega/T)} \frac{d^3 k_1}{2\omega_1 (2\pi)^3} \frac{d^3 k_2}{2\omega_2 (2\pi)^3}, \end{aligned} \quad (11)$$

where $\text{Im} \Pi_{\mu\nu}$ is the imaginary part of the retarded weak polarization tensor. The integration goes over the phase volume of neutrinos and antineutrinos of total energy $\omega = \omega_1 + \omega_2$ and total momentum $\mathbf{k} = \mathbf{k}_1 + \mathbf{k}_2$. The symbol \sum_{ν} indicates a summation over three neutrino flavors. The factor $[1 - \exp(\omega/T)]^{-1}$ occurs as a result of averaging over the Gibbs distribution, which must be performed at finite ambient temperatures.

By inserting $\int d^4 K \delta^{(4)}(K - K_1 - K_2) = 1$ in this equation and making use of the Lenard's integral

$$\begin{aligned} \int \frac{d^3 k_1}{2\omega_1} \frac{d^3 k_2}{2\omega_2} \delta^{(4)}(K - K_1 - K_2) \text{Tr}(l^\mu l^{\nu*}) \\ = \frac{4\pi}{3} (K^\mu K^\nu - K^2 g^{\mu\nu}) \Theta(K^2) \Theta(\omega), \end{aligned} \quad (12)$$

where $K_1 = (\omega_1, \mathbf{k}_1)$, $K_2 = (\omega_2, \mathbf{k}_2)$, $\Theta(x)$ is the Heaviside step function, and $g^{\mu\nu} = \text{diag}(1, -1, -1, -1)$ is the signature tensor, we can write

$$\begin{aligned} Q &= \frac{G_F^2 \mathcal{N}_\nu}{192\pi^5} \int_0^\infty d\omega \int d^3 k \\ &\cdot \frac{\omega \Theta(\omega - k)}{1 - \exp(\omega/T)} \text{Im} \Pi_{\mu\nu}(\omega, \mathbf{k}) (K^\mu K^\nu - K^2 g^{\mu\nu}), \end{aligned} \quad (13)$$

where $\mathcal{N}_\nu = 3$ is the number of neutrino flavors.



FIGURE 1: Graphs for the polarization tensor.

In general, the weak polarization tensor of the medium is a sum of the vector-vector, axial-axial, and mixed terms. The mixed vector-axial polarization has to be an antisymmetric tensor, and its contraction in (13) with the symmetric tensor $K^\mu K^\nu - K^2 g^{\mu\nu}$ vanishes. Thus only the pure-vector and pure-axial polarization should be taken into account. We then obtain

$$\text{Im } \Pi_{\mu\nu} = C_V^2 \text{Im } \Pi_{\mu\nu}^V + C_A^2 \text{Im } \Pi_{\mu\nu}^A, \quad (14)$$

where C_V and C_A are vector and axial-vector weak coupling constants of a neutron, respectively.

4. Weak Interactions in Superfluid Fermi Liquids

Physically, the polarization tensor represents a correction to the Z-boson self-energy in the medium. Making use of the adopted graphical notation for the ordinary and anomalous propagators, $\widehat{G} = \longrightarrow$, $\widehat{G}^-(p) = \longleftarrow$, $\widehat{F}^{(1)} = \longrightarrow\longleftarrow$, and $\widehat{F}^{(2)} = \longleftarrow\longrightarrow$, one can represent the polarization function in each of the channels as the sum of graphs depicted in Figure 1.

As can be seen, the field interaction with superfluid fermions should be described with the aid of four effective three-point vertices. There are two usual effective vertices (shown by dots) corresponding to the creation of a particle and a hole by the Z-field. Let us denote them as $\widehat{\tau}(\mathbf{n}; \omega, \mathbf{k})$ and $\widehat{\tau}^-(\mathbf{n}; \omega, \mathbf{k}) \equiv \widehat{\tau}^T(-\mathbf{n}; \omega, \mathbf{k})$, respectively. We omit the Dirac indices in these symbolic notations. In reality, according to (2) and (3), the nonrelativistic ordinary vector vertex is represented by its temporal component; that is, it is a scalar matrix in spin space. The ordinary axial-vector vertices of a particle and a hole are represented by space-vectors whose components consist of spin matrices.

Two more vertices, represented by triangles, correspond to the creation of two particles or two holes. These so-called ‘‘anomalous’’ vertices appear because the pairing interaction among quasiparticles is to be incorporated in the coupling vertex up to the same degree of approximation as in the self-energy of a quasiparticle [36, 37]. This means that the anomalous effective vertices are given by infinite sums of diagrams with allowance for pair interaction in the ladder approximation, in the same way as in the gap equations.

Given by the sum of ladder-type diagrams [38], the anomalous vertices are to satisfy Dyson’s equations symbolically depicted by graphs in Figure 2(a). In these graphs, the rectangles denote pairing interaction, which in the channel of two quasiparticles is given by (5). The vertex equations are to be supplemented by the gap equation shown graphically in Figure 2(b). This equation, whose solution is assumed to be known, serves to eliminate the amplitude of the pair interaction from the vertex equations near the Fermi surface. The standard gap equation involves integrations over the

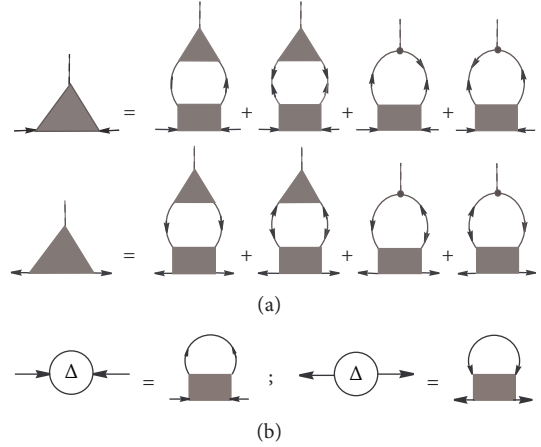


FIGURE 2: Dyson’s equations for the anomalous vertices (a) and the gap equations (b). Shaded rectangles represent the pairing interaction.

regions far from the Fermi surface. This integration can be eliminated by means of the renormalization of the pairing interaction, as suggested in [39]. Details of this calculation can be found in [34].

The analytic form of the quasiparticle propagators in the momentum representation can be written as

$$\begin{aligned} \widehat{G} &= G(\varepsilon_s, \mathbf{p}) \widehat{1}, \\ \widehat{F}^{(1)} &= F(\varepsilon_s, \mathbf{p}) (\overline{\mathbf{b}\hat{\sigma}}) i\hat{\sigma}_2, \\ \widehat{F}^{(2)} &= \widehat{F}^{(1)\dagger}(-\varepsilon_s, -\mathbf{p}) = i\hat{\sigma}_2 (\overline{\mathbf{b}\hat{\sigma}}) F(-\varepsilon_s, -\mathbf{p}). \end{aligned} \quad (15)$$

Making use of the Matsubara calculation technique we define the scalar part of the Green functions

$$\begin{aligned} G(\varepsilon_s, \mathbf{p}) &= \frac{-i\varepsilon_s - \xi_p}{\varepsilon_s^2 + E_p^2}, \\ F(\varepsilon_s, \mathbf{p}) &= \frac{\Delta}{\varepsilon_s^2 + E_p^2}. \end{aligned} \quad (16)$$

Here $\varepsilon_s = (2s+1)\pi T$ with $s = 0, \pm 1, \pm 2, \dots$ being the fermionic Matsubara frequency which depends on the temperature T , and

$$E = \sqrt{\xi^2 + \Delta_{\mathbf{n}}^2} \quad (17)$$

stands for the Bogolon energy. The angle-dependent energy gap is given by $\Delta_{\mathbf{n}}^2 \equiv \Delta^2 \overline{b^2}(\mathbf{n})$.

It should be noted that, by virtue of (7), the amplitude $\Delta(T)$ is chosen to represent the energy gap averaged over the Fermi surface. Thus determined, the energy gap gives a general measure of the pairing correction to the energy of the ground state in the preferred state.

In general, the ordinary vertices in the Dyson equations should be dressed owing to residual Fermi-liquid interactions. We neglect this effect and account for the residual interactions by means of the effective nucleon mass only.

In this case the ordinary vertices are as defined in (2) and (3). Namely, the nonrelativistic ordinary vector vertex is represented by its temporal component

$$\hat{\tau}_V = \hat{\tau}_V^- = \hat{1}. \quad (18)$$

The ordinary axial-vector vertices of a particle and a hole are to be taken as

$$\begin{aligned} \hat{\tau}_A &= \hat{\boldsymbol{\sigma}}, \\ \hat{\tau}_A^- &= \hat{\boldsymbol{\sigma}}^T, \end{aligned} \quad (19)$$

where the superscript ‘‘T’’ transposes the matrix.

In the case of pairing in the channel with spin, orbital, and total angular momenta, $S = 1$, $L = 1$, $J = 2$, respectively, one can search for the anomalous vertices near the Fermi surface in the form of expansions over the eigenfunctions of the total angular momentum (J, M) with $J = 2$ and $M = 0, \pm 1, \pm 2$. For our calculations it is convenient to use vector notation which involves a set of mutually orthogonal complex vectors $\mathbf{b}_M(\mathbf{n})$ in spin space which generates standard spin-angle matrices according to

$$\begin{aligned} \frac{1}{\sqrt{8\pi}} \mathbf{b}_M(\mathbf{n}) \hat{\boldsymbol{\sigma}} i \hat{\boldsymbol{\sigma}}_2 &\equiv \sum_{M_S+M_L=M} \left(\frac{1}{2} \frac{1}{2} \alpha \beta \mid 1M_S \right) \\ &\cdot (11M_S M_L \mid 2M) Y_{1,M_L}(\mathbf{n}), \end{aligned} \quad (20)$$

where $\alpha, \beta = \uparrow, \downarrow$ denote spin projections.

These vectors are of the form

$$\begin{aligned} \mathbf{b}_0 &= \sqrt{\frac{1}{2}} (-n_1, -n_2, 2n_3), \\ \mathbf{b}_1 &= -\sqrt{\frac{3}{4}} (n_3, in_3, n_1 + in_2), \\ \mathbf{b}_2 &= \sqrt{\frac{3}{4}} (n_1 + in_2, in_1 - n_2, 0), \\ \mathbf{b}_{-M} &= (-)^M \mathbf{b}_M^*. \end{aligned} \quad (21)$$

These are normalized by the condition

$$\langle \mathbf{b}_{M'}^* \mathbf{b}_M \rangle = \delta_{M'M}. \quad (22)$$

Generally speaking, the anomalous vertices are functions of the transferred energy and momentum (ω, \mathbf{k}) and the direction \mathbf{n} of the quasiparticle momentum. As was mentioned in Introduction, it is sufficient to evaluate the medium response function in the limit $\mathbf{k} \rightarrow 0$. Then the nonrelativistic anomalous vector vertex can be expanded in the eigenfunctions of the total angular momentum $J = 2$ in the form

$$\begin{aligned} \hat{\mathcal{T}}^{(1)} &= \sum_M \mathcal{B}_M^{(1)}(\omega) \mathbf{b}_M \hat{\boldsymbol{\sigma}} i \hat{\boldsymbol{\sigma}}_2, \\ \hat{\mathcal{T}}^{(2)} &= \sum_M \mathcal{B}_M^{(2)}(\omega) i \hat{\boldsymbol{\sigma}}_2 \hat{\boldsymbol{\sigma}} \mathbf{b}_M. \end{aligned} \quad (23)$$

Accordingly, the anomalous axial-vector vertices can be represented in the form

$$\begin{aligned} \hat{\mathbf{T}}^{(1)} &= \sum_M \mathbf{B}_M^{(1)}(\omega) \mathbf{b}_M \hat{\boldsymbol{\sigma}} i \hat{\boldsymbol{\sigma}}_2, \\ \hat{\mathbf{T}}^{(2)} &= \sum_M \mathbf{B}_M^{(2)}(\omega) i \hat{\boldsymbol{\sigma}}_2 \hat{\boldsymbol{\sigma}} \mathbf{b}_M. \end{aligned} \quad (24)$$

Making use of these general forms in the Dyson equations together with the corresponding ordinary vertices, after tedious computations, one can get [34] in the vector channel

$$\mathcal{B}_M^{(1)} = -\mathcal{B}_M^{(2)} \equiv \mathcal{B}_M, \quad (25)$$

where \mathcal{B}_M obeys the equation

$$\begin{aligned} \sum_{M'} 2 \langle [(\Omega^2 - \bar{b}^2) \mathbf{b}_M^* \mathbf{b}_{M'} + (\mathbf{b}_M^* \bar{\mathbf{b}}) (\mathbf{b}_{M'} \bar{\mathbf{b}})] \mathcal{J}_0 \rangle \\ \cdot \mathcal{B}_{M'} + \langle (b_M^2 - \bar{b}^2) A \rangle \mathcal{B}_M = 2\Omega \langle (\mathbf{b}_M^* \bar{\mathbf{b}}) \mathcal{J}_0 \rangle. \end{aligned} \quad (26)$$

In the axial-vector channel one finds

$$\mathbf{B}_M^{(1)} = \mathbf{B}_M^{(2)} \equiv \mathbf{B}_M \quad (27)$$

with \mathbf{B}_M satisfying the equation

$$\begin{aligned} \sum_{M'} 2 \langle [\Omega^2 \mathbf{b}_M^* \mathbf{b}_{M'} - (\mathbf{b}_M^* \bar{\mathbf{b}}) (\mathbf{b}_{M'} \bar{\mathbf{b}})] \mathcal{J}_0 \rangle \mathbf{B}_{M'} \\ + \langle (b_M^2 - \bar{b}^2) A \rangle \mathbf{B}_M = -2i\Omega \langle (\mathbf{b}_M^* \times \bar{\mathbf{b}}) \mathcal{J}_0 \rangle. \end{aligned} \quad (28)$$

In the above expressions, the following notation is used:

$$\Omega = \frac{\omega}{2\Delta}. \quad (29)$$

The functions $\mathcal{J}_0(\omega, \mathbf{n}, T)$ and $A(\mathbf{n}, T)$ are given by

$$\mathcal{J}_0(\omega, \mathbf{n}) = \int_{-\infty}^{\infty} \frac{d\xi}{E} \frac{\Delta^2}{4E^2 - (\omega + i0)^2} \tanh \frac{E}{2T}, \quad (30)$$

$$A(\mathbf{n}) \equiv \int_{-\infty}^{\infty} d\xi \left(\frac{1}{2E} \tanh \frac{E}{2T} - \frac{1}{2\xi} \tanh \frac{\xi}{2T} \right). \quad (31)$$

From (26) and (28) it is seen that an accurate calculation of the anisotropic anomalous vertices at arbitrary temperatures apparently requires numerical computations. It would be desirable, however, to get reasonable analytic expressions for the anomalous vertices, which can be applied to a calculation of the neutrino energy losses. To proceed, let us notice that the anisotropy of the functions $\mathcal{J}_0(\omega, \mathbf{n})$ and $A(\mathbf{n})$ is due to the dependence of the energy of the Bogolons (17) on the direction of the momentum relative to the quantization axis. In a uniform system without external fields and at absolute zero, the orientation of the quantization axis is arbitrary. For equilibrium at a nonzero temperature this leads to the formation of a loose domain structure [44], where each microscopic domain has a randomly oriented preferred axis. This fact is normally used in order to simplify the calculations by replacing the angle-dependent energy gap with some effective isotropic value (see, e.g., [45, 46]).

Making use of this trick we replace the angle-dependent energy gap $\Delta_{\mathbf{n}}^2 \equiv \Delta^2 \bar{b}^2(\mathbf{n})$ in the Bogolons energy by its average value $\langle \Delta^2 \bar{b}^2(\mathbf{n}) \rangle = \Delta^2$, in accordance with (7). Then the functions \mathcal{S}_0 and A can be moved out of the integrals over the solid angle in (26) and (28). Using further the axial symmetry of the order parameter, (22), and the fact that

$$\left\langle \left(\mathbf{b}_M^* \mathbf{b}_M - \bar{b}^2 \right) \right\rangle = 0, \quad (32)$$

we get for the vector channel the equation

$$\begin{aligned} & \left(\Omega^2 - \langle \bar{b}^2 \mathbf{b}_M^* \mathbf{b}_M \rangle \right) \mathcal{B}_M + \sum_{M'} \langle \left(\mathbf{b}_M^* \bar{\mathbf{b}} \right) \left(\mathbf{b}_{M'} \bar{\mathbf{b}} \right) \rangle \mathcal{B}_{M'} \\ & = \Omega \langle \mathbf{b}_M^* \bar{\mathbf{b}} \rangle. \end{aligned} \quad (33)$$

In the axial channel we obtain the equation

$$\begin{aligned} & \Omega^2 \mathbf{B}_M - \sum_{M'} \langle \left(\mathbf{b}_M^* \bar{\mathbf{b}} \right) \left(\mathbf{b}_{M'} \bar{\mathbf{b}} \right) \rangle \mathbf{B}_{M'} \\ & = -i\Omega \langle \left(\mathbf{b}_M^* \times \bar{\mathbf{b}} \right) \rangle. \end{aligned} \quad (34)$$

The specific form of solutions to (33) and (34) depends on the phase state of the condensate.

An inspection of (10) and (21) allows one to conclude that for the ground state with $M_J = 0$,

$$\bar{\mathbf{b}}_{M=0} = \mathbf{b}_0. \quad (35)$$

In this case we get $\langle \mathbf{b}_M^* \bar{\mathbf{b}} \rangle = \delta_{M,0}$, and the only nonvanishing values of $\langle \mathbf{b}_M^* \times \bar{\mathbf{b}} \rangle$ correspond to $M = \pm 1$. Simple calculations give

$$\mathcal{B}_M = \frac{2\Delta}{\omega} \delta_{M,0}, \quad (36)$$

$$\mathbf{B}_1 = \sqrt{\frac{3}{2}} \frac{\Delta\omega}{\omega^2 - \Delta^2/5} \mathbf{e}^*, \quad (37)$$

$$\mathbf{B}_{-1} = \sqrt{\frac{3}{2}} \frac{\Delta\omega}{\omega^2 - \Delta^2/5} \mathbf{e},$$

where

$$\mathbf{e} = (1, i, 0). \quad (38)$$

Substituting the obtained expressions to (23)–(24) we get the anomalous vertices which, together with the ordinary vertices (18) and (19), can be used to calculate the weak polarization tensor of the medium. We now turn to a calculation of the corresponding correlation functions separately in the vector and axial channel of weak interactions.

5. Correlation Functions of Weak Currents

5.1. Vector Channel. Following the graphs of Figure 1 the vector-vector part of the polarization tensor, $\Pi_{\mu\nu}^V = \delta_{\mu 0} \delta_{\nu 0} \Pi_{00}^V$, is given by analytic continuation of the following

Matsubara sums to the upper half-plane of the complex variable ω :

$$\begin{aligned} \Pi_{00}^V(\omega) = T \sum_{\mathbf{p}, \varepsilon_s} \text{Tr} & \left(\widehat{G}_+ \widehat{G} + \widehat{F}_+^{(1)} \widehat{F}^{(2)} + \widehat{F}_+^{(1)} \widehat{\mathcal{F}}^{(1)} \widehat{G} \right. \\ & \left. + \widehat{G}_+ \widehat{\mathcal{F}}^{(2)} \widehat{F}^{(2)} \right). \end{aligned} \quad (39)$$

We use the notations $\widehat{G}_+ = \widehat{G}(\varepsilon_s + \omega_n, \mathbf{p})$ and $\widehat{F}_+^{(1)} = \widehat{F}^{(1)}(\varepsilon_s + \omega_n, \mathbf{p})$, where $\omega_n = 2i\pi T n$ with $n = 0, \pm 1, \pm 2, \dots$ being a bosonic Matsubara frequency.

The two first terms in the right-hand side of (39) describe the medium polarization without anomalous contributions. The long-wave limit of this ordinary contribution in the vector channel can be found in the form

$$\left(\Pi_{00}^V \right)_{\text{ordin}} \simeq -4 \frac{P_F m^*}{\pi^2} \left\langle \bar{b}^2(\mathbf{n}) \mathcal{S}_0(\mathbf{n}, \omega) \right\rangle. \quad (40)$$

Evidently this expression does not satisfy the condition of current conservation $\omega \Pi_{00}^V = k_i \Pi_{i0}^V$, which in the long-wave limit $\mathbf{k} \rightarrow 0$ requires $\Pi_{00}^V(\omega > 0) = 0$.

The last two terms in (39), with the vertices indicated in (23), represent the anomalous contributions. According to (25) and (36) the anomalous vector vertices can be written as

$$\widehat{\mathcal{F}}^{(1)} = \frac{2\Delta}{\omega} \bar{\mathbf{b}} \hat{\sigma}_1 \hat{\sigma}_2, \quad (41)$$

$$\widehat{\mathcal{F}}^{(2)} = -\frac{2\Delta}{\omega} i \hat{\sigma}_2 \bar{\boldsymbol{\sigma}}.$$

Straightforward calculations give in the long-wave limit

$$\left(\Pi_{00}^V \right)_{\text{anom}} \simeq 4 \frac{P_F m^*}{\pi^2} \left\langle \bar{b}^2(\mathbf{n}) \mathcal{S}_0(\mathbf{n}, \omega) \right\rangle. \quad (42)$$

We finally find

$$\Pi_{00}^V(\omega, \mathbf{0}) = \left(\Pi_{00}^V \right)_{\text{ordin}} + \left(\Pi_{00}^V \right)_{\text{anom}} = 0, \quad (43)$$

as is required by the current conservation condition. This proves explicitly that the neutrino emissivity via the vector channel, as initially obtained in [6], is a subject of inconsistency.

5.2. Axial Channel. In the axial channel, the ordinary vertices (19) and anomalous vertices (46) consist of only space components, and thus $\Pi_{\mu\nu}^A \simeq \delta_{\mu i} \delta_{\nu j} C_A^2 \Pi_{ij}^A$, where Π_{ij}^A is to be found as the analytic continuation of the following Matsubara sums:

$$\begin{aligned} \Pi_{ij}^A(\omega) = T \sum_{\mathbf{p}, \varepsilon_s} \text{Tr} & \left(\hat{\sigma}_i \widehat{G}_+ \hat{\sigma}_j \widehat{G} + \hat{\sigma}_i \widehat{F}_+^{(1)} \hat{\sigma}_j \widehat{F}^{(2)} \right) \\ & + T \sum_{\mathbf{p}, \varepsilon_s} \text{Tr} \left(\hat{\sigma}_i \widehat{F}_+^{(1)} \widehat{T}_j^{(1)} \widehat{G} + \hat{\sigma}_i \widehat{G}_+ \widehat{T}_j^{(2)} \widehat{F}^{(2)} \right). \end{aligned} \quad (44)$$

Here the first line represents the ordinary contribution and the second line is the contribution of the anomalous interactions. The ordinary contribution can be evaluated in the form

$$\begin{aligned} & (\Pi_{ij}^A)_{\text{ordin}} \\ &= -4 \frac{p_F m^*}{\pi^2} \left\langle \left(\bar{b}^2(\mathbf{n}) \delta_{ij} - \bar{b}_i(\mathbf{n}) \bar{b}_j(\mathbf{n}) \right) \mathcal{S}_0(\mathbf{n}, \omega) \right\rangle. \end{aligned} \quad (45)$$

In the case of $M_J = 0$, when $\bar{\mathbf{b}} = \mathbf{b}_0$, from (24), (37), and (38), we get

$$\begin{aligned} \hat{\mathbf{T}}^{(1)} &= \sqrt{\frac{3}{2}} \\ &\cdot \frac{\omega \Delta}{(\omega + i0)^2 - \Delta^2/5} \left[\mathbf{e}^* (\hat{\sigma} \mathbf{b}_1) i \hat{\sigma}_2 + \mathbf{e} (\hat{\sigma} \mathbf{b}_{-1}) i \hat{\sigma}_2 \right], \\ \hat{\mathbf{T}}^{(2)} &= \sqrt{\frac{3}{2}} \\ &\cdot \frac{\omega \Delta}{(\omega + i0)^2 - \Delta^2/5} \left[i \hat{\sigma}_2 (\hat{\sigma} \mathbf{b}_1) \mathbf{e}^* + i \hat{\sigma}_2 (\hat{\sigma} \mathbf{b}_{-1}) \mathbf{e} \right]. \end{aligned} \quad (46)$$

Poles of the vertex function correspond to collective eigenmodes of the system (see, e.g., [34, 47, 48]). Thus, the pole at $\omega^2 = \Delta^2/5$ signals the existence of collective oscillations of the total angular momentum. The pole location on the complex ω -plane is chosen so as to obtain a retarded vertex.

Principally, the decay of these collective oscillations into neutrino pairs is also possible by giving the additive contribution into neutrino energy losses via the axial channel of weak interactions. Later we will return to this problem. Here we concentrate on the PBF processes. In this case we are interested in $\omega > 2\Delta \bar{b}(\theta) \geq \sqrt{2}\Delta$, and a small term $\Delta^2/5 \ll \omega^2$ in the denominator of (46) can be discarded to obtain simpler expressions

$$\begin{aligned} \hat{\mathbf{T}}^{(1)}(\mathbf{n}) &= \sqrt{\frac{3}{2}} \frac{\Delta}{\omega} \left[\mathbf{e}^* (\hat{\sigma} \mathbf{b}_1) i \hat{\sigma}_2 + \mathbf{e} (\hat{\sigma} \mathbf{b}_{-1}) i \hat{\sigma}_2 \right], \\ \hat{\mathbf{T}}^{(2)}(\mathbf{n}) &= \sqrt{\frac{3}{2}} \frac{\Delta}{\omega} \left[i \hat{\sigma}_2 (\hat{\sigma} \mathbf{b}_1) \mathbf{e}^* + i \hat{\sigma}_2 (\hat{\sigma} \mathbf{b}_{-1}) \mathbf{e} \right]. \end{aligned} \quad (47)$$

Substituting expressions (47) in the second line of (44) we obtain the anomalous part of the axial polarization tensor in the long-wave limit:

$$\begin{aligned} & (\Pi_{ij}^A)_{\text{anom}} \\ &= 3 \frac{p_F m^*}{\pi^2} \left\langle \left(\delta_{ij} - \delta_{i3} \delta_{j3} \right) \bar{b}^2(\mathbf{n}) \mathcal{S}_0(\mathbf{n}, \omega) \right\rangle. \end{aligned} \quad (48)$$

Summing together the contributions, given in (45) and (48), we obtain the complete response function in the axial channel:

$$\begin{aligned} \Pi_{ij}^A(M_J = 0) &= -4 \frac{p_F m^*}{\pi^2} \left\langle \left[\bar{b}^2 \delta_{ij} - \bar{b}_i \bar{b}_j \right] \mathcal{S}_0 \right\rangle \\ &+ 3 \frac{p_F m^*}{\pi^2} \left\langle \left(\delta_{ij} - \delta_{i3} \delta_{j3} \right) \bar{b}^2 \mathcal{S}_0 \right\rangle. \end{aligned} \quad (49)$$

The imaginary part of the function $\mathcal{S}_0(\mathbf{n}, \omega)$ arises from the poles of the integrand in (30) at $\omega = \pm 2E$:

$$\begin{aligned} & \bar{b}^2(\mathbf{n}) \text{Im} \mathcal{S}_0(\mathbf{n}, \omega) \\ &= \Theta(\omega - 2\Delta_{\mathbf{n}}) \frac{\pi \Delta_{\mathbf{n}}^2}{2\omega \sqrt{\omega^2 - 4\Delta_{\mathbf{n}}^2}} \tanh \frac{\omega}{4T}. \end{aligned} \quad (50)$$

Using (50) and (14), (43), and (49) we obtain the imaginary part of the weak polarization tensor for the ${}^3P_2(M_J = 0)$ superfluid neutron liquid:

$$\begin{aligned} \text{Im} \Pi_{\mu\nu}(\omega > 0) &= -\delta_{\mu\nu} \delta_{\nu j} C_A^2 p_F m^* \frac{2}{\pi} \frac{1}{\omega} \tanh \frac{\omega}{4T} \\ &\times \int \frac{d\mathbf{n}}{4\pi} \left[\delta_{ij} - \frac{\bar{b}_i \bar{b}_j}{\bar{b}^2} - \frac{3}{4} (\delta_{ij} - \delta_{i3} \delta_{j3}) \right] \\ &\cdot \frac{\Delta_{\mathbf{n}}^2 \Theta(\omega - 2\Delta_{\mathbf{n}})}{\sqrt{\omega^2 - 4\Delta_{\mathbf{n}}^2}}. \end{aligned} \quad (51)$$

6. PBF Neutrino Energy Losses

Now we substitute the obtained weak polarization tensor to (13) for the neutrino emissivity. Contraction of the tensor (51) with $(K^\mu K^\nu - K^2 g^{\mu\nu})$ gives

$$\begin{aligned} & \text{Im} \Pi_{\mu\nu}(\omega) (K^\mu K^\nu - K^2 g^{\mu\nu}) \\ &= -C_A^2 \frac{p_F m^*}{\pi} \frac{1}{\omega} \tanh \frac{\omega}{4T} \\ &\times \int \frac{d\mathbf{n}}{4\pi} \left[2(\omega^2 - k_{\parallel}^2) - k_{\perp}^2 \right] \frac{\Delta_{\mathbf{n}}^2 \Theta(\omega - 2\Delta_{\mathbf{n}})}{\sqrt{\omega^2 - 4\Delta_{\mathbf{n}}^2}}, \end{aligned} \quad (52)$$

where we denote

$$\begin{aligned} k_{\parallel}^2 &= \frac{1}{\bar{b}^2} (\mathbf{k} \bar{\mathbf{b}})^2, \\ k_{\perp}^2 &= k^2 - k_{\parallel}^2. \end{aligned} \quad (53)$$

After some algebra we find the neutrino emissivity in the following form:

$$\begin{aligned} Q &\simeq \frac{2}{15\pi^5} G_F^2 C_A^2 \mathcal{N}_{\nu} p_F m^* T^7 \int \frac{d\mathbf{n}}{4\pi} \frac{\Delta_{\mathbf{n}}^2}{T^2} \\ &\cdot \int_0^{\infty} dx \frac{z^4}{(1 + \exp z)^2}, \end{aligned} \quad (54)$$

where $\Delta_{\mathbf{n}}^2 \equiv \Delta^2 \bar{b}^2(\mathbf{n}) = (1/2)\Delta^2(1 + 3\cos^2\theta)$ and $z = \sqrt{x^2 + \Delta_{\mathbf{n}}^2}/T^2$.

It is necessary to notice that a definition of the gap amplitude is ambiguous in the literature. For example, in the case of $M_J = 0$, our gap amplitude is $\sqrt{2}$ times larger than the

gap amplitude in [6] (denote it by Δ_{YKL}), where it is defined by the relation $\Delta_{\mathbf{n}}^2 = \Delta_{\text{YKL}}^2 (1 + 3\cos^2\theta)$. However, the total anisotropic gap $\Delta_{\mathbf{n}}$ entering the energy of the quasiparticles is the same in both calculations, since $\Delta/\sqrt{2} = \Delta_{\text{YKL}}$.

Returning to the standard physical units we get the following [27]:

$$Q = \frac{4G_F^2 p_F m^*}{15\pi^5 \hbar^{10} c^6} (k_B T)^7 \mathcal{N}_\nu R \quad (55)$$

$$= 1.170 \times 10^{21} \frac{m^*}{m} \frac{p_F}{mc} T_9^7 \mathcal{N}_\nu R \frac{\text{erg}}{\text{cm}^3 \text{s}}.$$

Remember that G_F is the Fermi coupling constant, $C_A \approx 1.26$ is the axial-vector weak coupling constant of a neutron, and $\mathcal{N}_\nu = 3$ is the number of neutrino flavors; p_F is the Fermi momentum of neutrons, $m^* \equiv p_F/v_F$ is the effective neutron mass; m is bare nucleon mass, $T_9 = T/(10^9 \text{K})$, k_B is the Boltzmann constant, and

$$R = \frac{1}{2} C_A^2 F_t. \quad (56)$$

The function F_t is given by

$$F_t = \int \frac{d\mathbf{n}}{4\pi} y^2 \int_0^\infty dx \frac{z^4}{(1 + \exp z)^2}. \quad (57)$$

Here the notation used is $z = \sqrt{x^2 + y^2}$ with $y = \Delta_{\mathbf{n}}/T$. The unit vector $\mathbf{n} = \mathbf{p}/p$ defines the polar angles (θ, φ) on the Fermi surface.

It is necessary to stress that (54) as well as (55) involves the anomalous contributions into both the channels of weak interactions (vector and axial). A comparison of the formula (56) with (26) of the work [6], where the PBF neutrino losses were obtained ignoring the anomalous interactions, allows one to see that the anomalous contributions not only completely suppress the vector channel of weak interactions, but also suppress four times the energy losses through the axial channel. The resulting reduction of the emissivity of the PBF processes in neutron matter is as follows [27]:

$$\frac{C_A^2}{2(C_V^2 + 2C_A^2)} \approx 0.19. \quad (58)$$

In spite of the so strong reduction, the neutrino emissivity caused by the PBF processes can be the most powerful mechanism of the energy losses from the NS core below the critical temperature T_c . In Figure 3, the PBF neutrino emissivity, as given in (54), is shown together with the emissivities of modified Urca processes and bremsstrahlung multiplied by the corresponding suppression factors resulting from superfluidity, as obtained in [49].

The emissivity from the PBF dominates everywhere below the critical temperature for the ${}^3\text{P}_2$ superfluidity except the narrow temperature domain near the critical point, where the modified Urca processes are more operative.

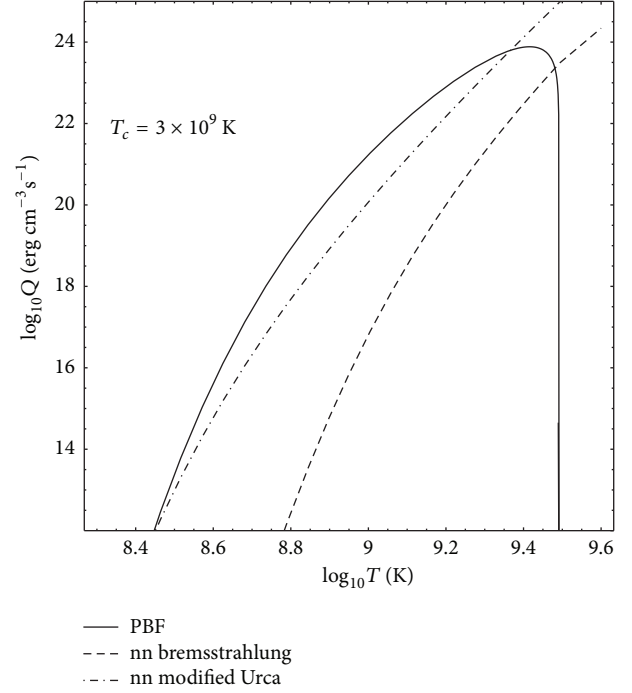


FIGURE 3: PBF neutrino emissivity versus temperature T in comparison with the modified Urca and bremsstrahlung emissivities at $k_F = 1.7$.

7. Decay of the Eigenmodes of the Condensate

We now turn to an estimate of the neutrino energy losses due to decay of thermally excited oscillations of the spin-triplet condensate of neutrons. These eigenmodes represent collective oscillations of the direction of total angular momenta of Cooper pairs which generate fluctuations of axial currents in the superfluid system (spin density fluctuations). The energy of the collective mode excitation $\omega = \Delta/\sqrt{5}$ is smaller than the energy gap in the quasiparticle spectrum. In this case the function $\mathcal{F}_0(\mathbf{n}, \omega)$, given in (30), is real, and the imaginary part of the axial polarization tensor (44) arises from the pole part of the functions $\hat{\mathbf{T}}^{(1,2)}$ at $\omega^2 - \Delta^2/5 = 0$.

With the aid of Sokhotsky's formula, $(\chi + i0)^{-1} = \mathcal{P}(1/\chi) - i\pi\delta(\chi)$, from the second line of (44) we get

$$\text{Im}\Pi_{\mu\nu}(\omega > 0) = -\delta_{\mu i}\delta_{\nu j}(\delta_{ij} - \delta_{i3}\delta_{j3}) \times \frac{3}{2\pi} C_A^2 p_F m^* \langle \bar{b}^2 \mathcal{F}_0 \rangle \omega \delta(\omega - \Delta/\sqrt{5}). \quad (59)$$

The neutrino luminosity per unit volume is proportional to the product of the total phase volume available to the outgoing neutrinos and the total energy of the neutrino pair. This explains the temperature dependence of the PBF neutrino emissivity, as given in (54). The presence of the delta-function $\delta(\omega - \Delta/\sqrt{5})$ in (59) restricts the total energy of the neutrino pair by the dispersion relation and thus substantially reduces the total volume available to neutrino

pairs in the phase space. Integration over the phase volume will result in appearance of the factor $(\Delta/\sqrt{5})^7$ instead of T^7 . Just below the superfluid transition temperature, where the main splash of the PBF neutrino emission occurs, the collective mode energy $\omega_s = \Delta(T)/\sqrt{5}$ is small as compared to the temperature. As a result the emissivity due to the collective mode decays is many orders of magnitude slower than the PBF emissivity.

One might expect the two emissivities to become comparable at sufficiently low temperature $T \lesssim \Delta(T)/\sqrt{5}$. It is necessary to notice, however, that our estimate is valid only when the anisotropic energy gap is replaced by its average value in the anomalous vertices. Such an approximation is good for the PBF processes but not for the eigen modes. The exact account of the anisotropy dramatically reduces the neutrino losses due to the collective mode decays [50].

8. Application to Cooling Modeling of Neutron Stars

The strong suppression of the vector PBF channel is basically incorporated in the cooling simulations codes (e.g., [18, 22, 28–30]). In the case of 1S_0 pairing of neutrons the suppression of the vector channel should be important in the cooling interpretation of a NS crust as the cooling time-scale of the crust is sensitive to the rates of neutrino emission. Quenching of the neutrino emission, found in the case of 1S_0 pairing, leads to higher temperatures that can be reached in the crust of an accreting NS. This allows one to explain the observed data of superbursts triggering [18, 19, 51, 52], which was in dramatic discrepancy with the previous theory of the crust cooling. However, the suppression of the neutron 1S_0 PBF process does not lead to a distinguishable effect in the long-term cooling (>1000 years) of the star [22].

The neutron pairing in the NS core is expected to occur into the spin-triplet 3P_2 state (a small 3F_2 admixture caused by tensor forces is normally neglected). Just a few years ago, suppression of the PBF neutrino emission due to spin-triplet neutron pairing in the NS core was included in the neutron star cooling codes only by complete suppression of the vector channel, while the emission in the axial-vector channel remained unchanged [22, 31]. This corresponds to the reduction factor of 0.76 with respect to the PBF emissivity previously obtained in [6], which led the authors to the conclusion that, within the minimal cooling paradigm, the closing of the vector channel of the PBF neutrino emission does not significantly affect the long-term cooling of NSs. The reason is that the long-term cooling is controlled by the axial channel of the PBF emissivities.

The suppression factor for PBF neutrino radiation given in (58) involves two physical phenomena: (i) total suppression of the vector channel and (ii) the fourfold suppression of the axial channel caused by the anomalous weak interactions. For the first time the suppression of the axial PBF channel was implemented in a simulation of the Cas A NS cooling in [32, 53]. It was found that the whole set of observations is quite consistent with the theoretical suppression factor of 0.19. This factor, presented in (58), is now commonly used

for suppression of the PBF reactions in spin-triplet superfluid neutron matter of the NS cores (e.g., [29, 30, 54, 55]).

An exhaustive numerical analysis of the anomalous axial PBF contribution to the temporal evolution of the NS cooling is presented in [56]. The interested reader can get a clear idea about importance of this contribution from Figures 2 and 3 of that work, where the authors present the NS cooling curves for the cases with and without the anomalous contribution.

9. Conclusion

We have discussed the important role of anomalous weak interactions in mechanisms of neutrino emission taking place in fermionic superfluids typical for the NS cores. It is established that due to the anomalous contributions the PBF neutrino emissivity from the vector channel is almost completely suppressed and can be ignored. This result is in agreement with the conservation of vector current in weak interactions. In the case of spin-singlet pairing the neutrino emission through the axial-vector channel is also suppressed because the total spin of the Cooper pair $S = 0$ is conserved in the nonrelativistic case. Thus the neutrino energy losses due to singlet-state pairing of baryons can, in practice, be ignored in simulations of NS cooling. This makes the PBF neutrino losses from pairing of protons or hyperons unimportant.

The minimal cooling paradigm assumes that the direct Urca processes and any exotic fast reactions are not operative in the NC core. In this scenario, neutrino emission at the long-term cooling epoch comes mainly from modified Urca processes, nn-bremsstrahlung, and from the ‘‘PBF’’ processes, which arise in the presence of spin-triplet superfluidity of neutrons [22]. We have shown that the anomalous weak interactions in the 3P_2 superfluid suppress the PBF neutrino emission, although not so sharply as in spin-singlet superfluid liquids. Namely, the vector channel of weak interactions is again strongly suppressed and can be ignored while the neutrino losses through the axial channel are suppressed only partially. Despite the approximately fivefold total suppression, the PBF mechanism of the neutrino energy losses is still operative. In many cases, especially for temperatures near the critical superfluidity temperature of neutrons, the PBF neutrino reactions can dominate and should be accurately taken into account.

Conflicts of Interest

The author declares that there are no conflicts of interest regarding the publication of this article.

References

- [1] B. L. Friman and O. V. Maxwell, ‘‘Neutrino emissivities of neutron stars,’’ *The Astrophysical Journal*, vol. 232, 541, 1979.
- [2] S. Tsuruta, ‘‘Neutron stars - Current cooling theories and observational results,’’ *Comments Astrophys*, vol. 11, p. 151, 1986.
- [3] E. Flowers, M. Ruderman, and P. Sutherland, ‘‘Neutrino pair emission from finite-temperature neutron superfluid and the cooling of young neutron stars,’’ *The Astrophysical Journal*, vol. 205, p. 541, 1976.

- [4] D. Voskresensky and A. Senatorov, "Emission of Neutrinos by Neutron Stars," *Journal of Experimental and Theoretical Physics*, vol. 63, 885, 1986.
- [5] D. Voskresensky and A. Senatorov, "Description of Nuclear Interaction in Keldyshs Diagram Technique and Neutrino Luminosity of Neutron Stars," *Soviet Journal of Nuclear Physics-Ussr*, vol. 45, p. 411, 1987.
- [6] D. G. Yakovlev, A. D. Kaminker, and K. P. Levenfish, "Neutrino emission due to Cooper pairing of nucléons in cooling neutron stars," *Astronomy & Astrophysics*, vol. 343, no. 2, pp. 650–660, 1999.
- [7] C. Schaab, D. Voskresensky, A. D. Sedrakian, F. Weber, and M. K. Weigel, "Impact of medium effects on the cooling of non-superfluid and superfluid neutron stars," *Astronomy & Astrophysics*, vol. 321, no. 2, pp. 591–604, 1997.
- [8] C. Schaab, S. Balberg, and J. Schaffner-Bielich, "Implications of hyperon pairing for cooling of neutron stars," *The Astrophysical Journal*, vol. 504, no. 2, pp. L99–L102, 1998.
- [9] S. Balberg and N. Barnea, "S-wave pairing of Λ hyperons in dense matter," *Physical Review C*, vol. 57, p. 409, 1998.
- [10] D. Page, *Many Faces of Neutron Stars*, R. Buccheri, J. Van Peredijis, and M. A. Alpar, Eds., 1998.
- [11] D. G. Yakovlev, A. D. Kaminker, and K. P. Levenfish, *Neutron Stars and Pulsars*, N. Shibazaki, Ed., Universal Academy Press, Tokio, 1998.
- [12] D. Page, J. M. Lattimer, M. Prakash, and A. W. Steiner, "Minimal cooling of neutron stars: A new paradigm," *The Astrophysical Journal Supplement Series*, vol. 155, no. 2, pp. 623–650, 2004.
- [13] L. B. Leinson and A. Pérez, "Vector current conservation and neutrino emission from singlet-paired baryons in neutron stars," *Physics Letters B*, vol. 638, no. 2-3, pp. 114–118, 2006.
- [14] L. B. Leinson, "BCS approximation to the effective vector vertex of superfluid fermions," *Physical Review C nuclear physics*, vol. 78, no. 1, Article ID 015502, 2008.
- [15] E. E. Kolomeitsev and D. N. Voskresensky, "Neutrino emission due to Cooper-pair recombination in neutron stars reexamined," *Physical Review C nuclear physics*, vol. 77, no. 6, Article ID 065808, 2008.
- [16] A. W. Steiner and S. Reddy, "Superfluid response and the neutrino emissivity of neutron matter," *Physical Review C nuclear physics*, vol. 79, no. 1, Article ID 015802, 2009.
- [17] A. Sedrakian, H. Müther, and P. Schuck, "Vertex renormalization of weak interactions and Cooper-pair breaking in cooling compact stars," *Physical Review C nuclear physics*, vol. 76, no. 5, Article ID 055805, 2007.
- [18] S. Gupta, E. F. Brown, H. Schatz, P. Möller, and K.-L. Kratz, "Heating in the Accreted Neutron Star Ocean: Implications for Superburst Ignition," *The Astrophysical Journal*, vol. 662, p. 1188, 2007.
- [19] A. Cumming, J. Macbeth, J. J. M. I. Zand, and D. Page, "Long Type I X-Ray Bursts and Neutron Star Interior Physics," *The Astrophysical Journal*, vol. 646, p. 429, 2006.
- [20] J. M. Lattimer, K. A. Van Riper, M. Prakash, and M. Prakash, "Rapid cooling and the structure of neutron stars," *The Astrophysical Journal*, vol. 425, no. 2, pp. 802–813, 1994.
- [21] D. Page, "Astrophysics & Space Science Library," in *Neutron Stars and Pulsars*, W. Becker, Ed., pp. 247–288, Springer Verlag, 2009.
- [22] D. Page, J. M. Lattimer, M. Prakash, and A. W. Steiner, "Neutrino emission from cooper pairs and minimal cooling of neutron stars," *The Astrophysical Journal*, vol. 707, no. 2, pp. 1131–1140, 2009.
- [23] R. Tamagaki, "Superfluid state in neutron star matter. I. Generalized Bogoliubov transformation and existence of $^3\text{P}_2$ gap at high density," *Progress of Theoretical Physics*, vol. 44, no. 905, 1970.
- [24] T. Takatsuka, "Energy Gap in Neutron-Star Matter," *Progress of Theoretical and Experimental Physics*, vol. 48, no. 5, pp. 1517–1533, 1972.
- [25] D. D. Ofengeim, A. D. Kaminker, D. Klochkov, V. Suleimanov, and D. G. Yakovlev, "Analysing neutron star in HESS J1731–347 from thermal emission and cooling theory," *Monthly Notices of the Royal Astronomical Society*, vol. 454, no. 3, pp. 2668–2676, 2015.
- [26] D. D. Ofengeim, M. Fortin, P. Haensel, D. G. Yakovlev, and J. L. Zdunik, "Neutrino luminosities and heat capacities of neutron stars in analytic form," *Physical Review D*, vol. 96, no. 4, Article ID 043002, 2017.
- [27] L. B. Leinson, "Neutrino emission from triplet pairing of neutrons in neutron stars," *Physical Review C nuclear physics*, vol. 81, no. 2, Article ID 025501, 2010.
- [28] S. Han and A. W. Steiner, "Cooling of neutron stars in soft x-ray transients," *Physical Review C: Nuclear Physics*, vol. 96, no. 3, Article ID 035802, 2017.
- [29] P. S. Shternin and D. G. Yakovlev, "Self-similarity relations for cooling superfluid neutron stars," *Monthly Notices of the Royal Astronomical Society*, vol. 446, no. 4, pp. 3621–3630, 2014.
- [30] A. Y. Potekhin, J. A. Pons, and D. Page, "Neutron Stars—Cooling and Transport," *Space Science Reviews*, vol. 191, no. 1-4, pp. 239–291, 2015.
- [31] D. Page, M. Prakash, J. M. Lattimer, and A. W. Steiner, "Rapid cooling of the neutron star in cassiopeia a triggered by neutron superfluidity in dense matter," *Physical Review Letters*, vol. 106, no. 8, Article ID 081101, 2011.
- [32] P. S. Shternin, D. G. Yakovlev, C. O. Heinke, W. C. G. Ho, and D. J. Patnaude, "Cooling neutron star in the Cassiopeia A supernova remnant: Evidence for superfluidity in the core," *Monthly Notices of the Royal Astronomical Society*, vol. 412, no. 1, pp. L108–L112, 2011.
- [33] L. B. Leinson, "Superfluid phases of triplet pairing and rapid cooling of the neutron star in Cassiopeia A," *Physics Letters B*, vol. 741, pp. 87–91, 2015.
- [34] L. B. Leinson, "Collective modes of the order parameter in a triplet superfluid neutron liquid," *Physical Review C nuclear physics*, vol. 85, no. 6, Article ID 065502, 2012.
- [35] L. B. Okun, *Leptons and Quarks*, World Scientific Publishing Co. Pte. Ltd., 2014.
- [36] N. N. Bogoliubov, "A new method in the theory of superconductivity. I.," *Journal of Experimental and Theoretical Physics*, vol. 34, p. 41, 1958.
- [37] Y. Nambu, "Quasi-particles and gauge invariance in the theory of superconductivity," *Physical Review*, vol. 117, no. 3, pp. 648–663, 1960.
- [38] A. I. Larkin and A. B. Migdal, "Theory of superfluid Fermi liquid. Application to the nucleus," *Journal of Experimental and Theoretical Physics*, vol. 17, p. 1146, 1963.
- [39] A. J. Leggett, "Theory of a superfluid Fermi liquid. I. General formalism and static properties," *Physical Review A: Atomic, Molecular and Optical Physics*, vol. 140, no. 6A, pp. A1869–A1888, 1966.
- [40] M. Hoffberg, A. E. Glassgold, R. W. Richardson, and M. Ruderman, "Anisotropic Superfluidity in Neutron Star Matter," *Physical Review Letters*, vol. 24, no. 14, pp. 775–777, 1970.

- [41] M. Baldo, J. Cugnon, A. Lejeune, and U. Lombardo, "Proton and neutron superfluidity in neutron star matter," *Nuclear Physics A*, vol. 536, no. 2, pp. 349–365, 1992.
- [42] O. Elgarøy, L. Engvik, M. Hjorth-Jensen, and E. Osnes, "Triplet pairing of neutrons in 3P 2-stable neutron star matter," *Nuclear Physics A*, vol. 607, no. 4, pp. 425–441, 1996.
- [43] J. B. Ketterson and S. N. Song, *Superconductivity*, Cambridge University Press, 1999.
- [44] K. A. Brueckner, T. Soda, P. W. Anderson, and P. Morel, "Level structure of nuclear matter and liquid He₃," *Physical Review A: Atomic, Molecular and Optical Physics*, vol. 118, no. 5, pp. 1442–1446, 1960.
- [45] D. A. Baiko, P. Haensel, and D. G. Yakovlev, "Thermal conductivity of neutrons in neutron star cores," *Astronomy & Astrophysics*, vol. 374, no. 1, pp. 151–163, 2001.
- [46] M. E. Gusakov and P. Haensel, "The entrainment matrix of a superfluid neutron-proton mixture at a finite temperature," *Nuclear Physics A*, vol. 761, no. 3-4, pp. 333–348, 2005.
- [47] L. B. Leinson, "Neutrino emission from spin waves in neutron spin-triplet superfluid," *Physics Letters B*, vol. 689, no. 2-3, pp. 60–65, 2010.
- [48] L. B. Leinson, "New eigen-mode of spin oscillations in the triplet superfluid condensate in neutron stars," *Physics Letters B*, vol. 702, no. 5, pp. 422–428, 2011.
- [49] D. G. Yakovlev, A. D. Kaminker, O. Y. Gnedin, and P. Haensel, "Neutrino emission from neutron stars," *Physics Reports*, vol. 354, no. 1-2, p. 1155, 2001.
- [50] L. B. Leinson, "Neutrino emissivity of anisotropic neutron superfluids," *Physical Review C nuclear physics*, vol. 87, no. 2, Article ID 025501, 2013.
- [51] L. Keek, J. J. M. In 't Zand, E. Kuulkers, A. Cumming, E. F. Brown, and M. Suzuki, "First superburst from a classical low-mass X-ray binary transient," *Astronomy & Astrophysics*, vol. 479, no. 1, pp. 177–188, 2008.
- [52] E. F. Brown and A. Cumming, "Mapping crustal heating with the cooling light curves of quasi-persistent transients," *The Astrophysical Journal*, vol. 698, no. 2, pp. 1020–1032, 2009.
- [53] K. G. Elshamouty, C. O. Heinke, G. R. Sivakoff et al., "Measuring the cooling of the neutron star in cassiopeia a with all chandra X-ray observatory detectors," *The Astrophysical Journal*, vol. 777, no. 1, article no. 22, 2013.
- [54] S. Beloin, S. Han, A. W. Steiner, and D. Page, "Constraining superfluidity in dense matter from the cooling of isolated neutron stars," *Physical Review C: Nuclear Physics*, vol. 97, no. 1, 2018.
- [55] M. Fortin, G. Taranto, G. F. Burgio, P. Haensel, H. Schulze, and J. L. Zdunik, "Thermal states of neutron stars with a consistent model of interior," *Monthly Notices of the Royal Astronomical Society*, vol. 475, no. 4, pp. 5010–5022, 2018.
- [56] A. Y. Potekhin and G. Chabrier, "Magnetic neutron star cooling and microphysics," *Astronomy & Astrophysics*, vol. 609, 2018.

Research Article

Light WIMP Searches Involving Electron Scattering

J. D. Vergados ^{1,2,3,4}, Ch. C. Moustakidis ⁵, Yeuk-Kwan E. Cheung,⁴ H. Ejiri ⁶,
Yeongduk Kim,⁷ and Jeong-Yeon Lee⁷

¹TEI of Western Macedonia, 501 00 Kozani, Greece

²CAPP, IBS, Yuseong, Daejeon 34144, Republic of Korea

³CoEPP and Centre for the Subatomic Structure of Matter (CSSM), University of Adelaide, Adelaide, SA 5005, Australia

⁴Department of Physics, Nanjing University, 22 Hankou Road, Nanjing 210093, China

⁵Department of Theoretical Physics, Aristotle University of Thessaloniki, 54124 Thessaloniki, Greece

⁶RCNP, Osaka University, Osaka 567-0047, Japan

⁷Center for Underground Physics, IBS, Daejeon 34074, Republic of Korea

Correspondence should be addressed to Ch. C. Moustakidis; moustaki@auth.gr

Received 20 November 2017; Accepted 8 March 2018; Published 15 April 2018

Academic Editor: Filipe R. Joaquim

Copyright © 2018 J. D. Vergados et al. This is an open access article distributed under the Creative Commons Attribution License, which permits unrestricted use, distribution, and reproduction in any medium, provided the original work is properly cited. The publication of this article was funded by SCOAP³.

In the present work we examine the possibility of detecting electrons in light dark matter searches. These detectors are considered to be the most appropriate for detecting dark matter particles with a mass in the MeV region. We analyze theoretically some key issues involved in such detection. More specifically we consider a particle model involving WIMPs interacting with fermions via Z -exchange. We find that for WIMPs with mass in the electron mass range the cross section for WIMP-atomic electron scattering is affected by the electron binding. For WIMPs more than 20 times heavier than the electron, the binding affects the kinematics very little. As a result, many electrons can be ejected with energy which increases linearly with the WIMP mass, but the cross section is somewhat reduced depending on the bound state wave function employed. On the other hand for lighter WIMPs, the effect of binding is dramatic. More specifically at most 10 electrons, namely, those with binding energy below 10 eV, become available even in the case of WIMPs with a mass as large as 20 times the electron mass. Even fewer electrons contribute if the WIMPs are lighter. The cross section is, however, substantially enhanced by the Fermi function corrections, which become more important at low energies of the outgoing electrons. Thus events of 0.5–2.5 per kg-y become possible.

1. Introduction

The combined MAXIMA-1 [1–3], BOOMERANG [4, 5] DASI [6], and COBE/DMR Cosmic Microwave Background (CMB) observations [7] imply that the universe is flat [8] and that most of the matter in the universe is dark [9], that is, exotic. These results have been confirmed and improved by the recent WMAP [10] and Planck [11] data. Combining the data of these quite precise measurements one finds

$$\begin{aligned}\Omega_b &= 0.0456 \pm 0.0015, \\ \Omega_{\text{CDM}} &= 0.228 \pm 0.013, \\ \Omega_\Lambda &= 0.726 \pm 0.015;\end{aligned}\tag{1}$$

(the more recent Planck data yield a slightly different combination, $\Omega_{\text{CDM}} = 0.274 \pm 0.020$, $\Omega_\Lambda = 0.686 \pm 0.020$). It is worth mentioning that both the WMAP and the Planck observations yield essentially the same value of $\Omega_m h^2$, but they differ in the value of h , namely, $h = 0.704 \pm 0.013$ (WMAP) and $h = 0.673 \pm 0.012$ (Planck). Since any “invisible” nonexotic component cannot possibly exceed 40% of the above Ω_{CDM} [12], exotic (nonbaryonic) matter is required and there is room for cold dark matter candidates or WIMPs (Weakly Interacting Massive Particles).

Even though there exists firm indirect evidence for a halo of dark matter in galaxies from the observed rotational curves, see, for example, the review [13], it is essential to directly detect such matter in order to unravel the nature

of the constituents of dark matter. The possibility of such detection, however, depends on the nature of the dark matter constituents and their interactions.

The WIMPs are expected to have a velocity distribution with an average velocity which is close to the rotational velocity v_0 of the Sun around the galaxy; that is, they are completely nonrelativistic. In fact a Maxwell-Boltzmann leads to a maximum energy transfer which is close to the average WIMP kinetic energy $\langle T \rangle \approx 0.4 \times 10^{-6} mc^2$. Thus for GeV WIMPs this average is in the keV regime, not high enough to excite the nucleus, but sufficient to measure the nuclear recoil energy. For light dark matter particles in the MeV region, which we will also call WIMPs, the average energy that can be transferred is in the few eV regions. So this light WIMPs can be detected by measuring the electron recoil after the collision. Electrons may of course be produced by heavy WIMPs after they collide with a heavy target which results in a shakeup of the atom yielding ‘‘primordial’’ electron production [14–16]. This approach for sufficiently heavy WIMPs and target nuclei can produce electrons energies even in the 30 keV region, with a spectrum very different from that arising after a direct WIMP-electron collision. Furthermore WIMP-electron collisions involving WIMPs with masses in the few GeV region have also recently appeared [17, 18]. In the present work, however, we will restrict ourselves in the case of light WIMPs with a mass in the region of the electron mass.

We will draw from the experience involving WIMPs in the GeV region. The event rate for such a process can be computed from the following ingredients [19]: (i) the elementary WIMP-electron cross section. The total Higgs decay width [20] $\Gamma = 6.1_{-2.9}^{7.7} \text{ MeV}$ determined by the LHC data imposes severe constraints on the WIMP-fermion interactions mediated with Higgs exchange. Thus we will consider the case of a WIMP which interacts with fermions via Z -exchange. In this case we will relate the needed WIMP-electron cross to the isovector spin dependent WIMP-nucleon cross and exploit the information available for the latter. (ii) The knowledge of the WIMP particle density in our vicinity: this is extracted from WIMP density in the neighborhood of the solar system, obtained from the rotation curves measurements. The number density of these MeV WIMPs, however, is expected to be six orders of magnitude bigger than that of the standard WIMPs due to the smaller WIMP mass involved. (iii) The WIMP velocity distribution: in the present work we will consider a Maxwell-Boltzmann (MB) distribution.

In the electron recoil experiments, like the nuclear measurements first proposed more than 30 years ago [21], one has to face the problem that the process of interest does not have a characteristic feature to distinguish it from the background. So since low counting rates are expected the background is a formidable problem. Some special features of the WIMP interaction can be exploited to reduce the background problems, such as the modulation effect: this yields a periodic signal due to the motion of the Earth around the Sun. Unfortunately this effect, also proposed a long time ago [22] and subsequently studied by many authors [19, 23–31],

is small in the case of nuclear recoils, but we expect it to be a bit larger in the case of the electron recoils. There has always been an interest in light WIMPs, see, for example, the recent work [32]. In fact the first direct detection limits on sub-GeV dark matter from XENON10 have recently been obtained [33]. This is encouraging, but based on our experience with standard nuclear recoil experiments to excited states [34], one has to make sure that the proper kinematics has to be used in dealing with bound electrons. Clearly the binding electron energy plays a similar role as the excitation energy of the nucleus, in determining the small fraction of the WIMP’s energy to be transferred to the recoiling system. It is therefore clear that light WIMPs are quite different in energy, mass, interacting particle, and flux. Accordingly one needs detectors capable of detecting low energy light WIMPs in the midst of formidable backgrounds, that is, detectors which are completely different from current WIMP detectors employed for heavy WIMP searches.

2. The Particle Model

The narrow decay width of the Higgs boson obtained with LHC data imposes severe constraints on the Higgs mediated WIMP-SM fermion interaction. It may thus be more favorable to look for Z -boson mediated interactions, which have so far been considered only in the hadron spin induced dark matter searches. One finds that the SM coupling of the Z to the electron takes the form $\bar{e}\gamma_\lambda(1 - 2\sin^2_{\theta_W} - \gamma_5)e \approx -\bar{e}\gamma_\lambda\gamma_5e$, where θ_W is the Weiberg angle. On the other hand the corresponding isovector quark interaction, expected to dominate in the scattering, takes the form $-\bar{q}\tau_3\gamma_\lambda\gamma_5q$, which leads to $-g_A\bar{N}\tau_3\gamma_\lambda\gamma_5N$ at the nucleon level. It is therefore natural to relate, if possible, the elementary WIMP-electron cross section to that of the spin induced isovector elementary WIMP-nucleon interaction, since for the latter there exists more theoretical and experimental information

Indeed if both the WIMP χ and the target with mass m are nonrelativistic particles the cross section can be cast in the form

$$d\sigma = \frac{1}{v} \mathcal{M}^2 \frac{1}{(2\pi)^2} d^3\mathbf{p}'_\chi d^3\mathbf{q} \delta(\mathbf{p}_\chi - \mathbf{p}'_\chi - \mathbf{q}) \cdot \delta\left(\frac{\mathbf{p}_\chi^2}{2m_\chi} - \frac{\mathbf{p}'_\chi{}^2}{2m_\chi} - \frac{\mathbf{q}^2}{2m}\right). \quad (2)$$

Integrating over the momenta we find

$$d\sigma = \frac{1}{v} \mathcal{M}^2 \frac{1}{(2\pi)^2} 2\pi q^2 dq d\xi \delta\left(qv\xi - \frac{q^2}{2\mu_r}\right), \quad (3)$$

where

$$\frac{1}{\mu_r} = \frac{1}{m_\chi} + \frac{1}{m}, \quad \mu_r = \frac{m_e m_\chi}{m_e + m_\chi} = \text{reduced mass} \quad (4)$$

with $\xi = \hat{\mathbf{p}}_\chi \cdot \hat{\mathbf{q}} \geq 0$. Thus

$$d\sigma = \frac{1}{v} \mathcal{M}^2 \frac{1}{2\pi} d\xi \frac{(2\mu_r v \xi)^2}{|v\xi|} = \frac{1}{\pi} \mathcal{M}^2 \mu_r^2 2\xi d\xi. \quad (5)$$

To this end for the elementary isovector proton cross section we write

$$\sigma_1 = \Lambda \left(1 + \frac{m_p}{m_\chi} \right)^{-2} m_p^2, \quad (6)$$

where Λ is a constant. Before proceeding further let us examine available information on σ_1 [35], which is summarized here: (a) supersymmetric models in which the LSP (lightest supersymmetric particle) communicates with the quarks via the exchange of the Z -boson [36]. In this case in the constrained minimal supersymmetric standard model one finds sizable spin induced cross sections [37, 38], σ_p and σ_n as large as 10^{-3} pb (the proton neutron representation was chosen, since the experiments are analyzed this way). If, however, the isoscalar contribution is negligible the proton and the neutron amplitudes are opposite and $\sigma_n \approx \sigma_p \approx \sigma_1$. (b) Kaluza-Klein theories in models with Universal Extra Dimensions [39] in which the dark matter is a heavy neutrino communicating with matter via Z -exchange. In such models the couplings are of the order of the standard model couplings and one finds $\sigma_1 = (1/32\pi)(G_F m_p)^2 \approx 5 \times 10^{-4}$ pb. (c) The WIMP is a spin 3/2 particle [40]. In this case only the isovector contribution exists, leading to $\sigma_1(N) \approx 1.7 \times 10^{-38} \text{ cm}^{-2} = 1.7 \times 10^{-2}$ pb. (d) Experimental limits: there exist some, namely, for ^{129}Xe and ^{131}Xe [41] and ^{19}F [42–46]. From the Xe data a limit is extracted on the elementary neutron SD cross section of $\sigma_n = 2 \times 10^{-40} \text{ cm}^2 = 2 \times 10^{-4}$ pb and $\sigma_p = 2 \times 10^{-38} \text{ cm}^2 = 2.0 \times 10^{-2}$ pb for the proton SD cross section, while from the ^{19}F target a slightly smaller limit is extracted on the proton SD cross section, $\sigma_p = 1 \times 10^{-38} \text{ cm}^2 = 1.0 \times 10^{-2}$ pb. These limits were based on nuclear physics considerations, namely, the nuclear spin matrix elements in the proton neutron representation. This explains the difference of the two limits extracted from the Xe data. For illustration purposes we will adopt the value [35] $\sigma_1 \approx 1.7 \times 10^{-2}$ pb. With this value of σ_1 we find that the parameter relevant for electron scattering is

$$\sigma_0 = \sigma_1 \frac{m_e^2}{m_p^2} \approx 5.0 \times 10^{-9} \text{ pb}. \quad (7)$$

3. Experimental Aspects

Light WIMPs are quite different in energy, mass, interacting particle, and flux. Accordingly one needs detectors which are completely different from current WIMP detectors for heavy WIMPs. Detectors are required to observe low energy light WIMP signals beyond/among BG signals to identify the light WIMPs. Experimental aspects to be considered for light WIMP detectors are: (i) the particle to be detected, (ii) the event rate, (iii) the signal pulse height, (iv) the background rate, and (v) the detector threshold energy. We will now examine each of these items.

(1) *Particle to Be Detected.* Light WIMPs are detected by observing a recoil/scattered electron in the continuum region. In case that the WIMP interaction produces an ion-electron pair, one can detect the ion and/or the electron,

and/or photons associated with the ion-electron pair. If the recoil electron or the ion-electron pair energy is absorbed by the detector, one may measure the temperature change. These are similar to those from heavy WIMPs except that their energies are very different. It is noted that atomic bound electrons are not excited by the light WIMPs with $E \leq$ a few eV.

(2) *Event Rate.* The cross section of $\sigma_0 \approx 5.0 \times 10^{-9}$ pb is an order of magnitude larger than the present XENON limit of $\sigma_0 \approx 10^{-9}$ pb for heavy WIMPs [47]. The flux rate is around $n \approx 0.8 \times 10^{10} \text{ cm}^{-2} \text{ s}^{-1}$, which is larger by a factor of $50 \text{ GeV}/0.5 \text{ MeV} \approx 10^5$. Then the event rate for Xe detector is around $R \approx 1.1 \times 10^3 / (\text{t}\cdot\text{y})$, which is also a bit larger than the present limit for 50 GeV heavy WIMPs [47].

(3) *Signal Pulse Height.* The electron signal energy for light WIMPs is around 0.5–1 eV. This energy is 4 orders of magnitude smaller than the Xe nuclear recoil energy of around 25 keV for the 50 GeV WIMP. The nuclear recoil signal is quenched by a factor 2–20, depending on the atomic number, in most heavy WIMP detectors. Thus the actual signal height for the light WIMP is 3 orders of magnitude smaller than that for the heavy WIMP.

(4) *Background Rate.* There are three types of background origins for WIMP detectors, radioactive (RI) impurities, neutrons associated with cosmic rays, and electric noises. β - γ rays from RI impurities produce BG electron signals, which are similar to electron signals from light WIMPs as well as those encountered in the case of double β decay detectors, which measure β rays. BG rate for a typical future DBD (double β decay) detectors is around $1/(\text{t y keV}) = 10^{-3}/(\text{t y eV})$ at a few MeV regions [48]. Then one may expect a similar BG rate in the eV region. This is 3 orders of magnitude smaller than the signal rate. Neutrons do not contribute to BGs in light WIMP detectors, although nuclear recoils from neutron nuclear reactions are most serious BGs for heavy WIMP detectors. Electric noises are most serious for light WIMP detectors because of the very low energy signals. The nuclear recoil energy from heavy WIMPs is typically a few 10 keV, and the signal pulse height is around a few keV if they are quenched, depending on the detector. This is of the same order of magnitude as electric noise levels. Thus one can search for heavy WIMPs by measuring the higher velocity component above the electric noises. On the other hand, the signal height for light WIMP is far below that of typical electric noises for current heavy WIMP detector.

(5) *Energy Threshold.* The energy threshold E_{th} for WIMP detectors is set necessarily below the WIMP signal, but just above the electric noise to be free from the noise. Then a very low energy threshold of an order of sub eV is required for light WIMP searches. This is 3–4 orders of magnitude smaller than the level around 1–3 keV for most heavy WIMP detectors [47, 49]. Germanium semiconductor detectors are widely used to study low energy neutrinos and WIMPs. The ionization energy is 0.67 eV. Thus it can be used in principle for energetic light WIMPs. In practice, their

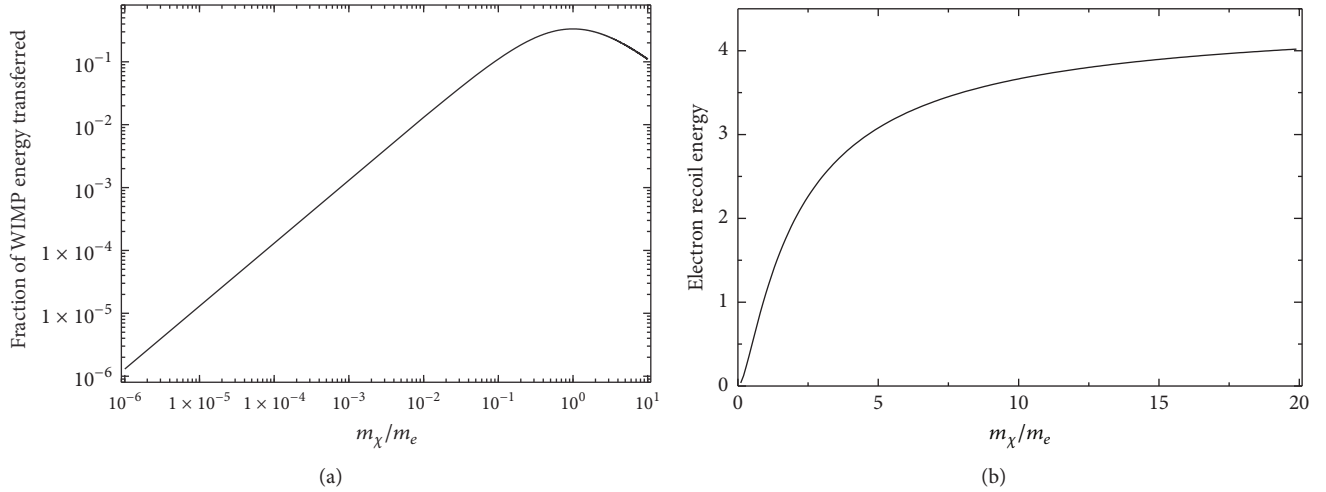


FIGURE 1: (a) The fraction of the energy of the WIMP that can be transferred to the electron as a function of $x = m_\chi/m_e$. (b) The electron recoil energy T as a function of $x = m_\chi/m_e$. As x increases it tends to 4.3 eV for $y_{\text{esc}} = 2.84$.

threshold of around 200 eV [50] or more is still far above the light WIMP signals. Bolometers are, in principle, low energy threshold and high energy resolution detectors, but the energy threshold of practical 10 kg-scale bolometers is orders of magnitude higher than the light WIMP signal. Thus light WIMP detectors are necessarily different types from the present heavy WIMP detectors.

It is indeed a challenge to develop light WIMP detectors with low-threshold energy of the order of eV. Since the event rate is as large as $2 \cdot 10^3/\text{t y}$, one can use a small volume detector of the order of 10 kgr at low temperature. In general, electric noises are random in time. Then, coincidence measurements of two signals are quite effective in reducing electric noise signals in case that one light WIMP produces 2 or more signals. One possible detector would be an ionization- scintillation detector, where one light WIMP interaction produces one ionized ion and one electron. In case that the ionized ion traps an electron nearby and emits a scintillation photon, one may measure the primary electron in coincidence with the scintillation photon. Nuclear emulsion may be of potential interest for low energy electrons. We briefly discuss possible new detection methods in Section 7.

4. The Differential WIMP-Electron Rate

The evaluation of the rate proceeds as in the case of the standard WIMP-nucleon scattering, but we will give the essential ingredients here to establish notation. We will begin by examining the case of a free electron.

4.1. Free Electrons. The differential cross section for WIMP-electron scattering in an atom can be cast in a form containing the electron recoil energy:

$$T = \frac{q^2}{2m_e} = \frac{(2\mu r v \xi)}{2m_e}. \quad (8)$$

Thus the differential cross section takes the form

$$\frac{d\sigma}{dT} = \sigma_e \frac{1}{2v^2} \frac{m_e}{\mu_r^2}, \quad (9)$$

or

$$\begin{aligned} \frac{d\sigma}{dT} &= \frac{1}{2v^2} \sigma_0 \frac{1}{m_e}, \\ \sigma_0 &= \sigma_1 \frac{m_e^2}{m_p^2}. \end{aligned} \quad (10)$$

We find from (8) that the average energy of the electron is given by

$$\begin{aligned} \langle T \rangle &= \frac{2}{3(1+x)^2} \langle \beta^2 \rangle m_e c^2, \\ \langle \beta^2 \rangle &= \left\langle \left(\frac{v}{c} \right)^2 \right\rangle = 0.8 \times 10^{-6}. \end{aligned} \quad (11)$$

From (8) we also find that the fraction of the energy of the WIMP transferred to the electron, when taking $\langle \xi^2 \rangle = 1/3$ for scattering at forward angles, is

$$\begin{aligned} \frac{T}{T_\chi} &= \frac{4}{3} \frac{x}{(1+x)^2}, \quad x = \frac{m_e}{m_\chi}, \\ T_{\text{max}} &= \frac{2\mu_r^2 v_{\text{esc}}^2}{m_e}. \end{aligned} \quad (12)$$

This situation is exhibited in Figure 1. We thus see that this fraction attains a maximum when $x = 1$, that is, when the two masses are equal. Away from this value it becomes smaller. The effect is more crucial for very light WIMPs, since their average energy is much smaller. Thus for MeV WIMPs the average energy transfer is in the eV region, which is reminiscent of the standard WIMPs where GeV mass leads

to an energy transfer in the keV region. The maximum energy transfer corresponds to the escape velocity which is $v_{\text{esc}} \approx 2\sqrt{\langle v^2 \rangle}$, which leads to a value four times higher. The exact expression of the maximum electron energy will be given below.

From (8) we find that

$$\begin{aligned} v &= \sqrt{\frac{m_e T}{2\mu_r^2 \xi^2}} \longrightarrow \\ v &\geq \sqrt{\frac{m_e T}{2\mu_r^2}} \longrightarrow \\ v_{\text{min}} &= \sqrt{\frac{m_e T}{2\mu_r^2}}. \end{aligned} \quad (13)$$

In other words the minimum velocity consistent with the energy transfer T and the WIMP mass is constrained as above. The maximum velocity allowed is determined by the velocity distribution and it will be indicated by v_{esc} . From this we can obtain the differential rate per electron in a given velocity volume $v^2 dv d\Omega$ as follows:

$$dR = \frac{\rho_\chi}{m_\chi} v \sigma_0 \frac{1}{2} \frac{1}{m_e} dT f(v) dv d\Omega, \quad (14)$$

where $f(v)$ is the velocity distribution of WIMPs in the laboratory frame. Integrating over the allowed velocity distributions we obtain

$$\begin{aligned} dR &= \frac{\rho_\chi}{m_\chi} \sigma_0 \frac{1}{2} \frac{1}{m_e} dT \eta(v_{\text{min}}), \\ \eta(v_{\text{min}}) &= \int_{v_{\text{min}}}^{v_{\text{esc}}} f(v) v dv d\Omega. \end{aligned} \quad (15)$$

$\eta(v_{\text{min}})$ is a crucial parameter. Before proceeding further we find it convenient to express the velocities in units of the Sun's velocity. We should also take note of the fact the velocity distribution is given with respect to the center of the galaxy. For a M-B distribution this takes the form

$$\frac{1}{\pi\sqrt{\pi}} e^{-y'^2}, \quad y' = \frac{v'}{v_0}, \quad v_0 = 220 \text{ km/s}. \quad (16)$$

We must transform it to the local coordinate system:

$$\mathbf{y}' \longrightarrow \mathbf{y} + \hat{v}_s + \delta (\sin \alpha \hat{x} - \cos \alpha \cos \gamma \hat{y} + \cos \alpha \sin \gamma \hat{v}_s), \quad \delta = \frac{v_E}{v_0} \quad (17)$$

with $\gamma \approx \pi/6$, \hat{v}_s a unit vector in the Sun's direction of motion, \hat{x} a unit vector radially out of the galaxy in our position, and $\hat{y} = \hat{v}_s \times \hat{x}$. The last term in parenthesis in (17) corresponds to the motion of the Earth around the Sun with $v_E \approx 28$ km/s being the modulus of the Earth's velocity around the Sun and α the phase of the Earth ($\alpha = 0$ around June 3rd). The above formula assumes that the motion of both the Sun around the Galaxy and of the Earth around the Sun are uniformly circular. Since δ is small, we expand the distribution in powers of δ and we keep terms up to linearity in δ . Then (15) can be cast in the form

$$\begin{aligned} dR &= \left(\frac{\rho_\chi}{m_\chi} v_0 \right) \sigma_0 \frac{m_t Z_{\text{eff}}}{A m_p} 1.9 \\ &\times 10^6 \frac{1}{2} \frac{1}{m_e} dT (\Psi_0(y_{\text{min}}) + \Psi_1(y_{\text{min}}) \cos \alpha), \end{aligned} \quad (18)$$

where, in the above equation, the first term in parenthesis represents the average flux of WIMPs, the second provides the scale of the elementary cross section (in the present model the elementary cross section contains an additional mass dependence), the third term gives the number of electrons available for the scattering in a target of mass m_t containing atoms with mass number A and active electrons Z_{eff} , and the fourth is essentially the inverse of the square of the Sun's

velocity in units of c (its origin has its root in (10)). Moreover, $\Psi_0(y_{\text{min}})$ and $\Psi_1(y_{\text{min}})$ are functionals of y_{min} and y_{esc} , where

$$\begin{aligned} y_{\text{min}} &= \frac{v_{\text{min}}}{v_0} = \frac{1}{v_0} \sqrt{\frac{m_e T}{2\mu_r^2}}, \\ y_{\text{esc}} &= \frac{v_{\text{esc}}}{v_0}. \end{aligned} \quad (19)$$

In the above expression the Heaviside function H guarantees that the required kinematical condition is satisfied. One can factor the constants out in the above equation to get

$$\begin{aligned} \frac{dR}{d(T/1 \text{ eV})} &= \Lambda \left(\Sigma_0 \left(\frac{m_\chi}{m_e}, \frac{T}{1 \text{ eV}} \right) + \Sigma_1 \left(\frac{m_\chi}{m_e}, \frac{T}{1 \text{ eV}} \right) \cos \alpha \right), \end{aligned} \quad (20)$$

where

$$\begin{aligned} \Sigma_i(t, s) &= \frac{1}{t} \Psi_i \left(1.23 \left(1 + \frac{1}{t} \right) \sqrt{s} \right), \quad i = 0, 1, \\ \Lambda &= 1.4 \frac{\rho_\chi}{m_e} v_0 \sigma_0 \frac{m_t Z_{\text{eff}}}{A m_p}. \end{aligned} \quad (21)$$

The meaning of Z_{eff} will become clear after we consider the fact that the electrons are not free but bound in the atom. Thus they are not all available for scattering; that is, $Z_{\text{eff}} < Z$. We will now estimate Λ considering the following input: (a) the

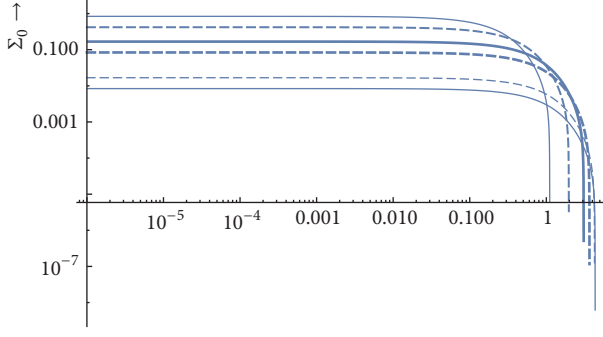


FIGURE 2: The shape of the differential cross section as a function of the electron energy T in eV for the WIMP masses $(1, 2, 5, 10, 50, 100)m_e$. The electrons are assumed to be free. The WIMP masses specifying the curves are increasing downwards. The spectrum does not exhibit any special structure.

elementary cross section $\sigma_0 = 5.0 \times 10^{-9} \text{ pb} = 5.0 \times 10^{-45} \text{ cm}^2$; (b) the total cross section, in units of σ_0 , for example, $\sigma_{\text{av}} = 0.2$ for a WIMP mass about the electron mass (see below); (c) the particle density of WIMPs in our vicinity: $n = 0.3 \times 10^3 \text{ (MeV/cm}^3\text{)}/0.511 \text{ MeV} \approx 600 \text{ cm}^{-3}$ (we use the electron mass in this estimate; the correct mass dependence has been included in evaluating σ_{av}); this value leads to a flux: $n \times 220 \text{ km/s} = 1.3 \times 10^{10} \text{ cm}^{-2} \text{ s}^{-1}$; (d) The number of electrons in a Kg of Xe: $(1/(131 \times 1.67 \times 10^{-27})) Z_{\text{eff}} = 4.6 \times 10^{24} Z_{\text{eff}}$. Taking $Z_{\text{eff}} = 54$, that is, all electrons in Xe participating, we expect about ≈ 0.3 events per kg-y. Encouraged by this estimate, even though it has been obtained with a much smaller elementary cross section than previous estimates [32], we are going to proceed in evaluating the expected spectrum of the recoiling electrons.

The shape of the differential cross section $\Sigma_0(t, s)$ as a function of the electron energy T in eV for various WIMP masses is exhibited in Figure 2. The electrons are assumed to be free. Obviously, this does not exhibit any special structure.

The various atomic physics approximations previously considered involve relatively high electron energies, as, for example, in the recent works [17, 18], which are not important in our case. The obtained rate, however, can be modified substantially at low energies by including the correction of the outgoing electron wave due to the Coulomb field. In beta decay this is done via the simple Fermi function [51]:

$$F(k, Z, \eta, \gamma) = (kR)^{2\gamma-2} e^{\pi\nu} \left| \frac{\Gamma(\gamma + i\eta)}{\Gamma(2\gamma)} \right|^2 |M(\gamma + i\eta, 2\gamma, 2ikr)|^2, \quad (22)$$

$$J = \frac{1}{(2\pi)^2} \int d^3\mathbf{p} |\tilde{\phi}_{ne}(\mathbf{p})|^2 \int d^3\mathbf{q} d^3\mathbf{p}'_x \delta(\mathbf{p} + \mathbf{p}_x - \mathbf{p}'_x - \mathbf{q}) \delta\left(\frac{\mathbf{p}_x^2}{2m_x} - \frac{\mathbf{p}'_x{}^2}{2m_x} - \frac{\mathbf{q}^2}{2m_e^2} - b\right), \quad (26)$$

where $\tilde{\phi}_{ne}(\mathbf{p})$ is the electron wf in momentum space. A plane wave outgoing electron has been assumed. Deviations from

where

$$\gamma = \sqrt{1 - \alpha^2 Z^2},$$

$$\eta = Z\alpha \frac{T + m_e c^2}{\sqrt{T^2 + 2m_e c^2 T}} \quad (23)$$

and $M(\gamma + i\eta, 2\gamma, 2ikr)$ is the Coulomb function represented by a confluent hypergeometric function.

After some approximations (see, e.g., Landau's book [52]) one finds the Fermi function

$$F(T, Z, n, \eta, \gamma) \approx \left(\sqrt{T^2 + 2m_e T} \bar{r}(n, Z, \gamma) \right)^{2\gamma-2} f_c^2(\gamma, n) \frac{2\pi\eta}{1 - e^{-2\pi\eta}}. \quad (24)$$

This function, which depends on the electron energy as well as the atomic parameters n and Z , may lead to an enhancement for low energy electrons. Integrating the differential rate given by (20) over the electron spectrum we obtain the total rate:

$$R = \Lambda (\sigma_{\text{av}} + \sigma_{\text{td}} \cos \alpha), \quad (25)$$

where σ_{av} and $\sigma_{\text{td}} \cos \alpha$ are the average and time dependent (modulated) cross sections, respectively, in units of σ_0 , that is, of the elementary cross section. The obtained quantity σ_{av} is shown in Figure 3 for free electrons both without the Fermi function as well as with the Fermi function for two values n and Z , n assumed to be sort of average. We see that the effect on the total cross section is large. Thus we find that the cross sections (in units of σ_0), for a WIMP with the mass of the electron we get values 0.2, 0.8, and 2.2 for cases (a), (b), and (c) respectively (see Figure 3), while for $n = 2$ and $Z = 50$ we find 0.3. In our estimates we will adopt an average enhancement factor of 8 due to the Fermi function taking into account the Fermi function the above estimate becomes 2.5 events/(kg-y).

5. Effects of Binding of Electrons

The binding of the electrons comes in two ways. The first is the most obvious. A portion of the energy of the WIMP will not go to recoil, but it will be spent to release the bound electron. The second comes from the fact that the initial electron is not at rest but it has a momentum distribution, which is the Fourier transform of its wave function in coordinate space.

Since the propagator involves the Z - exchange with a large mass, the momentum transfer can be neglected. So the cross section for WIMP-electron scattering is proportional to

plane wave will be accounted for in the usual way, that is, by the Fermi function as described in the previous section. After

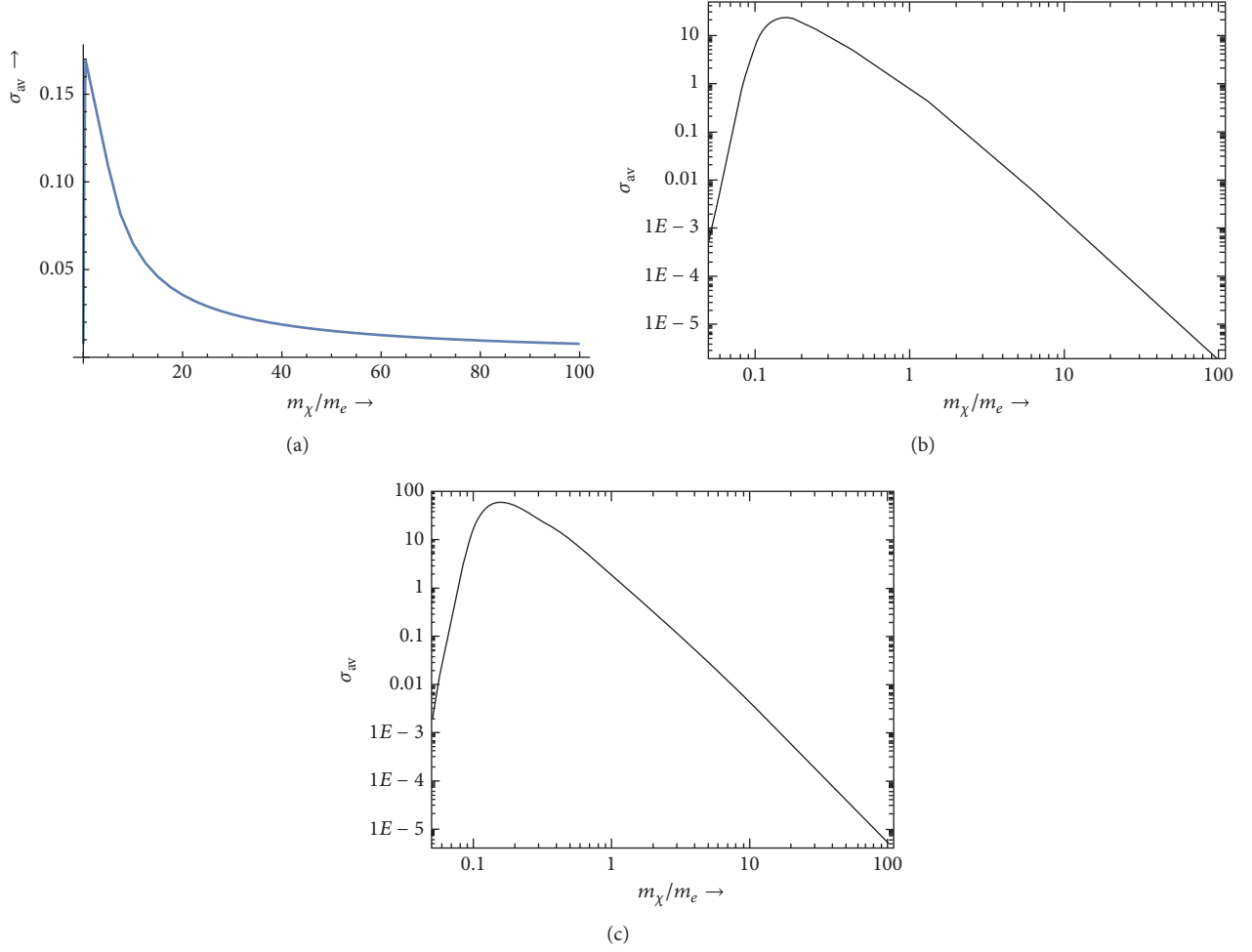


FIGURE 3: The total average WIMP-electron cross section in units σ_0 as a function of the WIMP mass in units of the electron mass. In panel (a) the Fermi function was neglected, while in panels (b) and (c) the Fermi function F for $n = 3$ and $Z = 50$ and $n = 4$ and $Z = 60$, respectively, has been employed.

the integration over the momentum \mathbf{p} via the δ function we obtain

$$J = \frac{1}{(2\pi)^2} \int |\tilde{\phi}_{ne}(\mathbf{p}'_x - \mathbf{p}_x + \mathbf{q})|^2 d^3 \mathbf{p}'_x d^3 \mathbf{q} \delta\left(\frac{\mathbf{p}'_x{}^2}{2m_\chi} - \frac{\mathbf{p}'_x{}'^2}{2m_\chi} - \frac{\mathbf{q}^2}{2m_e^2} - b\right). \quad (27)$$

The integration over the magnitude of \mathbf{p}'_x can be done using the energy conserving δ function and we obtain

$$J = \frac{1}{(2\pi)^2} \int d^3 \mathbf{q} Q^2 d\Omega_{\mathbf{Q}} |\tilde{\phi}_{ne}(\mathbf{Q} - \mathbf{p}_x + \mathbf{q})|^2 \frac{m_\chi}{Q}, \quad (28)$$

$$\mathbf{Q} = \hat{e} \sqrt{(m_\chi v)^2 - q^2 x - 2m_\chi b}$$

with $x = m_\chi/m_e$ and \hat{e} a unit vector in the direction of \mathbf{p}'_x . We thus find the important constraint

$$v > v_{\min}, \quad v_{\min} = \sqrt{\frac{2}{m_\chi} (T + b)}. \quad (29)$$

This already sets a limit on the range of the variables b and T of interest to experiments.

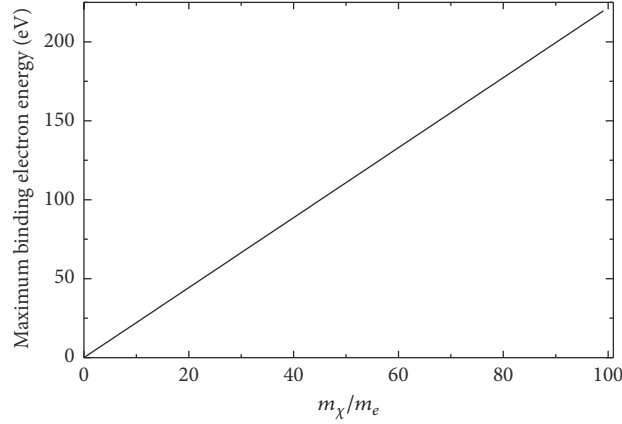


FIGURE 4: The maximum binding electron energy b_{\max} in eV as a function of m_χ/m_e accessible to WIMP-electron scattering.

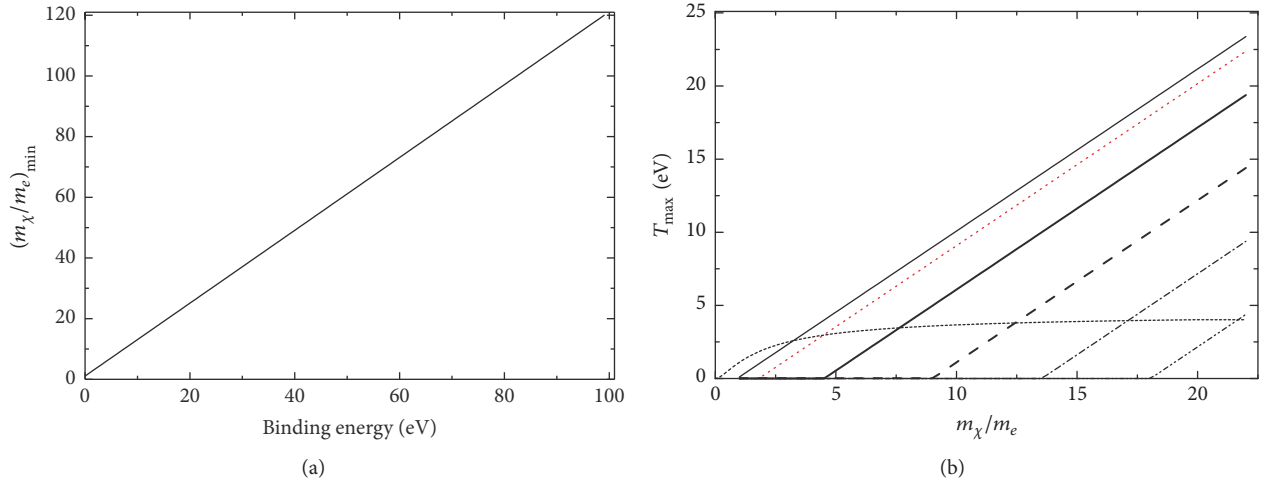


FIGURE 5: The minimum m_χ/m_e required to eject an electron with binding energy b in eV (a). The maximum outgoing electron energy T_{\max} as a function of $x = m_\chi/m_e$ for various binding energies b (b). In this panel the graphs correspond to $b = 1, 2, 5, 10, 15,$ and 20 eV from left to right. For convenience we also show again the curve which corresponds to a free electron (long dashed). It yields the same maximum electron energy for $b = 20$ eV and $x = 22$.

5.1. *The Allowed Range of Binding Energy (b) and Recoil Energy (T).* The range of these quantities is not affected by the specific form of the bound electron wave function. In particular regarding b the above conditions imply

$$\begin{aligned} (T)_{\max} &= \frac{1}{2}m_\chi v_{\text{esc}}^2 - b, \\ b_{\max} &= \frac{1}{2}m_\chi v_{\text{esc}}^2, \end{aligned} \quad (30)$$

where b_{\max} is associated with zero maximum recoil energy and is exhibited as a function of WIMP mass in Figure 4. What seriously affects the detection of light WIMPs in the presence of large binding energies is the minimum WIMP velocity required to eject an electron. One finds that in order to surpass the barrier of a given binding energy b the WIMP must have a minimum velocity at most v_{esc} and a high mass, even if the electron energy is zero. The minimum $x = m_\chi/m_e$ required for this purpose is exhibited in Figure 5(a). The

actual value of $x = m_\chi/m_e$ must, of course, be larger to get a reasonable rate.

Finally we present in Figure 5(b) the maximum possible energy for outgoing electrons as a function of the WIMP mass for various binding energies. We see that the maximum energy of the electron increases due to the binding provided that the binding energy is small. Thus the threshold energy needs not be extremely low, provided that for $x \leq 20$ there exist enough electrons in the atom with low enough binding energies. For heavier WIMPs the binding energy of the electron plays a minor role and the electron recoil energy increases linearly with the WIMP mass.

5.2. *The Effect of the Bound Electron Wave Function.* To proceed further we must evaluate the integral in (28). Firstly, we must select a suitable coordinate system, for example, one with the z -axis along the initial WIMP velocity, the x -axis in the direction of the outgoing WIMP, and y -axis perpendicular to the plane of the other two. Actually, there

is no hope for obtaining an analytic expression even for the angular integrals without further approximations. So we will assume hydrogenic wave functions. This approximation is expected to be reasonable for electrons which are not tightly bound, which are of interest to us in the present work. We concentrate on the case of s states and find that the cross section is given by

$$d\sigma = \frac{1}{v} |\mathcal{M}|^2 dJ, \quad (31)$$

where dJ is a complicated functional given by

$$dJ = \frac{q}{p_0(n, Z)} q dq \psi_2(q, v, b, p_0(n, Z)), \quad (32)$$

$$\psi_2(q, v, b, p_0(n, Z)) = \int_{-1}^1 d\xi \psi_1(\xi, q, v, b, p_0(n, Z)),$$

where

$$\begin{aligned} \psi_1(\xi, q, v, b, p_0(n, Z)) \\ = \frac{m_\chi}{(q\xi - m_\chi v)} \int_{\eta_+}^{\eta_-} z dz |\tilde{\phi}_{n\ell}(z)|^2 \end{aligned} \quad (33)$$

and $p_0(n, Z) = (\alpha Z/n)m_e$, the scale of momentum of the bound electron wave function. \mathcal{M} is the invariant amplitude for the process which has the form

$$|\mathcal{M}|^2 = \sigma_e \frac{\pi}{\mu_r^2} = \sigma_0 \frac{\pi}{m_e^2}. \quad (34)$$

Now, since

$$d\sigma = \sigma_0 \frac{1}{v} \frac{\pi}{m_e^2} dJ \quad (35)$$

one can cast (35) in a form similar to the expression for free electrons, namely,

$$d\sigma = \sigma_0 \frac{1}{2v^2} \frac{1}{m_e} dT \quad (36)$$

or

$$d\sigma = \sigma_0 \frac{1}{v^2} \frac{1}{m_e} dT \tilde{\Lambda}(T, v, b, p_0(n, Z)), \quad (37)$$

where

$$\begin{aligned} \tilde{\Lambda}(T, v, b, p_0(n, Z)) \\ = 2\pi v \frac{\sqrt{2m_e T}}{p_0(n, Z)} \psi_2\left(\sqrt{2m_e T}, v, b, p_0(n, Z)\right). \end{aligned} \quad (38)$$

In order to get the differential rate one must fold the above expression with the velocity distribution $f(v)$ in a similar fashion as in (15), that is,

$$\begin{aligned} \frac{dR}{dT} = \frac{\rho_\chi}{m_\chi} \frac{1}{2} \sigma_0 \frac{1}{m_e} \left[\int_{\sqrt{2(b+T)/m_\chi}}^{v_{\text{esc}}} \tilde{\Lambda}(T, v, b, p_0(n, Z)) \right. \\ \left. \cdot f(v) v dv d\tilde{v} \right]. \end{aligned} \quad (39)$$

Note the appearance of the quantities b and $\tilde{\Lambda}$ as a result of the electron binding. The behavior of the function $\tilde{\Lambda}$ as a function of the velocity and its numerical value significantly affects the obtained rates. In order to obtain $\tilde{\Lambda}$ exactly one must evaluate the remaining integrals numerically for each electron orbit separately. After that, in order to obtain the total rate, one must sum up over all available electrons involved in any orbit of a given atom, which is not trivial. This is currently under study, but here we will report results obtained in an approximate scheme valid for relatively low mass WIMPs, which is adequate for our purposes.

5.3. A Convenient Approximation for Light WIMPs. We have seen that the momentum of the outgoing electron is small compared to $p_0(n, Z)$. Let us assume that

$$\frac{Qm_\chi v}{p_0^2(n, Z)} < 1. \quad (40)$$

This means that

$$x^2 v \sqrt{v - v_1} \leq \alpha^2, \quad v_1 = \sqrt{\frac{2(b+T)}{xm_e}} \leq v_{\text{esc}}. \quad (41)$$

This quantity is small as long as

$$x < \frac{(\alpha Z)}{v_{\text{esc}}} = 1.2Z \approx 50 \text{ for a large atom.} \quad (42)$$

For such values of x we can expand the integral $\int_{\eta_+}^{\eta_-} z dz |\tilde{\phi}_{n\ell}(z)|^2$ up to second order in the small parameter. The result, for example, for $1s$ hydrogenic wave functions, is

$$J_1 = \frac{16Q(m_\chi v - q\xi)}{\pi^2 p_0^2(n, Z)}. \quad (43)$$

Integrating over the angles of the outgoing electron we obtain

$$dJ = q^2 dq \frac{64Q^2 m_\chi m_\chi v}{\pi p_0^5(n, Z)}. \quad (44)$$

Proceeding as above we obtain

$$\tilde{\Lambda} = \tilde{\Lambda}_0(Z) \sqrt{\frac{2T}{m_e}} \frac{x^4}{(\alpha Z)^5} v^2 (v^2 - v_1^2) \quad (45)$$

or

$$\begin{aligned} \tilde{\Lambda} = \tilde{\Lambda}_0(Z) x^4 \sqrt{T} y^2 \left(y^2 - \frac{6.59(b+T)}{x} \right), \\ \tilde{\Lambda}_0(1) = 3.5 \times 10^{-3}, \end{aligned} \quad (46)$$

where b and T are in eV and y is the WIMP velocity in units of the Sun's velocity. A similar expression with a slightly different constant $\tilde{\Lambda}_0(Z)$ is expected to hold for other electron orbitals. This function must be multiplied with the velocity distribution before proceeding with the needed integrations to obtain the rate.

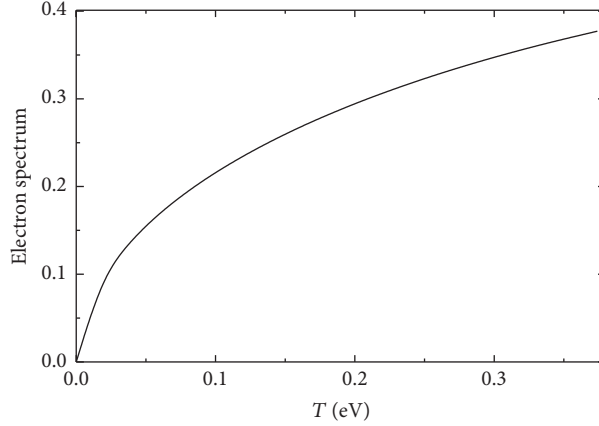


FIGURE 6: The electron spectrum for bound electrons corresponding to $x = 1$. Only electrons with $b < 1$ eV can be ejected.

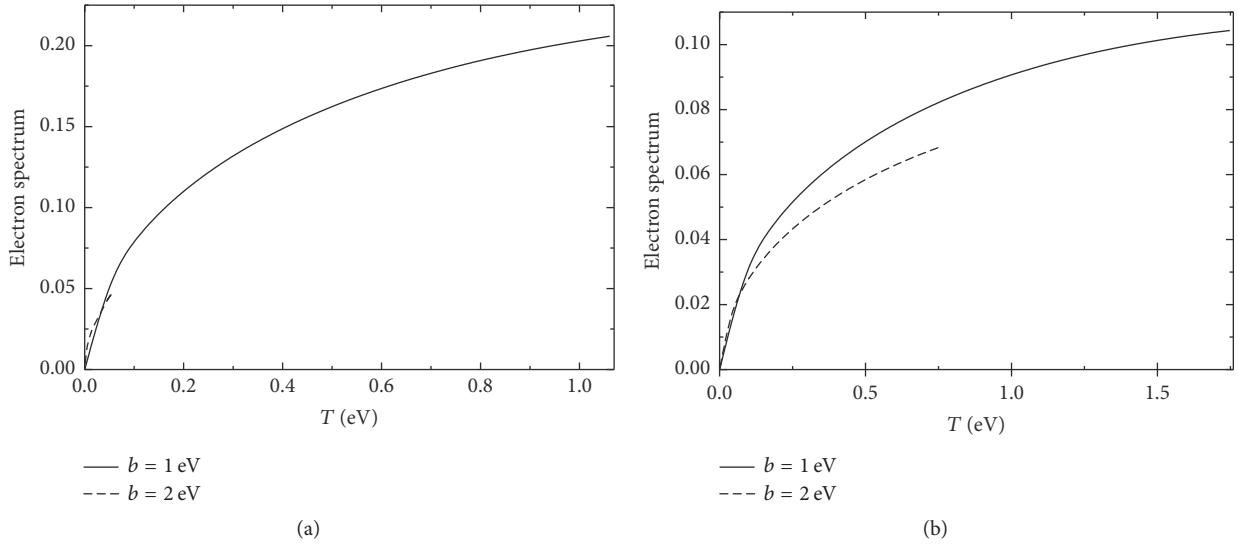


FIGURE 7: The same as in Figure 6, but for $x = 10$ in panel (a) and $x = 20$ in panel (b). In both cases only electrons with $b < 3$ eV can be ejected. Notice, however, that the spectrum is suppressed for $b = 2$ (dashed line) compared to the corresponding one for $b = 1$ (solid line).

6. Some Results for Bound Electrons

We will limit ourselves to $b \geq 1$ eV and $x \leq 100$. After integrating with the velocity distribution we obtain the electron spectra shown in Figures 6–8. After integrating over the energy spectrum we obtain the cross section σ_{av} in units of σ_0 shown in Figure 9 as a function of the WIMP mass for various binding energies. It is perhaps better to show σ_{av} as a function of the binding energy. For $x = 10$ only $b \leq 1$ are available. For $b = 1$ we find $\sigma_{av} = 0.1$ in units of σ_0 . For larger x , σ_{av} is exhibited in Figure 10.

We thus see that using hydrogenic wave functions we find that, for m_χ , greater $10m_e$, electrons with $b < 15$ eV become available. The number of electrons with relatively small binding energy for some targets of interest is shown in Table 1. Anyway there seems to be a wide range of the parameters which leads to $Z_{eff} = 5$ for a suitable atom with large Z . Thus for $Z_{eff} = 5$ one can conservatively set σ_{av} to be ≈ 0.15 , which leads to about 0.6 event per kg-y compared

to the 2.0 per kg-y we got above for lighter WIMPs without the electron binding. The Fermi function is incorporated into the results.

7. Discussion

We have seen that the use of electron detectors may be a good way for directly detecting light WIMPs in the MeV region. The electron density in our vicinity is very high, the elementary WIMP-electron cross section may be quite large, and the event rate may be further enhanced by the behavior of the Fermi function at low energies. This is fine for WIMPs heavier than 20 times the electron mass. For WIMPs less than about 20 times the mass of the electron, however, there appears to be a problem arising from the electron binding. A small fraction of electrons can be exploited, namely, those electrons with binding energies below the 10 eV range. This is reminiscent of the difficulty encountered in the inelastic WIMP nucleus scattering, whereby only very low excited

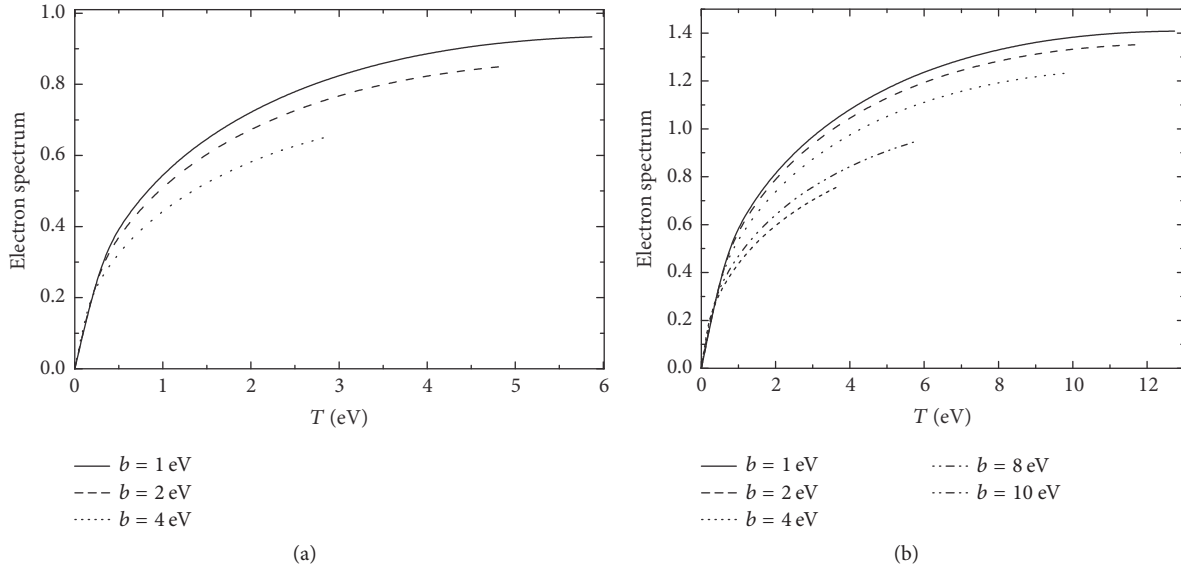


FIGURE 8: The same as in Figure 7, but for $x = 50$ in panel (a) and $x = 100$ in panel (b). In panel (a) the spectrum is shown for $b = 1, 2$ and 4 eV. In panel (b) the spectra for $b = 1, 2, 4$ and 8 eV are shown with b increasing downwards.

TABLE 1: The number of electrons with binding energies less than b_{upb} for a given set of targets.

Target	$b_{\text{upb}} = 5$ eV	$b_{\text{upb}} = 10$ eV	$b_{\text{upb}} = 15$ eV	$b_{\text{upb}} = 20$ eV	$b_{\text{upb}} = 30$ eV
${}^9\text{F}$	-	-	-	5	5
${}^{11}\text{Na}$	1	1	1	1	1
${}^{32}\text{Ge}$	4	4	4	4	14
${}^{52}\text{Te}$	4	4	6	6	6
${}^{53}\text{I}$	5	5	7	7	7
${}^{54}\text{Xe}$	-	-	6	6	8
${}^{83}\text{Bi}$	3	5	5	5	15

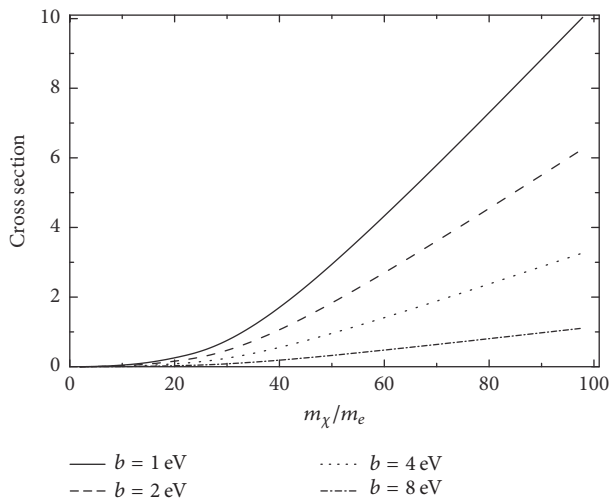


FIGURE 9: The cross section σ_{av} in units of σ_0 as a function of $x = m_\chi/m_e$ for binding energies $b = 1, 2, 4,$ and 8 eV increasing downwards (the curve for $b = 10$ is not visible).

states can be reached. We have seen, however, that, due to the behavior of the Fermi function in the case of very low energy

electron recoils, the rates may increase up to factors of 8. So event rates of about 0.8 to 2.4 events per kg-y are possible.

It has recently been suggested that it is possible to detect even very light WIMPs, much lighter than the electron, utilizing Fermi-degenerate materials like superconductors [53]. In this case the energy required is essentially the gap energy of about $1.5kT_c$, which is in the meV region; that is, the electrons are essentially free. The authors are perhaps aware of the fact that the average energy for very light WIMPs is small and not all of it can be transferred to their system (the maximum fraction occurs if the mass of the WIMP is equal to m_e , i.e., for $x = 1$ in Figure 1). With their detector these authors probably have a way to circumvent the fact that a small amount of energy will be deposited, if they manage to accumulate a large number of loosely bound electrons in their targets so that the obtained rates are sufficient. More recently it is claimed that even smaller energies in meV can be detected in the case of Liquid Helium [54]. The expected event rates and the total energy deposited in such essentially bolometer type detectors are currently being estimated more precisely and they will appear elsewhere.

It thus appears that light WIMPs in the MeV region can, in principle, be detected. The detection techniques and targets

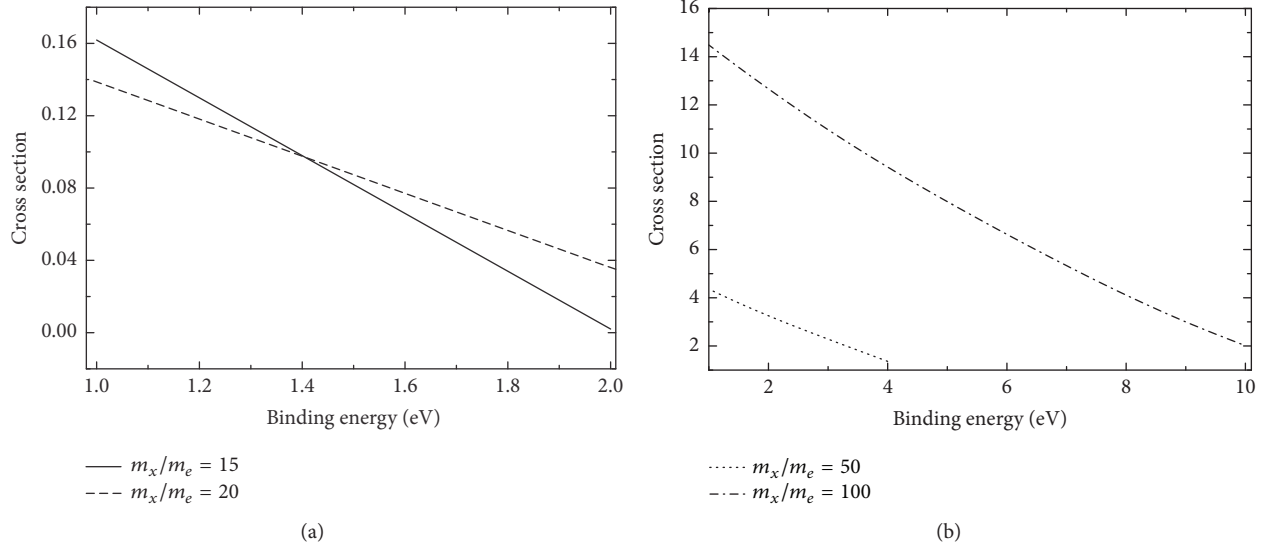


FIGURE 10: The cross section σ_{av} in units of σ_0 as a function of b in eV for $x = m_\chi/m_e = 15$ (solid line) and 20 (dashed line) (a) and for $x = m_\chi/m_e = 50$ and 100 (b) (the lower curve corresponds to the smaller x).

employed, however, may have to be different than the ones employed in standard WIMP searches.

Disclosure

The permanent address of J. D. Vergados is University of Ioannina, 451 10 Ioannina, Greece.

Conflicts of Interest

The authors declare that there are no conflicts of interest regarding the publication of this paper.

Acknowledgments

J. D. Vergados is happy to acknowledge support of this work by (i) the National Experts Council of China via a “Foreign Master” grant and (ii) IBS-R017-D1-2016-a00 in the Republic of Korea. A substantial part of this work performed while J. D. Vergados was on a visit to the University of Adelaide, supported by CoEPP and the Centre for the Subatomic Structure of Matter (CSSM). He is happy to thank Professors Yannis K. Semertzidis of KAIST, Anthony Thomas of Adelaide, and Edna Cheung of Nanjing University for their hospitality. Yeuk-Kwan E. Cheung acknowledges support from the Jiangsu Ministry of Science and Technology under Contract BK20131264 and the Priority Academic Program Development for Jiangsu Higher Education Institutions (PAPD).

References

- [1] S. Hanay, “MAXIMA-1: a measurement of the cosmic microwave background anisotropy on angular scales of 10° – 5° ,” *The Astrophysical Journal*, vol. 545, no. 1, pp. L5–L10, 2000.
- [2] J. H. P. Wu, A. Balbi, J. Borrill et al., “Tests for Gaussianity of the MAXIMA-1 Cosmic Microwave Background Map,” *Physical Review Letters*, vol. 87, article 251303, 2001.
- [3] M. G. Santos, A. Balbi, J. Borrill et al., “Estimate of the Cosmological Bispectrum from the MAXIMA-1 Cosmic Microwave Background Map,” *Physical Review Letters*, vol. 88, article 241302, 2002.
- [4] P. D. Mauskopf, P. A. Ade, and P. de Bernardis, “Measurement of a peak in the cosmic microwave background power spectrum from the North American test flight of boomerang,” *The Astrophysical Journal*, vol. 536, no. 2, pp. L59–L62, 2002.
- [5] S. Mosi, P. de Bernardis, and G. de Troia, “The BOOMERanG experiment and the curvature of the universe,” *Progress in Particle and Nuclear Physics*, vol. 48, no. 1, pp. 243–261, 2002.
- [6] N. W. Halverson, E. M. Leitch, and C. Pryke, “Degree Angular Scale Interferometer First Results: A Measurement of the Cosmic Microwave Background Angular Power Spectrum,” *The Astrophysical Journal*, vol. 568, article 38, 2002.
- [7] G. F. Smoot, C. L. Bennett, A. Kogut et al., “Structure in the COBE differential microwave radiometer first-year maps,” *Astrophysical Journal*, vol. 396, article L1, 1992.
- [8] A. H. Jaffe, P. A. Ade, A. Balbi et al., “Cosmology from MAXIMA-1, BOOMERANG, and COBE DMR Cosmic Microwave Background Observations,” *Physical Review Letters*, vol. 86, article 3475, 2001.
- [9] D. N. Spergel, L. Verde, and H. V. Peiris, “First Year Wilkinson Microwave Anisotropy Probe (WMAP) Observations: Determination of Cosmological Parameters,” *The Astrophysical Journal*, vol. 148, article 175, 2003.
- [10] D. N. Spergel, R. Bean, O. Doré et al., “Wilkinson Microwave Anisotropy Probe (WMAP) Three Year Results: Implications for Cosmology,” *The Astrophysical Journal Supplement Series*, vol. 170, article 377, 2007.
- [11] The Planck Collaboration, P. A. R. Ade, N. Aghanim, C. Armitage-Caplan et al., “Planck 2013 results. XVI. Cosmological parameters,” *Astronomy & Astrophysics*, 2013.

- [12] D. P. Bennett, C. Alcock, R. A. Allsman et al., “Experimental Limits on the Dark Matter Halo of the Galaxy from Gravitational Microlensing,” *Physical Review Letters*, vol. 74, article 2867, 1995.
- [13] P. Ullio and M. Kamiokowski, “Velocity distributions and annual-modulation signatures of weakly-interacting massive particles,” *Journal of High Energy Physics*, vol. 2001, no. 03, p. 049, 2001.
- [14] J. Vergados and H. Ejiri, “The role of ionization electrons in direct neutralino detection,” *Physics Letters B*, vol. 606, no. 3-4, pp. 313–322, 2005.
- [15] H. Ejiri, C. C. Moustakidis, and J. D. Vergados, “Dark matter search by exclusive studies of X-rays following WIMPs nuclear interactions,” *Physics Letters B*, vol. 639, no. 3-4, pp. 218–222, 2006.
- [16] C. C. Moustakidis, J. D. Vergados, and H. Ejiri, “Direct dark matter search by observing electrons produced in neutralino–nucleus collisions,” *Nuclear Physics B*, vol. 727, article 406, 2005.
- [17] B. Roberts, V. Flambaum, and G. Gribakin, “Ionization of atoms by slow heavy particles, including dark matter,” *Physical Review Letters*, vol. 116, article 023201, 2016.
- [18] B. M. Roberts, V. A. DZUba, V. V. Flambaum et al., “Dark matter scattering on electrons: Accurate calculations of atomic excitations and implications for the DAMA signal,” *Physical Review D*, vol. 93, article 115037, 2016.
- [19] J. D. Lewin and P. F. Smith, “Review of mathematics, numerical factors, and corrections for dark matter experiments based on elastic nuclear recoil,” *Astroparticle Physics*, vol. 6, article 87, 1996.
- [20] V. Barger, M. Ishida, and W. Keung, “Total Width of 125 GeV Higgs Boson,” *Physical Review Letters*, vol. 108, no. 26, 2012.
- [21] M. W. Goodman and E. Witten, “Detectability of certain dark-matter candidates,” *Physical Review D: Particles, Fields, Gravitation and Cosmology*, vol. 31, no. 12, pp. 3059–3063, 1985.
- [22] A. K. Drukier, K. Freese, and D. N. Spergel, “Detecting cold dark-matter candidates,” *Physical Review D: Particles, Fields, Gravitation and Cosmology*, vol. 33, no. 12, pp. 3495–3508, 1986.
- [23] J. R. Primack, D. Seckel, and B. Sadoulet, “Detection of Cosmic Dark Matter,” *Annual Review of Nuclear and Particle Science*, vol. 38, article 751, 1988.
- [24] A. Gabutti and K. Schmieemann, “Detection rate of weakly interacting massive particles,” *Physics Letters B*, vol. 308, no. 3-4, pp. 411–417, 1993.
- [25] R. Bernabei, “Research on dark matter,” *Riv. Nuovo Cimento*, vol. 18, no. 5, pp. 1–68, 1995.
- [26] D. Abriola, F. T. AvignoneIII, and R. L. Brodzinski, “Search for an annual modulation of dark-matter signals with a germanium spectrometer at the Sierra Grande Laboratory,” *Astroparticle Physics*, vol. 10, article 133, 1999.
- [27] F. Hasenbalg, “Annual modulation sensitivity in cold dark matter searches,” *Astroparticle Physics*, vol. 9, article 339, 1998.
- [28] J. D. Vergados, “Theoretical directional and modulated rates for direct supersymmetric dark matter detection,” *Physical Review D: Particles, Fields, Gravitation and Cosmology*, vol. 67, no. 10, 2003.
- [29] A. M. Green, “Effect of realistic astrophysical inputs on the phase and shape of the WIMP annual modulation signal,” *Physical Review D: Particles, Fields, Gravitation and Cosmology*, vol. 68, article 023004, 2004.
- [30] C. Savage, K. Freese, and P. Gondolo, “Annual modulation of dark matter in the presence of streams,” *Physical Review D: Particles, Fields, Gravitation and Cosmology*, vol. 74, no. 4, 2006.
- [31] P. J. Fox, J. Kopp, M. Lisanti, and N. Weiner, “A CoGeNT modulation analysis,” *Physical Review D: Particles, Fields, Gravitation and Cosmology*, vol. 85, no. 3, Article ID 036008, 2012.
- [32] R. Essig, J. Mardon, and T. Volansky, “Direct detection of sub-GeV dark matter,” *Physical Review D: Particles, Fields, Gravitation and Cosmology*, vol. 85, Article ID 076007, 2012.
- [33] R. Essig, A. Manalaysay, J. Mardon, P. Sorensen, and T. Volansky, “First direct detection limits on Sub-GeV dark matter from XENON10,” *Physical Review Letters*, vol. 109, no. 2, Article ID 021301, 2012.
- [34] J. Vergados, H. Ejiri, and K. Savvidy, “Theoretical direct WIMP detection rates for transitions to excited states,” *Nuclear Physics B*, vol. 877, article 36, 2013.
- [35] J. Vergados, F. T. Avignone-III, M. Kortelainen et al., “Inelastic WIMP-nucleus scattering to the first excited state in ^{125}Te ,” *Journal of Physics G: Nuclear and Particle Physics*, vol. 49, Article ID 150021, 2016.
- [36] J. D. Vergados, “Searching for cold dark matter,” *Journal of Physics G: Nuclear and Particle Physics*, vol. 22, no. 2, pp. 253–272, 1996.
- [37] M. Cannoni, “On the formalism and upper limits for spin-dependent cross sections in dark matter elastic scattering with nuclei,” *Physical Review D*, vol. 84, article 095017, 2011.
- [38] M. Cannoni, J. D. Vergados, and M. E. Gómez, “Scheme for the extraction of WIMP-nucleon scattering cross sections from total event rates,” *Physical Review D: Particles, Fields, Gravitation and Cosmology*, vol. 83, no. 7, 2011.
- [39] V. K. Oikonomou, J. D. Vergados, and C. C. Moustakidis, “Direct detection of dark matter rates for various wimps,” *Nuclear Physics B*, vol. 773, no. 1-2, pp. 19–42, 2007.
- [40] K. G. Savvidy and J. D. Vergados, “Direct dark matter detection: A spin,” *Physical Review D: Particles, Fields, Gravitation and Cosmology*, vol. 87, article 075013, 2013.
- [41] E. Aprile, K. Arisaka, F. Arneodo et al., “Dark Matter Results from 100 Live Days of XENON100 Data,” *Physical Review Letters*, vol. 107, article 131302, 2011.
- [42] E. Behnke, J. Behnke, S. J. Brice et al., “First dark matter search results from a 4-kg CF3I bubble chamber operated in a deep underground site,” *Physical Review D*, vol. 86, article 052001, 2012, see also Erratum: *Phys. Rev. D* 90, 079902 (2014).
- [43] M. Felizardo, T. Morlat, A. C. Fernandes et al., “First Results of the Phase II SIMPLE Dark Matter Search,” *Physical Review Letters*, vol. 108, article 201302, see also Erratum: *Phys. Rev. D* 90, 079902 (2014).
- [44] S. Archambault, “Constraints on Low-Mass WIMP Interactions on 19F from PICASSO,” *Physics Letters B*, vol. 711, article 153, 2012.
- [45] S. Archambault, F. Aubin, and M. Auger, “Dark Matter Spin-Dependent Limits for WIMP Interactions on 19-F by PICASSO,” *Physics Letters B*, vol. 682, article 185, 2009.
- [46] F. Aubin, M. Auger, and M.-H. Genest, “Discrimination of nuclear recoils from alpha particles with superheated liquids,” *New Journal of Physics*, vol. 10, article 103017, Article ID 103017, 2008.
- [47] E. Aprile, M. Alfonsi, K. Arisaka et al., “Dark Matter Results from 225 Live Days of XENON100 Data,” *Physical Review Letters*, vol. 109, article 181301, Article ID 181301, 2012.

- [48] N. Abgrall, E. Aguayo, F. T. Avignone III et al., “The MAJORANA DEMONSTRATOR Neutrinoless Double-Beta Decay Experiment,” *Advances in High Energy Physics*, vol. 2014, Article ID 365432, 18 pages, 2014.
- [49] R. Agnese et al., “Silicon detector dark matter results from the final exposure of cdms II,” *Phys. Rev. Lett.*, vol. 111, Article ID 251301, 2013.
- [50] J.-W. Chen, H.-C. Chi, and H.-B. Li, “Constraints on millicharged neutrinos via analysis of data from atomic ionizations with germanium detectors at sub-keV sensitivities,” *Physical Review D*, vol. 90, article 011301(R), 2014.
- [51] P. Venkataramaiah, K. Gopala, A. Basavaraju, S. S. Suryanarayana, and H. Sanjeeviah, “A simple relation for the Fermi function,” *Journal of Physics G: Nuclear and Particle Physics*, vol. 11, no. 3, article no. 014, pp. 359–364, 1985.
- [52] L. D. Landau and E. M. Lifshitz, *Quantum Mechanics, Non-relativistic Theory*, Pergamon Press, 3rd edition, 1977.
- [53] Y. Hochberg, M. Pyle, Y. Zhao, and K. M. Zurek, “Detecting superlight dark matter with Fermi-degenerate materials,” *Journal of High Energy Physics*, vol. 2016, no. 8, article no. 57, 2016.
- [54] K. Schutz and K. M. Zurek, “On the Detectability of Light Dark Matter with Superfluid Helium,” *Physical Review Letters*, vol. 117, article 121302, 2016.

Research Article

Heavy Sterile Neutrino in Dark Matter Searches

Paraskevi C. Divari ¹ and John D. Vergados ²

¹Department of Physical Sciences and Applications, Hellenic Army Academy, Vari, 16673 Attica, Greece

²TEI of Western Macedonia, 501 00 Kozani, Greece

Correspondence should be addressed to John D. Vergados; vergados@uoi.gr

Received 23 November 2017; Accepted 28 January 2018; Published 15 March 2018

Academic Editor: Athanasios Hatzikoutelis

Copyright © 2018 Paraskevi C. Divari and John D. Vergados. This is an open access article distributed under the Creative Commons Attribution License, which permits unrestricted use, distribution, and reproduction in any medium, provided the original work is properly cited. The publication of this article was funded by SCOAP³.

Sterile neutrinos are possible dark matter candidates. We examine here possible detection mechanisms, assuming that the neutrino has a mass of about 50 keV and couples to the ordinary neutrino. Even though this neutrino is quite heavy, it is nonrelativistic with a maximum kinetic energy of 0.1 eV. Thus new experimental techniques are required for its detection. We estimate the expected event rate in the following cases: (i) measuring electron recoil in the case of materials with very low electron binding; (ii) low temperature crystal bolometers; (iii) spin induced atomic excitations at very low temperatures, leading to a characteristic photon spectrum; (iv) observation of resonances in antineutrino absorption by a nucleus undergoing electron capture; (v) neutrino induced electron events beyond the end point energy of beta decaying systems, for example, in the tritium decay studied by KATRIN.

1. Introduction

There exists evidence for existence of dark matter in almost all scales, from the dwarf galaxies, galaxies, and cluster of galaxies, with the most important ones being the observed rotational curves in the galactic halos; see, for example, the review [1]. Furthermore cosmological observations have provided plenty of additional evidence, especially the recent WMAP [2] and Planck [3] data.

In spite of this plethora of evidence, it is clearly essential to directly detect such matter in the laboratory in order to unravel its nature. At present there exist many such candidates, called Weakly Interacting Massive Particles (WIMPs). Some examples are the LSP (Lightest Supersymmetric Particle) [4–11], technibaryon [12, 13], mirror matter [14, 15], and Kaluza-Klein models with universal extra dimensions [16, 17]. Among other things these models predict an interaction of dark matter with ordinary matter via the exchange of a scalar particle, which leads to a spin independent interaction (SI) or vector boson interaction and therefore to a spin dependent (SD) nucleon cross section.

Since the WIMPs are expected to be extremely nonrelativistic, with average kinetic energy $\langle T \rangle \approx 50 \text{ keV} (m_{\text{WIMP}}/100 \text{ GeV})$, they are not likely to excite the nucleus, even

if they are quite massive, $m_{\text{WIMP}} > 100 \text{ GeV}$. Therefore they can be directly detected mainly via the recoiling of a nucleus, first proposed more than 30 years ago [18]. There exists a plethora of direct dark matter experiments with the task of detecting WIMP event rates for a variety of targets such as those employed in XENON10 [19], XENON100 [20], XMASS [21], ZEPLIN [22], PANDA-X [23], LUX [24], CDMS [25], CoGENT [26], EDELWEISS [27], DAMA [28, 29], KIMS [30], and PICASSO [31, 32]. These consider dark matter candidates in the multi-GeV region.

Recently, however, an important dark matter particle candidate of the Fermion variety in the mass range of 10–100 keV, obtained from galactic observables, has arisen [33–35]. This scenario produces basically the same behavior in the power spectrum (down to Mpc scales) with that of standard Λ CDM cosmologies, by providing the expected large-scale structure [36]. In addition, it is not too warm; that is, the masses involved are larger than $m = 1\text{--}3 \text{ keV}$ to be in conflict with the current $L\alpha$ forest constraints [37] and the number of Milky Way satellites [38], as in standard Λ WDM cosmologies. In fact an interesting viable candidate has been suggested, namely, a sterile neutrino in the mass region of 48–300 keV [33–35, 39–43], but most likely around 50 keV. For a recent

review, involving a wider range of masses, see the white paper [44].

The existence of light sterile neutrinos had already been introduced to explain some experimental anomalies like those claimed in the short baseline LSND and MiniBooNE experiments [45–47], the reactor neutrino deficit [48], and the Gallium anomaly [49, 50], with possible interpretations discussed, for example, in [51, 52] as well as in [53, 54] for sterile neutrinos in the keV region. The existence of light neutrinos can be expected in an extended see-saw mechanism involving a suitable neutrino mass matrix containing a number of neutrino singlets not all of which being very heavy. In such models it is not difficult to generate more than one sterile neutrino, which can couple to the standard neutrinos [55]. As it has already been mentioned, however, the explanation of cosmological observations requires sterile neutrinos in the 50 keV region, which can be achieved in various models [33, 56].

In the present paper we will examine possible direct detection possibilities for the direct detection of these sterile neutrinos. Even though these neutrinos are quite heavy, their detection is not easy. Since like all dark matters candidates move in our galaxies with no relativistic velocities, with average value about $10^{-3}c$, and with energies about 0.05 eV, not all of them can be deposited in the detectors. Therefore the standard detection techniques employed in the standard dark matter experiments like those mentioned above are not applicable in this case. Furthermore, the size of the mixing parameter of sterile neutrinos with ordinary neutrinos is

$$d\sigma = \frac{1}{v} C_\nu^2 (g_V^2 + g_A^2) \left(\frac{G_F}{2\sqrt{2}} \right)^2 \frac{d^3 \mathbf{p}'_\nu}{(2\pi)^3} \frac{d^3 \mathbf{p}_e}{(2\pi)^3} (2\pi)^4 \delta(\mathbf{p}_\nu - \mathbf{p}'_\nu - \mathbf{p}_e) \delta \left(\frac{p_\nu^2}{2m_\nu} - \frac{(p'_\nu)_y}{2m_\nu} - \frac{p_e^2}{2m_e} \right), \quad (1)$$

where C_ν^2 is the square of the mixing of the sterile neutrino with the standard electron neutrino ν_e and $G_F = G \cos \theta_c$, where $G = 1.1664 \times 10^{-5} \text{ GeV}^{-2}$ denotes the Fermi weak coupling constant and $\theta_c \approx 13^\circ$ is the Cabibbo angle [58]. The integration over the outgoing neutrino momentum is trivial due to the momentum δ function yielding

$$d\sigma = \frac{1}{v} C_\nu^2 (g_V^2 + g_A^2) \left(\frac{G_F}{2\sqrt{2}} \right)^2 \frac{1}{(2\pi)^2} \cdot d^3 \mathbf{p}_e \delta \left(p_e v \xi - \frac{p_e^2}{2\mu_r} \right), \quad (2)$$

where $\xi = \hat{\mathbf{p}}_e \cdot \hat{\mathbf{p}}_\nu$, $0 \leq \xi \leq 1$, v is the WIMP velocity, and μ_r is the WIMP-electron reduced mass, $\mu_r \approx m_\nu$. The electron energy T is given by

$$T = \frac{p_e^2}{2m_e} = 2 \frac{m_\nu^2}{m_e} (v\xi)^2 \implies 0 \leq T \leq 2 \frac{m_\nu^2}{m_e} v_{\text{esc}}^2, \quad (3)$$

crucial for detecting sterile neutrinos. Thus our results concerning the expected event rates will be given in terms of this parameter.

The paper is organized as follows. In Section 2 we study the option on neutrino-electron scattering. In Section 3 we consider the case of low temperature bolometers. In Section 4 the possibility of neutrino induced atomic excitations is explored. In Section 5 we will consider the antineutrino absorption on nuclei, which normally undergo electron capture, and finally in Section 6 the modification of the end point electron energy in beta decay, for example, in the KATRIN experiment [57], is discussed. In Section 7, we summarize our conclusions.

2. The Neutrino-Electron Scattering

The sterile neutrino as dark matter candidate can be treated in the framework of the usual dark matter searches for light WIMPs except that its mass is very small. Its velocity follows a Maxwell-Boltzmann (MB) distribution with a characteristic velocity about $10^{-3}c$. Since the sterile neutrino couples to the ordinary electron neutrino it can be detected in neutrino-electron scattering experiments with the advantage that the neutrino-electron cross section is very well known. Both the neutrino and the electron can be treated as nonrelativistic particles. Furthermore we will assume that the electrons are free, since the WIMP energy is not adequate to ionize an the atom. Thus the differential cross section is given by

where v_{esc} is the maximum WIMP velocity (escape velocity). Integrating (2) over the angles, using the δ function for the ξ integration we obtain

$$d\sigma = C_\nu^2 \frac{1}{v} (g_V^2 + g_A^2) \left(\frac{G_F}{2\sqrt{2}} \right)^2 \frac{1}{2\pi} p_e^2 dp_e \frac{1}{|p_e v|} \implies \quad (4)$$

$$d\sigma = C_\nu^2 \frac{1}{v^2} (g_V^2 + g_A^2) \left(\frac{G_F}{2\sqrt{2}} \right)^2 \frac{1}{2\pi} m_e dT.$$

We are now in a position to fold the velocity distribution assuming it to be MB with respect to the galactic center:

$$f(v') = \frac{1}{(\sqrt{\pi}v_0)^3} e^{-(v'/v_0)^2}. \quad (5)$$

In the local frame, assuming that the sun moves around the center of the galaxy with velocity $v_0 = 220 \text{ km/s}$, $\mathbf{v}' = \mathbf{v} + v_0 \hat{\mathbf{z}}$, we obtain

$$f_\ell(y, \xi) = \frac{1}{(\sqrt{\pi}v_0)^3} e^{-(1+y^2+2y\xi)}, \quad y = \frac{v}{v_0}, \quad (6)$$

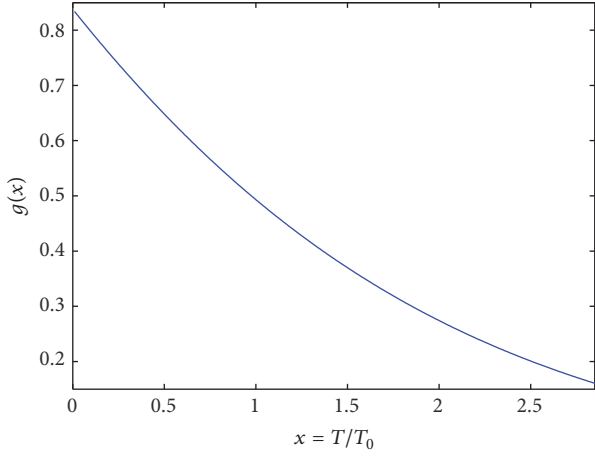


FIGURE 1: The shape of the spectrum of the emitted electrons in sterile neutrino-electron scattering.

where ξ is now the cosine of the angle between the WIMP velocity \mathbf{v} and the direction of the sun's motion. Eventually we will need the flux so we multiply with the velocity v before we integrate over the velocity. The limits of integration are between v_{\min} and v_{esc} . The velocity is given via (3); namely,

$$v = \frac{\sqrt{2m_e T}}{2m_\nu \xi} \implies v_{\min} = \frac{\sqrt{2m_e T}}{2m_\nu} \quad (7)$$

We find it convenient to express the kinetic energy T in units of $T_0 = 2(m_\nu^2/m_e)v_0^2$. Then

$$y_{\min} = \sqrt{x}, \quad x = \frac{T}{T_0}. \quad (8)$$

Thus

$$\begin{aligned} \left\langle v \frac{d\sigma}{dT} \right\rangle &= \frac{1}{v_0} \frac{1}{T_0} \frac{m_e}{16\pi} C_\nu^2 G_F^2 (g_V^2 + g_A^2) \\ &\cdot \int_{\sqrt{x}}^{y_{\text{esc}}} dy y \frac{2}{\sqrt{\pi}} e^{-(1+y^2)} \int_{-1}^1 d\xi e^{-2y\xi}. \end{aligned} \quad (9)$$

These integrals can be done analytically to yield

$$\begin{aligned} \left\langle v \frac{d\sigma}{dT} \right\rangle &= \frac{1}{v_0} \frac{m_e}{16\pi} C_\nu^2 G_F^2 (g_V^2 + g_A^2) g(x), \\ g(x) &= \frac{1}{2} (\text{erf}(1 - \sqrt{x}) + \text{erf}(\sqrt{x} + 1)) \\ &+ \text{erfc}(1 - y_{\text{esc}}) + \text{erfc}(y_{\text{esc}} + 1) - 2, \end{aligned} \quad (10)$$

where erf is the error function and $\text{erfc}(x)$ is its complement. The function $g(x)$ characterizes the spectrum of the emitted electrons and is exhibited in Figure 1 and it is without

any particular structure, which is the case in most WIMP searches. For a 50 keV sterile neutrino we find that

$$T_0 = 2 \left(\frac{m_\nu}{m_e} \right)^2 \left(\frac{2.2}{3} \right)^2 10^{-6} m_e c^2 \approx 5.0 \times 10^{-3} \text{ eV} \quad (11)$$

$$T_{\max} = T_0 y_{\text{esc}}^2 = 5 \times 10^{-3} 2.84^2 \approx 0.04 \text{ eV}$$

$$\langle T \rangle = 1.6 T_0 = 8.0 \times 10^{-3} \text{ eV}.$$

Now $dT = T_0 dx$. Thus

$$\begin{aligned} \frac{\langle v\sigma \rangle}{v_0} &= \frac{1}{v_0^2} \frac{m_e T_0}{16\pi} C_\nu^2 G_F^2 (g_V^2 + g_A^2) \int_0^{y_{\text{esc}}} dx g(x) \\ &= 1.43 \frac{m_\nu^2}{8\pi} C_\nu^2 G_F^2 (g_V^2 + g_A^2), \end{aligned} \quad (12)$$

where

$$\int_0^{y_{\text{esc}}} dx g(x) = 1.43. \quad (13)$$

It is clear that with this amount of energy transferred to the electron it is not possible to eject an electron out of the atom. One therefore must use special materials such that the electrons are loosely bound. It has recently been suggested that it is possible to detect even very light WIMPs, much lighter than the electron, utilizing Fermi-degenerate materials like superconductors [59]. In this case the energy required is essentially the gap energy of about $1.5kT_c$, which is in the meV region; that is, the electrons are essentially free. In what follows, we assume the values

$$\begin{aligned} g_A &= 1, \\ g_V &= 1 + 4 \sin^2 \theta_W = 1.92, \\ G_F^2 &= 5.02 \times 10^{-44} \text{ cm}^2/\text{MeV}^2 \end{aligned} \quad (14)$$

while C_ν^2 is taken as a parameter and will be discussed in Section 7. Thus we obtain

$$\frac{\langle v\sigma \rangle}{v_0} = 3.47 \times 10^{-47} C_\nu^2 \text{ cm}^2. \quad (15)$$

The neutrino particle density is

$$N_\nu = \frac{\rho}{m_\nu} = \frac{0.3 \text{ GeV/cm}^3}{50 \times 10^{-6} \text{ GeV}} = 6 \times 10^3 \text{ cm}^{-3} \quad (16)$$

while the neutrino flux

$$\Phi_\nu = \frac{\rho}{m_\nu} v_0 = 1.32 \times 10^{11} \text{ cm}^{-2} \text{ s}^{-1}, \quad (17)$$

TABLE I: The frequency modes below the Debye temperature for α -TeO₂ obtained from Table VIII of [60] (for notation see text).

$\nu_i = \frac{\omega_i}{2\pi}$ (cm ⁻¹)	52	124	128	152	157	176	177	179
Symmetry	B_1	E	B_1	A_1	B_2	A_2	E	B_1
ω_i (eV)	0.006	0.015	0.016	0.019	0.019	0.022	0.022	0.022
N_i	16	6	6	5	5	4	4	4
$E_{\max}(i)$ (meV)	106	100	102	103	107	98	99	100

where $\rho = 0.3 \text{ GeV/cm}^3$, being the dark matter density. Assuming that the number of electron pairs in the target is $2 \times N_A = 2 \times 10^{24}$ we find that the number of events per year is

$$\Phi_\nu \frac{\langle v\sigma \rangle}{v_0} 2 \times N_A = 2.89 \times 10^{-4} C_\nu^2 \text{Y}^{-1}. \quad (18)$$

The authors of [59] are perhaps aware of the fact that the average energy for very light WIMPS is small and as we have seen above a small portion of it is transferred to their system. With their bolometer detector these authors probably have a way to circumvent the fact that a small amount of energy will be deposited, about 0.4 eV in a year for $N_A \approx 10^{24}$. Perhaps they may manage to accumulate a larger number of loosely bound electrons in their target.

3. Sterile Neutrino Detection via Low Temperature Bolometers

Another possibility is to use bolometers, like the CUORE detector exploiting Low Temperature Specific Heat of Crystalline ¹³⁰TeO₂ at low temperatures. The energy of the WIMP will now be deposited in the crystal, after its interaction with the nuclei via Z-exchange. In this case the Fermi component of interaction with neutrons is coherent, while that of the protons is negligible. Thus the matrix element becomes

$$\text{ME} = \frac{G_F}{2\sqrt{2}} N g_V, \quad (19)$$

N = number of neutrons in the nucleus.

A detailed analysis of the frequencies of ¹³⁰TeO₂ can be found [60]. The analysis involved crystalline phases of tellurium dioxide: paratellurite α -TeO₂, tellurite β -TeO₂, and the new phase γ -TeO₂, recently identified experimentally. Calculated Raman and IR spectra are in good agreement with available experimental data. The vibrational spectra of α and β -TeO₂ can be interpreted in terms of vibrations of TeO₂ molecular units. The α -TeO₂ modes are associated with the symmetry D_4 or 422, which has 5 irreducible representations, two 1-dimensional representations of the antisymmetric type indicated by A_1 and A_2 , two 1-dimensional representations of the symmetric types B_1 and B_2 , and one 2-dimensional representation, usually indicated by E . They all have been tabulated in [60]. Those that can be excited must be below the

Debye frequency which has been determined [61] and found to be quite low:

$$T_D = (232 \pm 7) \text{K} \implies \omega_D = 0.024 \text{eV}. \quad (20)$$

This frequency is smaller than the maximum sterile neutrino energy estimated to be $T_{\max} = 0.11 \text{eV}$. Those frequency modes of interest to us are given in Table 1. The differential cross section is, therefore, given by

$$\begin{aligned} d\sigma = & \frac{1}{v} C_\nu^2 N^2 (g_V^2) \left(\frac{G_F}{2\sqrt{2}} \right)^2 \sum_{k=1}^8 \sum_{n_i=0}^{N_k} \frac{d^3 \mathbf{p}'_v}{(2\pi)^3} \frac{d^3 \mathbf{q}}{(2\pi)^3} (2\pi)^4 \\ & \cdot F^2(\mathbf{q}^2) \delta(\mathbf{p}_v - \mathbf{p}'_v - \mathbf{q}) \\ & \cdot \delta \left(\frac{p_v^2}{2m_\nu} - \frac{(p'_v)^2}{2m_\nu} - \left(n_i + \frac{1}{2} \right) \omega_k \right), \end{aligned} \quad (21)$$

where N_i will be specified below and \mathbf{q} is the momentum transferred to the nucleus. The momentum transfer is small and the form factor $F^2(\mathbf{q}^2)$ can be neglected.

In deriving this formula we tacitly assumed a coherent interaction between the WIMP and several nuclei, thus creating a collective excitation of the crystal, that is, a phonon or few phonons. This of course is a good approximation provided that the energy transferred is small, of a few tens of meV. We see from Table 1 that the maximum allowed energy is small, around 100 meV. We find that, if we restrict the maximum allowed energy by a factor of 2, the obtained results are reduced only by a factor of about 10%. We may thus assume that this approximation is good.

Integrating over the nuclear momentum we get

$$\begin{aligned} d\sigma = & \frac{1}{v} C_\nu^2 N^2 (g_V^2) \left(\frac{G_F}{2\sqrt{2}} \right)^2 \frac{1}{(2\pi)^2} \\ & \cdot \sum_{k=1}^8 \sum_{n_i=0}^{N_k} d^3 \mathbf{p}'_v \delta \left(\frac{p_v^2}{2m_\nu} - \frac{(p'_v)^2}{2m_\nu} - \left(n_i + \frac{1}{2} \right) \omega_k \right) \\ d\sigma = & \frac{1}{v} C_\nu^2 N^2 (g_V^2) \left(\frac{G_F}{2\sqrt{2}} \right)^2 \frac{1}{(2\pi)^2} \\ & \cdot \sum_{k=1}^8 \sum_{n_i=0}^{N_k} d^3 \mathbf{p}'_v \delta \left(\frac{p_v^2}{2m_\nu} - \frac{(p'_v)^2}{2m_\nu} - \left(n_i + \frac{1}{2} \right) \omega_k \right); \end{aligned} \quad (22)$$

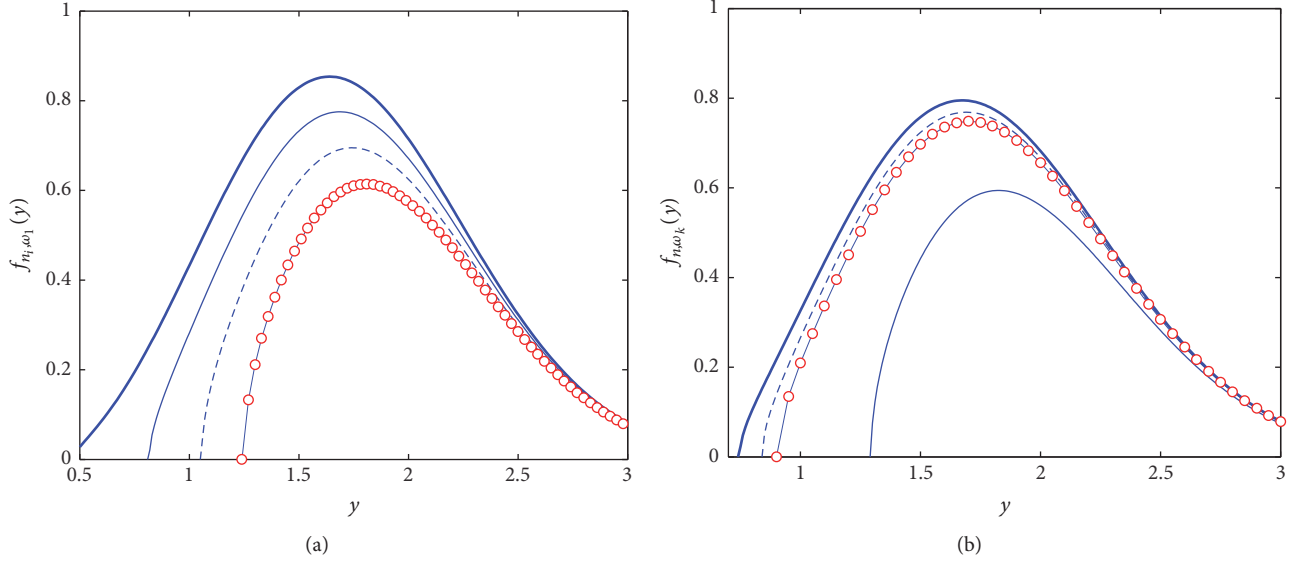


FIGURE 2: (a) The function $f_{n_i, \omega_1}(y)$, exhibited as a function of y , associated with the mode $\nu_1 = 52 \text{ cm}^{-1}$ for $n = 0, 1, 2, 3$ increasing downwards. (b) The functions $f_{n_i, \omega_2}(y)$ associated with $\nu_2 = 124 \text{ cm}^{-1}$ for $n = 0, 1$ and f_{0, ω_4} for $\nu_4 = 157 \text{ cm}^{-1}$, $n = 0$, and f_{0, ω_6} for $\nu_6 = 176 \text{ cm}^{-1}$, $n = 0$, exhibited as a function of y , for thick solid, solid, dashed, and dotted lines, respectively. For definitions see text.

performing the integration using the δ function we get

$$\begin{aligned} \sigma &= \frac{1}{v} C_\nu^2 N^2 (g_V^2) \left(\frac{G_F}{2\sqrt{2}} \right)^2 \frac{1}{\pi} \\ &\cdot m_\nu \sqrt{2m_\nu} \sum_{k=1}^8 \sum_{n_i=1}^{N_k} \sqrt{E_\nu - \left(n_i + \frac{1}{2} \right) \omega_k} \\ \sigma &= \frac{v_0}{v} C_\nu^2 N^2 (g_V^2) \left(\frac{G_F}{2\sqrt{2}} \right)^2 \frac{1}{\pi} \\ &\cdot m_\nu^2 \sum_{k=1}^8 \sum_{n_i=0}^{N_k} \sqrt{y^2 - \frac{(n_i + 1/2) \omega_k}{T_1}}, \end{aligned} \quad (23)$$

where $T_1 = (1/2)m_\nu v_0^2$, $y = v/v_0$

Folding with the velocity distribution we obtain

$$\begin{aligned} \langle v\sigma \rangle &= v_0 C_\nu^2 N^2 (g_V^2) \left(\frac{G_F}{2\sqrt{2}} \right)^2 \frac{1}{\pi} m_\nu^2 \sum_{k=1}^8 \sum_{n_i=0}^{N_k} I_{n_i, \omega_k}, \\ I_{n_i, \omega_k} &= \int_{y_{\min}}^{y_{\text{esc}}} dy f_{n_i, \omega_k}(y), \\ f_{n_i, \omega_k}(y) &= \sqrt{y^2 - \frac{(n_i + 1/2) \omega_k}{T_1}} y e^{-1-y^2} \sinh 2y, \\ y_{\min} &= \sqrt{\frac{(n_i + 1/2) \omega_k}{T_1}}. \end{aligned} \quad (24)$$

We see that we have the constraint imposed by the available energy; namely,

$$N_k = \text{IP} \left[\frac{y_{\text{esc}}^2 T_1}{\omega_k} - \frac{1}{2} \right], \quad (25)$$

where $\text{IP}[x] = \text{integer part of } x$. We thus find N_k listed in Table 1. The functions $f_{n_i, \omega_k}(y)$ are exhibited in Figure 2. The relevant integrals are $I_n(\omega_1) = (1.170, 0.972, 0.785, 0.621)$ for $n = 0, 1, 2, 3$, $I_n(\omega_2) = (1.032, 0.609)$, for $n = 0, 1$, $I_n(\omega_3) = (1.025, 0.592)$, for $n = 0, 1$, and $I_0(\omega_k) = (0.979, 0.970, 0.934, 0.932, 0.929)$ for $k = 4, \dots, 8$. Thus we obtain a total of 17.8. The event rate takes with a target of mass m_t which takes the form

$$R = \Phi_\nu C_\nu^2 N^2 (g_V^2) G_F^2 \frac{1}{8\pi} \frac{m_t}{A m_p} m_\nu^2 17.8. \quad (26)$$

If we restrict the maximum allowed energy to half of that shown in Table 1 by a factor of two, we obtain 15.7 instead of 17.8.

For a $^{130}\text{TeO}_2$ target ($N = 78$) of 1 kg of mass get

$$R = 1.7 \times 10^{-6} C_\nu^2 \text{ per kg-s} = 51 C_\nu^2 \text{ per kg-y} \quad (27)$$

This is much larger than that obtained in the previous section, mainly due to the neutron coherence arising from the Z-interaction with the target (the number of scattering centers is approximately the same, 4.5×10^{24}). In the present case, however, targets can be larger than 1kg. Next we are going to examine other mechanisms, which promise a better signature.

4. Sterile Neutrino Detection via Atomic Excitations

We are going to examine the interesting possibility of excitation of an atom from a level $|j_1, m_1\rangle$ to a nearby level

$|j_2, m_2\rangle$ at energy $\Delta = E_2 - E_1$, which has the same orbital structure. The excitation energy has to be quite low; that is,

$$\begin{aligned} \Delta &\leq \frac{1}{2} m_\nu v_{\text{esc}}^2 = \frac{1}{2} 50 \times 10^3 2.84^2 \left(\frac{2.2}{3}\right)^2 10^{-6} \\ &= 0.11 \text{ eV}. \end{aligned} \quad (28)$$

The target is selected so that the two levels $|j_1, m_1\rangle$ and $|j_2, m_2\rangle$ are closer than 0.11 eV. This can result from the splitting of an atomic level by the magnetic field so that they can be connected by the spin operator. The lower one $|j_1, m_1\rangle$ is occupied by electrons but the higher one $|j_2, m_2\rangle$ is completely empty at sufficiently low temperature. It can be populated only by exciting an electron to it from the lower one by the oncoming sterile neutrino. The presence of such an excitation is monitored by a tuned laser which excites such an electron from $|j_2, m_2\rangle$ to a higher state $|j_3, m_3\rangle$, which cannot be reached in any other way, by observing its subsequent decay by emitting photons.

Since this is a one-body transition the relevant matrix element takes the form

$$\begin{aligned} &|\text{ME}(j_1, m_1; j_2, m_2)|^2 \\ &= g_V^2 \delta_{j_1, j_2} \delta_{m_1, m_2} + g_A^2 (C_{\ell, j_1, m_1, j_2, m_2})^2 \end{aligned} \quad (29)$$

(in the case of the axial current we have $g_A = 1$ and we need evaluate the matrix element of $\sigma_\nu \cdot \sigma_e$ and then square it and sum and average over the neutrino polarization).

$$\begin{aligned} C_{\ell, j_1, m_1, j_2, m_2} &= \langle n\ell j_2 m_2 | \sigma | n\ell j_1 m_1 \rangle \\ &= \langle j_1 m_1, 1 m_2 - m_1 | j_2 m_2 \rangle \\ &\cdot \sqrt{(2j_1 + 1) 3 \sqrt{2\ell + 1} \sqrt{6}} \begin{Bmatrix} \ell & \frac{1}{2} & j_1 \\ \ell & \frac{1}{2} & j_2 \\ 0 & 1 & 1 \end{Bmatrix} \end{aligned} \quad (30)$$

expressed in terms of the Clebsch-Gordan coefficient and the nine-j symbol. It is clear that in the energy transfer of interest only the axial current can contribute to excitation.

The cross section takes the form

$$d\sigma = \frac{1}{v} C_\nu^2 \left(\frac{G_F}{2\sqrt{2}}\right)^2 |\text{ME}(j_1, m_1; j_2, m_2)|^2 \frac{d^3 \mathbf{p}'_\nu}{(2\pi)^3} \frac{d^3 \mathbf{p}_A}{(2\pi)^3} (2\pi)^4 \delta(\mathbf{p}_\nu - \mathbf{p}'_\nu - \mathbf{p}_A) \delta(E_\nu - \Delta - E'_\nu). \quad (31)$$

Integrating over the atom recoil momentum, which has negligible effect on the energy, and over the direction of the final neutrino momentum and energy via the δ function we obtain

$$\begin{aligned} \sigma &= \frac{1}{v} C_\nu^2 \left(\frac{G_F}{2\sqrt{2}}\right)^2 |\text{ME}(j_1, m_1; j_2, m_2)|^2 \frac{1}{\pi} (E_\nu - \Delta) \\ &\cdot \sqrt{2(E_\nu - \Delta - m_\nu) m_\nu} = \frac{1}{v} C_\nu^2 \left(\frac{G_F}{2\sqrt{2}}\right)^2 \\ &\cdot |\text{ME}(j_1, m_1; j_2, m_2)|^2 \frac{1}{\pi} m_\nu^2 \sqrt{\frac{2T_1}{m_\nu}} f\left(y, \frac{\Delta}{T_1}\right) \\ f\left(y, \frac{\Delta}{T_1}\right) &= \left(y^2 - \frac{\Delta}{T_1}\right)^{1/2}, \quad T_1 = \frac{1}{2} m_\nu v_0^2, \end{aligned} \quad (32)$$

where we have set $E - \Delta = m_\nu + T_1 - \Delta \approx m_\nu$.

Folding the cross section with the velocity distribution from a minimum $\sqrt{\Delta/T_1}$ to y_{esc} we obtain

$$\begin{aligned} &\langle v\sigma \rangle \\ &= C_\nu^2 \left(\frac{G_F}{2\sqrt{2}}\right)^2 m_\nu^2 |\text{ME}(j_1, m_1; j_2, m_2)|^2 \frac{1}{\pi} g\left(\frac{\Delta}{T_1}\right) \\ g\left(\frac{\Delta}{T_1}\right) &= \frac{2}{\sqrt{\pi}} \int_{\sqrt{\Delta/T_1}}^{y_{\text{esc}}} dy y^2 \left(y^2 - \frac{\Delta}{T_1}\right)^{1/2} e^{-(1+y^2)} \frac{\sinh 2y}{y}. \end{aligned} \quad (33)$$

Clearly the maximum excitation energy that can be reached is $\Delta_{\text{max}} = 2.84^2 T_0 = 0.108 \text{ eV}$. The function $g(\Delta/T_1)$ is exhibited in Figure 3.

Proceeding as in Section 2 and noting that for small excitation energy $g(\Delta/T_1) \approx 1.4$ we find

$$R = 1.8 \times 10^{-2} C_\nu^2 \frac{1}{A} (C_{\ell, j_1, m_1, j_2, m_2})^2 \text{ kg}\cdot\text{y}. \quad (34)$$

The expected rate will be smaller after the angular momentum factor $C_{\ell, j_1, m_1, j_2, m_2}$ is included (see Appendix A). Anyway, leaving aside this factor, which can only be determined after a specific set of levels is selected, we see that the obtained rate is comparable to that expected from electron recoil (see (18)). In fact for a target with $A = 100$ we obtain

$$R = 1.8 \times 10^{-4} C_\nu^2 (C_{\ell, j_1, m_1, j_2, m_2})^2 \text{ kg}\cdot\text{y}. \quad (35)$$

This rate, however, decreases as the excitation energy increases (see Figure 3). In the present case, however, we have two advantages.

- (i) The characteristic signature of photons spectrum is following the deexcitation of the level $|j_3, m_3\rangle$ mentioned above. The photon energy can be changed if the target is put in a magnetic field by a judicious choice of $|j_3, m_3\rangle$.
- (ii) The target now can be much larger, since one can employ a solid at very low temperatures. The ions

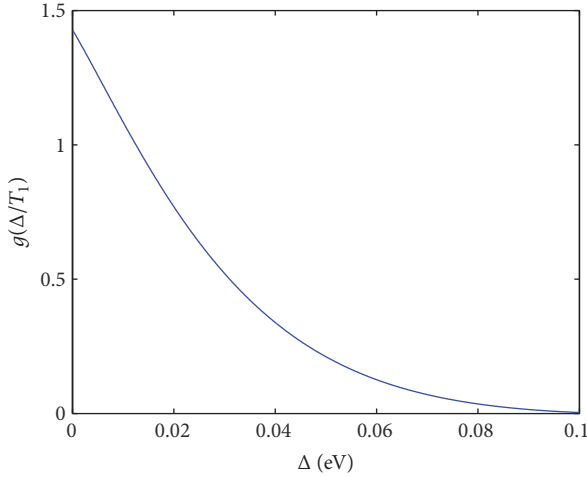


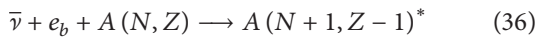
FIGURE 3: The function $g(\Delta/T_1)$ for sterile neutrino scattering by an atom as a function of the excitation energy in eV.

of the crystal still exhibit atomic structure. The electronic states probably will not carry all the important quantum numbers as their corresponding neutral atoms. One may have to consider exotic atoms (see Appendix B) or targets which contain appropriate impurity atoms in a host crystal, for example, chromium in sapphire.

In spite of this it seems very hard to detect such a process, since the expected counting rate is very low.

5. Sterile Neutrino Capture by a Nucleus Undergoing Electron Capture

This is essentially the process:



involving the absorption of a neutrino with the simultaneous capture of a bound electron. It has already been studied [62] in connection with the detection of the standard relic neutrinos. It involves modern technological innovations like the Penning Trap Mass Spectrometry (PT-MS) and the Microcalorimetry (MC). The former should provide an answer to the question of accurately measuring the nuclear binding energies and how strong the resonance enhancement is expected, whereas the latter should analyze the bolometric spectrum in the tail of the peak corresponding to L-capture to the excited state in order to observe the relic antineutrino events. They also examined the suitability of ^{157}Tb for relic antineutrino detection via the resonant enhancement to be considered by the PT-MS and MC teams. In the present case the experimental constraints are expected to be less stringent since the sterile neutrino is much heavier.

Let us measure all energies from the ground state of the final nucleus and assume that Δ is the mass difference of the two neutral atoms. Let us consider a transition to the final state with energy E_x . The cross section for a neutrino (here as well as in the following we write neutrino, but it is

understood that we mean antineutrino) of given velocity v and kinetic energy E_ν is given by

$$\sigma(E_\nu) = C_\nu^2 \frac{1}{v} |\text{ME}(E_x)|_{\text{Inuc}}^2 \langle \phi_e \rangle^2 \cdot \left(\frac{G_F}{2\sqrt{2}} \right)^2 \frac{d^3 p_A}{(2\pi)^3} (2\pi)^4 \delta(\mathbf{p}_A - \mathbf{p}_\nu) \delta(E_\nu + m_\nu + \Delta - E_x - b), \quad (37)$$

where \mathbf{p}_A is the recoiling nucleus momentum. Integrating over the recoil momentum using the δ function we obtain

$$\sigma(E_\nu) = C_\nu^2 2\pi \frac{1}{v} |\text{ME}(E_x)|_{\text{Inuc}}^2 \langle \phi_e \rangle^2 \left(\frac{G_F}{2\sqrt{2}} \right)^2 \cdot \delta(E_\nu + m_\nu + \Delta - E_x - b). \quad (38)$$

We note that since the oncoming neutrino has a mass, the excited state must be higher than the highest excited state at $E'_x = \Delta - b$. With indicating by $\epsilon = E_x - E'_x$ the above equation can be written as

$$\sigma(E_\nu) = C_\nu^2 2\pi \frac{1}{v} |\text{ME}(E_x)|_{\text{Inuc}}^2 \langle \phi_e \rangle^2 \left(\frac{G_F}{2\sqrt{2}} \right)^2 \cdot \delta(E_\nu + m_\nu - \epsilon). \quad (39)$$

Folding it with the velocity distribution as above we obtain

$$\langle v\sigma(E_\nu) \rangle = C_\nu^2 2\pi |\text{ME}(E_x)|_{\text{Inuc}}^2 \langle \phi_e \rangle^2 \left(\frac{G_F}{2\sqrt{2}} \right)^2 \cdot \int_0^{y^{\text{esc}}} dy y^2 \frac{2}{\sqrt{\pi}} e^{-(1+y^2)} \frac{\sinh 2y}{y} \cdot \delta\left(m_\nu + \frac{1}{2}m_\nu v_0^2 y^2 - \epsilon\right) \quad (40)$$

or using the delta function

$$\begin{aligned} \langle v\sigma(E_\nu) \rangle &= 2\pi C_\nu^2 |\text{ME}(E_x)|_{\text{Inuc}}^2 \frac{\langle \phi_e \rangle^2}{m_\nu v_0^2} \left(\frac{G_F}{2\sqrt{2}} \right)^2 F(X), \\ F(X) &= \frac{2}{\sqrt{\pi}} e^{-(1+X^2)} \sinh 2X, \end{aligned} \quad (41)$$

$$X = \frac{1}{v_0} \sqrt{2 \left(\frac{\epsilon}{m_\nu} - 1 \right)}.$$

As expected the cross section exhibits resonance behavior though the normalized function $F(X)$ as shown in Figure 4. It is, of course, more practical to exhibit the function $F(X)$ as a function of the energy ϵ . This is exhibited in Figure 5. From this figure we see that the cross section resonance is quite narrow. We find that the maximum occurs at $\epsilon = m_\nu(1 + 2.8 \times 10^{-7}) = 50 \text{ keV} + 0.014 \text{ eV}$ and has a width $\Gamma = m_\nu(1 + 9.1 \times 10^{-7}) - m_\nu(1 + 0.32 \times 10^{-7}) \approx 0.04 \text{ eV}$. So for all practical purposes it is a line centered at the neutrino

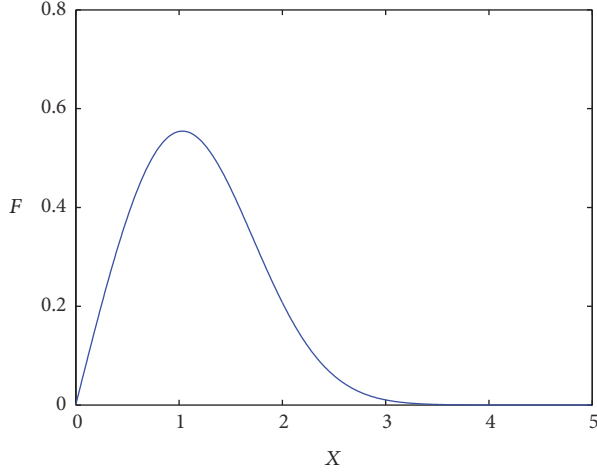


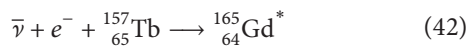
FIGURE 4: The cross section exhibits resonance behavior. Shown is the resonance properly normalized as a function of $X = (1/\nu_0)\sqrt{2(\epsilon/m_\nu - 1)}$. The width is $\Gamma = 1.49$ and the location of the maximum is at 1.03.

mass. The width may be of some relevance in the special case whereby the excited state can be determined by atomic deexcitations at the sub-eV level, but it will not show up in the nuclear deexcitations.

If there is a resonance in the final nucleus at the energy $E_x = \epsilon + (\Delta - b)$ with a width Γ then perhaps it can be reached even if ϵ is a bit larger than m_ν ; for example, $\epsilon = m_\nu + \Gamma/2$. The population of this resonance can be determined by measuring the energy of the deexcitation γ -ray, which should exceed by ϵ the maximum observed in ordinary electron capture.

For antineutrinos having zero kinetic energy the atom in the final state has to have an excess energy $\Delta - (b - m_\nu)$ and this can only happen if this energy can be radiated out via photon or phonon emission. The photon emission takes place either as atomic electron or nuclear level transitions. In the first case photon energies are falling in the eV-keV energy region and this implies that only nuclei with a very small Δ -value could be suitable for this detection. In the second case, there should exist a nuclear level that matches the energy difference $E_x = \Delta - (b - m_\nu)$ and therefore the incoming antineutrino has no energy threshold. Moreover, spontaneous electron capture decay is energetically forbidden, since this is allowed for $E_x < \Delta - (b + m_\nu)$.

As an example we consider the capture of a very low energy $\bar{\nu}$ by the $^{157}_{65}\text{Tb}$ nucleus:



taking the allowed transitions from the ground state ($3/2^+$) of parent nucleus, $^{157}_{65}\text{Tb}$, to the first excited $5/2^+$ state of the daughter nucleus $^{165}_{64}\text{Gd}$. The spin and parity of the nuclei involved obey the relations $\Delta J = 1$, $\Pi_f \Pi_i = +1$, and the

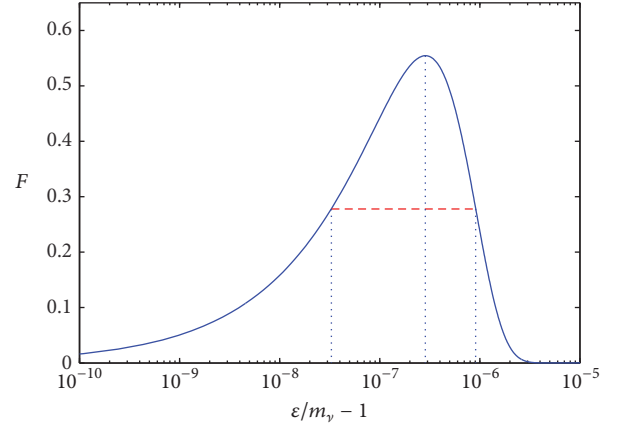


FIGURE 5: The cross section exhibits resonance behavior. Shown is $F(X)$ as a function of $(\epsilon/m_\nu - 1)$.

transition is dubbed as allowed. The nuclear matrix element ME can be written as

$$|\text{ME}|^2 = \left(\frac{g_A}{g_V} \right)^2 \langle \text{GT} \rangle^2, \quad (43)$$

where $g_A = 1.2695$ and $g_V = 1$ are the axial and vector coupling constants, respectively. The nuclear matrix element is calculated using the microscopic quasi-particle-phonon (MQPM) model [63, 64] and it is found to be $|\text{ME}|^2 = 0.96$. The experimental value of first excited $5/2^+$ is at 64 keV [65] while that predicted by the model is at 65 keV. The Δ -value is ranging from 60 to 63 keV [65].

For K-shell electron capture where $\langle \phi_e \rangle^2 = ((\alpha Z/\pi)m_e)^3$ (1s capture) with binding energy $b = 50.24$ keV, the velocity averaged cross section takes the value

$$\langle \sigma v \rangle = 8.98 \times 10^{-46} C_\nu^2 \text{ cm}^2 \quad (44)$$

and the event rate we expect for mass $m_t = 1$ kg is

$$R = 8.98 \times 10^{-46} C_\nu^2 \times 6 \cdot 10^3 \times 6.023 \cdot 10^{23} \times \frac{m_t}{A} \times 9.28 \times 10^{17} \text{ y}^{-1} = 19 C_\nu^2 \text{ y}^{-1}. \quad (45)$$

The life time of the source should be suitable for the experiment to be performed. If it is too short, the time available will not be adequate for the execution of the experiment. If it is too long, the number of counts during the data taking will be too small. Then one will face formidable backgrounds and/or large experimental uncertainties.

The source should be cheaply available in large quantities. Clearly a compromise has to be made in the selection of the source. One can be optimistic that such adequate quantities can be produced in Russian reactors. The nuclide parameters

TABLE 2: Nuclides relevant for the search of the keV sterile neutrinos in the electron capture process. We give the life time $T_{1/2}$, the Q-value, the electron binding energy B_i for various captures, and the value of $\Delta = Q - B_i$. For details see [66].

Nuclide	$T_{1/2}$	EC transition	Q (keV)	B_i (keV)	B_j (keV)	$Q - B_i$ (keV)
^{157}Tb	71 y	$3/2^+ \rightarrow 3/2^-$	60.04(30)	K: 50.2391(5)	LI: 8.3756(5)	9.76
^{163}Ho	4570 y	$7/2^- \rightarrow 5/2^-$	2.555(16)	MI: 2.0468(5)	NI: 0.4163(5)	0.51
^{179}Ta	1.82 y	$7/2^+ \rightarrow 9/2^+$	105.6(4)	K: 65.3508(6)	LI: 11.2707(4)	40.2
^{193}Pt	50 y	$1/2^- \rightarrow 3/2^+$	56.63(30)	LI: 13.4185(3)	MI: 3.1737(17)	43.2
^{202}Pb	52 ky	$0^+ \rightarrow 2^-$	46(14)	LI: 15.3467(4)	MI: 3.7041(4)	30.7
^{205}Pb	13 My	$5/2^- \rightarrow 1/2^+$	50.6(5)	LI: 15.3467(4)	MI: 3.7041(4)	35.3
^{235}Np	396 d	$5/2^+ \rightarrow 7/2^-$	124.2(9)	K: 115.6061(16)	LI: 21.7574(3)	8.6

relevant to our work can be found in [66] (see also [67]), summarized in Table 2.

6. Modification of the End Point Spectra of β Decaying Nuclei

The end point spectra of β decaying nuclei can be modified by the reaction involving sterile (anti)neutrinos:

$$\nu + A(N, Z) \longrightarrow A(N-1, Z+1) + e^- \quad (46)$$

or

$$\bar{\nu} + A(N, Z) \longrightarrow A(N+1, Z-1) + e^+. \quad (47)$$

This can be exploited in ongoing experiments, for example, in the tritium decay:

$$\nu + {}^3_1\text{H} \longrightarrow {}^3_2\text{He} + e^-. \quad (48)$$

The relevant cross section is

$$\sigma(E_\nu) = C_\nu^2 \frac{1}{v} |\text{ME}(E_x)|_{\text{nuc}}^2 \left(\frac{G_F}{2\sqrt{2}} \right)^2 \frac{d^3 p_A}{(2\pi)^3} \frac{d^3 p_e}{(2\pi)^3} (2\pi)^4 \delta(\mathbf{p}_\nu - \mathbf{p}_A - \mathbf{p}_e) \delta(E_\nu + \Delta - E_e), \quad (49)$$

where Δ is the atomic mass difference. Integrating over the nuclear recoil momentum and the direction of the electron momentum we get

$$\sigma(E_\nu) = C_\nu^2 \frac{1}{v} |\text{ME}(E_x)|_{\text{nuc}}^2 \left(\frac{G_F}{2\sqrt{2}} \right)^2 \frac{1}{\pi} E_e P_e, \quad (50)$$

where

$$E_e = m_\nu + \frac{1}{2} m_\nu v^2 + \Delta + m_e, \quad (51)$$

$$P_e = \sqrt{E_e^2 - m_e^2}.$$

Folding the cross section with the velocity distribution we find

$$\langle \sigma v \rangle = C_\nu^2 \left(\frac{G_F}{2\sqrt{2}} \right)^2 \frac{2}{\pi^{3/2}} \int_0^{y_{\text{esc}}} dy f(y), \quad (52)$$

where

$$f(y) = |\text{ME}|^2 y \sinh(2y) E_e P_e e^{-(1+y^2)} F(Z_f, E_e) \quad (53)$$

with

$$y = \frac{v}{v_0}. \quad (54)$$

The Fermi function, $F(Z_f, E_e)$, encapsulates the effects of the Coulomb interaction for a given lepton energy E_e and final state proton number Z_f . The function $f(y)$ is exhibited in Figure 6.

In transitions happening inside the same isospin multiplet ($J^\pi \rightarrow J^\pi, J \neq 0$) both the vector and axial form factors contribute and in this case the nuclear matrix element $\text{ME}(E_x)$ can be written as

$$|\text{ME}|^2 = \langle \mathbf{F} \rangle^2 + \left(\frac{g_A}{g_V} \right)^2 \langle \mathbf{GT} \rangle^2, \quad (55)$$

where $g_A = 1.2695$ and $g_V = 1$ are the axial and vector coupling constants, respectively. In case of ${}^3\text{H}$ target we adopt $\langle \mathbf{F} \rangle^2 = 0.9987$ and $\langle \mathbf{GT} \rangle^2 = 2.788$ from [68]. Thus $|\text{ME}|^2 = 5.49$.

Thus the velocity averaged cross section takes the value

$$\langle \sigma v \rangle = 3.44 \times 10^{-46} C_\nu^2 \text{cm}^2 \quad (56)$$

and the expected event rate becomes

$$R = 3.44 \times 10^{-46} C_\nu^2 \times 6 \times 10^3 \times 6.023 \times 10^{23} \times \frac{m_t}{A} \times 9.28 \times 10^{17} \text{y}^{-1}. \quad (57)$$

For a mass of the current KATRIN target, that is, about 1 gr, we get

$$R = 0.380 C_\nu^2 y^{-1}. \quad (58)$$

It is interesting to compare the neutrino capture rate

$$\begin{aligned} R_\nu &= \langle \sigma v \rangle \frac{\rho}{m_\nu} \\ &= 3.44 \times 10^{-46} C_\nu^2 \times 6 \cdot 10^3 \times 9.28 \times 10^{17} \\ &= 1.91 \times 10^{-24} C_\nu^2 y^{-1} \end{aligned} \quad (59)$$

with that of beta decay process ${}^3\text{H} \rightarrow {}^3\text{He} + e^- + \bar{\nu}_j$, whose rate R_β is given by

$$R_\beta = \frac{G_F^2}{2\pi^3} \int_{m_e}^{W_o} p_e E_e F(Z, E_e) |\text{ME}|^2 E_\nu p_\nu dE_e, \quad (60)$$

where W_o is the maximal electron energy or else beta decay endpoint

$$W_o = K_{\text{end}} + m_e \quad (61)$$

with

$$\begin{aligned} K_{\text{end}} &= \frac{(m_{{}^3\text{H}} - m_e)^2 - (m_{{}^3\text{He}} + m_\nu)^2}{2m_{{}^3\text{H}}} \simeq \Delta \\ &= 18.591 \text{ keV}, \end{aligned} \quad (62)$$

the electron kinetic energy at the endpoint, and

$$\begin{aligned} m_e &\approx 510.998910 (13) \text{ keV} \\ m_{{}^3\text{H}} &\approx 2808920.8205 (23) \text{ keV} \\ m_{{}^3\text{He}} &\approx 2808391.2193 (24) \text{ keV}. \end{aligned} \quad (63)$$

Masses $m_{{}^3\text{H}}$ and $m_{{}^3\text{He}}$ are nuclear masses [58, 69, 70]. The calculation of (60) gives $R_\beta = 0.055 y^{-1}$. The ratio of R_ν to corresponding beta decay R_β is very small.

$$R_\nu = 0.034 \cdot 10^{-21} C_\nu^2 R_\beta. \quad (64)$$

The situation is more optimistic in a narrow interval $W_o - \delta < E_e < W_o$ near the endpoint. As an example, we consider an energy resolution $\delta = 0.2 \text{ eV}$ close to the expected sensitivity of the KATRIN experiment [57]. Then the ratio of the event rate $R_\beta(\delta = 0.2 \text{ eV})$ to that of neutrino capture R_ν , gives

$$R_\nu = 5.75 \cdot 10^{-9} C_\nu^2 R_\beta(\delta = 0.2 \text{ eV}). \quad (65)$$

In Figure 7 we present the ratio of the event rate decay rate of $R_\beta(\delta)$ for the beta decay compared with the neutrino capture rate R_ν , as a function of the energy resolution δ in the energy region $W_o - \delta < E_e < W_o$.

Moreover, the electron kinetic energy K_e due to neutrino capture process (48) is

$$K_e = E_\nu + K_{\text{end}} > m_\nu + 18.591 \text{ keV}; \quad (66)$$

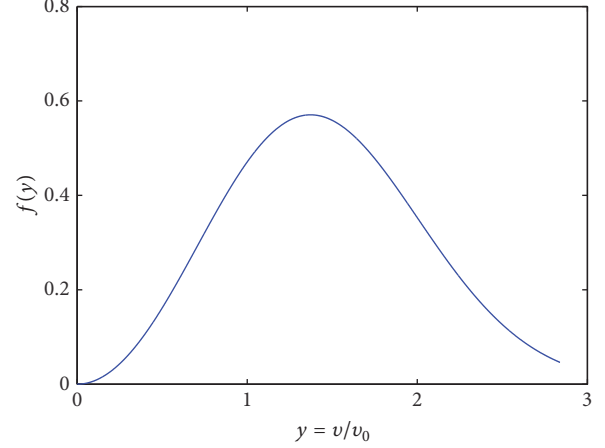


FIGURE 6: The shape of $f(y)$ for the decay of ${}^3\text{H}$, where the atomic mass difference between ${}^3\text{H}$ and ${}^3\text{He}$ is taking $\Delta = 18.591 \text{ keV}$ [69].

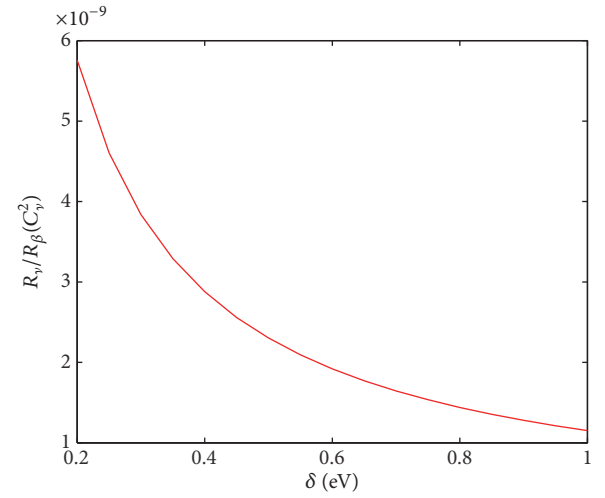


FIGURE 7: Ratio of decay rates R_ν/R_β (in units of C_ν^2) as a function of energy resolution δ near the endpoint.

this means that the electron in the final state has a kinetic energy of at least m_ν above the corresponding beta decay endpoint energy. There is no reaction induced background there, but, unfortunately, the ratio obtained above is much lower than the expected KATRIN sensitivity.

7. Discussion

In the present paper we examined the possibility of direct detection of sterile neutrinos of a mass 50 keV, in dark matter searches. This depends on finding solutions to two problems. The first is the amount of energy expected to be deposited in the detector and the second one is the expected event rate. In connection with the energy we have seen that, even though these neutrinos are quite heavy, their detection is not easy, since like all dark matters candidates move in our galaxies with not relativistic velocities, $10^{-3} c$ on the average, and with energies about 0.05 eV, not all of which can be deposited in the detectors. Thus the detection techniques employed in

the standard dark matter experiments, like those looking for heavy WIMP candidates, are not applicable in this case.

We started our investigation by considering neutrino-electron scattering. Since the energy of the sterile neutrino is very small one may have to consider systems with very small electron binding, for example, electron pairs in superconductors, which are limited to rather small number of electron pairs. Alternatively one may use low temperature bolometers, which can be larger in size resulting in a higher expected event rate. These experiments must be able to detect very small amount of energy.

Then we examined more exotic options by exploiting atomic and nuclear physics. In atomic physics we examined the possibility of spin induced excitations. Again to avoid background problems the detector has a crystal operating at low temperatures. Then what matters is the atomic structure of the ions of the crystal or of suitably implanted impurities. The rate in this case is less than that obtained in the case of bolometers, but one may be able to exploit the characteristic feature of the spectrum of the emitted photons.

From the nuclear physics point of view, we consider the antineutrino absorption on an electron capturing nuclear system leading to a fine resonance in the $(N+1, Z-1)$ system, centered 50 keV above the highest excited state reached by the ordinary electron capture. The deexcitation of this resonance will lead to a very characteristic γ ray. Finally the sterile neutrino will lead to $\nu + A(N, Z) \rightarrow e^- + A(N-1, Z+1)$ reaction. The produced electrons will have a maximum energy which goes beyond the end point energy of the corresponding β decay essentially by the neutrino mass. The signature is less profound than in the case of antineutrino absorption.

Regarding the event rate, as we have mentioned before, it is proportional to the coupling of the sterile neutrino to the usual electron neutrino indicated above as C_ν^2 . This parameter is not known. In neutrino oscillation experiments a value of $C_\nu^2 \approx 10^{-2}$ has been employed. With such a value our results show that the 50 keV neutrino is detectable in the experiments discussed above. This large value of C_ν^2 is not consistent, however, with a sterile 50 keV neutrino. In fact such a neutrino would have a life time [71] of 2×10^5 y, much shorter than the age of the universe. A cosmologically viable sterile 50 keV neutrino is allowed to couple to the electron neutrino with coupling $C_\nu^2 < 1.3 \times 10^{-7}$. Our calculations indicate that such a neutrino is not directly detectable with experiments considered in this work. The results, however, obtained for the various physical processes considered in this work, can be very useful in the analysis of the possible experimental searches of lighter sterile neutrinos in the mass range of 1–10 keV.

Appendix

A. Angular Momentum Coefficients Entering Atomic Excitations

The angular momentum coefficients entering single particle transitions are shown in (A.1) and (B.4).

Equation (A.1). The coefficients $(C_{\ell, j_1, m_1, j_2, m_2})^2$ connect via the spin operator a given initial state $|i\rangle = |n\ell, j_1, m_1\rangle$ with all possible states $|f\rangle = |n\ell, j_2, m_2\rangle$, for $\ell = 0, 1$. Note s-states are favored.

$$\left(\begin{array}{c|c} \begin{array}{ccccc} \ell & j_1 & m_1 & j_2 & m_2 \\ 0 & \frac{1}{2} & -\frac{1}{2} & \frac{1}{2} & \frac{1}{2} \end{array} & C_{\ell, j_1, m_1, j_2, m_2}^2 \\ \hline & 2 \end{array} \right),$$

$$\left(\begin{array}{cc|c} |i\rangle & |f\rangle & \\ \hline \ell & j_1 & m_1 & j_2 & m_2 & C_{\ell, j_1, m_1, j_2, m_2}^2 \end{array} \right) \quad (A.1)$$

ℓ	j_1	m_1	j_2	m_2	$C_{\ell, j_1, m_1, j_2, m_2}^2$
1	$\frac{1}{2}$	$-\frac{1}{2}$	$\frac{1}{2}$	$\frac{1}{2}$	$\frac{2}{9}$
1	$\frac{1}{2}$	$-\frac{1}{2}$	$\frac{3}{2}$	$-\frac{3}{2}$	$\frac{4}{3}$
1	$\frac{1}{2}$	$-\frac{1}{2}$	$\frac{3}{2}$	$-\frac{1}{2}$	$\frac{8}{9}$
1	$\frac{1}{2}$	$-\frac{1}{2}$	$\frac{3}{2}$	$\frac{1}{2}$	$\frac{4}{9}$
1	$\frac{1}{2}$	$\frac{1}{2}$	$\frac{3}{2}$	$-\frac{1}{2}$	$\frac{4}{9}$
1	$\frac{1}{2}$	$\frac{1}{2}$	$\frac{3}{2}$	$\frac{1}{2}$	$\frac{8}{9}$
1	$\frac{1}{2}$	$\frac{1}{2}$	$\frac{3}{2}$	$\frac{3}{2}$	$\frac{4}{3}$
1	$\frac{3}{2}$	$-\frac{3}{2}$	$\frac{3}{2}$	$-\frac{1}{2}$	$\frac{2}{3}$
1	$\frac{3}{2}$	$-\frac{1}{2}$	$\frac{3}{2}$	$\frac{1}{2}$	$\frac{8}{9}$
1	$\frac{3}{2}$	$\frac{1}{2}$	$\frac{3}{2}$	$\frac{3}{2}$	$\frac{2}{3}$

B. Exotic Atomic Experiments

As we have mentioned the atomic experiment has to be done at low temperatures. It may be difficult to find materials exhibiting atomic structure at low temperatures. It amusing to note that one may be able to employ at low temperatures some exotic materials used in quantum technologies (for a recent review see [72]) like nitrogen-vacancy (NV), that is, materials characterized by spin $S = 1$, which in a magnetic field allow transitions between $m = 0$, $m = 1$ and $m = -1$. These states are spin symmetric. Antisymmetry requires the space part to be antisymmetric, that is, a wave function of the form

$$\psi = \phi_{ne}^2(r) [L = \text{odd}, S = 1] \quad J = L - 1, L, L + 1. \quad (B.1)$$

Of special interest are

$$\psi = \phi_{ne}^2(r)^3 P_J, \quad \phi_{ne}^2(r)^3 F_J. \quad (B.2)$$

Then the spin matrix element takes the form

$$\begin{aligned} & \langle {}^3L_{J_2 m_2} | \sigma | {}^3L_{J_1 m_1} \rangle \\ & = \frac{1}{\sqrt{2J_2 + 1}} \langle J_1 m_1, 1 m_2 - m_1 | J_2 m_2 \rangle \\ & \cdot \langle {}^3L_{J_2} \| \sigma \| {}^3L_{J_1} \rangle, \quad L = P, F. \end{aligned} \quad (B.3)$$

The reduced matrix elements are given in (B.5), as well as the full matrix element $\langle {}^3P_{J_2 m_2} | \sigma | {}^3P_{J_1 m_1} \rangle^2$ of the most important component.

Equation (B.4). The same as in equation (A.1), the coefficients $(C_{\ell, j_1, m_1, j_2, m_2})^2$ for $\ell = 2$ are

ℓ	$ i\rangle$		$ f\rangle$		$C_{\ell, j_1, m_1, j_2, m_2}^2$
	j_1	m_1	j_2	m_2	
2	3	3	3	1	6
2	2	-2	2	-2	25
2	3	3	5	5	8
2	2	-2	2	-2	5
2	3	3	5	3	16
2	2	-2	2	-5	25
2	3	3	5	1	4
2	2	-2	2	-2	25
2	3	1	3	1	8
2	2	-2	2	2	25
2	3	1	5	3	24
2	2	-2	2	2	25
2	1	1	5	1	24
2	2	-2	2	-2	25
2	3	1	5	1	12
2	2	-2	2	2	25
2	3	1	3	3	6
2	2	2	2	2	25
2	3	1	5	1	12
2	2	2	2	-2	25
2	3	1	5	1	24
2	2	2	2	2	25
2	3	3	5	1	4
2	2	2	2	2	25
2	3	3	5	3	16
2	2	2	2	2	25
2	3	3	5	5	8
2	2	2	2	2	5
2	5	5	5	3	2
2	2	-2	2	-2	5
2	5	3	5	1	16
2	2	-2	2	-2	25
2	5	1	5	1	18
2	2	-2	2	2	25
2	5	1	5	3	16
2	2	2	2	2	25
2	5	3	5	5	2
2	2	2	2	2	5

(B.4)

J_1	J_2	$\langle {}^3P_{J_2} \sigma {}^3P_{J_1} \rangle$
0	1	$\sqrt{\frac{2}{3}}$
1	1	$\frac{1}{\sqrt{2}}$
1	2	$\sqrt{\frac{5}{6}}$
2	2	$\sqrt{\frac{5}{2}}$

J_1	J_2	$\langle {}^3F_{J_2} \sigma {}^3F_{J_1} \rangle$
2	2	$-\frac{\sqrt{10}}{3}$
2	3	$\frac{2\sqrt{5}}{3}$
3	3	$\frac{\sqrt{7}}{6}$
3	4	$\frac{3}{2}$
4	4	$\frac{\sqrt{15}}{2}$

J_1	m_1	J_2	m_2	$\langle {}^3P_{J_2 m_2} \sigma {}^3P_{J_1 m_1} \rangle^2$
0	0	1	m_2	$\frac{2}{9}$
1	-1	1	-1	$\frac{1}{6}$
1	-1	1	0	$\frac{1}{6}$
1	0	1	0	0
1	0	1	1	$\frac{1}{6}$
1	1	1	1	$\frac{1}{6}$

(B.5)

Disclosure

Permanent address of John D. Vergados is as follows: University of Ioannina, 451 10 Ioannina, Greece.

Conflicts of Interest

The authors declare that they have no conflicts of interest.

Acknowledgments

The authors are indebted to Professor Marco Bernasconi for useful suggestions in connection with the phonon excitations of low temperature bolometers.

References

- [1] P. Ullio and M. Kamiokowski, "Velocity distributions and annual-modulation signatures of weakly-interacting massive particles," *Journal of High Energy Physics*, vol. 2001, no. 03, 2001.

Equation (B.5). The coefficients are $\langle {}^3P_{J_2} | \sigma | {}^3P_{J_1} \rangle$, $\langle {}^3F_{J_2} | \sigma | {}^3F_{J_1} \rangle$, and $\langle {}^3P_{J_2 m_2} | \sigma | {}^3P_{J_1 m_1} \rangle^2$. For the notation see text.

- [2] D. Spergel, R. Bean, O. Doré et al., “Three-Year Wilkinson Microwave Anisotropy Probe (WMAP) Observations: Implications for Cosmology,” *The Astrophysical Journal Supplement Series*, vol. 170, no. 2, 2007.
- [3] P. A. R. Ade, M. Arnaud, and M. Ashdown, “Planck 2013 results. XXXI. Consistency of the Planck data,” *Astronomy & Astrophysics*, vol. 571, 2014.
- [4] A. Bottino, V. de Alfaro, N. Fornengo, A. Morales, J. Puimedon, and S. Scopel, “Exploring the supersymmetric parameter space by direct search for WIMPs,” *Physics Letters B*, vol. 402, no. 1-2, pp. 113–121, 1997.
- [5] R. Arnowitt and P. Nath, “Event rates in dark matter detectors for neutralinos including constraints from $b \rightarrow s$ gamma decay,” *Physical Review Letters*, vol. 74, no. 23, pp. 4592–4595, 1995.
- [6] R. Arnowitt and P. Nath, “Predictions of neutralino dark matter event rates in minimal supergravity unification,” *Physical Review D: Particles, Fields, Gravitation and Cosmology*, vol. 54, no. 3, pp. 2374–2384, 1996.
- [7] V. Bednyakov, H. Klapdor-Kleingrothaus, and S. Kovalenko, “Possible constraints on SUSY-model parameters from direct dark matter search,” *Physics Letters B*, vol. 329, no. 1, pp. 5–9, 1994.
- [8] J. Ellis and L. Roszkowski, “Supergravity dark matter,” *Physics Letters B*, vol. 283, pp. 252–260, 1992.
- [9] J. Ellis and R. A. Flores, “Elastic supersymmetric relic-nucleus scattering revisited,” *Physics Letters B*, vol. 263, pp. 259–266, 1991.
- [10] J. Ellis and R. A. Flores, “Prospects for neutralino detection with a $73\text{Ge} + 76\text{Ge}$ detector,” *Physics Letters B*, vol. 300, no. 1-2, pp. 175–182, 1993.
- [11] J. Ellis and R. A. Flores, “Implications of LEP on laboratory searches for dark matter neutralinos,” *Nuclear Physics B*, vol. 400, pp. 25–36, 1993.
- [12] S. Nussinov, “Some estimates of interaction in matter of neutral technibaryons made of colored constituents,” *Physics Letters B*, vol. 279, no. 1-2, pp. 111–116, 1992.
- [13] S. B. Gudnason, C. Kouvaris, and F. Sannino, “Dark matter from new technicolor theories,” *Physical Review D: Particles, Fields, Gravitation and Cosmology*, vol. 74, Article ID 095008, 2006.
- [14] R. Foot, H. Lew, and R. R. Volkas, “A model with fundamental improper spacetime symmetries,” *Physics Letters B*, vol. 272, no. 1-2, pp. 67–70, 1991.
- [15] R. Foot, “Mirror & hidden sector dark matter in the light of new CoGeNT data,” *Physics Letters B*, vol. 703, no. 1, pp. 7–13, 2011.
- [16] G. Servant and T. M. P. Tait, “Is the lightest Kaluza–Klein particle a viable dark matter candidate?” *Nuclear Physics B*, vol. 650, no. 1-2, pp. 391–419, 2003.
- [17] V. Oikonomou, J. Vergados, and C. C. Moustakidis, “Direct detection of dark matter rates for various wimps,” *Nuclear Physics B*, vol. 773, no. 1-2, pp. 19–42, 2007.
- [18] M. W. Goodman and E. Witten, “Detectability of certain dark-matter candidates,” *Physical Review D: Particles, Fields, Gravitation and Cosmology*, vol. 31, no. 12, pp. 3059–3063, 1985.
- [19] J. Angle, E. Aprile, F. Arneodo et al., “Search for light dark matter in XENON10 data,” *Physical Review Letters*, vol. 107, p. 051301, 2013.
- [20] E. Aprile, K. Arisaka, F. Arneodo et al., “Dark matter results from 100 live days of XENON100 data,” *Physical Review Letters*, vol. 107, p. 131302, 2011.
- [21] K. Abea, J. Hosakaa, and T. Iida, “Distillation of liquid xenon to remove krypton,” *Astroparticle Physics*, vol. 31, no. 4, pp. 290–296, 2009.
- [22] C. Ghag, D. Y. Akimov, H. M. Araújo et al., “Performance of the veto detector incorporated into the ZEPLIN-III experiment,” *Astroparticle Physics*, vol. 35, no. 2, pp. 76–86, 2011.
- [23] K. Ni, *Proceedings of the Dark Side of the Universe, DSU2011*, Beijing, China, 2011.
- [24] D. C. Malling, “After LUX: The LZ Program,” <https://arxiv.org/abs/1110.0103>.
- [25] D. S. Akerib and et al., “Limits on spin-dependent WIMP-nucleon interactions from the Cryogenic Dark Matter Search,” *Physical Review D*, vol. 73, 011102, 2006.
- [26] C. E. Aalseth, P. S. Barbeau, N. S. Bowden et al., “Results from a search for light-mass dark matter with a p -type point contact germanium detector,” *Physical Review Letters*, vol. 106, p. 131301, 2011.
- [27] E. Armengaud, C. Augier, A. Benoît et al., “Final results of the EDELWEISS-II WIMP search using a 4-kg array of cryogenic germanium detectors with interleaved electrodes,” *Physics Letters B*, vol. 702, no. 5, pp. 329–335, 2011.
- [28] R. Bernabei, P. Belli, F. Cappella et al., “First results from DAMA/LIBRA and the combined results with DAMA/NaI,” *The European Physical Journal C*, vol. 56, no. 3, pp. 333–355, 2008.
- [29] P. Belli, R. Bernabei, and A. Bottino, “Observations of annual modulation in direct detection of relic particles and light neutralinos,” *Physical Review D*, vol. 84, 055014, 2011.
- [30] H. S. Lee et al., “Limits on Interactions between Weakly Interacting Massive Particles and Nucleons Obtained with CsI(Tl) Crystal Detectors,” *Physical Review Letters*, vol. 99, 091301, 2007.
- [31] S. Archambault, F. Aubin, M. Auger et al., “Dark matter spin-dependent limits for WIMP interactions on ^{19}F by PICASSO,” *Physics Letters B*, vol. 682, no. 2, pp. 185–192, 2009.
- [32] S. Archambault, F. Aubin, M. Auger et al., “New Insights into Particle Detection with Superheated Liquids,” *New J. Phys. volume*, vol. 13, Article ID 043006, 2011.
- [33] C. Argüelles, N. Mavromatos, J. Rueda, and R. Ruffini, “The role of self-interacting right-handed neutrinos in galactic structure,” *Journal of Cosmology and Astroparticle Physics*, vol. 2016, no. 04, pp. 038–038, 2016.
- [34] R. Ruffini, C. R. Argüelles, and J. A. Rueda, “On the core-halo distribution of dark matter in galaxies,” *Monthly Notices of the Royal Astronomical Society*, vol. 451, no. 1, p. 622, 2015.
- [35] R. Argüelles, R. Ruffini, and J. A. Rueda, “Novel constraints on fermionic dark matter from galactic observables,” <https://arxiv.org/abs/1606.07040>.
- [36] A. Boyarsky, O. Ruchayskiy, and M. Shaposhnikov, “The role of sterile neutrinos in cosmology and astrophysics,” *Annual Review of Nuclear and Particle Science*, vol. 59, no. 1, pp. 359–379, 2009.
- [37] A. Boyarsky, J. Lesgourgues, O. Ruchayskiy, and M. Viel, “Realistic sterile neutrino dark matter with keV mass does not contradict cosmological bounds,” *Physical review letters*, vol. 102, 201304, 2009.
- [38] E. J. Tollerud, J. S. Bullock, L. E. Strigari, and B. Willman, “Hundreds of milky way satellites? Luminosity bias in the satellite luminosity function,” *The Astrophysical Journal*, vol. 688, no. 1, pp. 277–289, 2008.
- [39] M. D. Campos and W. Rodejohann, “Testing keV sterile neutrino dark matter in future direct detection experiments,” *Physical Review D: Particles, Fields, Gravitation and Cosmology*, vol. 94, no. 9, 2016.

- [40] Y. Li, X. Z. zhong, and L. Shu, "Direct detection of the cosmic neutrino background including light sterile neutrinos," *Physics Letters B*, vol. 692, no. 4, 1010.
- [41] Y. F. Li and Z. zhong Xing, "Captures of hot and warm sterile antineutrino dark matter on EC-decaying Ho-163 nuclei," *Journal of Cosmology and Astroparticle Physics*, vol. 08, p. 006, 2011.
- [42] A. Giorgio, "The Waning of the WIMP? A Review of Models, Searches, and Constraints," <https://arxiv.org/abs/1703.07364>.
- [43] W. Liao, *Physical Review D*, vol. 82, 073001 pages, 2010.
- [44] R. Adhikari, M. Agostini, and N. Anh Ky, "A White Paper on keV sterile neutrino Dark Matter," *Journal of Cosmology and Astroparticle Physics*, vol. 2017, 2017.
- [45] A. Aguilar-Arevalo et al., "Evidence for neutrino oscillations from the observation of $\bar{\nu}e$ appearance in a $\bar{\nu}\mu$ beam," *Physical Review D*, vol. 64, 112007, 2001.
- [46] A. A. Aguilar-Arevalo, B. C. Brown, and L. Bugel, "Improved Search for $\bar{\nu}\mu \rightarrow \bar{\nu}e$ Oscillations in the MiniBooNE Experiment," *Physical Review Letters*, vol. 110, 6 pages, 2013.
- [47] T. Katori and J. M. Conrad, "Beyond Standard Model Searches in the MiniBooNE Experiment," *Advances in High Energy Physics*, vol. 2015, Article ID 362971, 19 pages, 2015.
- [48] T. A. Mueller, D. Lhuillier, and M. Fallot, "Improved predictions of reactor antineutrino spectra," *Physical Review C: Nuclear Physics*, vol. 83, no. 5, Article ID 054615, 2011.
- [49] J. N. Abdurashitov et al., "Measurement of the response of a Ga solar neutrino experiment to neutrinos from a ^{37}Ar source," *Physical Review C*, vol. 73, 045805, 2006.
- [50] J. Kopp, P. A. N. Machado, M. Maltoni, and T. Schwetz, "Sterile neutrino oscillations: the global picture," *Journal of High Energy Physics*, vol. 1305, 2013.
- [51] C. Giunti, M. Laveder, Y. F. Li, and H. W. Long, "Pragmatic view of short-baseline neutrino oscillations," *Physical Review D: Particles, Fields, Gravitation and Cosmology*, vol. 88, no. 7, 2013.
- [52] G. Mention, M. Fechner, and T. H. Lasserre, "Reactor antineutrino anomaly," *Physical Review D*, vol. 83, 073006, 2011.
- [53] T. Asaka, S. Blanchet, and M. Shaposhnikov, "The νMSM , dark matter and neutrino masses," *Physics Letters B*, vol. 631, no. 4, pp. 151–156, 1985.
- [54] A. Kusenko, "Sterile neutrinos: The dark side of the light fermions," *Physics Reports*, vol. 481, no. 1-2, pp. 1–28, 2009.
- [55] L. Heurtier and D. Teresi, "Dark matter and observable lepton flavor violation," *Physical Review D: Particles, Fields, Gravitation and Cosmology*, vol. 94, no. 12, 2016.
- [56] N. E. Mavromatos and A. Pilaftsis, "Anomalous Majorana Neutrino Masses from Torsionful Quantum Gravity," *Physical Review D*, vol. 86, p. 124038, 2012.
- [57] KATRIN collaboration, "KATRIN: A next generation tritium beta decay experiment with sub-eV sensitivity for the electron neutrino mass," <https://arxiv.org/abs/hep-ex/0109033>.
- [58] J. Beringer et al., "Review of Particle Physics," *Physical Review D*, vol. 86, article 010001, Article ID 010001, 2012.
- [59] Y. Hochberg, M. Pyle, Y. Zhao, and K. M. Zurek, "Detecting superlight dark matter with Fermi-degenerate materials," *Journal of High Energy Physics*, vol. 2016, no. 8, article no. 57, 2016.
- [60] M. Ceriotti, F. Pietrucci, and M. Bernasconi, *Physical Review B: Condensed Matter and Materials Physics*, vol. 73, no. 10, 2006.
- [61] M. Barucci, C. Brofferio, A. Giuliani, E. Gottardi, I. Peroni, and G. Ventura, "Measurement of Low Temperature Specific Heat of Crystalline TeO₂ for the Optimization of Bolometric Detectors," *Journal of Low Temperature Physics*, vol. 123, no. 5-6, pp. 303–314, 2001.
- [62] J. Vergados and Y. N. Novikov, "Prospects of detection of relic antineutrinos by resonant absorption in electron capturing nuclei," *Journal of Physics G: Nuclear and Particle Physics*, vol. 41, article 125001, Article ID 125001, 2014.
- [63] J. Toivanen and J. Suhonen, "Microscopic quasiparticle-phonon description of odd-A Xe isotopes," *Journal of Physics*, vol. 21, no. 11, 1995.
- [64] J. Toivanen and J. Suhonen, "Microscopic quasiparticle-phonon description of odd-mass $^{127-133}\text{Xe}$ isotopes and their β decay," *Physical Review C: Nuclear Physics*, vol. 57, no. 3, pp. 1237–1245, 1998.
- [65] R. G. Helmer, "Nuclear data sheets for A = 157," *Nuclear Data Sheets*, vol. 103, no. 4, pp. 565–782, 2004.
- [66] P. E. Filianin, K. Blaum, S. A. Eliseev et al., "On the keV sterile neutrino search in electron capture," *Journal of Physics G: Nuclear and Particle Physics*, vol. 41, no. 9, Article ID 095004, 2014.
- [67] J. D. Vergados and Y. N. Novikov, "Exploring new features of neutrino oscillations with very low energy monoenergetic neutrinos," *Nuclear Physics B*, vol. 839, no. 1-2, pp. 1–20, 2010.
- [68] R. Schiavilla, V. G. J. Stoks, and W. Glöckle, "Weak capture of protons by protons," *Physical Review C*, vol. 58, no. 1263, 1998.
- [69] G. Audi, A. Wapstra, and C. Thibault, "The Nubase evaluation of nuclear and decay properties," *Nuclear Physics A*, vol. 729, no. 1, pp. 3–128, 2002.
- [70] J. A. Bearden and A. F. Burr, "Reevaluation of X-ray atomic energy levels," *Reviews of Modern Physics*, vol. 39, no. 1, pp. 125–142, 1967.
- [71] A. D. Dolgov and S. H. Hansen, "Massive sterile neutrinos as warm Dark Matter," *Astroparticle Physics*, vol. 16, no. 3, pp. 339–344, 2002.
- [72] M. W. Doherty, N. B. Manson, P. Delaney, F. Jelezko, J. Wrachtrup, and L. C. L. Hollenberg, "The nitrogen-vacancy colour centre in diamond," *Physics Reports*, vol. 528, no. 1, pp. 1–45, 2013.